UAB

Universitat Autònoma de Barcelona

DEVELOPMENT OF MICROELECTROMECHANICAL SYSTEMS FOR RF SIGNAL PROCESSING

PhD Thesis

Joan Josep Giner de Haro

Supervised by

Arantxa Uranga Del Monte

ECAS

ELECTRONIC CIRCUITS AND SYSTEMS

Bellaterra (Cerdanyola del Vallès), Juliol del 2012

AGRAÏMENTS:

La el contingut d'aquesta tesis es la meva contribució al desenvolupament dels sistemes microelectromecànics, una petita empenta cap endavant, un pas mes en un camí que es va iniciar fa molt de temps i del que encara queda molt per recórrer: aconseguir el un capçal de radio freqüència que combina elements mecànics i elèctrics completament integrat.

Durant el recorregut d'aquest camí he trobat acompanyat que han ajudat a fer la feina menys feixuga, mes interessat i mes emocionant i als que, ara, aprofito per agrair-los-hi.

En primer lloc a l'Arantxa Uranga, la meva directora de tesis, amb la que he passat mes hores que amb la meva mare. Gracies per ser tant pacient, tant positiva i saber en tot moment quan i quant exigir-me més. Ha esta un plaer compartir xerrades, discussions, tensions i emocions.

A la Nuria Barniol per acollir-me al grup ECAS. La seva visió, quasi sempre crítica, i la seva experiència m'han permès enfocar els problemes des d'altres punts de vista i ser curós en les reflexions.

Agrair (o no) al Gabriel Abadal, que gracies al Gerard Zamora, em va"reclutar" fa 5 anys per formar part del Departament d'Enginyeria Electrònica de la Universitat Autònoma de Barcelona. Gracies a tu, he gaudit de l'experiència docent. Ens ha quedat pendent anar-hi amb algun MEMS al Sonar, a fer una demostració.

A tots el altres membres del grup ECAS, per que tots haveu contribuït: Francesc Torres, per els coneixements sobre tecnologia i física, a l'Eloi Marigò, sobre tot, per fer-me totes i cada una de les imatges SEM d'aquesta tesis, mentre que jo somiava despert a la sala blanca. Al tito Gon per ser tan "agradable", al Jordi Agustí per compartir aquelles converses sobre temes diametralment oposats a la recerca. Al Gabriel Vidal per ensenyar-me que no em vull dedicar a la ciència teòrica, i en especial al Jose Luis Muñoz que ha compartit la obsessió pel "culte al cos" amb mi.

A tots els membres del departament, al Yepes per el servei de taxi i en especial a, per una banda al Javier Hellin, per el seu suport tècnic a la docència i la recerca, i al trio de secretaria, Xio, Mª Carmen i Toñi per ser pacient i deixar-me les claus del meu despatx al menys un cop al mes durant uns anys, soc un despistat.

Per suposat als meus pares, l'Angel i la Maribel, que des de petit em van ensenyar la cultura del esforç, la importància del estudi. Gracies per estar en els moments mes complicats, sobretot, d'aquest últim any, per aconsellar-me sempre i per comprendre'm.

Finalment a la Lorena, la meva futura dona, que ha entès, quasi sempre, la feina que feia i m'ha animat i suportat.

Realment en aquesta tesis hi ha contribucions de tothom amb qui he compartit moments els darrers 4 anys, estic segur que tots heu deixat alguna petjada en mi que de manera intrínseca consta en aquest llibre.

Resum:

El objectiu d'aquesta tesis ha sigut l'estudi de ressonadors CMOS-MEMS monolíticament integrats per a la seva aplicació en transceptors de radio freqüència. En concret s'ha treballat sobre filtre y ressonadors de RF així com la seva caracterització.

En el camp del filtres s'han investigat dos tipus de conceptes: el filtres series i els filtres paral·lels. Els filtre sèrie desenvolupats en aquesta tesi consten de dos tipus d'acoblament: acoblament mecànic, dintre dels quals s'han estudiat dos tipus d'acobladors (en forma de U i en forma de V) i l'acoblament electrostàtic. En els filtres mecànics el ample de banda es defineix amb el disseny de l'acoblador i el punt d'acoblament amb el ressonador mentre que en els filtre electrostàtics, en teoria, el ample de banda el fixa la diferencia de tensió entre els ressonadors. Els filtres en paral·lel, permeten aconseguir, gracies a la seva integració amb la circuiteria, una millor del rebuig fora de banda comparats amb els filtres anteriors. D'altra banda s'ha combinat el filtrat paral·lel i els filtres series per aconseguir un filtre dual.

En el camp dels ressonador en el rang de VHF i UHF s'han dissenya fabricat i mesurat dos tipus de ressonador basat en la ressonància longitudinal de la estructura (LBAR): el LBAR millorat, al que se li han afegit dues masses en els seus extrem lliures, i que treballa a una freqüència de 250MHz i el LBAR hiperbòlic, capaç d'assolir freqüències al voltant dels 380MHz

S'ha estudiat la caracterització dels elements ressonant d'aquesta tesis, transduits electrostàticament. S'ha proposat una nova topologia basada en la fabricació de quatre elèctrodes que permet eliminar per complert la capacitat paràsita en aquest tipus de transducció.

Summary:

The objective of this thesis is the study of CMOS MEMS monolithically integrated resonators, for RF transceivers applications. In particular, it has focuses on design and characterization of RF resonators and filters.

Two types of filter concepts have been investigated: series filtering and parallel filtering. The series filters are composed of two different coupling methods: mechanical couplings that are divided into two types of couplers (the U-coupler and the V-coupler), and the electrostatic coupling. In mechanical coupled resonator filters, the bandwidth is fixed through the coupler design and the selection of its coupling point with the resonator whereas in the electrostatic filters the voltage applied between the constituent resonators fixes the bandwidth. The parallel filter allows increasing the out of band rejection due to the integration with circuitry. Finally, the parallel filtering and series filtering have been combined to achieve a dual filter.

In the field of RF resonators, two types of resonator based on longitudinal acoustic resonance have been designed, fabricated, and measured: The enhanced LBAR, that includes to masses at the free ends in order to increase the coupling area, works at 250MHz and the hyperbolic LBAR that is capable to reach 380MHz resonant frequency.

The electrostatic actuated mad capacitive read MEM devices characterization has been studied. In addition a new four-electrode based topology has been propose in order to cancel the feedthrough current that exists in this type of transduction.

CONTENTS:

x

Chapter.1 INTRODUCTION

MEMS devices have become in the future keys to obtain a fully integrated, low power consumption, low cost, and high performance RF transceiver. In consumer electronics world the milestone is to obtain a handset on chip and recent advances in RF-MEMS promise that the way to reach it is even shorter. To understand the modest contribution of this work to this huge task is necessary to understand the basic concepts of RF signal processing, MEMS fabrication and integrations and the objectives of this work.

1.1 INTRODUCTION

Microelectromechanical systems (MEMS) are a loosely defined term for mechanical components that are characterized by small size. Taking literally the forming words, MEMS have to be in the micro-scale, and are capable to deal with mechanical and electrical variables [1]. However, many other micromachined devices such as microfluidical-oriented systems are commonly known as MEMS and they are not enabled with any electrical signal.

The earliest reference of the power of miniaturization, which is also considered as one of the most enlightening vision of the MEMS topic, was provided by Dr. Feynmann in a conference given in the annual meeting of the American Physics Society in 1959("there is a plenty of room at the bottom"), which was later reprinted in the Journal of MEMS in [2]. Starting one year later, researchers experimented with using integrated circuit technologies, for instance lithography, silicon etching, and thin film growth, to make mechanical structures. It was Nathanson in [3] who obtained the earliest MEM device. Due the immaturity of the MEMS technology, it was not commercially successful. However, this work established the solid base to adopt the microelectromechanical techniques to develop pressure sensors and accelerometers. Many of the early processes and applications are summarized in [4].

However, the MEMS technology took off in early 90's when several commercial products become available in mass market applications: ink-jet printer heads [5], and airbag accelerometers [6]. Other current application are addressed to sensing: pressure sensors [7], gyroscopes [8], digital light processors (DLP) [9], memories [10]chemical and biological applications [11-12]as well as actuators and microphones [13].

The advantages provided by the miniaturization of MEMS have driven the research effort towards the RF applications. It was Howe and Nguyen [14] one of the pioneers on applying the micro machined devices into the signal processing. They established the first stone to construct this thesis.

The most illustrative example of the importance and ubiquitous of MEMS devices can be found in the current smartphones. Currently the new commercial smartphones agglutinate almost all the above-mentioned components in a small area (for instance 50mm x 110 mm for an Iphone) (see Figure 1.1)
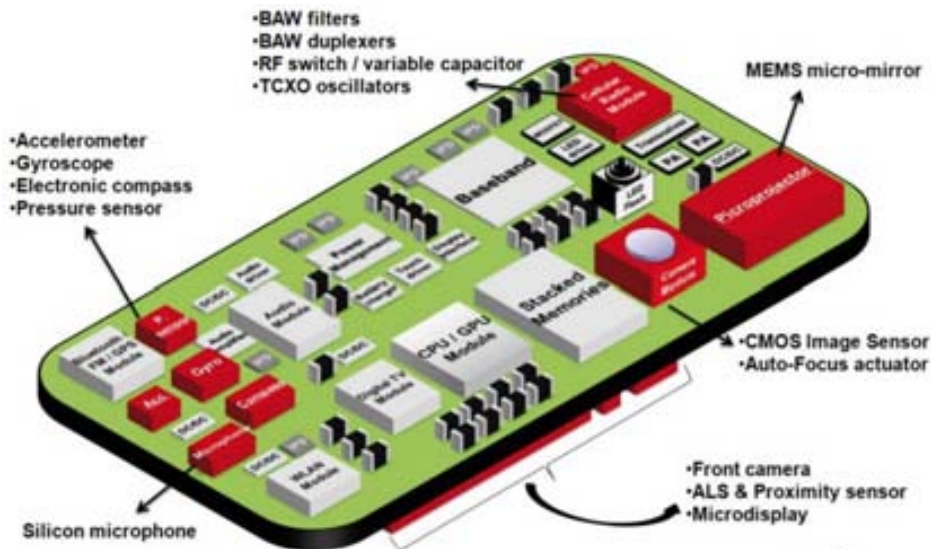
Figure 1.1. Simplified schema of a smartphone board.

In this chapter, the use of MEMS in RF processor is explained. The main fabrication techniques and the three integration approaches are reviewed. Since this thesis is based on the post-CMOS process over a commercial CMOS technology, our CMOS-MEMS approach is explained from the design to the electrical characterization. The research framework of this work and the objectives that we expect to reach are listed in the last section.

1.2 MEMS IN RF: OVERVIEW AND RESEARCH MOTIVATION.

The high demand on wireless communications and devices is driven into a miniaturization of radio frequency transceivers. In this miniaturization process, tradeoff between cost, size, performance, and power consumption is crucial. In terms of size, for instance, the off-chip components in RF front-ends suppose one of miniaturization bottleneck. It is here where the MEMS are the advantageous alternative.

The possibility to use micromechanical devices to mechanically process electrical high frequency signals has allowed labeling these devices as RF-MEMS. Into this enormous group, switches, filters, phase shifters, tunable capacitors, high Q inductors, and MEM resonators can be found.

2

1.2.1 MARKET PERSPECTIVES FOR RF-MEMS

Current RF-MEMS market is divided into two different needs: a) to provide communicability to wireless sensor nodes and b) to increase the application and the performance in next generation mobile handsets.

Wireless Sensors Network consists on spatially distributed autonomous devices that use sensors to cooperatively monitor physical or environmental conditions, such as temperature, sound, vibration at different location, it is known as "internet of things" [15]. The node that constitutes the network has to be capable to process RF signal in the transmission and reception direction. Depending on the communication standard, different requirements for the RF-MEMS will be set.

On the other hand, new generation of portable handsets are including more and more functionalities and applications that usually implies the use of different communication standards in the same device. For cellular communication, GSM, UMTS and HDSPA are already available in all the commercial cellphones. Therefore, multiplexer, switches and different filters banks are needed. The interconnectivity technologies such us Wi-Fi or Bluetooth require of a specific signal processing capabilities

For all these reasons, the forecast of turnover related to RF-MEMS component is expected to increase from 359M in 2010 to 850M in 2016 that means to double the turnover (see Figure 1.2).
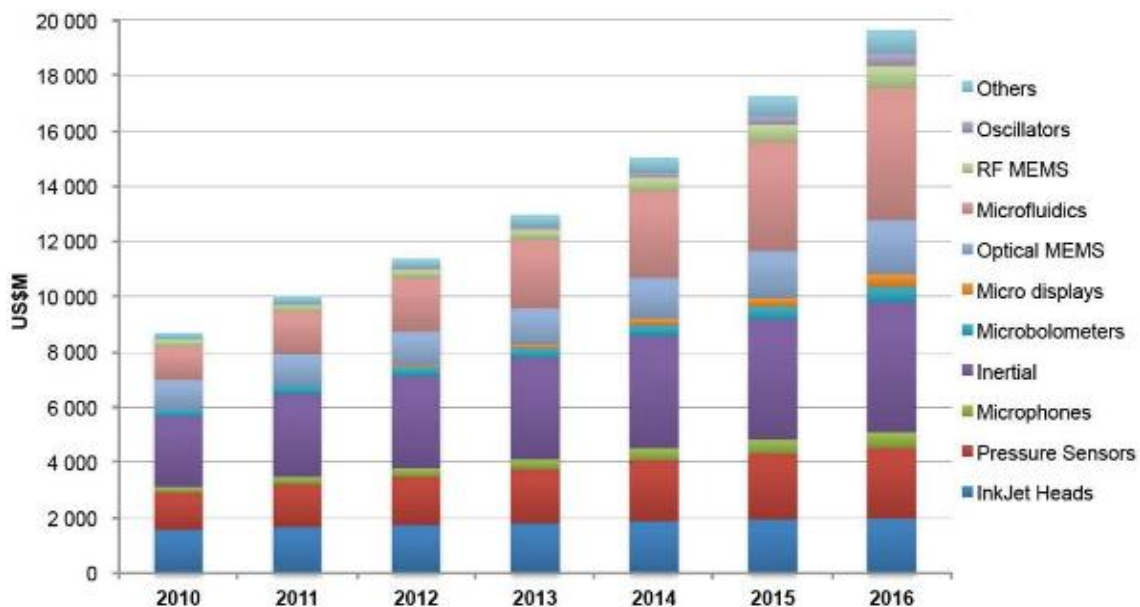
Figure 1.2. Market perspectives forecast in MEMS industry. Obtained from a public summary of the Status of the MEMS Industry Report 2011 [16].

1.2.2 RF APPLICATION IN A RF FRONT-END. MECHANICAL RADIO.

In the previous paragraph, we have seen that wireless communications are still in the bull's eye of MEMS industry. However, there is a question to solve; How the RF-MEMS can improve the wireless radios?

Figure 1.3 shows the diagram a super heterodyne transceiver where the blue shadowed parts indicates that are suitable to be replaced by MEMS devices.
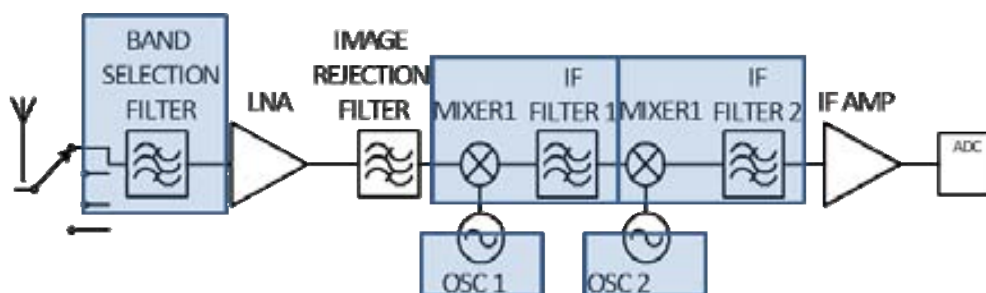
Figure 1.3. Diagram of a super-heterodyne transceiver- Shades squares indicated the parts of the front end that can be replaced by MEMS.

The band selection filter discriminates the useful range of frequency for a determined application (GSM, UMTS...). This filter is allocated immediately after the antenna. A low noise amplifier (LNA) boosts the received signal to be electrical and efficiently processed by the following stages. The image interference is rejected by the image filter and the signal is down converted to IF frequencies by one or more mixing stages. The mixing stages are driven by a local oscillator (OSC). The channel filter is located immediately after the mixing stage. One of the reasons is to relax the Q requirements of the IF filter. Since the channel filter has to filter a narrow band the Q factor at IF frequencies may be lower. Depending on the type of transceiver, it may present one or more mixing stages to relax more or less the specifications of the component. However having more than one mixing stage supposes and increment on the number of components.

In RF front-end, the control frequency devices, *e.g.* resonators, are required to have high quality factor (<1000) in the VHF to UHF range. A high quality factor means that the resonator vibrates in a very narrow range of frequencies. The great advances in MEM resonators allow to obtain devices with Q factors in the range of thousands [17-20] in the GHz range. These advances allow very high selective filters that can play the band-selection filter role to be fabricated. In range of HF and VHF, MEMS can constitute very good channel filters [21-22]. Furthermore, the non-linear properties the electrically transduced MEM devices allows the replace the mixer and the IF filter by "Mixlers" [23]. The frequency generator in oscillators that are used to down convert the received signal can replace by microelectromechanical resonator [24].

The most innovative use of MEMS resonators is based on more aggressive architectures proposals. For instance, since high Q high frequency MEMS can be used as a band selection filter it is possible to fabricate a band-selection filter bank after the antenna. However, we can go further and propose a more aggressive approach that would have channel selection filter bank immediately after the antenna. This approach would suppose to have hundreds of MEMS parallel filters and would require a large amount of space if it was implemented with other type of off-chips components. On the other hand, the oscillator that down-converts the selected channel into IF frequencies can be implemented by means of a bank of voltage tunable resonators (each resonator for a certain range of frequencies). Figure 1.4 shows the diagram of a modified super-

heterodyne transceiver where the green shadowed parts shows the replaceable frequency control components.
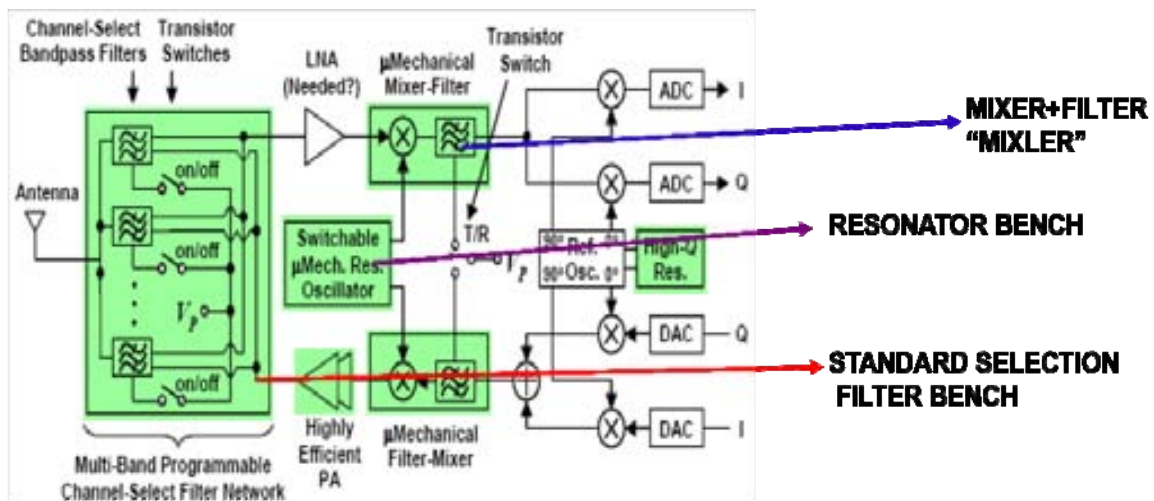
Figure 1.4. Diagram of a super heterodyne transceiver with all the replaceable-by-MEMS off-chip components shaded.

However, the benefits afforded by vibrating RF MEMS technology go far beyond mere component replacement. In fact, the extent to which they offer performance and economic benefits grows exponentially as researchers and designers begin to perceive these devices more as on-chip building blocks than as discrete stand-alone devices. In particular, by mechanically linking vibrating mechanical structures into more general networks, "integrated micromechanical circuits" can be conceived capable of implementing virtually any signal processing function presently realizable via transistor circuits, and with potential power and linearity advantages, especially for functions that involve frequency processing [25]. In this approach, the integration of MEMS with the circuitry is the key issue.

1.3 MEMS FABRICATION TECHNOLOGIES. TOWARDS THE FULLY INTEGRATED DEVICES

MEMS resonator are fabricated using two basic techniques: bulk micromachining and surface micromachining.

Bulk micromachining covers all the techniques that remove significant amount of substrate, or bulk, material (see Figure 1.5 b). Silicon is considered as the basic mechanical material, however, sometimes the diamond is used as structural material whereas the silicon is used as a sacrificial material [26].

Surface micromachining involves the deposition of different material films on the wafer surface and selectively removing one or more of these layers (sacrificial layers) to leave freestanding structures. In Figure 1.5 a), a schema of the process is shown.

Generally, the structures obtained by means of the bulk micromachining are better from the mechanical properties point of view. However, the surface micromachining presents a more simple fabrication process flow since it can include etching stoppers.

1.3.1   INTEGRATION APPROACHES. DO IT IN THE MIDDLE.

The integration of electronics and mechanics is the way to widen the performances range for different MEMS application. In RF applications, for instance, where the signal processing at the baseband has to be performed digitally makes necessary to consider the linkage between the mechanics and electronics (usually CMOS). Due to the integration of MEMS and IC, a high diversification level can be achieved (see Figure 1.6). Currently the semiconductor industry is constantly downscaling as well as the mechanics industry. However, the scaling trend is different for both parts. The electronics scaling trend is known as the Moore's law, whereas the mechanical devices is not scaling with that law but also the More than Moore [27] law

a)   b)

Figure 1.5. a) Shows a simple Surface Micromachining process. In this case, a Focused Ion Beam (FIB) has been used to define the polysilicon structure. b) shows a bulk micromachining process.

Figure 1.6. Conceptual map of the integration of MEMS and IC extracted from [28]

From the integration point of view, there are two different concepts to integrate both parts: a) System-in-Package, SiP, or b) System- on Chip, SoC.

The System-in-Package, SiP, consists on the fabrication of the MEMS and IC in different substrates. This approach offers the best performance for both parts since it allows using state-of-the-art techniques for circuits and mechanics. For instance, thicker layer for the mechanical device fabrication or low power electronics for the IC fabrication are achieved. However, it has the integration cost drawback since both separate substrates has to be interconnected finally. To link both parts, multiple chip wafer bonding [29], flip-chip [30], or 3-D stacking of multiple chips [31] (see Figure 1.7) may be used.

In addition, in systems composed by separate chips, the parasitic capacitances and resistances of the interconnections, bond pads, and bond wires can attenuate the signal, contribute significant noise, and place a ceiling on the maximum operating frequency [32].
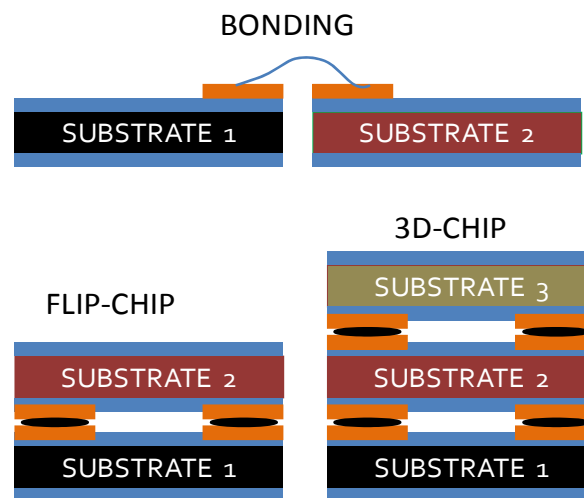
Figure 1.7. Types of system in Package interconnection techniques.

The System-on-chip (SoC) approach is based on having both the MEMS and the IC in the same die. This monolithic approach reduces the integration costs related with the bonding process. In addition, the parasitic associated to the interconnections are mitigated. For this reason, this is the approach considered in the most of the works produced in the Electronic Circuits and System Group (ECAS) in the Universitat Autónoma de Barcelona.

Several considerations have to be taken into account in order to be successful in the monolithically integration:

A low thermal budget is required after metallization of the IC. High temperatures can case metal diffusion into dielectrics.

The thick MEMS structural and sacrificial layers can be a problem for the required high resolution lithography of the CMOS circuits (that usually is compressed of several tens/hundred of nanometers)

Electrical interconnects between the MEMS and electronics are an important consideration, since they should be minimum length and be made in a highly conductive layer.

It is necessary to protect the electronics (pads, electrical paths made of topper metals) from the MEMS release etchant.

In general, there are three basic approaches oriented to obtain the monolithically integrated devices. Depending on when the MEMS are fabricated, they can be sorted in: two modular approaches such us: a) Pre-CMOS or MEMS first and b) Post CMOS, and finally an interleaved process: c) Intra-CMOS

In the *pre-CMOS* approach, the MEMS are fabricated before the CMOS process. In this approach, the CMOS circuitry is not affected by the micromachining, however, the MEMS has to be protected during the CMOS process. Silicon on Insulator (SoI) wafers are used to fabricate the mechanical components. The wafer that includes the MEMS is delivered to a CMOS foundry. One of the main restrictions is that the wafer has to meet very stringent criteria respect the contaminations to be able to be accepted by the foundry.

The pre-CMOS approach was utilized successfully in Stanford University to fabricate humidity sensors, accelerometer, and other MEMS devices, [33-36]. In Figure 1.8, the cross section of the fabrication pre-CMOS process used in Stanford is shown. Besides to provide the MEMS before the CMOS fabrication, this process allows to obtain a sealed (vacuum encapsulated) MEMS. In Figure 1.9, the SEM image of a tuning fork cross section fabricated using the aforementioned process is shown.
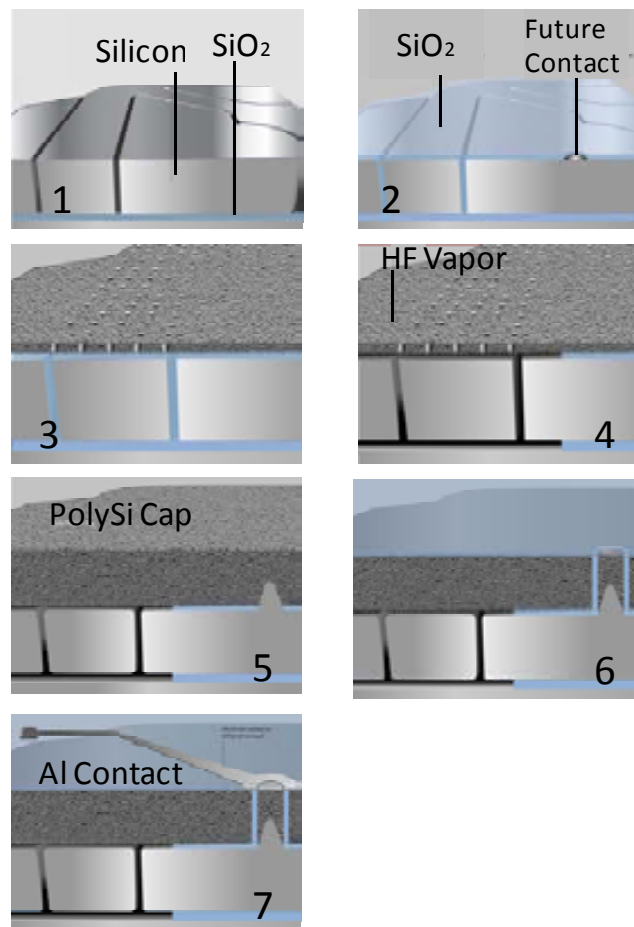
Figure 1.8 Cross section pre-CMOS-MEMS fabrication process used in Stanford University [37].
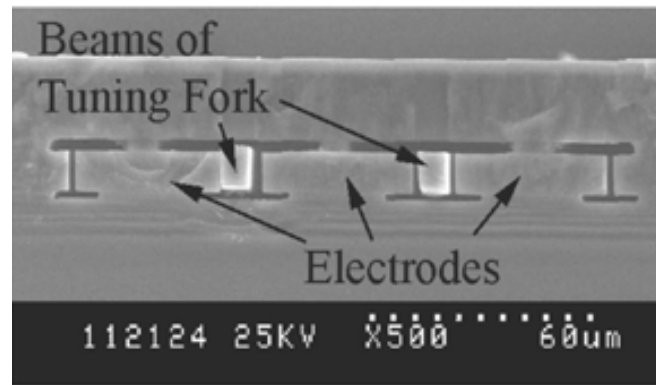
Figure 1.9 Cross-Section of a fabricated tuning fork.[38].

In the *post-CMOS* process, the MEMS and the IC are fabricated in two separated processes. The MEMS is fabricated once the CMOS devices are completely finished. One of the advantages of this process is that no chip area is used to implement the mechanical parts. The price to pay for this fabrication flexibility is that the thermal budget for the MEMS fabrication is reduced [39]. The most of aluminum (Al) metallization supports up to 450ºC and that excludes the most of the micromachining process (depositions, annealing…).

There are two types of post-CMOS approximations: Micromachining of Add-on layers and micromachining of the CMOS layers. Into the first alternative, the work presented by Huang *et.al* in [40] presents a fully integrated (MEMS+IC) oscillator. The Micromechanical resonator was fabricated over the CMOS layer using electroplated nickel as structural material with a temperature ceiling of only 50ºC.

The post-CMOS approaches that were invented in Carnegie Mellon University in [41-42] can be sorted into the second alternative. In Figure 1.10, a cross section of the technological process steps of the CMU approach is shown. The undesired dielectric was removed by oxide plasma etch process using the top metal layer as a mask. An anisotropic silicon plasma etch was done using an SF_6/O_2 etch process and a passivation process to set the depth of the etch pit between the MEMS devices and the substrate. The moveable elements were released from the substrate during isotropic silicon etching process.

Intra-CMOS usually means that special MEMS process steps are inserted between the front-end-of-line and back-end-of-line in the CMOS process flow. This process consists on modify slightly the process by adding, interleaving or customizing any fabrication steps [43] to obtain the desired mechanical module [44]. In particular, the MEMS process takes place after the transistors definition and before the last metallization step. In Figure 1.11 the cross section a well-known intra-CMOS process is depicted.

In this thesis, a post-CMOS approach has been used, as it will be explained in section 1.4. A commercial CMOS technology is used to define the circuitry and the structural material in the same chip. The use of a well-established microfabrication technology takes advantage of its robust process as well as the good circuitry performances. A micromachining process is used to eliminate the sacrificial layer and release the structure.
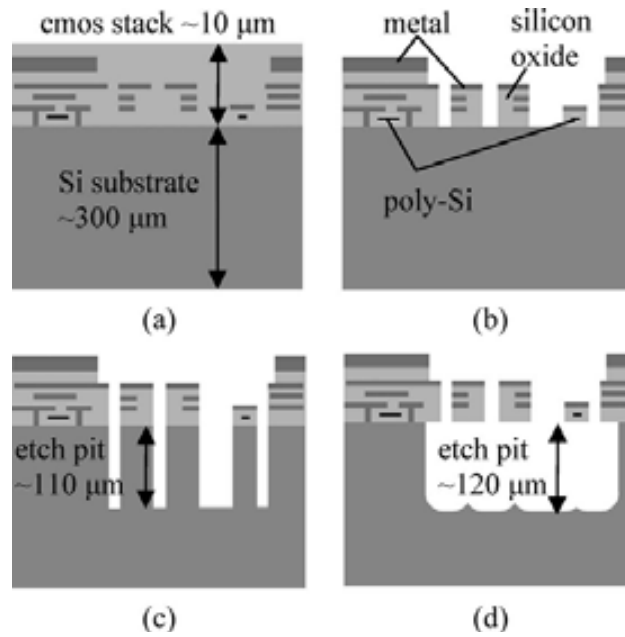
Figure 1.10. Cross section process of the post CMOS micromachining used in [45]. A presents the cross section of the unprocessed CMOS layer.
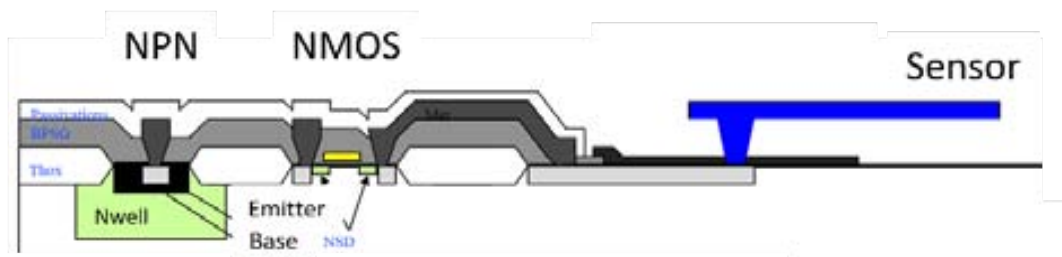
Figure 1.11. Cross section of the intra CMOS process (adapted from [43])

1.4 CMOS-MEMS FABRICATION

In this section, the fabrication process used to obtain all the devices of this thesis is explained. The process flow is described in Figure 1.12. The first step consists on choosing the right CMOS technology. Commercial foundries present different available CMOS technologies from 800nm to 45nm. The selection of the right technology to fabricate MEMS depends on the quantity of metal and polysilicon layers and its properties (wide, thickness, minimum widths and minimum separation). In our case, the good results obtained in previous works developed in our research group [46-54] and the availability of two different polysilicon layers point out the selection of the commercial CMOS technology provided by Austria Microsystems (AMS) [55]. The Universitat Autónoma de Barcelona gets the access to the foundry through Europractice [56].

Figure 1.12. Diagram of the process used in this thesis.

Once the technology is selected, we proceed with the design of the structure. In first place, the operating frequency of the resonator or filter is fixed. Analytical expressions are used to obtain the dimensions if the structure is simple such as Clamped-Clampled Beam resonator (C-C Beam) or longitudinal bulk acoustic resonator (LBAR). In complex structures, such as filters and enhanced LBARs (all that devices are explained in the corresponding chapters of this thesis) the Finite Element Simulator (FEM) is used. In this work Coventor simulator [57] has been used for all the devices.

The designed resonator is introduced in a layout editor. In our case, Cadence [58] is used. The designed layout is sent to the commercial foundry and they fabricate the wafer during the following three months.

Once the chips are received, the structures are released by means of a mask-less wet etching. Finally the electrical characterization is performed.

In the following sections, each step summarized in the abovementioned paragraphs is detailed.

1.4.1 THE AMS 0.35 TECHNOLOGY

In Figure 1.13 the cross section, including all the metal and polysilicon layers, of the commercial CMOS technology used to fabricate all the devices in this thesis is presented. The technology has four metal layers oriented to interconnection in electronics circuit. In some cases this metal layers may be used as structural materials for integrated MEMS devices [50]. However, this approach is not used in this work. In addition the technology include as Poly1-Poly2 capacitance module. This module is composed of two polysilicon layers (Poly 1 and Poly2) separated by a thin silicon dioxide layer or interpoly oxide (IOX). In this thesis the polysilicon layers are used as structural layers to obtain the MEMS

In Table 1.1 the summary of the dimension of the polysilicon layer such as minimum width, minimum layer separation, and thickness is included. Note that both polysilicon

layers are in the two hundred nanometers range. This thickness is quite thinner that the silicon layers used in the state-of-the-art MEMS technologies [59-62]. The polysilicon layers thickness supposes a handicap since that decreases the coupling area. However, as it will be seen en the following section our CMOS-MEMS approach allows very narrow gaps to be obtained.
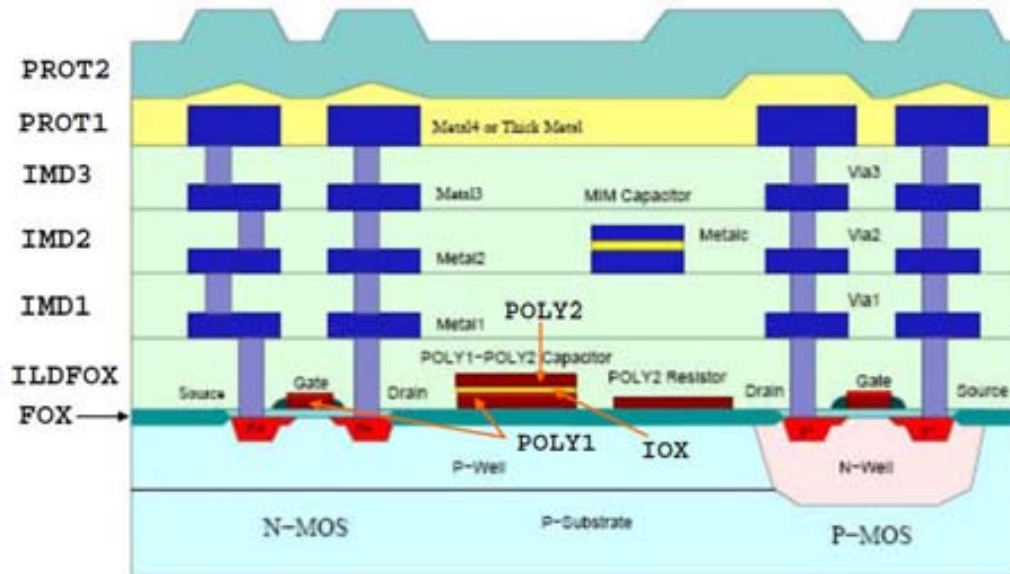
Figure 1.13. Cross section of the commercial CMOS technology from Austria Microsystems (AMS) 0.35μm [63].

Table 1.1. Summary of the main dimensions of the Poly1-Poly2 capacitance module.

Layer	Thickness	Minimum line width	Minimum line separation
Poly1	280nm	350nm	450nm
Poly2	200nm	650nm	500nm
IOX	40nm	-	-

1.4.2 DRAWING THE DEVICE. BREAKING THE RULES

After designing the structure, the layout of our MEMS devices is transferred into a layout editor. In particular, Cadence software has been used in this work. Usually in this thesis, The Poly 1 layer is used to construct the movable part of the MEMS, whereas the Poly 2 layer is used to fabricate the electrodes to drive and read the movement. The drawn distance between the Poly 1 and Poly 2 layers is 100nm. This distance is below the allowed minimum distance determined by the design rules provided by Austria Microsystems. However, previous works addressed to optimize the fabrication process has shown that a distance around 100 nm can be fabricated with a 10% tolerance. This fact offers the possibility to have narrow gaps.

In Figure 1.14 a Cadence snapshot presents a top view of a Cadence-extracted layout. This design corresponds to U-Filter (it will be detailed chapter 4). The red shape corresponds to the poly 1 layer that will be used as movable part constituent layer. The white shapes correspond to the Poly 2 layer. This layer is used as electrodes. The drawn

distances between the Poly 1 and Poly 2 layers are 100nm in this thesis. This distance is below the allowed distances defined by the design rules.
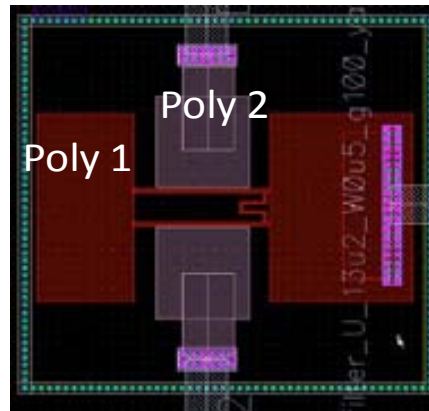
a)

b)

Figure 1.14. a) Top view of a U-Filter Cadence Layout. The red shapes correspond to the Poly1 layers, and the Poly 2 layers are presented as white shapes. b) MEMS and PADS interconnection view.

The actuation and the read of the MEMS is done through the access pads. The microelectromechanical structure is connected to the interconnection pads by means of metal or polysilicon paths as it can be seen in Figure 1.4 b).

1.4.3 THE SPACER TECHNIQUE

In previous section, the fabrication of the MEMS using the two polysilicon layers present in the polysilicon capacitance module present in AMS 0.35μm has been commented. In the polysilicon capacitance module the Poly 1 layer is deposited in first place. Over the Poly 1 layer the inter poly oxide layer is deposited about all the Poly1 area and finally, the Poly 2 layer is covers the insulator (see Figure 1.15 a)

a)

b)

c)
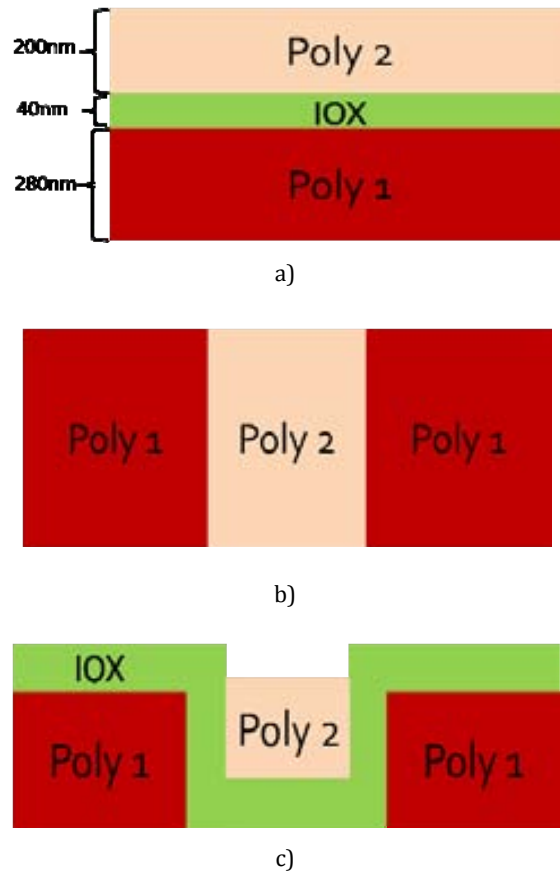
Figure 1.15. a) Polysilicon module. B) Drawn top view of the Poly1-Poly2 device using the spacer technique. c) Fabricated cross section of the Poly1-Poly2 device using the spacer technique.

In the spacer technique, one of the polysilicon is used as structural layer and the other is employed as electrode. The thin film oxide is used to define the distance between both layers. In Figure 1.15 b), the top view of a drawn design formed by two different polysilicon is shown. Note that the distance between the two polysilicon layers is zero nm. However, since the interpoly oxide is grown by default it will be present in the final fabricated device. In Figure 1.15 c), a cross section of the fabricated device is shown. Note that conformal oxide layer is deposited after the Poly 1 deposition and there will be an oxide layer under the Poly2. After the releasing process, the interpoly oxide will be removed and the air gap between the two-layer will corresponds to the interpoly thickness. Note the spacer technique introduces a high misalignment between the two layers that could affect the coupling area between the electrode and the movable part.

1.4.4 RELEASING

The post-CMOS micromachining is based on a mask-less wet etching. The most important is that any photolithographic step is required and the releasing of the structure is quiet simple. The releasing is performed by and HF-based solution that is selective with the aluminum present in the electrical connection pads. In order to ease the releasing of the polysilicon structure two considerations has been taken:

A pad window is opened into the passivation layer over the MEMS structure in order to allow the etchant to attack the oxide. The passivation layer presents in the CMOS technology is resistant to the etchant.

Since the mechanical structure are fabricated using the polysilicon, that are the deepest front-end CMOS layers, VIA holes without metal are opened to provide a better access to the etchant, and hence, reduce the etching time. By reducing the time, the damage to the metals is reduced. This metal damage is observed in long etching times.

In Figure 1.16 the cross section of the AMS technology before and after the releasing process is shown. Note the figures include the PAD window and the VIA's holes. The etching time is fixed at 18+10 minutes.
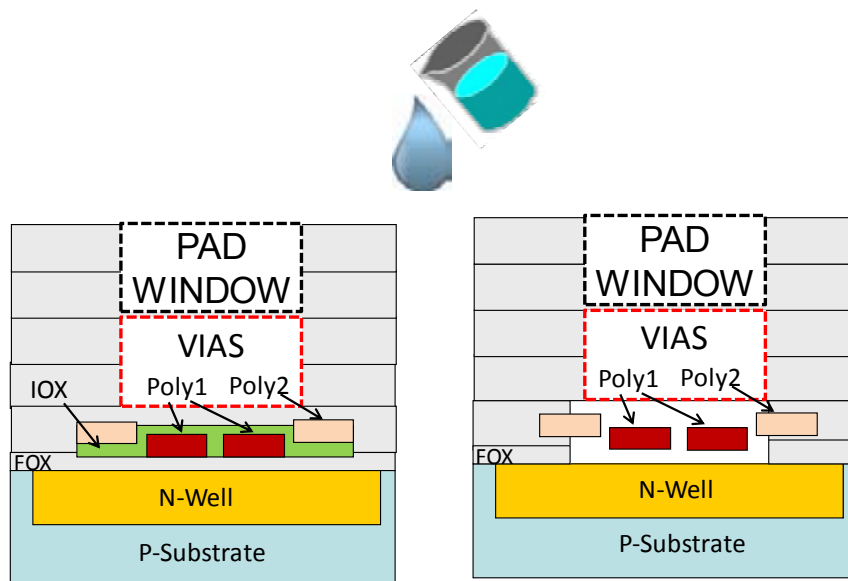
Figure 1.16. Cross section of the AMS technology before the releasing process and after the releasing process.

In Figure 1.17 a SEM image of the U-Filter before the releasing process and after 18+10 minutes of wet etching. Observe the two concentric squares that corresponds to the PAD window (the outer square) and the bias hole (inner square)

a)   b)
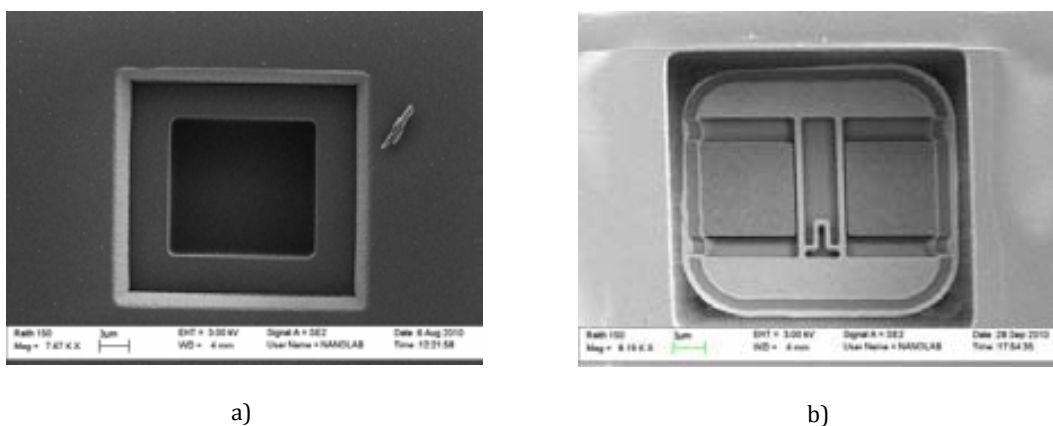
Figure 1.17. SEM image of a U-filter a) before the wet etching and b) after the releasing

1.5 RESEARCH FRAME WORK

The research presented in this thesis has been carried out in the electronics Circuits and System (ECAS) group in the Universitat Autónoma de Barcelona. The main activity of the group is the development of new electronics systems based on high performance microelectronic circuits. Currently the research lines of the group involve the development of RF MEMS systems on chip for communication, non-linear device to be used as memories, MEMS for energy harvesting, zero-level packaging techniques, ultrasensitive sensors, collaborative effects MEMS/NEMS and new transduction mechanisms.

During my stage in ECAS, I have been involved in two different research projects MEMSPORT and NEMESYS.

1.5.1 MEMSPORT (TEC 2006-03698/MIC)

The objective of the present project is to develop monolithic and heterogeneous MEMS-CMOS elements that allow to the portability and autonomy of an integrated global system of high performance and high functionality. The application scenario is a wireless sensor network node that is composed as the diagram in Figure 1.18

Figure 1.18. Diagram of the conceptual wireless sensor node.

1.5.2 NEMESYS ()

The aim of the project is to design new micro and nanoelectromechanical systems integrated with commercial CMOS technologies as well as to explore new applications in which these MEMS/NEMS devices provide enhanced performance. Two are the general objectives:

Design of resonant or vibrating CMOS-MEMS for signal generation (oscillators for frequency reference) and processing (filters and mixers) for low power wireless communication systems in the radiofrequency range (MHz-GHz)

Establish the minimum attainable dimensions of the vibrating electromechanical devices using deep sub-micrometric CMOS technologies (90nm, 65nm or 45nm), and evaluate and define applications in which these new devices (in fact NEMS devices) can contribute to novel and relevant scientific results.

1.6 THESIS OBJECTIVES.

The research of this thesis is a natural continuation of the works developed by previous members [63-64] in the field of RF-MEMS. In that previous works, a part of the efforts were addressed to:

Obtain VHF resonator be means of short beams and ring resonators [49]. However, the use of CMOS-MEMS longitudinal bulk acoustic resonator was not investigated.

Obtain filter by coupling in parallel two C-C Beam resonator [22] or tuning forks [65]. However, these filter have not design expressions. In addition, the presence of feedthrough current in the parallel filters was not detailed.

Both work contributed exceptionally towards the definitive goal: the fully integrated RF front-end.

After the previous work the investigation of the CMOS-MEMS devices for application to RF had to be extended. The main objectives of this thesis are the development and study of MEMS resoantors for RF application using the commercial CMOS technology provided by AMS. This objective can be divided into small objectives.

Study of different characterization techniques to alleviate the parasitic capacitance effects over the electrostatically transduced MEMS

1) Study of the electromechanical model of MEMS resonators to predict and control the feed through current effect.

2) Implementation of different type of coupling between resonator to control the resonant frequencies and obtain bandpass IF filters. The type of couplings are:

    a. Electrical coupling.

    b. Mechanical coupling

3) Extraction of the electromechanical model of the filter to have an equivalent circuit that allows the electrical simulation.

4) Study of parallel filtering technique to obtain filter and multi band filter. Fabricate a multiband filter

5) Integrate the filter with circuitry in order to increase the filter performances.

6) Design, fabricate and test new resonators in the VHF and UHF bands using bulk acoustic resonance.

1.7 THESIS OVERVIEW

This thesis is divided into six chapters.

Chapter 1: introduces the work realized. It offers a general view of MEMS devices and it goes focusing into our particular research framework

Chapter 2. The fundamentals of MEMS resonator is presented in this chapter. Constituent expressions and the electromechanical model explanation can be founded into it.

Chapter 3 is focused on characterization techniques and the effect of the feed through capacitance present in the most of electrostatically transduced MEMS. The phase inversion mechanism that takes place under the feedthrough current presence very detailed.

Chapter 4 offers a very complete stat of the art in MEMS filter field. The IF filter achieve during our work are presented. From mechanical coupled filter to dual band pass filter through electrostatically filter and parallel filters are designed, fabricated, and tested.

Chapter 5 explores the possibility of implement new resonator topologies that works in the VHF and UHF range

Chapter 6 summarizes the conclusion of the work

1.8 REFERENCES

[1]   V. Kaajakari, *Practical MEMS*. Las Vegas: Small Gear Publishing, 2009.

[2]   R. P. Feynman, "There's plenty of room at the bottom [data storage]," *Microelectromechanical Systems, Journal of,* vol. 1, pp. 60-66, 1992.

[3]   H. C. Nathanson, W. E. Newell, R. A. Wickstrom, and J. R. Davis, Jr., "The resonant gate transistor," *Electron Devices, IEEE Transactions on,* vol. 14, pp. 117-133, 1967.

[4]   K. E. Petersen, "Silicon as a mechanical material," *Proceedings of the IEEE,* vol. 70, pp. 420-457, 1982.

[5]   P. Krause, E. Obermeier, and W. Wehl, "Backshooter - A New Smart Micromachined Single-chip Inkjet Printhead," in *Solid-State Sensors and Actuators, 1995 and Eurosensors IX.. Transducers '95. The 8th International Conference on*, 1995, pp. 325-328.

[6]   K. H. L. Chau, S. R. Lewis, Y. Zhao, R. T. Howe, S. F. Bart, and R. G. Marcheselli, "An Integrated Force-balanced Capacitive Accelerometer For Low-G Applications," in *Solid-State Sensors and Actuators, 1995 and Eurosensors IX.. Transducers '95. The 8th International Conference on*, 1995, pp. 593-596.

[7]   P. C. Eccardt, K. Niederer, T. Scheiter, and C. Hierold, "Surface micromachined ultrasound transducers in CMOS technology," in *Ultrasonics Symposium, 1996. Proceedings., 1996 IEEE*, 1996, pp. 959-962 vol.2.

[8]   http://www.analog.com.

[9]   L. J. Hornbeck, "Digital Light Processing™. A New MEMS-Based Display Technology," *Texas Instruments white paper* (http://focus.ti.com/pdfs/dlpdmd/107_DLP_MEMS_Overview.pdf).

[10]   P. Vettiger, G. Gross, M. Despont, U. Drechsler, U. During, W. Haberle, W. P. King, M. I. Lutwyche, H. Rothuizen, R. Stutz, R. Widmer, and G. K. Binnig, "The "Millipede";- more than one thousand tips for parallel and dense AFM data storage," in *Asia-Pacific Magnetic Recording Conference, 2000. APMRC 2000*, 2000, pp. MC1/1-MC1/2.

[11]   J. Z. Hilt, A. K. Gupta, R. Bashir, and N. A. Peppas, "A bioMEMS sensor platform based on a cantilever with a precisely patterned environmentally sensitive hydrogel," in *Engineering in Medicine and Biology, 2002. 24th Annual Conference and the Annual Fall Meeting of the Biomedical Engineering Society EMBS/BMES Conference, 2002. Proceedings of the Second Joint*, 2002, pp. 1650-1651 vol.2.

[12]   L. De Stefano, K. Malecki, L. Moretti, F. Della Corte, and I. Rendina, "Integrated silicon-glass opto-chemical sensor for lab-on-chip applications," in *Lasers and Electro-Optics Society, 2004. LEOS 2004. The 17th Annual Meeting of the IEEE*, 2004, pp. 354-355 Vol.1.

[13]   K. M. Brunson, "MEMS microphone technology," in *MEMS Sensor Technologies, 2005. The IEE Seminar and Exhibition on*, 2005, p. 11 pp.

[14]   R. T. Howe and C. T. C. Nguyen, "Micromechanical resonators for frequency references and signal processing," in *Electron Devices Meeting, 1994. IEDM '94. Technical Digest., International*, 1994, p. 343.

[15]   L. Coetzee and J. Eksteen, "The Internet of Things - promise for the future? An introduction," in *IST-Africa Conference Proceedings, 2011*, 2011, pp. 1-9.

[16]   *http://www.i-micronews.com/upload/Rapports/Yole_Status_of_the_MEMS_Industry_flyer.pdf*.

[17]   T. O. Rocheleau, T. L. Naing, Z. Ren, and C. T. C. Nguyen, "Acoustic whispering gallery mode resonator with Q >109,000 at 515MHz," in *Micro Electro Mechanical Systems (MEMS), 2012 IEEE 25th International Conference on*, 2012, pp. 672-675.

[18]   L.-W. Hung and C. T. C. Nguyen, "Capacitive-piezoelectric AlN resonators with Q>12,000," in *Micro Electro Mechanical Systems (MEMS), 2011 IEEE 24th International Conference on*, 2011, pp. 173-176.

[19]   J. R. Clark, W. T. Hsu, M. A. Abdelmoneum, and C. T. C. Nguyen, "High-Q UHF micromechanical radial-contour mode disk resonators," *Microelectromechanical Systems, Journal of,* vol. 14, pp. 1298-1310, 2005.

[20]   W. Jing, Z. Ren, and C. T. C. Nguyen, "1.156-GHz self-aligned vibrating micromechanical disk resonator," *Ultrasonics, Ferroelectrics and Frequency Control, IEEE Transactions on,* vol. 51, pp. 1607-1628, 2004.

[21]   L. Sheng-Shian, M. U. Demirci, L. Yu-Wei, R. Zeying, and C. T. C. Nguyen, "Bridged micromechanical filters," in *Frequency Control Symposium and Exposition, 2004. Proceedings of the 2004 IEEE International*, 2004, pp. 280-286.

[22]   J. L. Lopez, J. Verd, A. Uranga, J. Giner, G. Murillo, F. Torres, G. Abadal, and N. Barniol, "A CMOS-MEMS RF-Tunable Bandpass Filter Based on Two High-Q 22-MHz Polysilicon Clamped-Clamped Beam Resonators," *Electron Device Letters, IEEE,* vol. 30, pp. 718-720, 2009.

[23]   A.-C. Wong and C. T. C. Nguyen, "Micromechanical mixer-filters ("mixlers")," *Microelectromechanical Systems, Journal of,* vol. 13, pp. 100-112, 2004.

[24]   L. Yu-Wei, L. Sheng-Shian, R. Zeying, and C. T. C. Nguyen, "Low phase noise array-composite micromechanical wine-glass disk oscillator," in *Electron Devices Meeting, 2005. IEDM Technical Digest. IEEE International*, 2005, pp. 4 pp.-281.

[25]   C. T. C. Nguyen, "Integrated Micromechanical Circuits for RF Front Ends," in *Solid-State Circuits Conference, 2006. ESSCIRC 2006. Proceedings of the 32nd European*, 2006, pp. 7-16.

[26]   H. Bjorkman, P. Rangsten, P. Hollman, and K. Hjort, "Diamond microstructures for optical MEMS," in Broadband Optical Networks and Technologies: An Emerging Reality/Optical MEMS/Smart Pixels/Organic Optics and Optoelectronics. 1998 IEEE/LEOS Summer Topical Meetings, 1998, pp. II/77-II/78.

[27]   J. P. Raskin, "SOI substrates for More than Moore roadmap," in Devices, Circuits and Systems (ICCDCS), 2012 8th International Caribbean Conference on, 2012, pp. 1-4.

[28]   "International Technology Roadmap for Semiconductors. Micro-Electro-Mechanical Systems (MEMS)," 2011.

[29]   S. Rai and B. Otis, "A 1V 600uW 2.1GHz Quadrature VCO Using BAW Resonators," in *Solid-State Circuits Conference, 2007. ISSCC 2007. Digest of Technical Papers. IEEE International*, 2007, pp. 576-623.

[30]   K. Boustedt, K. Persson, and D. Stranneby, "Flip chip as an enabler for MEMS packaging," in *Electronic Components and Technology Conference, 2002. Proceedings. 52nd*, 2002, pp. 124-128.

[31]   L. Kang-Wook, A. Noriki, K. Kiyoyama, T. Fukushima, T. Tanaka, and M. Koyanagi, "Three-Dimensional Hybrid Integration Technology of CMOS, MEMS, and Photonics Circuits for Optoelectronic Heterogeneous Integrated Systems," *Electron Devices, IEEE Transactions on,* vol. 58, pp. 748-757, 2011.

[32]   A. E. Franke, J. M. Heck, K. Tsu-Jae, and R. T. Howe, "Polycrystalline silicon-germanium films for integrated microsystems," *Microelectromechanical Systems, Journal of,* vol. 12, pp. 160-171, 2003.

[33]   K.-L. Chen, S. Wang, J. C. Salvia, R. Melamud, R. T. Howe, and T. W. Kenny, "Wafer-Level Epitaxial Silicon Packaging for Out-of-Plane RF MEMS Resonators With Integrated Actuation Electrodes," *Components, Packaging and Manufacturing Technology, IEEE Transactions on,* vol. 1, pp. 310-317, 2011.

[34]   A. B. Graham, M. Messana, P. Hartwell, J. Provine, S. Yoneoka, B. Kim, R. Melamud, R. T. Howe, and T. W. Kenny, "Wafer Scale Encapsulation of Large Lateral Deflection MEMS Structures," in *Micro Electro Mechanical Systems, 2009. MEMS 2009. IEEE 22nd International Conference on*, 2009, pp. 745-748.

[35]   C. Kuan-Lin, J. Salvia, R. Potter, R. T. Howe, and T. W. Kenny, "Performance Evaluation and Equivalent Model of Silicon Interconnects for Fully-Encapsulated RF MEMS Devices," *Advanced Packaging, IEEE Transactions on,* vol. 32, pp. 402-409, 2009.

[36]   P. Woo-Tae, R. N. Candler, V. Ayanoor-Vitikkate, M. Lutz, A. Partridge, G. Yama, and T. W. Kenny, "Fully encapsulated sub-millimeter accelerometers," in *Micro Electro Mechanical Systems, 2005. MEMS 2005. 18th IEEE International Conference on*, 2005, pp. 347-350.

[37]   *http://www.sitime.com/*.

[38]   R. N. Candler, P. Woo-Tae, L. Huimou, G. Yama, A. Partridge, M. Lutz, and T. W. Kenny, "Single wafer encapsulation of MEMS devices," *Advanced Packaging, IEEE Transactions on,* vol. 26, pp. 227-232, 2003.

[39]   O. Brand, "Microsensor Integration Into Systems-on-Chip," *Proceedings of the IEEE,* vol. 94, pp. 1160-1176, 2006.

[40]   W.-L. Huang, Z. Ren, Y.-W. Lin, H.-Y. Chen, J. Lahann, and C. T. C. Nguyen, "Fully monolithic CMOS nickel micromechanical resonator oscillator," in *Micro Electro*

Mechanical Systems, 2008. MEMS 2008. IEEE 21st International Conference on, 2008, pp. 10-13.

[41]   G. K. Fedder, S. Santhanam, M. L. Reed, S. C. Eagle, D. F. Guillou, M. S. C. Lu, and L. R. Carley, "Laminated high-aspect-ratio microstructures in a conventional CMOS process," in *Micro Electro Mechanical Systems, 1996, MEMS '96, Proceedings. 'An Investigation of Micro Structures, Sensors, Actuators, Machines and Systems'. IEEE, The Ninth Annual International Workshop on*, 1996, pp. 13-18.

[42]   G. K. Fedder, "Mems fabrication," in *Test Conference, 2003. Proceedings. ITC 2003. International*, 2003, pp. 691-698.

[43]   J. H. Smith, S. Montague, J. J. Sniegowski, J. R. Murray, and P. J. McWhorter, "Embedded micromechanical devices for the monolithic integration of MEMS with CMOS," in *Electron Devices Meeting, 1995., International*, 1995, pp. 609-612.

[44]   Y. Weijie, R. T. Howe, and P. R. Gray, "Surface micromachined, digitally force-balanced accelerometer with integrated CMOS detection circuitry," in *Solid-State Sensor and Actuator Workshop, 1992. 5th Technical Digest., IEEE*, 1992, pp. 126-131.

[45]   P. J. Gilgunn, L. Jingwei, N. Sarkar, and G. K. Fedder, "CMOS-MEMS Lateral Electrothermal Actuators," *Microelectromechanical Systems, Journal of,* vol. 17, pp. 103-114, 2008.

[46]   J. Verd, A. Uranga, G. Abadal, J. L. Teva, F. Torres, J. L. Lopez, E. Perez-Murano, J. Esteve, and N. Barniol, "Monolithic CMOS MEMS Oscillator Circuit for Sensing in the Attogram Range," *Electron Device Letters, IEEE,* vol. 29, pp. 146-148, 2008.

[47]   J. Teva, G. Abadal, A. Uranga, J. Verd, F. Torres, J. L. Lopez, J. Esteve, F. Perez-Murano, and N. Barniol, "From VHF to UHF CMOS-MEMS monolithically integrated resonators," presented at the Micro Electro Mechanical Systems, 2008. MEMS 2008. IEEE 21st International Conference on, 2008.

[48]   J. Verd, A. Uranga, G. Abadal, J. Teva, F. Torres, F. Perez-Murano, J. Fraxedas, J. Esteve, and N. Barniol, "Monolithic mass sensor fabricated using a conventional technology with attogram resolution in air conditions," *Applied Physics Letters,* vol. 91, pp. 013501-013501-3, 2007.

[49]   J. Teva, G. Abadal, A. Uranga, J. Verd, F. Torres, J. L. Lopez, J. Esteve, F. Perez-Murano, and N. Barniol, "VHF CMOS-MEMS resonator monolithically integrated in a standard 0.35um CMOS technology," in *Micro Electro Mechanical Systems, 2007. MEMS. IEEE 20th International Conference on*, 2007, pp. 779-782.

[50]   J. Verd, G. Abadal, J. Teva, A. Uranga, F. Perez-Murano, J. Esteve, and N. Barniol, "Resonant Metal Cantilever with Attogram/Hz Mass Sensitivity Fully Integrated in a Standard 0.35-&#956;m CMOS Process," in *Micro Electro Mechanical Systems, 2006. MEMS 2006 Istanbul. 19th IEEE International Conference on*, 2006, pp. 638-641.

[51]   A. Uranga, J. Teva, J. Verd, J. L. Lopez, F. Torres, G. Abadal, N. Barniol, J. Esteve, and F. Perez-Murano, "CMOS integrated MEMS resonator for RF applications," in

Circuits and Systems, 2006. ISCAS 2006. Proceedings. 2006 IEEE International Symposium on, 2006, p. 4 pp.

[52]   A. Uranga, J. Teva, J. Verd, J. L. Lopez, F. Torres, J. Esteve, G. Abadal, F. Perez-Murano, and N. Barniol, "Fully CMOS integrated low voltage 100 MHz MEMS resonator," *Electronics Letters,* vol. 41, pp. 1327-1328, 2005.

[53]   J. L. Lopez, J. Verd, J. Giner, A. Uranga, G. Murillo, E. Marigo, F. Torres, G. Abadal, and N. Barniol, "High Q CMOS-MEMS resonators and its applications as RF tunable band-pass filters," in *Solid-State Sensors, Actuators and Microsystems Conference, 2009. TRANSDUCERS 2009. International*, 2009, pp. 557-560.

[54]   J.L.Lopez, J.Verd, J.Teva, G.Murillo, J.Giner, F.Torres, A.Uranga, G. Abadal, and N.Barniol, "Integration of RF-MEMS Resonators on Submicrometric Commercial CMOS Technologies," *Journal of Micromechanical and Microengineering,* vol. 19, p. 10, 2009.

[55]   *http://www.ams.com*.

[56]   *http://www.europractice-ic.com*.

[57]   *http://www.coventor.com/*.

[58]   *www.cadence.com/*.

[59]   D. Weinstein and S. A. Bhave, "Internal Dielectric Transduction of a 4.5 GHz Silicon Bar Resonator," in *Electron Devices Meeting, 2007. IEDM 2007. IEEE International*, 2007, pp. 415-418.

[60]   T. Mattila, J. Kiihamäki, T. Lamminmäki, O. Jaakkola, P. Rantakari, A. Oja, H. Seppä, H. Kattelus, and I. Tittonen, "A 12 MHz micromechanical bulk acoustic mode oscillator," *Sensors and Actuators A: Physical,* vol. 101, pp. 1-9, 2002.

[61]   S.Pourkamaly and F.Ayazy, "Electrically Coupled MEMS Bandpass Filter, Part I. With Coupling Element

" *Sensors and Actuators,* vol. 122, pp. 311-316, 2005.

[62]   S.Pourkamaly and F.Ayazy, "Electrically Coupled MEMS Bandpass Filter, Part II. Without Coupling Element," *Sensors And Actuators,* vol. 122, 2005.

[63]   J. Teva, "Integration of CMOS-MEMS resonators for radiofrequency applications in the VHF adn UHF bands," PhD. Thesis, Universitat Autonoma de Barcelona, 2007.

[64]   J. L. Lopez, "Application of CMOS-MEMS Integrated Resonators to RF Communication Systems," Universitat Autonoma de Barcelona, 2009.

[65]   J. L. Lopez, F. Torres, G. Murillo, J. Giner, J. Teva, J. Verd, A. Uranga, G. Abadal, and N. Barniol, "Double-ended tuning fork resonator in 0.35um CMOS technology for RF applications," in *Research in Microelectronics and Electronics, 2008. PRIME 2008. Ph.D.*, 2008, pp. 89-92.

Chapter.2 MEMS Resonators Characteristics

In this chapter the fundamentals of the electrostatic driven and capacitive readout MEMS working principle are detailed. All the involved processes on the electromechanical transduction from the excitation to the movement sensing through the dynamics of the resonator are detailed and explained. Both the procedure to obtain the electromechanical model and the equivalent electrical circuit which predicts the frequency response of the basic devices which are investigated in this work are also detailed in this chapter

2.1 INTRODUCTION

In this chapter the physical fundamentals of an AC electrostatic driven and capacitive read Microelectromechanical (MEM) resonators are explained. MEM resonators are electromechanical transducers which converts the incoming electrical signal into a mechanical movement and vice versa, the mechanical movement into electrical current. Resonators studied in this work are excited with an AC electrostatic force produced by the application of voltages on the input port. When the AC voltage frequency matches the resonant frequency of the structure the electrostatic force produces a movement of the released structure which is read using the capacitive detection. Both electrical mechanisms, excitation and sensing, allow using resonators in the electric domain since the input and output signals are electrical.

Due to the electrical excitation and sensing the resonator can be represented by means of an electrical model whose lumped parameter have a mechanical counterpart [66]. The procedure to obtain the electromechanical model from the mechanical movement is detailed in this chapter. The electrical model of a mechanical device eases the simulation of the device in an electrical simulator. This fact is especially useful when the MEMS are used along with electronics to obtain oscillators [67-69], or as standalone RF building blocks such as filters [62, 70-71] or mixers.

The movement of the resonator implies several physics effects as well defined as MEMS dynamics. On one hand the mechanical movement is affected by the intrinsic properties of the resonator: materials and geometry. On the other hand the position dependence of the force exerted produces a change in the effective stiffness of the

resonator which changes its resonant frequency. This phenomenon, known as frequency softening, gives to the resonator the tunability capability that is very useful in RF applications since it allows to adjust the nominal frequency after the fabrication applying a electrical signals. In this chapter both the frequency softening and the mechanical resonance are studied.

The first part of this chapter is summarized in the following conceptual map (see Figure 2.1). The input of the scheme is the electrostatic excitation, presented in section 2.2, which produces the resonance of the MEMS. The MEMS dynamics are detailed in section 2.3. The resonance of the capacitive MEM device is read capacitively in the output port. This mechanism is explained in the section 2.4:

Figure 2.1 Conceptual map which illustrate the working principle of the electrostatic excitated and capacitive sensed micromechanical resonator.

The electromechanical modeling, which is useful to include the MEMS behavior in an electrical simulator, is developed in section 2.5. The extraction of the values of the lumped elements which conform the electromechanical model will be extracted for the flexural beams, concretely the Clamped-Clamped beam in section 2.6 and for the two longitudinal bulk acoustic resonators (LBAR) proposed in this work (section 0).

2.2 ELECTROSTATIC EXCITATION

The micromechanical devices studied in this work are mainly formed by a movable part (micromechanical resonator) and electrodes. Usually one (or more) electrode is used as the input port (driver) while the other (or others) electrode is used as output port or sensing port (readout electrode). In Figure 2.2 a simplified diagram of a typical two-port (two electrodes) Clamped-Clamped beam resonator is depicted. A time dependent signal is applied to the driver (V_{ac}) and a DC voltage (V_{DC}) is applied to the resonator. The DC voltage applied to the beam has two tasks:

The DC voltage along with the AC voltage generates the electrostatic force (*Fx*) exerted into the resonator which enables the physical movement of the beam. Due to the quadratic dependence of the force with the input voltage the frequency of the electrostatic force not only has the same frequency that the V_{ac} applied to the driver but also other frequency components such as double frequency. The displacement of the structure occurs if the frequency of the force corresponds to the natural resonance frequency of the resonator.

The V_{DC} voltage is necessary to sense the movement of the resonator capacitively as will be detailed in next sections.

Figure 2.2 Diagram of a basic MEMS resonator with the signals applied to the structure. The movement of the resonator is in plane with the electrodes (driver and readout)

In Figure 2.2 the thickness of the resonator (h) its width and length (W and L) as well as the distance between the electrode and the resonator, also called gap, (g) and the length of the electrodes (L_e) are highlighted. The substrate and the sacrificial oxide remaining under the electrodes are included in the picture. More detailed information will be shown in the fabrication chapter.

In Figure 2.3 the diagram of a simple clamped-clamped beam resonator is presented. Capacitances, C_D and C_R, correspond to the driver to resonator and readout to resonator capacitances. The diagram presented will be taken as reference to explain the working principle of the resonator. For simplicity the first lateral mechanical mode will be studied. This mode is known as in plane mode. In the in plane resonance the beam moves further away from the input electrode at the same time it gets closer to the output electrode as is detailed in Figure 2.4.

Figure 2.3 Diagram of the resonator with the capacitances between the electrodes and the resonator and AC and DC voltages applied to the different parts.

Figure 2.4 Diagram of the movement of a clamped-clamped beam resonator. The solid line labelled with C-C Beam represents the beam in it relaxed position. The combed dashed line shows the movement in the abovementioned mode.

The relation between the input and output capacitances in the first lateral mechanical mode is described in expression (2.1).

$$\frac{\partial C_D}{dx} = -\frac{\partial C_R}{dx} \tag{2.1}$$

Considering a small beam deflection, it is $x<<s$, (being x the displacement of the beam and the s the gap between the electrode and the resonator of the resonator) the capacitor can be expressed using the parallel plate capacitor expressions in (2.2) and (2.3):

$$C_D = \frac{\varepsilon A}{(g+x)} \tag{2.2}$$

$$C_R = \frac{\varepsilon A}{(g-x)} \tag{2.3}$$

Where A is the coupling area which depends on the length and thickness of the electrodes (see expression (2.4)), g is the static gap between the beam and input or output electrodes and x is the beam displacement.

$$A = L_e \cdot h \tag{2.4}$$

If an input voltage, v_{ac}, is applied on the input electrode and a DC voltage, V_{DC}, is applied to the beam an effective input voltage, (V_D), between the driver electrode and the resonator can be expressed as:

$$V_D = v_{ac} - V_{DC} \tag{2.5}$$

In the same way an effective output voltage can be expressed as the difference between the DC voltage applied to the beam and the time dependent output voltage, v_{out}, on the readout electrode.

$$V_R = V_{DC} - v_{out} \tag{2.6}$$

Voltage v_{out} is usually much smaller than the voltage applied to the resonator, V_{DC}, therefore only the V_{DC} is considered as the output voltage V_R.

The electrostatic energy stored in a capacitor is:

$$W = \frac{1}{2} C V^2 \tag{2.7}$$

The energy stored in the input or output capacitor, W, can be calculated replacing C in expression (2.7) by C_D or C_R respectively. The voltage, V in the expression (2.7), will be substituted by V_D or V_R, respectively. The electrostatic force is a negative gradient of energy and can be written as:

$$F_E = -\frac{dW}{dx} = -\frac{1}{2}\frac{\partial}{\partial x}\left(C_D V_D^2 + C_R V_R^2\right) \tag{2.8}$$

The force over the resonator depends on the voltage applied over the electrodes as is illustrated in expression (2.8). Since the voltage applied over the driver and readout electrodes is a time-dependent variable, expression (2.8) leads to the expression (2.9):

$$F_E = -\frac{1}{2}\left(\frac{\partial C_D}{\partial x}V_D^2 + \frac{\partial C_R}{\partial x}V_R^2\right) \tag{2.9}$$

Using the Taylor's series approximation (assuming that the resonator moves slightly) the following expression for the capacitance variation is obtained.

$$\frac{\partial C_D}{\partial x} = -\frac{\varepsilon A}{g^2}\left(1 - 2\frac{x}{g} + 3\left(\frac{x}{g}\right)^2 - .... + (n+1)\left(\frac{x}{g}\right)^n\right) \approx -\frac{\varepsilon A}{g^2}\left(1 - 2\frac{x}{g}\right) \tag{2.10}$$

$$\frac{\partial C_R}{\partial x} = \frac{\varepsilon A}{g^2}\left(1 + 2\frac{x}{g} + 3\left(\frac{x}{g}\right)^2 - .... + (n+1)\left(\frac{x}{g}\right)^n\right) \approx \frac{\varepsilon A}{g^2}\left(1 + 2\frac{x}{g}\right) \tag{2.11}$$

Replacing expressions (2.5), (2.6), (2.10) and (2.11) into the expression (2.9) the applied force on the resonator corresponds to expression (2.12)

$$F_E = \frac{1}{2}v_{in}^2\frac{C_o}{g} - v_{in}V_{DC}\frac{C_o}{g} - x\frac{C_o}{g^2}\left(v_{in}^2 - 2V_{DC}v_{in} + V_{DC}^2\right) \tag{2.12}$$

Note that v_{out} has been neglected in comparison with v_{ac} and V_{DC}. If the input time dependent signal is a sinusoidal $v_{ac}=A_{ac}sin(\omega t)$ expression (2.12) changes to expression (2.13)

$$F_E = \frac{1}{2} A_{ac}^2 sin^2\left(\omega t\right)\frac{C_o}{g} - A_{ac}V_{DC}\frac{C_o}{g}sin\left(\omega t\right) -$$

$$-x\frac{C_o}{g^2}\left(A_{ac}^2 sin^2\left(\omega t\right) - 2V_{DC}A_{ac}sin\left(\omega t\right) + V_{DC}^2\right)$$

(2.13)

Since $sin^2(\omega t) = 1/2 \cdot (1 - cos(2\omega t))$

$$F_E = \frac{1}{4} A_{ac}^2 \frac{C_o}{g} - V_{ac}V_{DC}\frac{C_o}{g}sin\left(\omega t\right) - \frac{1}{4}A_{ac}^2\frac{C_o}{g}cos\left(2\omega t\right) -$$

$$-x\frac{C_o}{g^2}\left[\frac{1}{2}A_{ac}^2 - \frac{1}{2}A_{ac}^2 cos\left(2\omega t\right) - 2V_{DC}A_{ac}sin\left(\omega t\right) + 2V_{DC}^2\right]$$

(2.14)

Expression (2.14) suggests that the force applied over the resonator which presents a slight movement (*x*) has frequency components at DC, ω and 2 ω. The DC component is proportional to the amplitude of the input AC signal. The component corresponding to the input signal frequency depends on the V_{DC} and A_{ac} Finally the component set at twice of the input frequency is proportional to the square of the AC signal amplitude (A_{ac}). Equation (2.14) indicates that a DC voltage is necessary to actuate the resonator.

Considering only the single frequency component in expression (2.14) and assuming slight displacement of the resonator the relation between the input voltage and the force exerted to the resonator is quantified using the electromechanical coupling factor, η_e:

$$\eta_e = \frac{F_E}{v_{ac}} = \frac{\varepsilon A}{g^2}V_D = V_D\frac{\partial C_D}{dx}$$

(2.15)

It should be noted that V_D corresponds to the voltage difference between the electrodes and resonator for the input or output gap detailed in expression (2.5). Note that the electromechanical coupling factor can expressed as the different voltage in the gap between the electrode and the resonator and the variation of the capacitance for slight movement of the structure.

2.3 MEMS DYNAMICS

The AC excitation explained in section 2.2 enables the mechanical movement of the resonator which is explained in the following paragraphs. The mechanical movement (resonant frequency and displacement) of the resonator depends mainly on the physical parameters such as dimensions and material properties as well as the force exerted to the movable part. The frequency of the movement depends also on the applied DC voltage. This perturbation is called frequency softening and will be explained detail in this section.

2.3.1   MOVEMENT OF THE RESONATOR.

As it has been said, the dynamics of the mechanical structure put through an AC force will be studied. The force exerted to the resonator is provided by DC and AC voltage

components applied to the driver. As an oscillatory system the behaviour of the resonator in its linear regime can be conceived as a lumped mass-spring-dump system. In this sense, the movement of the resonator can be expressed in terms of the elastic constant *(k)* and the effective mass (m_{eff}). Note that in this approximation the effective mas is considered as a punctual mass. For the C-C beam the mass is supposed at the very center of the bar and for the cantilever the mass is considered at the free end. Both parameters are detailed in this section. The dissipated energy is modelled by the damping, *D.* In Figure 2.5 a diagram of the aforementioned system is shown. The movement of the mass is in the *x* direction which is the same direction than the applied force, F_x.
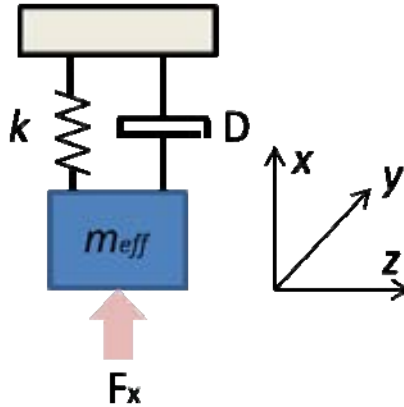
Figure 2.5 Diagram of the mass-spring-damper system which represents the behavior of a resonator under an applied force, F_x.

The resonator responds to the force applied with its movement. The movement of the resonator is governed by the forced harmonic oscillation movement equation presented in (2.16):

$$m_{eff}\frac{\partial^2 x}{\partial t^2} + D\frac{\partial x}{\partial t} + kx = F_x = A_f\cos(\omega t) \qquad (2.16)$$

In expression (2.16) A_f is the magnitude of the applied sinusoidal force. Note that non linear terms of the stiffness and damping have not been considered. The natural frequency of the resonator is defined as:

$$\omega_o = \sqrt{\frac{k}{m_{eff}}} \qquad (2.17)$$

The expression for quality factor of the resonator is:

$$Q = \frac{m_{eff}\omega_o}{D} = \frac{\sqrt{m_{eff}k}}{D} \qquad (2.18)$$

An exhaustive analysis of the previous equations (2.17) and (2.18) gives some interesting information about the MEMS devices. In the first place the mechanical Q factor of the resonator depends directly on the stiffness constant of the structure and the effective mass. To obtain high quality resonators "heavy and hard" structures are desired. In the second place small masses are necessaries to go up in frequency.

Going back to expression (1.16) *D* denotes the damping. This damping is caused by several energy dissipation mechanisms which affect MEMS devices [72] The ways in which the resonator can dissipate energy includes among other:

-*Air damping*: In mechanical resonators one of the most important damping factors is the squeeze force [73]. Since two rigid plates are very close the air trapped between them is compressed due to the movement of the structures and the force required to compress it is taken from the movement.

Clamping loss through the anchors. In major cases in which the resonator is clamped to the substrate through an anchor, part of the vibration energy can flow into the substrate producing a Q decreasing. The energy losing are more important in C-C Beam or Cantilevers [74]. In some cases the losses through the anchors have been minimized using well designed structures such as tuning forks [75], anchorage point selection and anchors enhancement [60, 76]

Surface losses are produced in cases when the thickness of the microstructure scales down [77]. In that situation the surface loses becomes more important. This energy losing mechanism is due to the surface stress.

Thermoelastic dissipation (TED) is due to the relaxation of mechanically induced temperature gradient. It is independent form the geometry and its strong dependent on the constituent material [75, 78]

This work not attempts directly to reduce the energy losing problem. But further in the text we will find some well known techniques addressed to increases the mechanical Q factor of the resonator

The amplitude of vibration is obtained solving the expression of the movement of the resonator (2.16) and is calculated in expression (2.19):

$$|x| = \frac{A_f/m_{eff}\,\omega_o}{\sqrt{\left(\omega^2 - \omega_o^2\right) + \left(\omega\omega_o/Q\right)^2}}$$

(2.19)

Figure 2.6 shows the normalized magnitude and phase of the resonator displacement. The maximum magnitude of the displacement occurs when the frequency of the *AC* input signal is the same than the natural mechanical frequency of the MEMS. At this frequency the maximum amplitude of movement is:

$$|x| = \frac{A_f Q}{k}$$

(2.20)

Expression (2.20) shows that the maximum amplitude is directly proportional to the Q facture and the amplitude of the external force and it is inversely related to the stiffness, *k*. From expression (2.20) it can be noted that the resonator movement amplitude will be larger as "softer" the resonator is. For "rigid" structures, considering that the same force is applied on it, the movement will be shorter.

The maximum phase shift is achieved at resonant frequency and the slope is directly related with the Q factor. In most of RF application the maximum phase shift is desired and the thus high Q resonators are required.
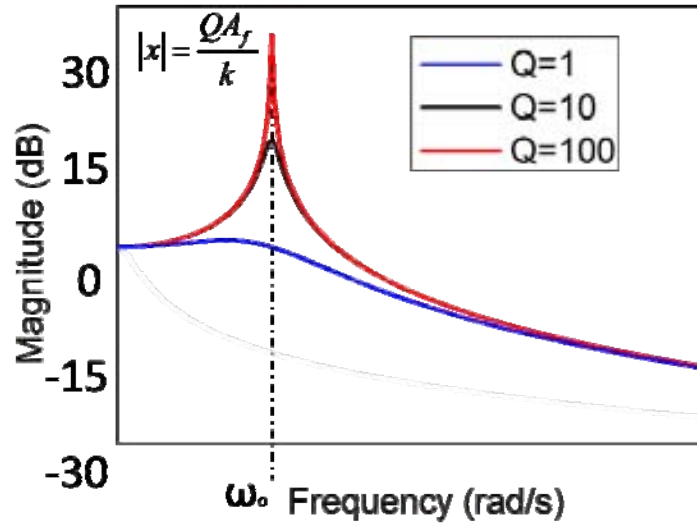
a)
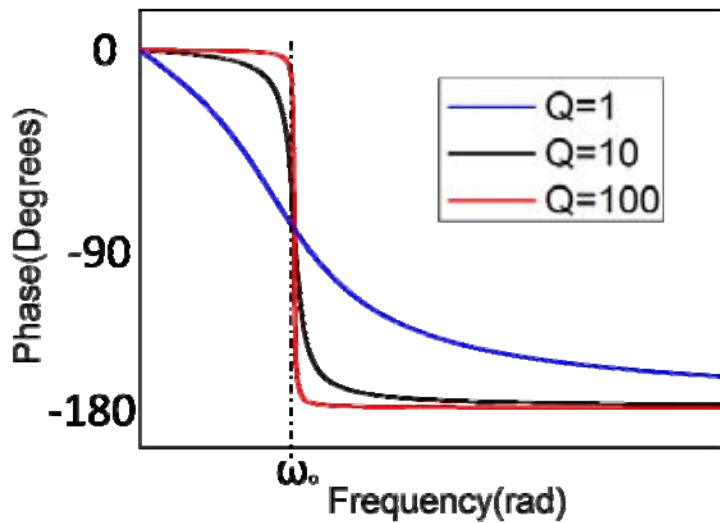
b)

Figure 2.6. Plot of the resonator displacement magnitude and phase under an arbitrary force.

2.3.2 SPRING SOFTENING

In section 2.3.1 the relation between the magnitude of the movement with the quality factors Q, dimensions and the amplitude of the external force has been studied. However the force exerted to the resonator has a component which depends on the resonator

position x (see expression (2.14)). This relation is illustrated as an electrical stiffness in expression (2.21):

$$k_e(t) = \frac{\partial F_x}{\partial x} \qquad (2.21)$$

If expression (2.14) is used into equation (2.21) the electrical stiffness can be written as:

$$k_e(t) = \frac{C_o}{g^2}\left[\frac{1}{2}A_{ac}^2 - \frac{1}{2}A_{ac}^2\cos(2\omega t) - 2V_{DC}A_{ac}\sin(\omega t) + 2V_{DC}^2\right] \qquad (2.22)$$

Expression (2.22) has two time dependent terms due to the sinusoidal input signal. The mean value of the electrical stiffness is:

$$k_e = \frac{C_o}{g^2}\left[\frac{1}{2}A_{ac}^2 + 2V_{DC}^2\right] \qquad (2.23)$$

Considering the movement of the resonator in one direction, the electrostatic force pushes the beam in that direction and the mechanical spring constant pull the beam toward the contrary direction. This effect is assimilated as a change in the effective spring constant of the mass-spring-damper system as is indicated in (2.24)

$$k_{eff} = k - |k_e| \qquad (2.24)$$

Where k is the mechanical spring constant defined by the dimensions and the material of the resonator and k_e is the electrical stiffness calculated in expression (2.23). The effect of the electrical stiffness is interpreted as a softening of the spring. Equation (2.25) shows the resonant frequency of the resonator in terms of effective spring constant and effective mass:

$$\omega_{eff} = \sqrt{\frac{k_{eff}}{m_{eff}}} = \sqrt{\frac{k - k_e}{m_{eff}}} \qquad (2.25)$$

Equation (2.25) indicates that a increasing of the electrical stiffness, produced by an increasing of the V_{DC} or V_{AC} decreases the effective stiffness and therefore it decreases the resonant frequency. The electrical spring softening effect is useful for RF application since it allows a tuning of the resonant frequency of the resonator. Considering the DC voltage higher that the AC voltage the DC component will be the main frequency tuning parameter. [79].

2.4 CAPACITIVE READOUT

The last stage in the way of the transduction mechanism comprehension is to measure the mechanical displacement or the velocity of the displacement using electrical variables The movement of the resonator induced by the force applied in the input electrode changes the value of the capacitance formed between the readout and the resonator, C_R. The variation on the capacitance along with the voltage difference between the resonator

and the readout electrode, V_R induces a current over the sensing electrode which can be calculated by means of equation (2.26).

$$I_o = \frac{\partial(C_R \cdot V_R)}{\partial t} = C_{OUT}\frac{\partial(V_R - v_{out})}{\partial t} + (V_{DC} - v_{out})\frac{\partial(C_R)}{\partial t} \qquad (2.26)$$

Since v_{out} is a time dependent voltage if equation (2.26) is operated it leads to expression (2.27).

$$I_o = \underbrace{C_{FT}\frac{\partial(v_{in} - v_{out})}{\partial t}}_{I_{F1}} \underbrace{- C_R\frac{\partial(v_{out})}{\partial t}}_{I_{F2}} + \underbrace{V_{DC}\frac{\partial(C_R)}{\partial t} - v_{out}\frac{\partial(C_R)}{\partial t}}_{I_M} \qquad (2.27)$$

In expression (2.27) the concept of feedthrough current and motional current are introduced. Despite they will be explained in next sections it is necessary to assume that the parasitic current contribution is present in main terms: the first term, referred in expression (2.27) as I_{F1} corresponds to the coupling of the input AC voltage from the input electrode to the output through a capacitance C_{FT} which models different contribution such as frienging filed or the propagation through the substrate. The second term, I_{F2} corresponds to the variation of the output voltage on the read-out electrode. If we consider v_{out} sufficiently small it can be neglected. The current induced exclusively by the movement of the resonator is considered as the motional current (I_M) and it depends on the variation of the output capacitance.

Assuming the abovementioned considerations the output (motional) current can be written as:

$$I_o = V_{DC}\frac{\partial(C_R)}{\partial t} = V_{DC}\frac{\partial(C_R)}{\partial x}\frac{\partial x}{\partial t} \qquad (2.28)$$

Equation (2.28) shows that a DC voltage is necessary to sense the movement of the resonator in the electrode. Previous expression relates the movement velocity of the resonator with the output current. This relationship is highlighted in expression (2.29)

$$\eta_r = \frac{I_o}{\partial x / \partial t} = \frac{\varepsilon A}{g^2}V_{DC} \qquad (2.29)$$

The electromechanical coupling factor, η_r connects the variation of the movement with the read current. It can be written in a similar ways as in expression (2.15). The excitation and readout electromechanical coupling factors are equals if the input and output gaps are equals and the movement of the resonator is symmetric. Then:

$$\eta_r = \eta_e = \eta \qquad (2.30)$$

The relation between the input applied voltage to the driver and the output currents is expressed by:

$$I_o = \eta^2 \frac{Q}{k}V_{DC}\frac{\partial V_i}{\partial t} \qquad (2.31)$$

From expression (2.31) important conclusions can be extracted. The output voltage depends directly on the input applied voltage and the DC voltage in the readout gap. The electromechanical coupling factor is the most important parameter because it is squared. The gap and the coupling are the determinant parameters of the electromechanical coupling factor. In order to obtain a higher input voltage and output current a high electromenchanical coupling factor is required. Resonator with large coupling areas and narrow gaps will offers higher coupling factor.

2.5 ELECTROMECHANICAL MODELING

In order to use the mechanical device as an electrical system an equivalent circuit which describes the resonator behaviour in the electrical domain is required. Using the electrical model of a MEMS it is possible to simulate the behaviour into an electrical simulator. This fact is especially important if the fabricated device is thought to be integrated in a more complex electrical system such as oscillators or integrated bank of filter or so on. In this section a step by step modelling procedure will be detailed in the case under study: the electrostatic driven and capacitive read resonator. It should be remembered that the resonator is driven via an input voltage through the input electrode and the motional current is read through a capacitive method.

Figure 2.7 shows the diagram of a generic clamped-clamped beam resonator. In the diagram the general case is considered since AC voltages v_{in1} and v_{in2} are applied to the electrodes apart from the DC voltages applied to resonator, V_{DC}. In this case an input current as well as the output current is considered entering to MEMS. This simple diagram can be applied to any complex MEMS system if the correct considerations are made.

Figure 2.7 Diagram of the Resonator for the general case when DC and AC voltages are applied to the electrodes.

The resonator shown in Figure 2.2 is modelled by a two port structure (see Figure 2.8 [80]). To obtain the complete electromechanical model the superposition method is used.

The first step the input port equivalent circuit will be described by short circuiting the output of the two port network. The output port equivalent circuit will be extracted later by short-circuiting the input port. The addition of both result will lead to the complet equivalent circuit.
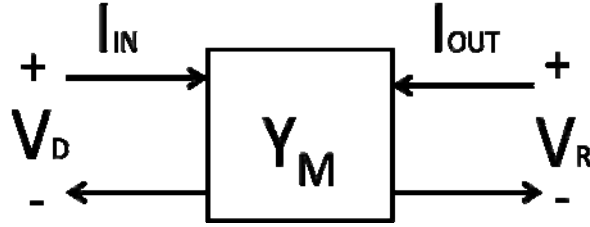

Figure 2.8 Diagram of the resonator considered a two port network.

2.5.1 INPUT PORT EQUIVALENT CIRCUIT MODELING

2.5.1.1 MODELING FROM THE INPUT

The analysis of the input port starts with the cancelation of all the independent AC and DC sources in the output port, thus V_R =0V. The input voltage, V_D has a DC component, V_{DC} and a frequency component provided by AC source and can be expressed as:

$$V_D = v_{in}(t) - V_{DC} = A_{ac}\cos(\omega t) - V_{DC} \qquad (2.32)$$

The movement of the resonator produces a change in the input capacitance. The input capacitance is composed by and static component, C_o, and the variation enforced by the movement of the resonator as is detailed in equation (2.33)

$$C_D = C_o + C_d(t) = C_o + \frac{\partial C_D}{\partial x}x(t) \qquad (2.33)$$

The input current is strong dependent on the displacement of the resonator and the input voltage and it is expressed in the following equation:

$$I_{IN} = C_D\frac{\partial(V_D)}{\partial t} + V_D\frac{\partial(C_D)}{\partial t} \qquad (2.34)$$

Replacing expressions (2.32) and (2.33) in (2.34)and developing it, the input current is expressed by means of expression (2.35):

$$I_{IN} = C_o\frac{\partial(v_{in}(t))}{\partial t} + \frac{\partial C_D}{\partial x}\left(x(t)\frac{\partial(v_{in}(t))}{\partial t} + v_{in}(t)\frac{\partial x(t)}{\partial t}\right) - V_{DC}\frac{\partial C_D}{\partial x}\frac{\partial x(t)}{\partial t} \qquad (2.35)$$

The term which relates the variation of the input capacitance and the *AC* contribution can be rewritten as:

$$\left(x(t)\frac{\partial(v_{in}(t))}{\partial t} + v_{in}(t)\frac{\partial x(t)}{\partial t}\right) = \frac{\partial}{\partial t}\left(x(t)\cdot v_{in}(t)\right) \qquad (2.36)$$

Which leads to expression (2.37)

$$\left(x(t) \cdot v_{in}(t) \right) \approx \cos \omega^2 t \tag{2.37}$$

This double frequency term is neglected in the present deduction to obtain the electrical model. Finally (2.35) leads to expression (2.38).

$$I_{IN} = \underbrace{C_O \frac{\partial \left(v_{in}(t) \right)}{\partial t}}_{I_P} - \underbrace{V_{DC} \frac{\partial \left(C_D \right)}{\partial x} \frac{\partial x(t)}{\partial t}}_{I_M} \tag{2.38}$$

The first term corresponds to the static capacitor current contribution, I_P. This current is a non desired contribution because does not depend on the movement of the resonator. The second term corresponds to the desired motional current, I_M. Both the mechanical movement of the resonator and the DC voltage between the electrode and the resonator are determines the motional current.

Expression (2.38) leads to model the input port with the circuit in Figure 2.9. The motional impedance, $Z_{MOTIONAL}$, which will be detailed in next pages, models the resonator movement.
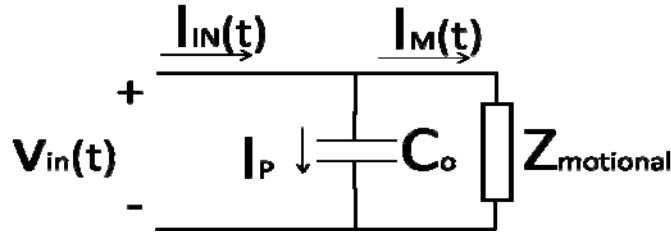

Figure 2.9 equivalent electrical circuit of the input port of resonator

The motional current in expression (2.38) can be written as follows:

$$I_M = -V_{DC} \frac{\partial \left(C_D \right)}{\partial x} \frac{\partial x(t)}{\partial t} = -V_{DC} \frac{\partial \left(C_D \right)}{\partial t} \tag{2.39}$$

For simplification, the current in its "phasor" form is expressed as:

$$I_M(j\omega) = -V_{DC} \frac{\partial \left(C_D \right)}{\partial x} j\omega X \left(j\omega \right) \tag{2.40}$$

In expression (2.40) the current in terms of displacement has been obtained. The motional admittance (Y_M) for the input port is calculated using expression (2.41):

$$Y_{IN}(j\omega) = \frac{I_M(j\omega)}{V_{IN}(j\omega)} = V_{DC} \frac{\partial \left(C_D \right)}{\partial x} j\omega \frac{X \left(j\omega \right)}{V_{IN}(j\omega)} \tag{2.41}$$

Where $V_{IN}(j\omega)$ is the phasor of $v_{in}(t)$. Equation (2.41) relates the admittance of the resonator with the displacement, $X(j\omega)$. It is possible express the admittance including the electrostatic coupling factor in equation (2.15). Taking into account the previous consideration expression (2.41) becomes expression (2.42):

$$Y_{IN}(j\omega) = -V_{DC} \frac{\partial(C_D)}{\partial x} j\omega \frac{X(j\omega)}{F_E(j\omega)} \frac{F_E(j\omega)}{V_{IN}(j\omega)} \tag{2.42}$$

Coming back to the movement equation and writing it as it in phasor form

$$-m_{eff}\omega^2 X(j\omega) + j\omega D X(j\omega) + kX(j\omega) = F_E(j\omega) \tag{2.43}$$

Using the relation in expressions (2.17) and (2.18)The force can be related to the movement as it is illustrated in expression (2.44)

$$\frac{X(j\omega)}{F_E(j\omega)} = \frac{{\omega_o}^2 / k}{-\omega^2 + \frac{\omega_o \omega}{Q} j + {\omega_0}^2} \tag{2.44}$$

Finally replacing **¡Error! No se encuentra el origen de la referencia.** and (2.44) into (2.42) the input admittance can be rewritten as:

$$Y_{IN}(j\omega) = j\omega\eta^2 \frac{{\omega_o}^2 / k}{-\omega^2 + \frac{\omega_o \omega}{Q} j + {\omega_0}^2} \tag{2.45}$$

The mechanical admittance can be compared with the electrical admittance a series RLC resonator and it is expressed in (2.46) :

$$\frac{I(j\omega)}{V(j\omega)} = \frac{j\omega{\omega_o}^2 C}{{\omega_o}^2 - \omega^2 + j\omega{\omega_o}^2 RC} \tag{2.46}$$

The following considerations for the natural resonance frequency (ω_o) and the mechanical quality factor (Q) have been taken into account:

$$\frac{1}{{\omega_o}^2} = LC,$$
$$Q = \frac{1}{\omega_o RC} \tag{2.47}$$

Comparing term by term between the expression (2.45) and (2.46) the following equivalences are directly obtained:

$$L_{x1} = \frac{m}{\eta^2} \tag{2.48}$$

$$C_{x1} = \frac{\eta^2}{k} \tag{2.49}$$

$$R_{x1} = \frac{\sqrt{mk}}{Q\eta^2} \tag{2.50}$$

39

2.5.1.2 MODELLING FORM THE OUTPUT

In the previous section the input admitance has been obtained. The movement of the resonant structure, which has been enabled by the input voltage, V_{IN}, produces a change in the output capacitance which induces a current in the readout electrode. In this section an equivalent electrical circuit to model this phenomenon will be extracted

For the given input voltage, V_D, and considering that $v_{in2}=0V$ (see Figure 2.8) the output current is:

$$I_{OUT} = V_R \frac{\partial C_R}{\partial t} = V_R \frac{\partial C_R}{\partial x} \frac{\partial x}{\partial t}$$
(2.51)

Expression (2.51) can be transformed into its "phasor" form as:

$$I_{OUT}(j\omega) = V_R \frac{\partial C_R}{\partial x} j\omega X(j\omega)$$
(2.52)

From expression (2.44) the displacement can be calculated using the following expression:

$$X(j\omega) = \frac{{\omega_o}^2/k}{-\omega^2 + \frac{\omega_o \omega}{Q} j + {\omega_0}^2} F_E(j\omega)$$
(2.53)

From equation (2.51) considering that $V_R=-V_{DC}$, which is the DC voltage applied to the resonator and expression (2.15)the output current can be expressed as:

$$I_{OUT}(j\omega) = \frac{\left[-V_{DC}^2 \frac{\partial C_R}{\partial x} \frac{\partial C_D}{\partial x} \right] \omega_o/k}{-\omega^2 + \frac{\omega_o \omega}{Q} j + {\omega_0}^2} j\omega V_{AC}(j\omega)$$
(2.54)

Once the output current has been obtained the relation between the input current and the output current can be written as :

$$\Phi_{21} = \frac{I_{OUT}(j\omega)}{I_{IN}(j\omega)} = \frac{V_{DC} \frac{\partial C_R}{\partial x} X(j\omega)}{V_{DC} \frac{\partial C_D}{\partial x} X(j\omega)}$$
(2.55)

$$I_{OUT}(j\omega) = \Phi_{21} I_{IN}(j\omega)$$
(2.56)

Where ϕ_{21} is named current gain and shows a strong dependence between the input and output current. The current gain value depends on the physical parameters such as gaps, dimensions and voltages and can be rewritten as:

$$\Phi_{21} = \frac{\eta_{out}}{\eta_{in}} = \frac{V_{DC}\dfrac{\partial C_R}{\partial x}}{V_{DC}\dfrac{\partial C_D}{\partial x}} \qquad (2.57)$$

In the case analyzed in this section we have considered equals gaps, voltages and equals input and output capacitances thus the current gain value is ϕ₂₁=1. In actual resonators the gaps can be different and then different than 1 values can be obtained. Equivalent Electrical Circuit

2.5.2 OUTPUT EQUIVALENT CIRCUIT MODELLING

The previous mathematical development, detailed in sections 2.5.1 allows to obtain an electrical equivalent circuit for the input port which is described in Figure 2.10. The complete equivalent circuit for output port can be obtained using the same developing considering that V_{AC2}≠0 and V_{AC1}=0.

2.5.3 COMPLETE EQUIVALENT CIRCUIT

Finally the small signal equivalent circuit of the two port network can be modelled as in Figure 2.11. C_{TH} capacitance is placed between the input and output port. This capacitance models the transmission of energy from one port to the other due mainly to two different effects:

-The bending of the electrical field from the input to the output, as well know as fringing fields.

-Part of the energy is transferred to the output through the substrate [81].

The value of the capacitance, $C_{TH,}$ can be obtained empirically.

Figure 2.10 Diagram of the input port signal electrical equivalent circuit.

If the output current is read over a load resistance hanged from the output electrode (grey resistance of R_{load} value in Figure 2.11) the circuit can be reduced to simpler schematic. The following simplification are assumed: :

1) Equal input and outputs gaps and electrodes.

2) Equal voltages $V_R=V_D$ in Figure 2.7.

3) The motional impedances are higher than the load resistance $R_{x1}>R_{load}$, $R_{x2}>R_{load}$

The output voltage can is the current through the load resistance as in expression

$$V_2 = -I_{OUT}R_{load} = -\left(\phi_{21}I_{M1} + I_{M2} + I_{co2} - I_{TH}\right)R_{load} \qquad (2.58)$$

Currents I_{M1} and I_{M2} cab ne obtained from the input and output voltages as in expressions (2.63) and (2.64)

Figure 2.11 Complete electrical equivalent circuit of the two port resonator.

$$I_{M1} = \frac{V_1}{R_{x1}} \qquad (2.59)$$

$$I_{M2} = \frac{V_2}{R_{x2}} \qquad (2.60)$$

If (2.59) and (2.60) are replaced in (2.58) and summing $R_{x1}>R_{load}$, the output voltage can be rewritten as:

$$V_{OUT} = R_{load} \left(-\frac{\phi_{21}}{R_{x1}} V_{IN} + I_{TH} \right) \qquad (2.61)$$

The simplified model can be depicted as in Figure 2.12. The transformed ratio is the current cage calculated in expression (2.55). The value and sign depend on the voltages applied between the electrode and the resonator and the gaps capacitance variation. If voltages and gaps are completely symmetric its absolute value will be $|\phi_{21}|=1$
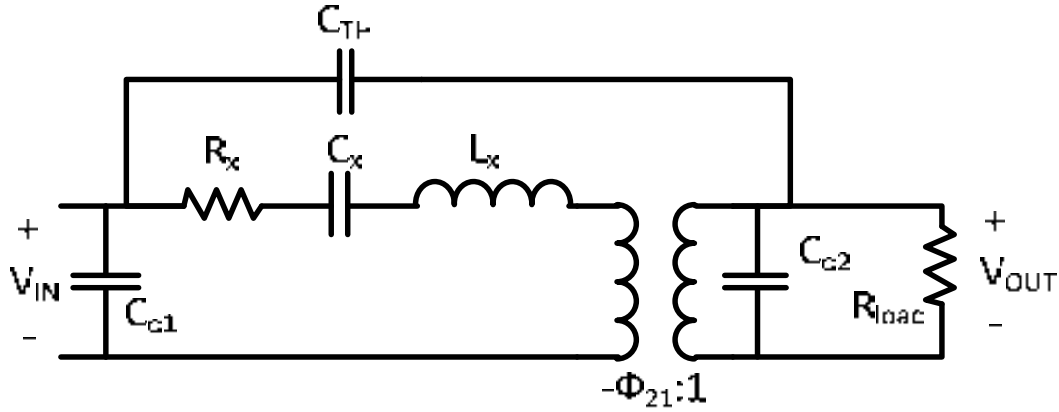

Figure 2.12 simplified Electrical circuit of the MEMS resonator.

2.5.4 CURRENT ANALOGY

Figure 2.12 shows a purely electrical circuit, but it is possible decouple the electrical world which involves the input voltage and the output current from the mechanical world which involves the movement of the resonator described by equation (2.16). to do that the current analogy method is used.

The equation of the resonator's movement in (2.16)can be rewritten as

$$m_{eff} \frac{\partial v}{\partial t} + Dv + k \int v dt = F_x \qquad (2.62)$$

Note that the velocity is: $\delta x/\delta t = v,$

Applying the current analogy [71] illustrated by the following relations:

$$F_X = V_f \qquad (2.63)$$

$$v = I_{VEL} \qquad (2.64)$$

$$m_{eff} = L \qquad (2.65)$$

$$\frac{1}{k} = C \qquad (2.66)$$

$$D = R \qquad (2.67)$$

43

Expression (2.62) can be rewritten as:

$$L\frac{\partial I_{vel}}{\partial t} + RI_{vel} + \frac{1}{C}\int I_{vel}dt = V_f \qquad (2.68)$$

Equation (2.68)is a series RLC network. In order to relate the mechanical current, I_{VEL}, and mechanical voltage, V_f, to the electrical current and voltage, I_{CIR} and V_{CIR}, respectively, in the case of capacitive coupling, we can use two transformers whose turn ratio relates both values as:

$$V_{CIR} = \frac{V_f}{\eta} \qquad (2.69)$$

$$I_{CIR} = \eta I_{VEL} \qquad (2.70)$$

Figure 2.13 shows the complete equivalent circuit of the electromechanical resonator.
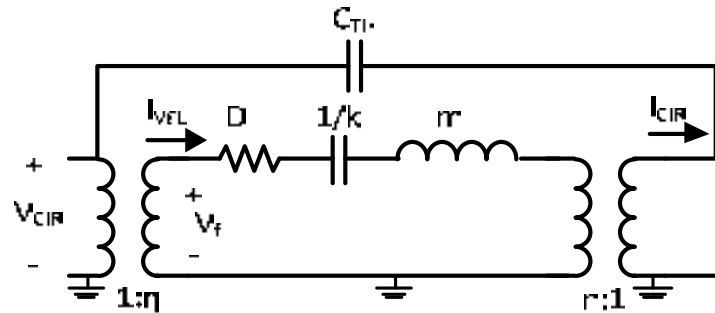

Figure 2.13. Equivalent electromechanical circuit of the electromechanical

In this circuit the input transformer model the transduction between the input voltage and the force described in the expression (2.15). The RLC branch is actually the mechanical magnitudes of the resonator: mass-spring-damper. Finally the output transformer with a η_r turn ratio translates the velocity of the movement into an output current as in the expression (2.29).

In this section the electromechanical modeling of an electrostatic excited and capacitive read resonator has been explained. In the following section the electromechnaical lumped elements values extraction is carried out. In some cases, the simulation of the models and the measurements are compared in order to observe the goodness of the models.

2.6 LUMPED ELEMENT VALUES EXTRACTION

In this section the calculation of the RLC values is carried out. As has been omented the electromechanical mode includes electrical and mechanical parameters and the the dynamics of the movement for a determined resonators as well as the electrical signals applied on it has to be known.

The lumped element values extraction is focused in this chapter on the beams. Note that different approach has to be made for other types of flexural resonators or bulk

resoantors. Fur a simple Clamped Clamped beam resonator the force produces a bending of the structure its diagram is shown in Figure 2.14
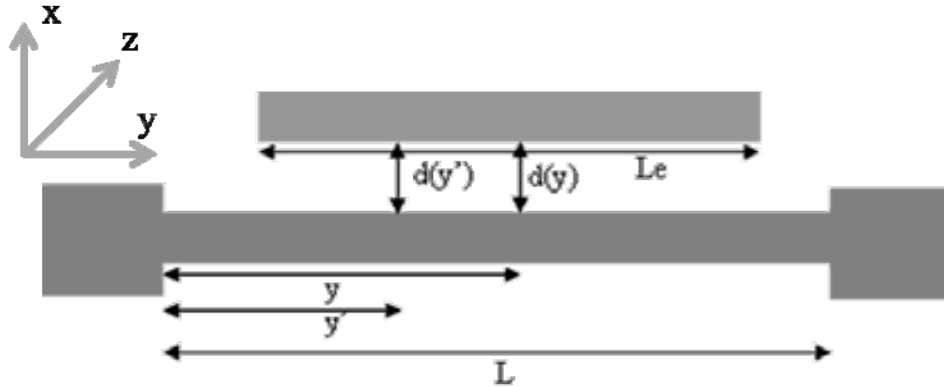

Figure 2.14 Scheme of the CCBeam and the electrode for the analysis

The upper grey rectangle models an electrode, and the lower grey bar models the beam with length *L*. The movement of the resonator is in *x* direction. The variable *y* denotes the position over the resonator. It should be noted that the displacement will be different according to the position over the beam.

Euler-Bernoulli equation is used as starting point. This expression is used to determine the vibration frequencies and the shape functions of all the vibrational modes of a mechanical structure. Euler-Benoulli equation is applicable to all shapes and structures but depending on the complexity of the structure it is necessary to use numerical methods.

The vibration of a beam with small amplitude is considered and can be described as partial differential equation ().

$$\rho A \frac{\partial^2 x}{\partial t^2} + EI \frac{\partial^4 x}{\partial t^4} = 0 \tag{2.71}$$

Where A is the cross section area (*h x W*) of the beam and *ρ* and *E* are the density and the Young's modulus of the material, respectively. *I* corresponds to the second moment of inertia of a rectangular cross section beam that can be calculated by means of the expression (2.72).

$$I = \frac{hW^3}{12} \tag{2.72}$$

The general solution for the expression (2.71) under the vibration in the *x* direction is:

$$x(y,t) = x(y)\cos(\omega_n t + \theta) \tag{2.73}$$

In expression (2.73) ω_n is the natural resonant frequency for the *n* mode of vibration and *θ* is and arbitrary phase. Replacing (2.73) into (2.71) and defining the variable κ_n as in expression (2.74)

$$\kappa_n^4 = \frac{\omega_n^2 \rho h W}{EI}$$ (2.74)

Equation (2.71)is reduced to:

$$\kappa_n^4 x(y) = \frac{\partial^4 x(y)}{\partial y^2}$$ (2.75)

The frequency for any n-mode is obtained through expression (2.76)

$$\omega_n = \kappa_n l \frac{W}{L^2} \sqrt{\frac{E}{12\rho}}$$ (2.76)

The general solution for any y position of expression (2.75) is illustrated in equation (2.77):

$$x(y) = A_n \sin\left(\kappa_n y\right) + B_n \cos\left(\kappa_n y\right) + C_n \sinh\left(\kappa_n y\right) + D_n \cosh\left(\kappa_n y\right)$$ (2.77)

Where $A_n\, B_n\, C_n$ and D_n are the integration constants whose values is determined by the boundary condition of the beam under study. For Clamped Clamped beam, concretely, the boundary conditions are:

$$x(y=0) = 0, x(y=L) = 0, \frac{\partial x}{\partial y}\bigg|_{y=0} = 0, \frac{\partial x}{\partial y}\bigg|_{y=L} = 0$$ (2.78)

The displacement, x, at the ends of the beam is null and then the velocity (displacement derivative) is null too. Considering the first and the third boundary condition and replacing it into (2.77) the integration constants become:

$$A_n = -C_n$$
$$B_n = -D_n$$ (2.79)

Then, applying the second and the fourth boundary conditions

$$0 = C_n\left[\sinh\left(\kappa_n y\right) - \sin\left(\kappa_n y\right)\right] + D_n\left[\cosh\left(\kappa_n y\right) - \cos\left(\kappa_n y\right)\right]$$ (2.80)

$$0 = D_n\left[\sinh\left(\kappa_n y\right) + \sin\left(\kappa_n y\right)\right] + C_n\left[\cosh\left(\kappa_n y\right) - \cos\left(\kappa_n y\right)\right]$$ (2.81)

The relation between D_n and C_n form expression (2.80) and (2.81) are:

$$\frac{D_n}{C_n} = \frac{\sin\left(\kappa_n y\right) - \sinh\left(\kappa_n y\right)}{\cosh\left(\kappa_n y\right) - \cos\left(\kappa_n y\right)}$$ (2.82)

$$\frac{D_n}{C_n} = \frac{\cos\left(\kappa_n y\right) - \cosh\left(\kappa_n y\right)}{\sinh\left(\kappa_n y\right) - \sin\left(\kappa_n y\right)}$$ (2.83)

Combining previous expressions the equation to obtain the nodal point of the beam is::

$$1 = \cos \kappa_n l \cosh \kappa_n l \tag{2.84}$$

For the first mode $\kappa_n l$=4.73

The mode of vibration, *X*, will determine the value of the effective mass in a certain point. Since the frequency of vibration is the same for all the points on the beam (*y*) and the displacement of the different points of the beam occurs at different the velocity, *v(y)*, if the total kinetic energy, KE_{TOT}, of the beam is conserved, the effective mass can be calculated as:

$$m_{eff}(y) = \frac{KE_{TOT}}{\frac{1}{2} v(y)} = \frac{\rho W t \int_0^L X\left(y'\right)^2 d(y)}{X(y)^2} \tag{2.85}$$

x(y') and *x(y)* are the lateral displacement related to the y' position on the beam and the displacement on the centre of the beam respectively. In the in this case, *y'=y*. The effective constant can be calculated as:

$$k_{eff(y)} = \omega_0{}^2 \cdot m_{eff}(y) \tag{2.86}$$

Finally the damping of the model has to be defined and it is expressed by the following expression:

$$c_{eff}(y) = \frac{\sqrt{k_{eff}(y)m_{eff}(y)}}{Q} = \frac{\omega_o m_{eff}(y)}{Q} = \frac{k_{eff}(y)}{\omega_0 Q} \tag{2.87}$$

The value of the input and output transformers turn ratio, η_e and η_r, respectively depends on the coupling area and the voltage applied to the resonator.

In order to validate the electromechanical model developed in this chapter a simulation of the equivalent circuit of the Clamped Clamped Beam resonator depicted on SEM image of the Figure 2.15is performed and compared with the measurements. A V_{DC} of 20V has been applied to the movable structure.
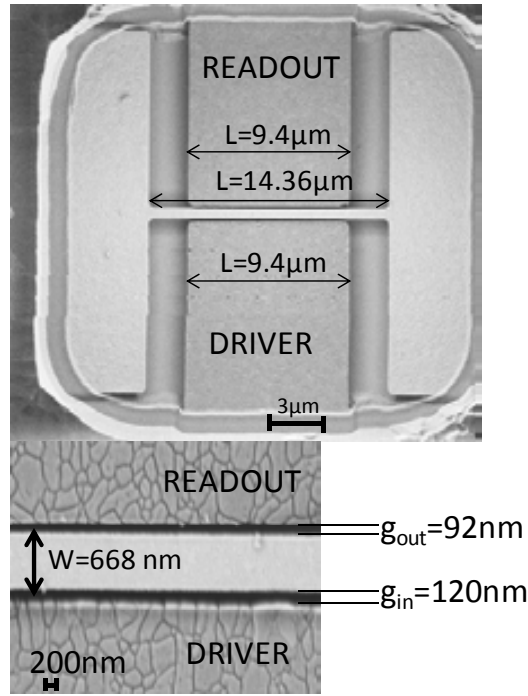
Figure 2.15 SEM image of a Clamped Clamped Beam resonator. The labels show the dimensions of the movable structure and the electrodes as well as the gaps spacing.

In the Table 2.1the dimensions used as inputs to obtain the values of the lumped element of the equivalent circuit are obtained. The Q (220) has been experimentally calculated with the bandwidth at 3dB, BW_{-3dB}, and the center frequency, f_o (see expression (2.88)) of the resonance peak of the transmission response which can be observed as a black line in Figure 2.16.

$$Q = \frac{f_o}{BW_{3dB}} \tag{2.88}$$

Table 2.1 Physical dimensions and mechanical parameters for the beam shown in the Figure 2.15

Physical dimension	Value
W	668nm
L	14.36μm
g_{in}	120nm
g_{out}	94nm
L_{in}	9.44μm
L_{out}	9.44μm

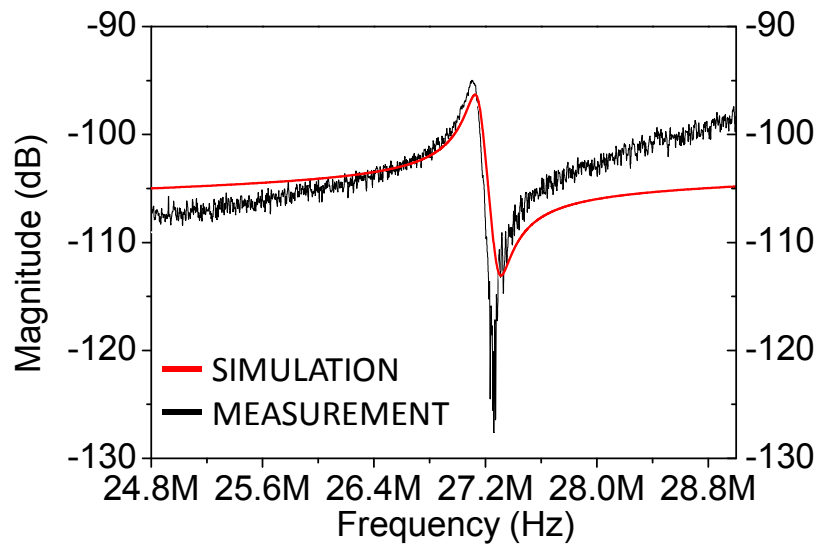| Mechanical parameter	Value
Q	220
D	$1.9 \cdot 10^{-9}$
t	280nm
K	72.15N/m
m	2.466 fg
C_{TH} (by fitting)	0.68aF
E	160 Gpa
ρ	2330 Kg/m³

Figure 2.16 Simulation versus simulation transmission response of the CCBeam Resonator.

2.7 CONCLUSIONS OF THE CHAPTER

In this chapter all the issues related with the electrical transduction of the MEMS have been reported. We have studied the electrostatic excitation of the beam that is possible due to the presence of both an AC and DC voltages. The dynamics of the resonator has been explained. We have studied both the frequency softening and the mechanical movement and all the issues related to it such us different energy losses present in MEMS, We have moved into the sensing of the movement in the readout electrode by means of the motional and feedthrough current.

The most extend part of the chapter has been dedicated to obtain the electromechanical model of a MEM resonator. The electromechanical model allows to have and equivalent electrical circuit very useful to predict the frequency response of the resonator in an electrical simulator. The model present allows to decouple the mechanical variable such as mass, stiffness and damping form the electrical variables such as DC voltages applied to the resonator of the electrode. The DC voltage along with the physical dimensions allows us to obtain the input and output transformer that are the link between two worlds. Dimension, dynamics of the movement and material properties allow us obtaining the value of the resistance, inductance and capacitance at resonance. The feedthrough current transmitted from the input and modeled with a feedthrough current has been introduced. All the issues related with that capacitance in the characterization of the resonator will be studied in Chapter 3.

Finally, the goodness of the electromechanical model has been checked by adjusting the simulated response to an actual measurement (of Clamped-Clamped beam)

2.8 References

[1]   H. A. C. Tilmans, "Equivalent Circuit Representation of Electromechanical Transducers:I. Lumped-parameter Systems," *Journal of Micromechanical and Microengineering,* vol. 6, p. 19, 1995.

[2]   J. C. Salvia, R. Melamud, S. A. Chandorkar, S. F. Lord, and T. W. Kenny, "Real-Time Temperature Compensation of MEMS Oscillators Using an Integrated Micro-Oven and a Phase-Locked Loop," *Microelectromechanical Systems, Journal of,* vol. 19, pp. 192-201, 2010.

[3]   H. M. Lavasani, P. Wanling, B. Harrington, R. Abdolvand, and F. Ayazi, "A 76 dBΩ 1.7 GHz 0.18 υm CMOS Tunable TIA Using Broadband Current Pre-Amplifier for High Frequency Lateral MEMS Oscillators," *Solid-State Circuits, IEEE Journal of,* vol. 46, pp. 224-235, 2011.

[4]   M. Pardo, L. Sorenson, and F. Ayazi, "A phase-noise model for nonlinear piezoelectrically-actuated MEMS oscillators," in *Circuits and Systems (ISCAS), 2011 IEEE International Symposium on*, 2011, pp. 221-224.

[5]   S.Pourkamaly and F.Ayazy, "Electrically Coupled MEMS Bandpass Filter, Part II. Without Coupling Element," *Sensors And Actuators,* vol. 122, 2005.

[6]   M. Motiee, R. R. Mansour, and A. Khajepour, "Novel MEMS, Filter for On-Chip Transceiver Architecture, Modeling and Experiment," *journal of Micromechanical and Microengineering,* vol. 16, pp. 407-418, 2006.

[7]   F.D.Bannon, J.R.Clark, and C.T.-C.Nguyen, "High-Q HF Microelectromechanical Filters," *IEEE Journal of Solid-State Circuits,* vol. 35, pp. 512-526, Abril 2000

[8]   H. Hosaka, K. Itao, and S. Kuroda, "Evaluation of energy dissipation mechanisms in vibrational microactuators," in *Micro Electro Mechanical Systems, 1994, MEMS '94, Proceedings, IEEE Workshop on*, 1994, pp. 193-198.

[9]   F. Ahmad, M. H. M. Khir, N. H. Hamid, and J. O. Dennis, "Analytical modeling of plus shape MEMS paddle bridge resonant sensor for weak magnetic fields," in *Micro and Nanoelectronics (RSM), 2011 IEEE Regional Symposium on*, 2011, pp. 310-314.

[10]   Y.-H. Park and K. C. Park, "High-fidelity modeling of MEMS resonators. Part I. Anchor loss mechanisms through substrate," *Microelectromechanical Systems, Journal of,* vol. 13, pp. 238-247, 2004.

[11]   R. N. Candler, A. Duwel, M. Varghese, S. A. Chandorkar, M. A. Hopcroft, P. Woo-Tae, K. Bongsang, G. Yama, A. Partridge, M. Lutz, and T. W. Kenny, "Impact of geometry on thermoelastic dissipation in micromechanical resonant beams," *Microelectromechanical Systems, Journal of,* vol. 15, pp. 927-934, 2006.

[12]   T. Mattila, J. Kiihamäki, T. Lamminmäki, O. Jaakkola, P. Rantakari, A. Oja, H. Seppä, H. Kattelus, and I. Tittonen, "A 12 MHz micromechanical bulk acoustic mode oscillator," *Sensors and Actuators A: Physical,* vol. 101, pp. 1-9, 2002.

[13]   H. Li-Wen, C. T. C. Nguyen, Y. Xie, Y.-W. Lin, S.-S. Li, and Z. Ren, "UHF Micromechanical Compound-(2,4) Mode Ring Resonators With Solid-Gap Transducers," in *Frequency Control Symposium, 2007 Joint with the 21st European Frequency and Time Forum. IEEE International*, 2007, pp. 1370-1375.

[14]   Y. Jinling, T. Ono, and M. Esashi, "Energy dissipation in submicrometer thick single-crystal silicon cantilevers," *Microelectromechanical Systems, Journal of,* vol. 11, pp. 775-783, 2002.

[15]   R. Lifshitz and M. L. Roukes, "Thermoelastic damping in micro- and nanomechanical systems," *Physical Review B,* vol. 61, pp. 5600-5609, 2000.

[16]   Q. Jing, H. Luo, T. Mukherjee, L. R. Carley, and G. K. Fedder, "CMOS micromechanical bandpass filter design using a hierarchical MEMS circuit library," presented at the Micro Electro Mechanical Systems, 2000. MEMS 2000. The Thirteenth Annual International Conference on, 2000.

[17]   C. T. C. Nguyen and R. T. Howe, "An integrated CMOS micromechanical resonator high-Q oscillator," *Solid-State Circuits, IEEE Journal of,* vol. 34, pp. 440-455, 1999.

[18]   K. Tanaka, R. Kihara, A. Sánchez-Amores, J. Montserrat, and J. Esteve, "Parasitic effect on silicon MEMS resonator model parameters," *Microelectronic Engineering,* vol. 84, pp. 1363-1368, 2007.

Chapter.3 ELECTRICAL CHARACTERIZATION: MEASUREMENT TECHNIQUES

One of the most important problems in electrically excited and read resonators is the presence of feedthrough current from the input to the output. In this chapter, different measurement techniques are analyzed and all the advantages and disadvantages are commented. A wide bench of experiments and the corresponding results addressed to alleviate the feedthrough capacitance problematic are presented.

3.1 THE FEEDTHROUGH CURRENT, AN ETERNAL PROBLEM: THE STATE OF THE ART

Electrostatic excited and capacitive read MEM resonators in this work are very suitable to be integrated with circuitry because they can be excited with an electrical input signal and they provide an electrical output signal. In summary they can be embedded in all the integrated circuits (IC) we desire. Furthermore, this kind of electrically transduced MEMS offers: a) frequency tuning by DC voltage applied to the device and b) the application of DC voltage can turn the resonator on or off if it is needed [82]. This tuning capability can be applied not only for adjusting the resonant frequency but also for temperature compensation [83-84].

However, this type of transduction methods always present some disadvantages compared with other techniques (optical detection, piezoelectric excitation) which can be a problem. This effect consists on a feedthrough signal obtained in the sensing port. The unwanted feedthrough current comes from a capacitance connected between the input and the output port and it reduces the electrical Q with affects the performance of the device. Furthermore, the signal coupled from the input to the output can difficult the measurement of the resonator frequency response.

In this work, and concretely in this chapter, the effect of the feedthrough capacitance is studied in different MEMS topologies. As starting point, the analysis of a two-port resonator, formed by a driver, the movable part and the readout electrode is analyzed. The understanding of its working principle can be extended to any types of MEMS resonators electrically actuated and read it.
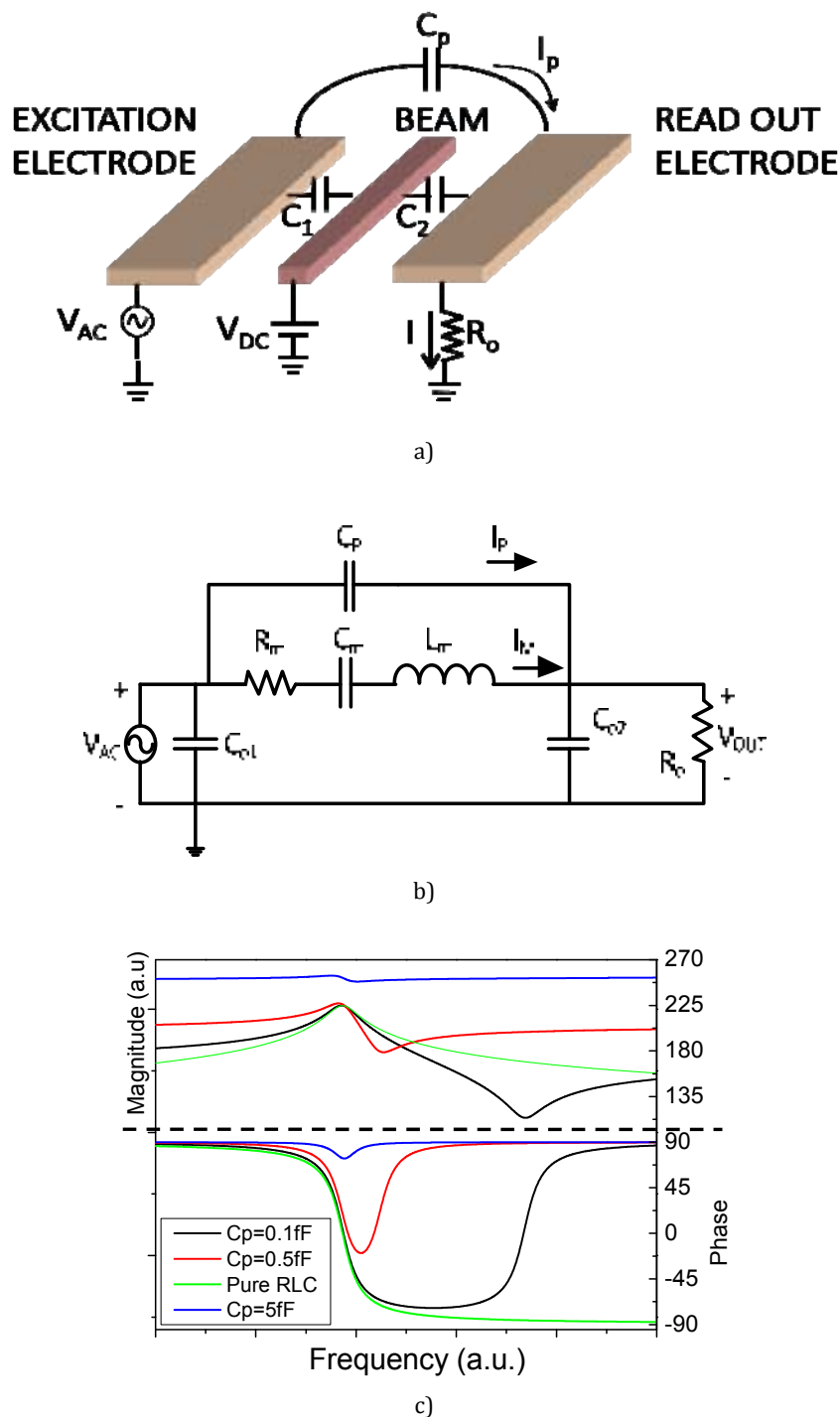
a)

b)

c)

Figure 3.1 a) Schematic of a classical C-C beam resonator b) simplified electrical schematic of a resonator. c) plot of the magnitude and phase frequency responses of the resonator under the effect of different parasitic capacitance values.

In MEMS devices under study, the movement of the resonator is forced by the application of an AC voltage (V_{AC}) plus a DC voltage (as it will be explained in chapter 2) in the capacitor formed between the excitation electrode (see Figure. 3.1a) and the movable structure, C_1. The applied voltage generates an attractive electrostatic force that bends the resonator. The capacitive sensing is based on the capacitive change measurement

originated between the read-out electrode and the resonator due to the MEMS movement. To detect this change, a DC voltage (V_{DC}) is applied in the output capacitance, C_2, and the induced output current is measured at the readout electrode. Equation (3.1) corresponds to the measured output current (assuming $V_{DC} \gg V_{ac}$) for the resonator shown in Figure 3.1 a).

$$ I \cong V_{DC} \frac{\partial C_2}{\partial t} + C_p \frac{\partial v_{ac}}{\partial t} \tag{3.1} $$

where C_2 is the variable capacitance between the suspended beam and the read-out electrode (not confuse with the capacitance of the electrical model of the resonator in Figure 3.1 b), and C_p is the parasitic capacitance between the excitation and read-out electrodes. The first term corresponds to the current created by the movement while the second term is called feedthrough current.

Figure 3.1b) shows the simplified electrical schematic of the MEMS resonator presented in Figure 3.1 a). The in-plane movement of the resonator is considered. The RLC branch models the motional behavior, I_M, while the parallel C_p corresponds to the feedthrough capacitance that generates the feedthrough current (I_P). The presence of this capacitance disturbs the MEMS measurement. If the parasitic capacitance value is high, most of the excitation signal goes through the parasitic capacitance and makes the measurement of the resonator characteristics difficult. Moreover, it generates a parallel resonance that makes the phase to have a 90 degrees value at high frequencies, and forces the phase to present two frequencies where its value is zero. [85-86]. The feedthrough capacitance becomes much more critic when frequency increases presenting major problems at high frequencies. Figure 3.1c shows the simulated effect of the increment of C_p on the resonant peak. It can be seen how a large value of the parasitic capacitance generates a feedthrough current that masks the motional current. On the contrary, a reduction of the feedthrough current allows to have a purely RLC behavior. In the case of filters, the reduction of the feedthrough capacitance allows to increase the performance of the filter, achieving a higher stop-band rejection. However, the presence of the parasitic capacitance can be beneficial. For instance, in MEMS filters it can provide a higher selectivity by forcing transmission notches at both sides of the bandpass as it will be seen later.

Note that in Figure 3.1 c), the parasitic capacitance affects directly the phase shift of the frequency response. A large feedthrough capacitance presents slight phase shift. On the contrary, if C_p decreases the phase variation becomes larger.

As it is shown in Figure 3.1 c), the position of the antiresonance peak depends on the value of the parasitic capacitance in addition of the motional capacitance. Actually, the relation between the parasitic capacitance and the motional capacitance will define the frequency of the antiresonance (expression 3.2).

$$ f_p = \frac{1}{2\pi \sqrt{L \dfrac{C \cdot C_p}{C + C_p}}} \tag{3.2} $$

Summarizing, feedthrough capacitance creates a feedthrough current that can mask the motional current. Furthermore, it can disturb the phase shift making the resonator not suitable for its integration on self-sustained oscillators. A pure RLC behavior is required in most of RF application. For these reasons many efforts are found in the literature addressed to cancel the feedthrough. In this chapter, the following techniques are detailed in order to suppress or minimize it:

1) Port configuration set up

2) Smart layout design

3) Capacitance compensation through the use of twin resonators or external capacitance

4) Non-linear techniques: Mixing and half frequency excitation.

Many studies can be found in the literature focused on reducing or eliminate the feedthrough effect in MEMS resonators. In this introduction, a brief review of the most relevant works on the field is included.

In order to attempt on different characterization set-ups Seshia et al. in [86] worked over different transduction methods. Its work is a complete review of the characterization techniques that can be used in MEMS devices. Besides the piezoresistive and mixing methods presented by Seshia, the use of different port configuration set up are deeply studied in that work. They observed slight differences between the one port and two port set ups in terms of resonant peak. However, they obtained a great difference in terms of feedthrough current. In this chapter a similar study over a C-C Beam is performed. Advantages and disadvantages are commented.

Smart layout design was the adopted technique by Arcamone et al in [85]. They have proposed a new balanced set-up scheme that allows eliminating the parasitic capacitance despite the presence of technological mismatching. A Lamé-mode resonator is used to corroborate the technique. The same approach will be extended to a flexural Clamped Clamped beam in this chapter.

The capacitance compensation principle is used in [87] and [88]. In this case the four electrodes of a square resonator working in its Lamé mode are used to differentially excite and read. Since the resonator to electrode capacitance is very similar for all the electrodes, the feedthrough current read at each output electrodes pair can be subtracted. The same principle was used by Li et.al. in [89]. They used the differential excitation and read of a mechanically coupled arrayed-disk resonators-based filter to reduce the feedthrough floor in their device. In this study, they achieve the reduction of the feedthrough not only using the electrical differential excitation and sensing technique but also using a smart mechanical coupling based on an optimized wavelength mechanical coupling to produce two out-of phase mechanical modes (see Figure 3.2)
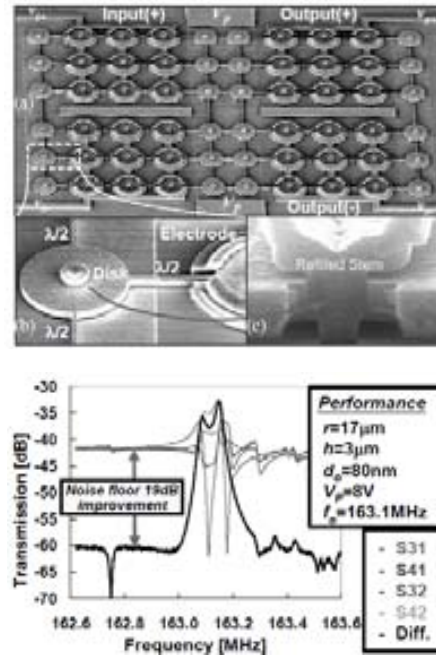
Figure 3.2 a) SEM image of the arrayed disks filter presented in [89]. Disks are mechanically coupled by means a half mechanical wavelength to force the in phase movement. Differential architecture can be observed. b) electrical measurement comparison between the single ended and differentia approaches

Other approach to cancel the feedthrough is based on the subtraction the feedthrough currents provided by two identical twin resonator as in [53] [90] and [91]. One of the resonators is enabled by biasing it. This resonator provides an output current comprised of the motional current and the feedthrough current. The other resonator is used as a dummy resonator and only provides the feedthrough current. Both resonators output currents are subtracted and only the motional current remains at the output.

Despite the use of capacitance compensation shown in the previous paragraph enhances qualitatively the frequency response of the resonators, the efficiency of this method implemented using twin resonator lies in the symmetry of the resonators. However, due to the fabrication tolerances in CMOS or specific MEMS foundries, the feedthrough capacitance does not use to be identical. The use of a tunable external capacitance instead of a dummy resonator to provide the corresponding feedthrough current was studied by Seshia *et.al* [92]. The external capacitance can be adjusted externally to provide exactly the same feedthrough current than the resonator.

The non-linear properties of MEMS devices can be used to decouple the feedthrough and the motional current in the frequency domain [93]. One of the solutions consists on the use of a MEMS as a mixer due to its quadratic dependence on the applied voltage [19]. In this approach, the excitation of the MEMS is done by two AC signals, which are not at the resonance frequency of the resonator, but their sum, or difference corresponds to the MEMS resonant frequency. This fact allows the removal of the effect of parasitic feedthrough, separating the parasitic and motional current in the frequency domain [52].

Besides the solutions presented in the previous paragraphs, other solutions based on the fabrication materials have been presented in the literature. For example Piazza *et.al* [94] included the piezoelectric actuation in order to decrease the motional resistance. Indirectly, the reduction of the motional resistance supposes an increment on the motional

current and then, the feedthrough is fewer critical. The final result was a resonator working at 1.7MHz with a Q factor around 6000. On the other hand, Weinstein *et.al.* presented a filter based on high-k dielectrically transduction. The use of dielectric transduction considerably reduces the motional resistance. Furthermore, they used the single ended to differential measurement. The final response was a filter with a 434MHz center frequency and 1MHz bandwidth[95].

However, there are some cases where the suppression of the feedthrough capacitance is actually difficult or simply the control of the feedthrough becomes a need. For example, the filter performance in many coupled electromechanical resonator systems is achieved by inducing the phase inversion, which is obtained by means of the control of the position of the parallel resonance frequency. If this effect is not achieved, the system will perform as an array [96]. Furthermore, the proper control of the parasitic capacitance can increase the filter selectivity.

3.2 PORT CONFIGURATION SET UPS

One of the most important issues in the electrostatic excited and capacitive read resonators is the measurement set up. The measurement technique used to obtain the frequency response of the resonator is critical from the feedthrough capacitance point of view. In this section, differences between the one port and two ports measurements are explained. The theory and experimental results of a measurement over a C-C beam resonator are discussed and the advantages and disadvantages are commented. Port configuration techniques offer interesting results when they are applied on the four electrode of a Lamé mode square resonator. In this section, a brief review of different strategies is included

Figure 3.3 shows the scanned electron microscopy (SEM) image of the C-C beam resonator used to illustrate the theory of the one and two port measurement. The resonator, fabricated in Poly 1, is separated from the electrodes, fabricated in Poly 2, by a 100 nm gap. The main physical features (dimension and materials) are labeled over the picture.
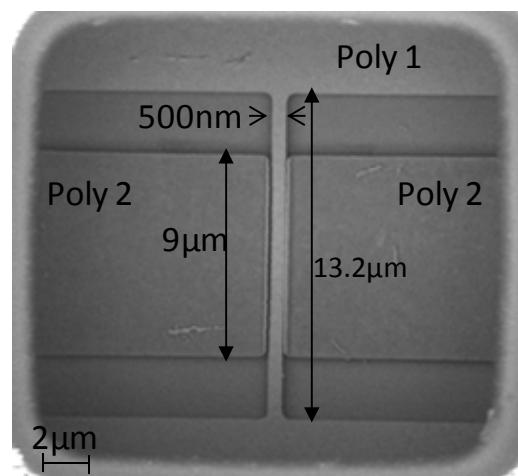

Figure 3.3 SEM image of a C-C beam resonator. The main dimensions are labeled over the picture. The resonant frequency is *f=25MHz*

3.2.1 ONE PORT MEASUREMENT.

Figure 3.4 shows the diagram of the one port measurement technique. The input signal is applied at the input electrode and the output signal is read over the resonator. The diagram shows the time dependent voltage v_{ac} that is added to a DC voltage V_{DC}.
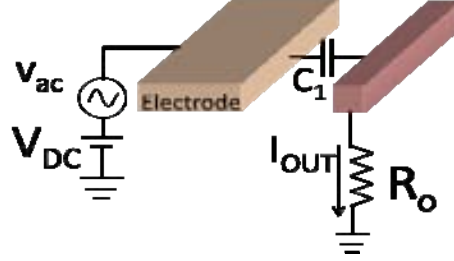

Figure 3.4 Diagram of the one port measurement set up. The ac signal is applied at the input electrode and the motional current is measured over the resonator. R_o corresponds to input network analyzer resistance.

The capacitance between the electrode and the resonator is modeled by C_1. The harmonic variation of the capacitance is illustrated in expression (3.3)

$$C_1 = C_{o1} \frac{s}{s - x} \tag{3.3}$$

Where x is the resonator harmonic movement and s is the gap between the electrode and the resonator. If the resonator moves slightly compared with the gap, $x<<s$, the capacitance variation can be rewritten as a Taylor's approximation:

$$C_1 = \frac{C_{o1}}{s}\left(1 + \frac{2x}{s} + 3\left(\frac{x}{s}\right)^2 + ...(n+1)\left(\frac{x}{s}\right)^n\right) \tag{3.4}$$

Only the first two terms will be considered. V_{DC} is considered much larger than v_{ac}. The current induced on the resonator depends on the capacitance variation and the DC voltage between the electrode and the resonator on one hand. On the other hand, the AC signal applied on the electrode generates a current due to the static capacitance, C_{o1}. Therefore, the total output current is expressed as:

$$I_{OUT} \cong V_{DC} \frac{\partial C_1}{\partial t} + C_{o1} \frac{\partial\left(v_{ac} - v_{out}\right)}{\partial t} \tag{3.5}$$

Replacing (3.4) into (3.5) expression (3.6) can be obtained

$$I_{OUT} = +V_{DC} \underbrace{\frac{C_{o1}}{s}\left(1 + 2\frac{x}{s}\right)\frac{\partial x}{\partial t}}_{I_M} + \underbrace{\frac{\partial(v_{ac} - v_{out})}{\partial t} C_{o1}}_{I_P} \tag{3.6}$$

In (3.6) the first term corresponds to the feedthrough current, I_P, whereas the second term corresponds to the motional current, I_M.

If the resonator moves slightly compared with the gap, $x<<s$, the motional current can be rewritten as:

$$I_m = V_{DC} \frac{C_{o1}}{s} \frac{F_E Q}{k} \omega_o \tag{3.7}$$

Note that the expression (3.7) has been obtained replacing the resonator displacement velocity, $\partial x/\partial t$ at the resonance frequency by the expression (2.57).

$$\frac{\partial x}{\partial t} = \frac{F_E Q}{k} \omega_o \tag{3.8}$$

The force exerted on the resonator at this frequency is:

$$F_E = |V_{DC}| |v_{ac}| \frac{C_{o1}}{s} \tag{3.9}$$

3.2.2 TWO PORT MEASUREMENT

Figure 3.5 shows the diagram of a C-C beam used to illustrate the two-port configuration set-up. In the two-port measurement approach presented in this work, one of the electrodes is used as input port or excitation electrode. This electrode is usually known as driver and the *AC* voltage is applied over it. A DC voltage is used to bias the resonator for two reasons: a) on one hand, to enable the movement and b) on the other hand to allow the detection of the movement on the output port. The output electrode plays the output port role where the load resistance is connected to (R_o). In Figure 3.5 C_1 and C_2 are the capacitances between the input electrode and the resonator and between the resonator and the output electrode respectively. C_p is the feedthrough capacitance between the input and the output.

Considering the variation of the output capacitance, C_2, in Figure 3.5 as:

$$C_2 = C_{o2} \frac{s}{s - x} \tag{3.10}$$

Using the two first Taylor's approximation terms as in (3.4), the output current is illustrated by expression (3.11).

$$I_{OUT} \cong \underbrace{V_{DC} \frac{C_{o2}}{s} \left(1 + 2\frac{x}{s}\right) \frac{\partial x}{\partial t}}_{I_M} + \underbrace{C_p \frac{\partial \left(v_{ac} - v_{out}\right)}{\partial t}}_{I_P} \tag{3.11}$$

The first term corresponds to the motional current whereas the second term corresponds to the feedthrough current. Note that the feedthrough current, I_p, depends on C_p, which models the parasitic capacitance. In the two-port configuration, the parasitic capacitance models either the bending of the electric fields (also called fringing fields) or the propagation of electrical energy through the substrate.

Figure 3.5 Diagram of a C-C beam resonator in the two port configuration.

The motional current considering symmetrical gaps and electrodes and small displacements, *x,* is:

$$I_m = V_{DC} \frac{C_{o2}}{s} \frac{F_E Q}{k} \omega_o \tag{3.12}$$

The force exerted into the resonator at resonance is illustrated by means of expression (3.13).

$$F_E = |V_{DC}||v_{ac}| \frac{C_{o1}}{s} \tag{3.13}$$

3.2.3 RESULTS AND DISCUSSION

In this section, the two measurement techniques presented in section 3.2.1 and 3.2.2 are compared. To perform the experiment the same excitation force is ensured for the two set-ups by means of applying the same DC voltages. The output currents are measured and compared. Figure 3.6 shows the frequency response in terms of phase and magnitude of the two measurements set-ups. The black line shows the performance of the one port set up. The blue line shows the two-port measurement.
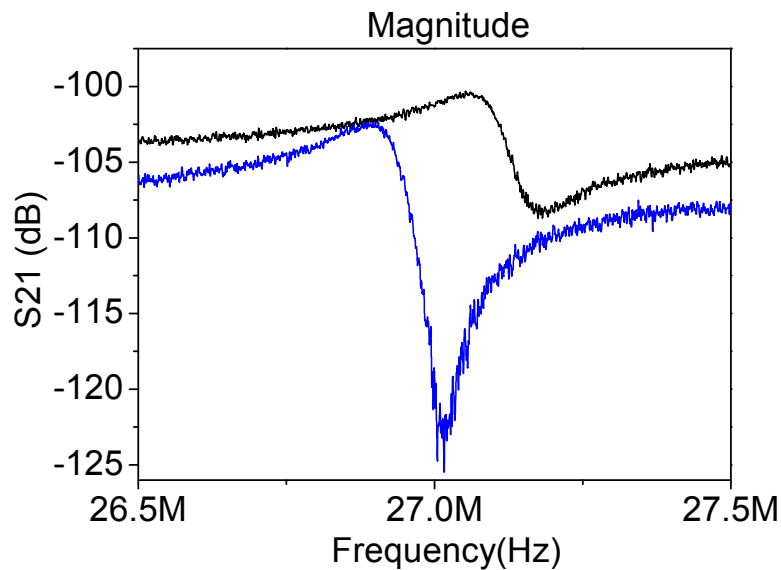
a)
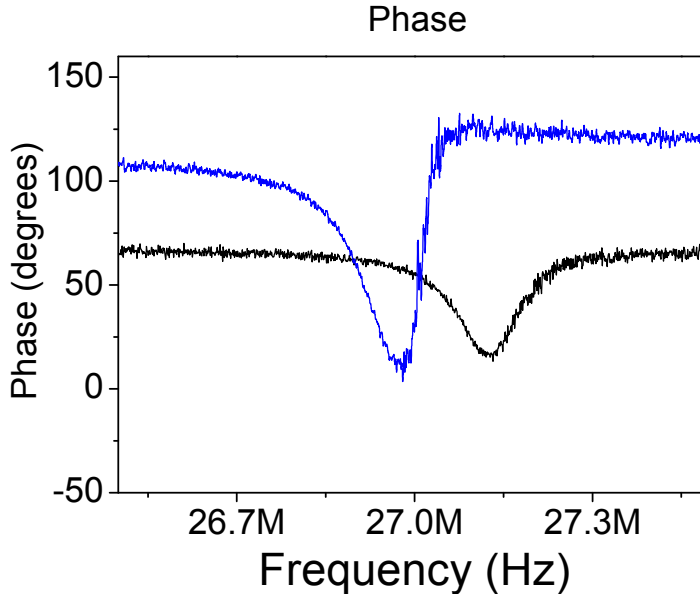
b)

Figure 3.6 Frequency response in terms of magnitude (a) and phase (b) one port (black) with, $V_{DC}=14V$ and two port (blue) with $V_1=0V$, $V_{DC}=14V$ and $V_2=0V$.

Table 3.1 summarizes the input force, the motional current and the electrical inputs and outputs. The first row shows the force exerted on the resonator. The motional and feedthrough currents are calculated in the second and third row respectively and the experimental results are shown in the two last rows.

Table 3.1 Summary of the main features used for electrical characterization of the Clamped C lamped Beam resonator.

Topology	ONE PORT	TWO PORT
Force	$F_E = \mid V_{DC} \mid\mid v_{ac} \mid \dfrac{C_o}{s}$	$F_E = \mid V_{DC} \mid\mid v_{ac} \mid \dfrac{C_o}{s}$
Motional current	$I_m = V_{DC} \dfrac{C_o}{s} \dfrac{F_E Q}{k} \omega_o$	$I_m = V_{DC} \dfrac{C_o}{s} \dfrac{F_E Q}{k} \omega_o$
Feedthrough Current	$\dfrac{\partial(v_{ac} - v_{out})}{dt} C_{o1}$	$C_p \dfrac{\partial(v_{ac} - v_{out})}{\partial t}$
Voltage	VDC=14V	VDC=14V
Total phase shift	60º	100º
Coupling level	-103dB	-106dB

The analysis of the results suggest that the feedthrough current determines the input to output coupling level in S21 magnitude measurement. The one port measure magnitude (black line) shows a higher coupling level (-103dB) than the two port measurement shown in red line (-106dB). The direct static capacitance between the electrode and the resonator (C_{o1} in Figure 3.4) in the one port measurement is bigger that the feedthrough capacitance, C_p in Figure 3.5. The phase shift in one port and two-port measurement is an indicator of the feedthrough current effect. The one port measurement phase shift (60º) is lower than

the two-port measurement (almost 100º). A simulation of the feedthrough capacitance effect over the phase shift was introduced in Figure 3.1 c).

3.2.4 ELECTRODES CONFIGURATION IN A FOUR ELECTRODES DEVICE

As it was commented at the beginning of section 3.2, four electrode devices allow different configuration to improve the read of the motional current. The typical four-electrode resonator used to perform the experiments is the square resonator working in its Lamé mode [85-86, 97]. In this chapter, we present a summary of the main characterization techniques applied to this resonator.

The Lame mode resonator is a square resonator, which is working as it is shown in Figure 3.7. In the Lame mechanical mode, two parallel horizontal sides of the resonator are expanding whereas the other two orthogonal vertical sides are compressing.

The feedthrough contribution of each driver to each readout electrode can be summarized as in Figure 3.8. C_{f1} and C_{f2} represent the feedthrough capacitance between the two input electrodes and one output electrode. The feedthrough capacitances of the other output electrode are the same. Two output currents are available and the subtraction of its feedthrough components is possible.
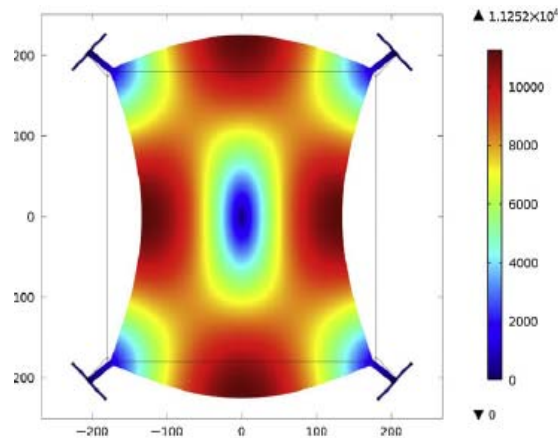
Figure 3.7. FEM simulation of a Lamé mode square resonator [98].
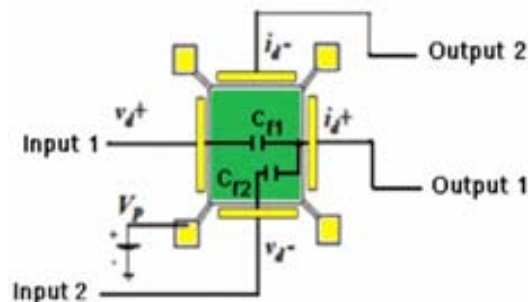

Figure 3.8 Diagram of a Lamé mode resonator. C_{f1} and C_{f2} represent the feedthrough capacitance between the two input electrodes and one output electrode. This schema can be used to represent the feedthrough contribution to the other output electrode, since the single device is assumed to be symmetric. [97]

In this section the Bhave's work addressed to the current cancellation using a square resonator has been used to illustrate it. In [87] three different port configurations are studied and they are summarized in Table 3.2. The Single ended excitation to single ended readout configuration is similar to the two-port configuration presented in section 3.2.2. The input is applied at two opposite electrodes while the readout is performed in the two orthogonal electrodes. This port configuration does not cancel the feedthrough contribution. The single ended to differential configuration, whose diagram can be observed in Table 3.2 allows the feedthrough contribution to be cancelled. The fully differential approach allows eliminating the feedthrough contribution besides enabling a better power handling.

It can be concluded that the fully differential approach offers an efficient way to cancel the feedthrough contribution.

Table 3.2. Summary of the main characterization set ups of a typical Lamé mode resonator.

Ref	Excitation	Read	Diagram	Key Feature
[87]	Single-Ended	Single-Ended		Feedthrough still present
[87]	Single Ended	Differential		Cancellation of the feedthrough.
[87]	Differential	Differential		Cancellation of the feedthrough.

In this section different transduction techniques of a single MEM device have been reviewed. All this techniques are based on the assumption that the fabricated resonator is completely symmetric. This is an imperative condition in order to have the same feedthrough contribution to the two differential outputs and can cancel it. In actual devices with the current fabrication processes, the symmetric resonators are rarely achieved and alternatives methods have been developed in this work to overcome it.

3.3 LAYOUT OPTIMIZATION

As it was introduced in section 3.1 the layout optimization is presented as a solution to suppress the feedthrough current in MEM resonators. This approach uses intrinsic methods to avoid the use of twin resonators or external capacitances. This idea was inspirited by the Arcamone's work in [85]. In this chapter, the layout optimization has

been applied to a flexural C-C beam. The layout includes two separate electrodes at both sides of the beam (see Figure 3.9). The objective of this technique is to compensate the feedthrough current due to the capacitance mismatching. The capacitance mismatching is produced by the fabrication tolerances.

3.3.1 FUNDAMENTALS OF THE TRANSDUCTION:

Figure 3.9 shows a diagram of the CC Beam with four electrodes along with the signal set-up. Electrodes 1 and 2 are used as drivers or input electrodes while electrodes 3 and 4 are used to control the gap spacing through the application of specific DC voltages. An AC voltage v_{ac} is applied in counter-phase on electrodes 1 and 2 to force the first mechanical flexural mode. Finally, the read-out is performed through the movable structure. A DC voltage V_3 is added to the AC (v_{ac}) voltage to allow the excitation of the electrode. Electrodes 3 and 4 are used as control electrodes. Voltages V_1 and V_2 are applied to the electrodes in order to electrostatically control the gaps between them and the resonator.

Figure 3.9. Diagram of the four-electrode resonator including the excitation and biasing voltages as well as the current induced over the resonator.

To compute the total output current, the motional and feedthrough current contribution of each electrode is calculated. Taking into account the beam movement and using a parallel plate capacitance approximation, the variation of the capacitances at both sides of the beam (C_1 versus C_2 and C_3 versus C_4) follows expressions (3.14) and (3.15)

$$\frac{\partial C_1}{\partial t} = -\frac{\partial C_2}{\partial t} \tag{3.14}$$

$$\frac{\partial C_3}{\partial t} = -\frac{\partial C_4}{\partial t} \tag{3.15}$$

Capacitances C_1, C_2, C_3 and C_4 are described by the following expressions

$$C_1 = C_{o1} \frac{s}{s+x}, \quad C_3 = C_{o3} \frac{s}{s+x} \tag{3.16}$$

$$C_2 = C_{o2} \frac{s}{s-x}, \quad C_4 = C_{o4} \frac{s}{s-x} \tag{3.17}$$

where x corresponds to the lateral displacement of the beam and the static capacitance, C_{o1}, C_{o2} C_{o3} and C_{o4} corresponds to

$$C_o = \frac{A\varepsilon}{s} \tag{3.18}$$

being A the coupling area, ε the air permittivity and s the gap between the each electrode and the resonator. The gap depends on the geometry of the structure after the fabrication but it can be modified by changing the voltage applied on the electrodes. By biasing electrodes, a variation on the equilibrium state is introduced. A variation on the gap produces a change in the static capacitance between the movable part and the electrode.

The current induced on the resonator by each excitation electrode, 1 and 2, can be expressed as:

$$I_1 = C_{o1} \frac{\partial(-v_{ac} - v_{out})}{\partial t} - V_3 \frac{C_{o1}}{s}\left(1 - 2\frac{x}{s}\right)\frac{\partial x}{\partial t} \tag{3.19}$$

$$I_2 = C_{o2} \frac{\partial(v_{ac} - v_{out})}{\partial t} + V_3 \frac{C_{o2}}{s}\left(1 + 2\frac{x}{s}\right)\frac{\partial x}{\partial t} \tag{3.20}$$

where x corresponds to the beam harmonic displacement. Note that two approximations have been done in previous expressions. First of all, in the first term the variation of the value of capacitances C_1, C_2 due to the sinusoidal movements has been neglected, since they have been computed as static capacitances (C_{o1} and C_{o2}). Finally, the AC excitation voltage v_{ac} and the output voltage v_{out} in the second term of expression (3.19) and (3.20) have been neglected in front of the DC voltage V_3. The same assumption will be considered in expression (3.21) and (3.22) Following the same criteria, electrodes number 3 and 4 generate on the resonator I_3 and I_4 currents:

$$I_3 = C_{o3} \frac{\partial(-v_{out})}{dt} - V_1 \frac{C_{o3}}{s}\left(1 - 2\frac{x}{s}\right)\frac{\partial x}{dt} \tag{3.21}$$

$$I_4 = C_{o4} \frac{\partial(-v_{out})}{dt} + V_2 \frac{C_{o4}}{s}\left(1 + 2\frac{x}{s}\right)\frac{\partial x}{dt} \tag{3.22}$$

In expressions (3.19), (3.20), (3.21) and (3.22) the Taylor's series approximation until the second term for the capacitance. The total output current can be calculated as:

$$I_{TOT} = I_1 + I_2 + I_3 + I_4 = \tag{3.23}$$

$$= \underbrace{\left(C_{o2} - C_{o1}\right)\frac{\partial V_{ac}}{\partial t}}_{I_{F1}} - \underbrace{\left(C_{o1} + C_{o2} + C_{o3} + C_{o4}\right)\frac{\partial\left(V_{out}\right)}{\partial t}}_{I_{F2}} +$$

$$+ \underbrace{\left[\frac{V_3}{s}\left(C_{o2} - C_{o1}\right) + x\frac{2V_3}{s^2}\left(C_{o1} + C_{o2}\right) + \left(V_2\frac{C_{o4}}{s} - V_1\frac{C_{o3}}{s}\right) + 2\frac{x}{s}\left(V_1\frac{C_{o3}}{s} + V_2\frac{C_{o4}}{s}\right)\right]\frac{\partial x}{\partial t}}_{I_M}$$

The total induced current corresponds to the sum of the four electrodes contribution. Its value is shown in expression (3.23). Three different terms can be distinguished. The two first, I_{F1} and I_{F2} correspond to the current contributions of the static capacitances (feedthrough current) while the last one, I_M, is the motional current.

The first term depends on the relation between the static capacitances C_{o2} and C_{o1}. The difference between capacitances can be cancelled by adjusting the voltage on electrodes 3 and 4.

In relation with the I_{F2}, it is necessary to consider the electrical transduction used. The output current can be expressed as the sum of both motional and feedthrough currents and, of course, it can be related with the output voltage v_{out}

$$I_{out} = I_M + I_{F2} = C_{IN}\frac{\partial v_{out}}{\partial t} \tag{3.24}$$

where v_{out} is the signal that will be amplified by the CMOS circuitry. The IC presents an input capacitance C_{IN}. In linear regime, the movement of the MEMS corresponds to a sinusoidal signal. As a first approximation, and considering that the sum of the 4 static capacitances will be 4 times one of them (simply assuming a parallel plate capacitance approximation between the two opposite electrodes) the feedthrough current I_{F2} can be written as:

$$I_{F2} = 4C_o\frac{\partial\left(v_{out}\right)}{\partial t} \tag{3.25}$$

If we replace dv_{out}/dt

$$I_{F2} = 4C_o\frac{I_M + I_{F2}}{C_{IN}} \tag{3.26}$$

The relation between the feedthrough current and the motional current is then:

$$\frac{I_{F2}}{I_M} = \frac{\dfrac{4C_o}{C_{IN}}}{1 - \dfrac{4C_o}{C_{IN}}} \tag{3.27}$$

To reduce the effect of the feedthrough current it is necessary that I_M presents a value larger than I_{F2}. According to the previous expression, this is obtained only if $C_{IN} >> 8C_o$. In the case under study, the amplifier input capacitance is much larger (400fF) than the

parallel plate capacitor between the electrode and the resonator (100aF for the dimensions of the device under study and specified in section 3.3.2) and thereby I_M is larger than I_{F2}.

Accordingly to the previous considerations, the strategy for the feedthrough current cancellation is focused on obtaining the same value for the input static capacitances (C_{o2}-C_{o1}=0). This condition can be fulfilled by a proper DC biasing on the 4 electrodes. In order to demonstrate it, Coventor simulations have been performed. These simulations consist on studying the variation of the capacitances with the DC voltages applied to the electrodes for a given initial mismatching on the electrode to resonator gap distances. Specifically the gap s_1 is considered 90nm while the gap s_2 is 110nm, (equivalent to a 10% fabrication tolerance during the CMOS process of a 100nm nominal gap distance). The electrical initial conditions are: V_3=20V and V_2=0V. A DC sweep has been performed over V_1 from 0 to 22V. Figure 3.10 a) shows the variation of the capacitances C_{o2} and C_{o1} (black and red line respectively) as well as the displacement of the center of the beam. The simulation of the structure shown in Figure 3.10 b) demonstrates that equal capacitances can be obtained with V_1=20V. Note that large central beam displacement (up to 35nm) can be achieved by the application of the proper voltage.

a)

b)
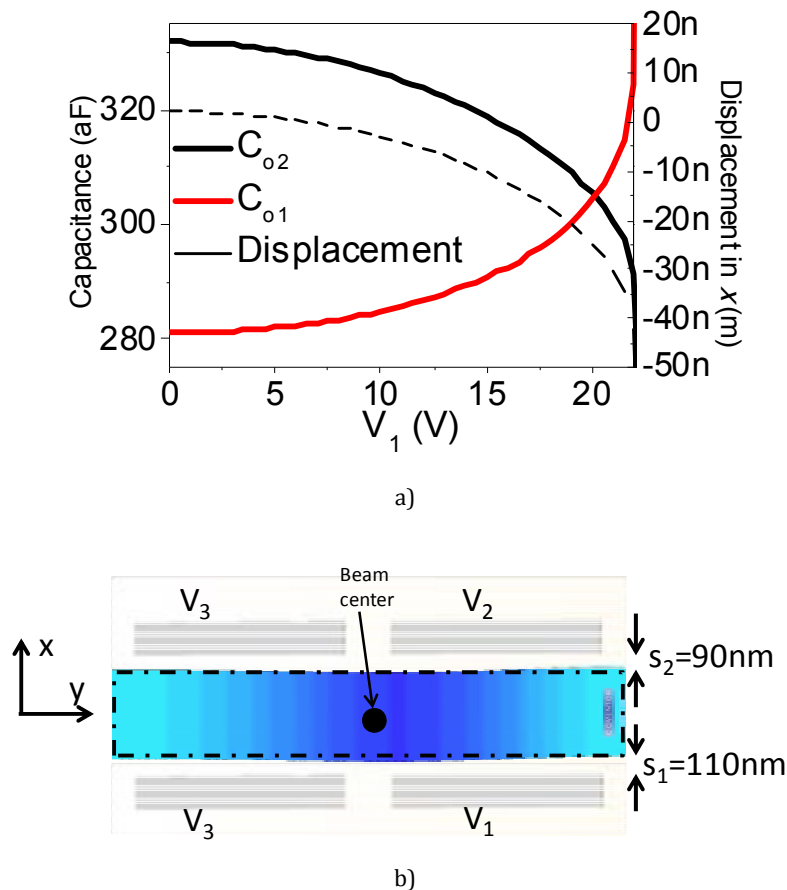
Figure 3.10 Static capacitances C_{o2} and C_{o1}.and the beam center displacement (in the x direction) for V_3=-20V, V_2=0V, and a voltage sweep in V_1. b) Schematic of the Coventor Scene 3D simulation under the DC bias polarization.

3.3.2 CHARACTERIZATION:

In this section a C-C beam resonator is designed and fabricated using the two polysilicon layers of the capacitance module of the Austria Microsystems 0.35µm CMOS technology. The resonator is designed to operate at 11 MHz in its first lateral (on plane) flexural mechanical mode. A 22µm length (*L*), 500nm wide (*W*) beam with 100 nm gap between the movable part and the four electrodes has been implemented. Each electrode has a length of 8µm.

Figure 3.11 a) shows the SEM image of the fabricated and released resonator. The first polysilicon layer with a 280nm thickness is used to implement the beam while the second polysilicon layer is used for the electrodes. To reduce the amount of silicon oxide that covers the resonator and reduce the etching time, 15µmx15µm vias holes are opened in all metal layers above the resonator. Finally a PAD window is opened to remove the passivation layers on top of the micromechanical resonator. Twenty-eight minutes are enough to eliminate the sacrificial oxide layer and release the structure.

The main advantage of using a CMOS technology to fabricate mechanical devices is the fabrication side by side with the CMOS electronics that provides extreme compactness and enhanced electrical signal-to-noise ratio. The optical image of Figure 3.11 b) shows the MEMS and the amplifier as well as the different connection pads used in the characterization stage.

a)   b)
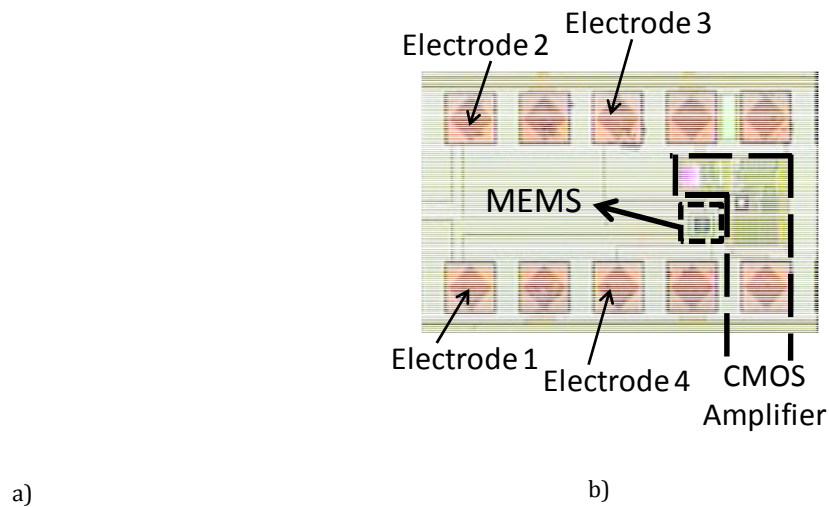
Figure 3.11. Scanning Electron Microscopy (SEM) image of the four-electrode resonator. In b) an optical image of the complete device (MEMS+IC) is shown. Interconnections pads, labeled with the corresponding input or output are shown

The electrical test of the four-electrode resonator has been performed as follows: port 1 of a network analyzer (Agilent E5100A) with a balun has been used to provide the differential AC input signal in electrodes 1 and 2. Port 2 is used to sense the MEMS frequency response that has been previously amplified. Measurements have been carried out in air conditions.
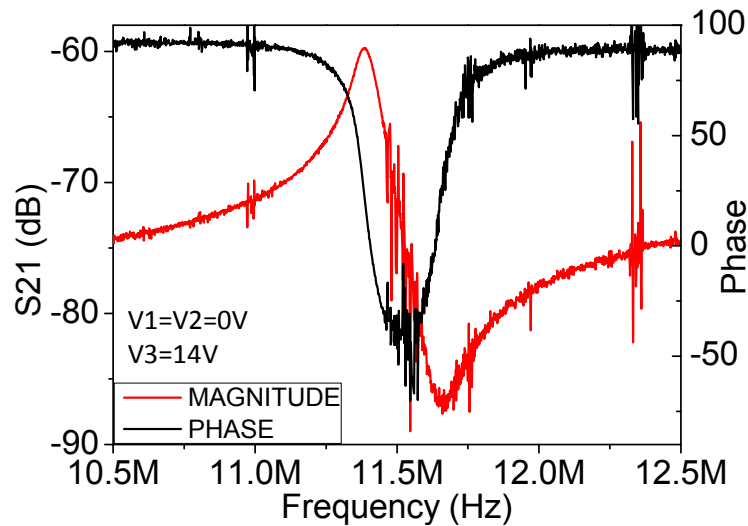
Figure 3.12 Magnitude (red line) and phase (black line) of the non-optimized polarized electrodes.

Figure 3.12 shows both the magnitude and phase response of the MEMS when the control voltages, V_1 and V_2, are set to 0V. The parasitic current forces the 11.38MHz resonant frequency to be followed with a parallel resonance. Finally, only a 150º phase-shift is obtained and the phase, recovers the 90º at high frequency.

In Figure 3.13, both magnitude and phase are shown when a smart biasing of the electrodes is proposed in order to suppress the effect of the feedthrough current (V_3 is set at -36V whereas V_1=14V and V_2=1.4V). It is clearly seen how the proposed biasing eliminates the effect of the parasitic feedthrough current since the parallel resonance is not present and only a resonant frequency of 10.94 MHz is shown. Moreover, a shift phase of 180º is achieved and there is only one frequency where the phase value is zero
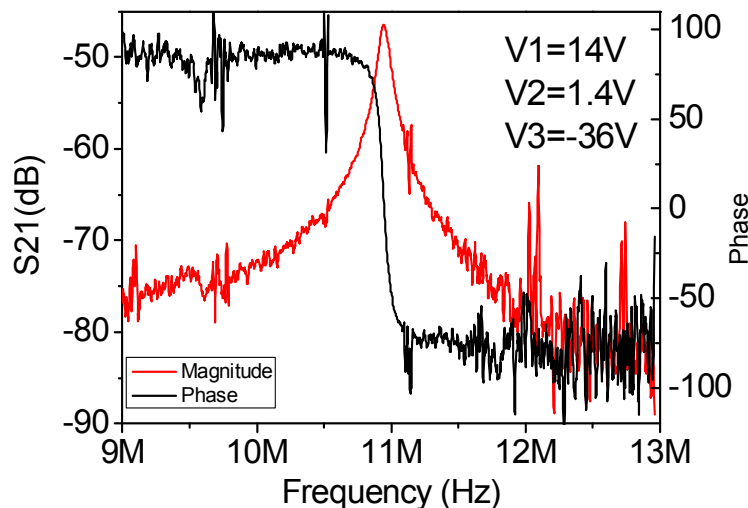
Figure 3.13 Phase (black line) and magnitude (red line) responses with the optimum DC bias

3.4 CAPACITANCE COMPENSATION

In section 3.1 the introduction to the state of the art of feedthrough signal suppression via the parasitic compensation has been explained. The two alternatives are:

1) Parasitic compensation using twin resonators

2) Capacitance compensation using external capacitance

In this section, both techniques will be analyzed from the theory to the measurement.

3.4.1 PARASITIC COMPENSATION USING TWIN RESONATORS.

The feedthrough compensation technique using two identical resonators consists on the subtraction of the feedthrough currents provided by the resonators. One of the resonators is used as a dummy (it is switched off) that provides only the feedthrough current and the other resonator provides both the motional current and the feedthrough. There are two ways to implement this feedthrough compensation method. In first place the signal exerted to one of the resonator is previously inverted, after that both signals provided by the resonator are summed at the output [92]. The second strategy is based on the use of a differential amplifier to subtract both resonator provided outputs signals. The first approach is presented in Figure 3.14. The output current of two identical resonator is added. The AC excitation voltage of one of the resonator is inverted in order to have an effective subtraction. Furthermore, the other resonator is disabled (in the case of electrostatic driven and capacitive read, a zero DC effective voltage between the electrode and the resonator). Then only the feedthrough current provided by the disabled structure adds to the signal provided by the enabled resonator.

Figure 3.14 diagram of the twin beam resonator capacitance compensation technique. One of the resonator input I inverted. The signals provided by the resonator are summed and the total current I_{OUT} is measured.

The output current, I_{OUT}, is calculated using expression (3.28):

$$I_{OUT} = -I_M - I_{F1} + I_{F2} \qquad (3.28)$$

If both resonators are completely symmetric, the feedthrough capacitances are equals, as specified in Figure 3.14, and therefore equal feedthrough currents are obtained ($I_{F1}=I_{F2}$). The resultant current is the motional current of the enabled resonator, I_M.

The second approach described at the beginning of the section is drawn in Figure 3.15. Both resonators are connected to a differential amplifier that is in charge to subtract both resonators output currents

Figure 3.15 Diagram of the capacitance compensation technique using twin resonators and a differential integrated amplifier. In the diagram a different feedthrough current for the two resonators are considered.

The performance of the circuit is as follows. The input signal, V_{ac}, is applied to the resonators common input. If resonators are biased at non-zero DC voltage, an electrostatic force is generated and the movement is enabled. Thanks to the DC voltage applied to the movable structure an output current is induced over the readout electrode. The output current corresponds to the motional current, I_M, and the feedthrough current, I_F. For each resonator the output current is calculated using expression (3.29) and (3.30):

$$I_{OUT1} \cong I_{M1} + I_{F1} \tag{3.29}$$

$$I_{OUT2} \cong I_{M2} + I_{F2} \tag{3.30}$$

The CMOS circuit output voltage corresponds to:

$$V_{OUT} \cong G\left(I_{M1} + I_{F1} - I_{M2} - I_{F2}\right) \tag{3.31}$$

where G is the differential transimpedance gain of the amplifier. If both resonators are physically equals, the resonant frequency will be the same. The motional and feedthrough currents are equals and voltage at the output of the amplifier is null. If the resonator 2 is switched off the output voltage is:

$$V_{OUT} = G\left(I_{M1} + I_{F1} - I_{F2}\right) \tag{3.32}$$

However if resonator 1 is switched off, the output signal corresponds to:

$$V_{OUT} = G\left(-I_{M2} + I_{F1} - I_{F2}\right) \tag{3.33}$$

Note that if not perfect feedthrough capacitance cancelation is realized the effective output current will include both currents. In Figure 3.16 the simulation results using Advance Design System are shown. If only resonator 1 works (Figure 3.16 a), the output current corresponds to expression (3.32). Note that if C_{TH2} is bigger than C_{TH1} the effective feedthrough current $I_F = I_{F1} - I_{F2}$, is opposite to the motional current, I_{M1}. If the perfect capacitance cancellation is achieved, both feedthrough currents are cancelled and only the

motional current of resonator 1 is amplified at the output. In this case, a perfect RLC behavior is achieved. Finally, if C_{TH2} is smaller than C_{TH1} the resultant feedthrough current keeps the same sense than the motional and the parallel resonance is located after the resonance. The same deduction can be applied if only resonator 2 is working. If motional and feedthrough current have opposite phases they are in phase inversion. This phenomenon will be detailed in section 3.6

In Table 3.3, a summary of the output voltage is shown. The result of the feedthrough cancelation will give an effective feedthrough current, I_F, whose sign will depend on which capacitance is bigger. To summary the table, the antiresonance peak appears when the two final currents (motional and effective feedthrough) are opposed in phase).

a)

b)
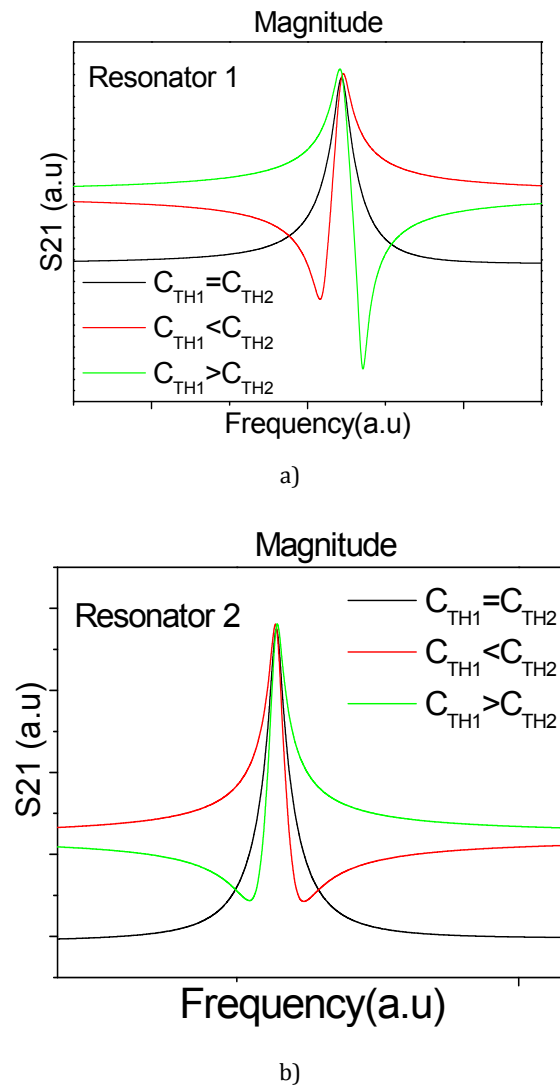
Figure 3.16. Frequency response at the amplifier output of the circuit shown in Figure 3.15. a) shows the output if only the resonator 1 is active and b) if only the resonator is active.

Table 3.3 Summary of the output currents as a function of the resonator and the relation of the feedthrough capacitances.

C's Relation	RESONATOR 1→ON RESONATOR 1→OFF	RESONATOR 1→OFF RESONATOR 1→ON
$C_{TH1} < C_{TH2}$	$V_{OUT} = G(I_{M1} + I_{F1} - I_{F2}) = G(I_{M1} - I_F)$	$V_{OUT} = G(-I_{M2} - I_{F2} + I_{F1}) = G(-I_{M2} - I_F)$
$C_{TH1} = C_{TH2}$	$V_{OUT} = G(I_{M1} + I_{F1} - I_{F2}) = G \cdot I_{M1}$	$V_{OUT} = G(-I_{M2} - I_{F2} + I_{F1}) = -G \cdot I_{M2}$
$C_{TH1} > C_{TH2}$	$V_{OUT} = G(I_{M1} + I_{F1} - I_{F2}) = G(I_{M1} + I_F)$	$V_{OUT} = G(-I_{M2} - I_{F2} + I_{F1}) = G(-I_{M2} + I_F)$

3.4.1.1 CHARACTERIZATION

The characterization of a C-C beam resonator by means of the feedthrough capacitance compensation technique is presented in this section. A differential amplifier is used to subtract the feedthrough currents provided by two twin resonators. Amplification and feedthrough suppression at the same time are obtained. The co-fabrication of the electronics and mechanical part in the same die is one of the most powerful advantages of our technological approach. The resonator is fabricated using the same dimensions and material than in section 3.2. In Figure 3.17 the optical image of the complete system formed by the mechanical part and the CMOS amplifier is shown. The inset corresponds to the SEM image of the two C-C beam resonators. Both resonators share the same input pad, where the input AC signal is exerted. Different DC pads allow enable or disable each resonator independently. The readout electrode of each resonator is connected to the differential and not differential inputs of the CMOS amplifier.
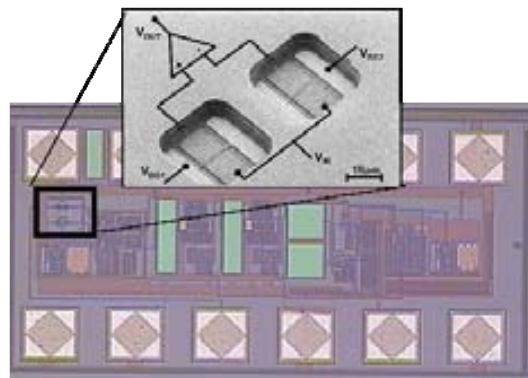
Figure 3.17 Optical image and detailed SEM image of the two C-C beam resonator with the differential amplifier.

Figure 3.18 shows the frequency response of the magnitude of the abovementioned set-up. Actually, both resonators are physically different due to the fabrication tolerance therefore, different resonant frequencies are measured for each one. Applying 0V on

resonator 2 and 18V on the resonator 1 the black line is obtained. However, if biasing voltages are inverted, 0V on resonator 1 and 18V on resonator 2, the response in red line is obtained. Note the antiresonance peak due to the feedthrough current has been eliminated near to the resonance.
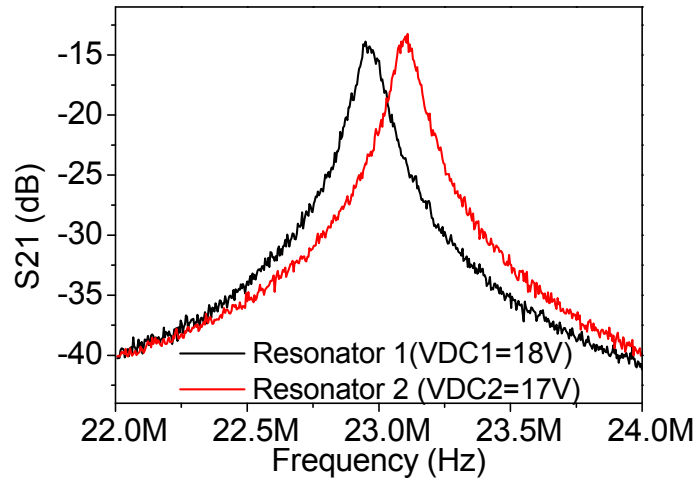

Figure 3.18. Frequency response of the differential amplifier with two C-C beam resonators. Red and black lines represent the response of the resonator 2 and 1 respectively (when the contrary resonator is disabled by enforcing the oV voltage difference between the resonator and the output electrode that is connected to the differential amplifier input.)

3.4.2 CAPACITANCE COMPENSATION USING EXTERNAL CAPACITANCE

In the previous compensation method, fabrication tolerances are a critic parameter in order to eliminate the feedthrough current. Different parasitic capacitances provide different feedhtorugh currents. In this section, a compensation method using a variable capacitance as a solution to overcome the MEMS fabrication tolerances is presented. In Figure 3.19 the diagram of the abovementioned method is shown. One of the branch is constituted by a MEMS resonator modeled by its RLC//C. In the other branch, a variable capacitor has been placed. The variable capacitance, $C_{VAR,}$ can be adjusted externally (mechanically or electrostatically) in order to obtain the same value than the feedthrough capacitance of the microelectromechanical resonator.
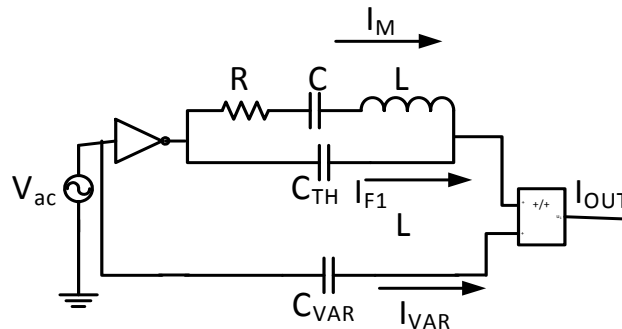
Figure 3.19 Diagram of the capacitance compensation using a variable capacitance to compensate the feedthrough capacitance of the microelectromechanical resonator.

The current at the output is calculated in expression (3.34)

$$I_{OUT} = -I_M - I_{F1} + I_{VAR} \qquad (3.34)$$

The current provided by the variable capacitor, I_{VAR}, compensates the feedthrough current of the resonator if $I_{VAR}=I_{F1}$.

3.5 NON LINEAR TECHNIQUES

The quadratic behavior of the force applied to the resonator offers an interesting advantage in order to decouple the feedthrough current and the motional current in the frequency domain. In this section, the advantage of using this property as a characterization technique is used.

The feedthrough current is considered as a part of the signal applied at the input electrode that is present at the output electrode. This signal is modeled as a feedthrough capacitance in expression (3.1). Expression for the force exerted into de resonator was described in chapter 2 as:

$$F_E = -\frac{\partial W}{\partial x} = -\frac{1}{2}\frac{\partial}{\partial x}\left(C_D V_D + C_R V_R\right)^2 \qquad (3.35)$$

where V_D and C_D are the input voltage and the input capacitance respectively and V_R and C_R are the output voltage and the output capacitance respectively

Two different method based on the non-linear properties of the resonator can be used. Mixing of the signals of the resonator and the excitation of the resonator at half resonant frequency.

Figure 3.20. Diagram of the mixing set-up of a C-C Beam resonator. The network analyzer applied a signal of ω_{RF} on the driver, a ω_{OL} is applied on the structure and the modulation of that frequency obtained at the readout. The lecture performed using spectra analyzer.

3.5.1 MIXING

MEMS resonator are capable to perform mixing between signals. Figure 3.20 shows the scheme that is in [99] for take advantage of the mixing technique. The input signal is applied at the input electrode. This signal is $v_{ac}=A_{ac}sin(\omega_{RF} t)$ where A_{ac} is the amplitude of the sinusoidal signal of frequency ω_{RF}. The second input port is the resonator itself. The signal applied on the resonator is: $v_{LO}=A_{LO}sin(\omega_{LO} t)$. In addition a DC voltage V_{DC} is applied through a Bias-T.

The force exerted to the resonator due to the signals applied at the input electrode and the resonator is

$$F_E = \frac{\partial E}{\partial x} = -\frac{1}{2}\left[\frac{\partial C_D}{\partial x}\left(v_{ac} - V_{DC} - v_{OL}\right)^2 + \frac{\partial C_R}{\partial x}\left(V_{DC} + v_{OL}\right)^2 \right] \tag{3.36}$$

Expression (3.36) can be expanded as in expression:

$$F_E = \frac{\partial E}{\partial x} = -\frac{1}{2}\frac{\partial C_E}{\partial x}\left(v_{ac}^{\ 2} - 2v_{ac}V_{DC} - 2v_{ac}v_{OL} + V_{DC}^{\ 2} + 2V_{DC}v_{OL} + v_{OL}^{\ 2}\right) -$$

$$-\frac{1}{2}\frac{\partial C_R}{\partial x}\left(V_{DC}^{\ 2} + 2V_{DC}v_{OL} + v_{OL}^{\ 2}\right) = \tag{3.37}$$

$$= -\frac{1}{2}\frac{\partial C_E}{\partial x}\left(v_{ac}^{\ 2} - 2v_{ac}V_{DC} - 2v_{ac}v_{OL}\right) - \frac{1}{2}\left[\frac{\partial C_E}{\partial x} + \frac{\partial C_R}{\partial x}\right]\left(V_{DC}^{\ 2} + 2V_{DC}v_{OL} + v_{OL}^{\ 2}\right)$$

In expression (3.37) the term that includes $\partial C_E/\partial x \cdot v_{ac}v_{OL}$ corresponds to the mixing of the two RF signals (v_{ac} and v_{OL}). Therefore, the frequency of this force is $\omega_{RF} \pm \omega_{OL}$. The resonator displacement is maxim when a force with frequency equal to the MEMS resonant frequency ω_o is applied. Therefore movement of the MEMS at the natural resonance frequency of the structure ω_o is generated only if the addition ($\omega_{RF} + \omega_{OL}$) or difference ($\omega_{RF} - \omega_{OL}$) corresponds to ω_o. Then, the force exerted into the resonator considering the mixing is:

$$F_E = v_{ac}v_{OL}\frac{\partial C_E}{\partial x} \tag{3.38}$$

The displacement of the beam at resonant frequency is:

$$x = \frac{Q}{k}v_{ac}v_{OL}\frac{\partial C_E}{\partial x} \tag{3.39}$$

The output current is

$$I_{OUT} \cong V_{DC}\frac{\partial C_R}{\partial t} + v_{LO}\frac{\partial C_R}{\partial t} + C_R\frac{\partial v_{LO}}{\partial t} + C_{TH}\frac{\partial v_{ac}}{\partial t} \tag{3.40}$$

The first term in expression (3.40) corresponds to the motional current produced by the vibration of the resonator at its operation frequency. Note that the feedthrough current corresponding to the third and fourth terms are at different frequency than the motional current. Motional current can be rewritten as:

$$I_m = V_{DC} \frac{C_{oR}}{s} \frac{F_E Q}{k} \omega_o \qquad (3.41)$$

Where C_{oR} corresponds to the static readout capacitance.

3.5.1.1 CHARACTERIZATION

In Figure 3.21 frequency response of a C-C beam with L=13µm, W=350nm and 150nm gaps is measured using the two port configuration. The resonance is observed at 22.5MHz. Note the effect of the feedthrough capacitance in the antiresonance peak. In Figure 3.21 b), the mixing technique response shows the characterization of the MEMS with an v_{ac} signal of 16 MHz and v_{LO} of 1.022 GHz. The suppression of the feedthrough is observed.

a)   b)
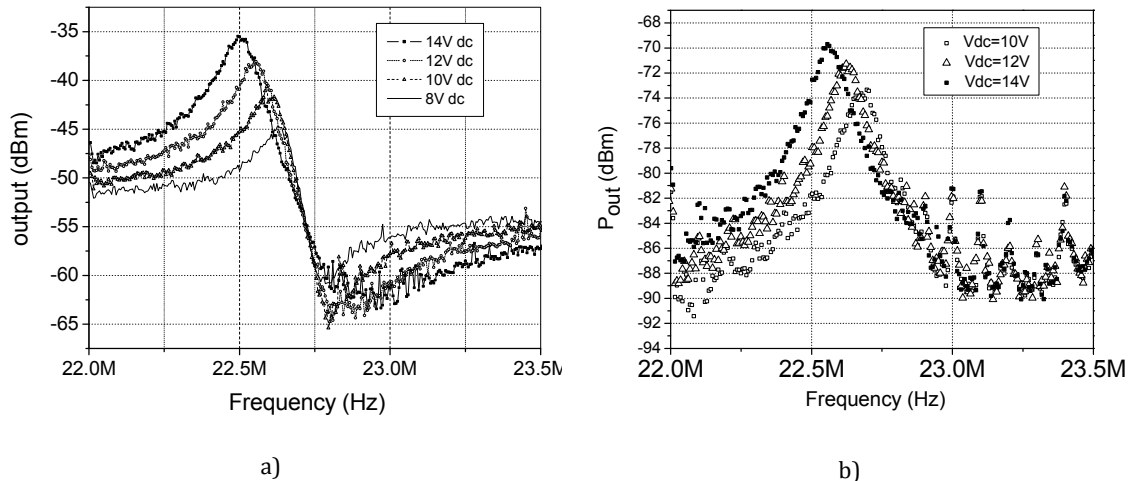
Figure 3.21.Frequency response magnitude a C-C Beam 13µmx350nm and 150nm gap and resonance frequency of 22.5MHz using a)the two port measurement b) the mixing using an input signal with frequency ωRF=1GHz and mixing signal ωOL=1.022GHz.

Figure 3.22. Diagram of the set-up used to characterize the MEMS by means of the excitation at half of the resonant frequency.

3.5.2 EXCITATION AT HALF OF THE RESONANT FREQUENCY.

Figure 3.22shows the diagram of the characterization set-up to characterize the resonator by means of the non-linear technique based on the excitation at half of the resonant frequency.The AC signal is applied at the electrode. Its frequency corresponds to $\omega_o/2$. The force exerted into the resonator is calculated in expression (3.42).

$$F_E = -\frac{1}{2}\frac{\partial}{\partial x}\left(C_1 V_{IN}{}^2\right)$$

(3.42)

where C_1 is the input gap capacitance. The input signal is $v_{ac}=A_{ac}sin(\omega_{in}t)+V_{DC,}$ where V_{DC} is the DC voltage applied to the electrode and ω_{in} corresponds to the half of the resonator operation frequency $\omega_{in}=\omega_o/2$. The force can be rewritten as:

$$F_E = \frac{1}{2}v_{ac}^2\frac{C_o}{g} - v_{ac}V_{DC}\frac{C_o}{g} - \frac{1}{2}V_{DC}^2\frac{C_o}{g}$$

(3.43)

At resonant frequency the force is:

$$F_E = -\frac{1}{2}A_{ac}\frac{C_o}{g}\cos\left(2\omega_{in}t\right)$$

(3.44)

Note that the resonator operation frequency is twice of the input signal frequency; therefore the force calculated in expression (3.44) will induce the movement of the structure. The output current at the resonator can be calculated using expression (3.45)

$$I_{OUT} \cong V_{DC}\frac{\partial C_2}{\partial t} + C_{TH}\frac{\partial v_{ac}}{\partial t}$$

(3.45)

The first term in expression (3.45) correspond to the motional current. The transduction capacitance variation, C_2, is at the resonant frequency. The second term corresponds to the feedthrough current. However, it will be at the excitation frequency that is a half of the read signal and therefore, it is separated from the motional in frequency.

3.5.2.1 CHARACTERIZATION

In Figure 3.23 the frequency response of the C-C beam resonator excited using a half frequency is shown. Note the resonant frequency variation with the voltage applied due to the frequency softening effect. In addition, the DC voltage increment produces a motional current increment than can be observed in the measurement.
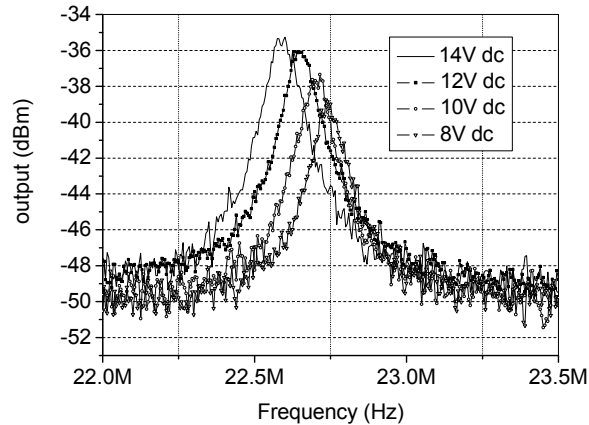
Figure 3.23. Electrical characterization of the C-C Beam resonator excited with a input signal of 45MHz, that is $\omega_{RF}=\omega o/2$

3.6 PHASE INVERSION

The feedthrough elimination is not always required. On the contrary, the control of feedthrough capacitance can be beneficial in some RF MEMS application such as filters [96, 100-103]. The antiresonance peak produced by the feedthrough current presence can smartly be controlled to create a more selective response by adding notches at both sides of a filter bandwidth. However, if the antiresonance peak is not controlled properly it may produce the opposite effect and eliminate the signal in a particular frequency range [104]. The control of the feedthrough capacitance respect to the resonant peak is known as phase inversion.

The phase inversion occurs when the feedthrough current and the motional current of a resonator are 180º shifted. There are two ways to achieve the phase inversion: a) mechanically and b) electrically. The mechanical phase inversion is based on the smart electrodes allocation. This technique requires the previous simulation of the resonator or coupled resonator system in order to decide where the electrodes have to be placed to obtain the desired phase inversion [96]. The electrical phase inversion can be obtained by applying the proper DC biasing [102] or by electrostatically coupling between resonators [102] after the fabrication. It can be useful to improve the response of a device after the fabrication [104].

This section is focused on the electrical phase inversion. The C-C beam is used as standalone resonator and fundamental component of coupled resonator filter and the electrodes are always placed at both sides of the filter or resonator, therefore only the electrical phase inversion can be applied. The phase inversion will be explained for the two-port configuration where the resonator is excited in the input electrode and the output electrode is used for sensing. Once the fundamental of the electrical phase inversion has been explained, a variation of the one port measurement with an extra electrode will be introduced. The readout will be done at the resonator and the excitation will be applied at the input electrode. Furthermore, a second electrode will be used to apply a DC voltage. This last alternative will be useful in the following chapters to understand the phase inversion in more complex structures (coupled resonator systems)

3.6.1 ELECTRICAL PHASE INVERSION IN A C-C BEAM WITH TWO PORTS

The electrical phase inversion is explained using a C-C beam resonator in the two-port configuration. Firstly, the working principle of the resonator phase inversion will be exposed. The theory will be proven by the electrical characterization of the two-port configuration C-C beam.

3.6.1.1 PHASE INVERSION: THEORY

In Figure 3.24 the diagram of the C-C beam resonator used to illustrate the phase inversion is shown. The main difference between this diagram and that presented in Figure 3.5 is that three different DC voltages are applied to electrode and beam. The combination of voltages allows obtaining current inversion as it will be seen in the following paragraphs. In fact, the voltage applied on the electrodes will control the phase between the motional current and the feedthrough current. In the following paragraphs, we will show the relationship between voltages applied on the electrodes and the phase shift between the motional and feedthrough current by means of the reduction of the complete equivalent electrical circuit of the C-C beam resonator to a simpler and comprehensive equivalent circuit.

From chapter 2 it is possible to obtain the equivalent circuit of the C-C Beam in its two-port configuration (see Figure 3.24). Capacitance C_{o1} and C_{o2} are the static capacitance between the excitation electrode and the resonator and between the resonator and the readout electrode respectively. In addition, C_p is the feedthrough capacitance that models the input voltage coupling to the output due to the fringing field and the substrate propagation.

Figure 3.24. Diagram of the C-C beam resonator used to show the electrical phase inversion. DC voltages are applied at the three ports in order to obtain the inversion.

Figure 3.25. Electrical equivalent circuit of the C-C Beam resonator.

For the first lateral flexural mode the relation between the capacitances is:

$$\frac{\partial C_1}{\partial x} = -\frac{\partial C_2}{\partial x} \tag{3.46}$$

The electromechanical coupling factor for the input and output electrodes are:

$$\eta_1 = \left(V_{p1} - V_{p2}\right)\frac{\partial C_1}{\partial x} \tag{3.47}$$

$$\eta_2 = \left(V_{p3} - V_{p2}\right)\frac{\partial C_2}{\partial x} \tag{3.48}$$

The current gains can be calculated using the expression (3.49)

$$\phi_{12} = \frac{\eta_1}{\eta_2}; \quad \phi_{21} = \frac{\eta_2}{\eta_1} \tag{3.49}$$

The output current, I_{OUT}, is the addition of the motional currents multiplied by the current gain plus the feedthrough current (3.50):

$$I_{OUT} = \phi_{21}\,I_M - I_P + I_{c_{o2}} \tag{3.50}$$

For simplification, similar voltage differences modulus between the electrodes and the resonator $|(V_{p1}-V_{p2})|=|(V_{p3}-V_{p2})|$ in order to keep the current gain, $|\phi_{21}|=1$ are considered. The objective is to express in a qualitative way the phase inversion mechanism. The capacitance variation in (3.46) is considered equal.

In expression (3.50) the output current depends on the motional current, multiplied by the current gain ($\phi_{21}I_M$), the parasitic currents provided by the feedthrough capacitance (I_P) and the static capacitance (I_{Co2}). Since the load resistance is much lower than the impedance of the output capacitance (C_{o2}), C_{o2} impedance can be neglected in front of R_o. Expression (3.50) implies that the phase between the output motional current $\phi_{21}I_M$ and the feedthrough current I_P is controlled by the current gain, ϕ_{21}. The sign of the current gain can be controlled, for the first lateral mechanical mode of the C-C Beam resonator by the voltages applied to the ports. Note the feedthrough current, I_P will be always in the same direction, from the input to the output electrodes.

3.6.1.2 IN-PHASE

Considering the current gain as $\phi_{21}=-1$, the phase of the output motional ($\phi_{21}I_M$), and feedthrough (I_P) currents have the same sense, therefore they are not inverted. In Figure 3.26 a), the equivalent electrical circuit of the non-inverted phase resonator is shown. The resonant frequency, f_r, can be obtained as:

$$f_r = \frac{1}{2\pi\sqrt{LC}}$$ (3.51)

Moreover, the antiresonance frequency, f_a, is obtained when the impedance of the resonator is considered infinite:

$$f_a = f_r \sqrt{\frac{C_p + C}{C_p}}$$ (3.52)

Note that the term that multiplies the resonant frequency is:

$$\sqrt{\frac{C_p + C}{C_p}} > 1$$ (3.53)

Expression (3.52) shows that the antiresonance frequency is higher than the resonant frequency. In Figure 3.26 c) and d) the dashed line corresponds to the simulated magnitude and phase of the circuit shown in Figure 3.26 a). The magnitude simulation shows the antiresonance at a higher frequency than the resonance. The phase shows the capacitive behaviour for frequencies out of the range between f_a and f_r. Into the before mentioned frequency range the phase is 180º negative shifted, so it starts to descends for reach -90º and after the resonance it starts to recover the 90º after the antiresonance.

3.6.1.3 OUT-OF-PHASE

If $\phi_{21}=1$, the phase of the motional and feedthrough currents are inverted. The equivalent circuit is shown in Figure 3.26 b). The resonant frequency has the same value that in the previous case (expression (3.51))

Since the phase inversion affects to the effective motional impedance by inverting the current, the impedance of the resonator is

$$Z_{RES} = \frac{\left[\dfrac{1}{sC} + sL\right]}{1 - sC_p\left[\dfrac{1}{sC} + sL\right]}$$ (3.54)

Note that the motional resistance has been neglected to calculate the antiresonance frequency. At the antiresonance frequency the resonator impedance takes the infinite value:

$$Z_{RES} = \infty$$ (3.55)

From (3.54) the antiresonance frequency can be calculated using expression (3.56)

$$f_a = f_r \sqrt{\frac{C_p - C}{C_p}} \qquad (3.56)$$

In the resonator designed in this work the feedthrough capacitance is considered bigger than the motional capacitance (C_p>C). Note that the term that multiplies the resonant frequency is:

$$\sqrt{\frac{C_p - C}{C_p}} < 1 \qquad (3.57)$$

From expression (3.56) it can be observed that the antiresonance frequency is lower than the resonant frequency. In Figure 3.26 c) and d) (solid line), the phase inverted magnitude and phase simulation are shown. The magnitude shows the antiresonance at lower frequencies and the phase response shows a positive 180º shift compared with the in-phase phase response.

a) (V_{p1}-V_{p2})=(V_{p3}-V_{p2})   b)-(V_{p1}-V_{p2})=-(V_{p3}-V_{p2})

c)   d)
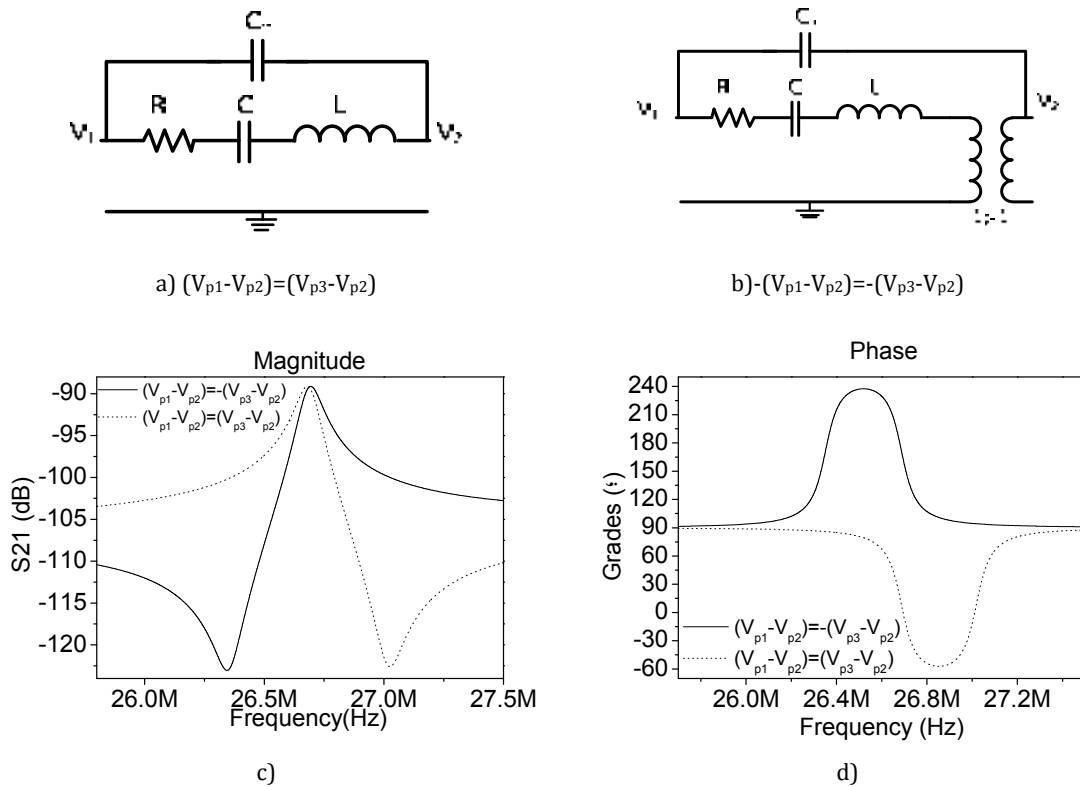
Figure 3.26 Small signal circuit of the two port C-C Beam configuration a) shows the equivalent RLC circuit for the non inverted phase resonator, (V_{p1}-V_{p2})=(V_{p3}-V_{p2}), and b) the equivalent circuit for the phase inverted resonator-(V_{p1}-V_{p2})=-(V_{p3}-V_{p2}). The simulated magnitude and phase are shown in graphs c) and d) where the solid line represents the (V_{p1}-V_{p2})=-(V_{p3}-V_{p2}) and the dotted line the -(V_{p1}-V_{p2})=(V_{p3}-V_{p2}) response.

Table 3.4 shows the summary of the different voltage combination set to do this experiment as well as the electromechanical coupling factor relation, the current gain value and the total output current as motional and feedthrough current function.

Table 3.4 Summary of the current gain for symmetrical bias conditions of the C-C Beam resonator under two port characterization set up (in-plane movement is considered).

Biasing Condition	Electromechanical coupling factors	Current gain	Iout	Phase inversion
$(V_{p1}-V_{p2})=(V_{p3}-V_{p2})$.	$\eta_1=-\eta_2$	$\phi_{21}=\dfrac{\eta_2}{\eta_1}=-1$	I_M+I_P	No
$(V_{p1}-V_{p2})=-(V_{p3}-V_{p2})$.	$\eta_1=\eta_2$	$\phi_{21}=\dfrac{\eta_2}{\eta_1}=1$	$-I_M+I_P$	Yes

Figure 3.26 a) and b) show the equivalent circuit corresponding to each voltage combination in Table 3.4. The expected frequency response are depicted in Figure 3.26 c) and d)

3.6.1.4 ELECTRICAL PHASE INVERSION CHARACTERIZATION.

The two-port configuration is used to electrically characterize the C-C Beam resonator under two phase conditions. Voltages to realize the experiment have been chosen in order to keep the same absolute value of the electromechanical coupling (η). Symmetric gaps are expected for the fabricated resonator and thus, unitary current gain should be obtained.

In Figure 3.27 the frequency response magnitude and phase is shown. Black line shows the response for voltages that accomplish $(V_{p1}-V_{p2})=-(V_{p3}-V_{p2})$. Note that these signals are phase inverted since the current gain is $\phi_{21}\approx1$. The red line shows the non phase inverted response $\phi_{21}\approx-1$, corresponding to $(V_{p1}-V_{p2})=(V_{p3}-V_{p2})$.
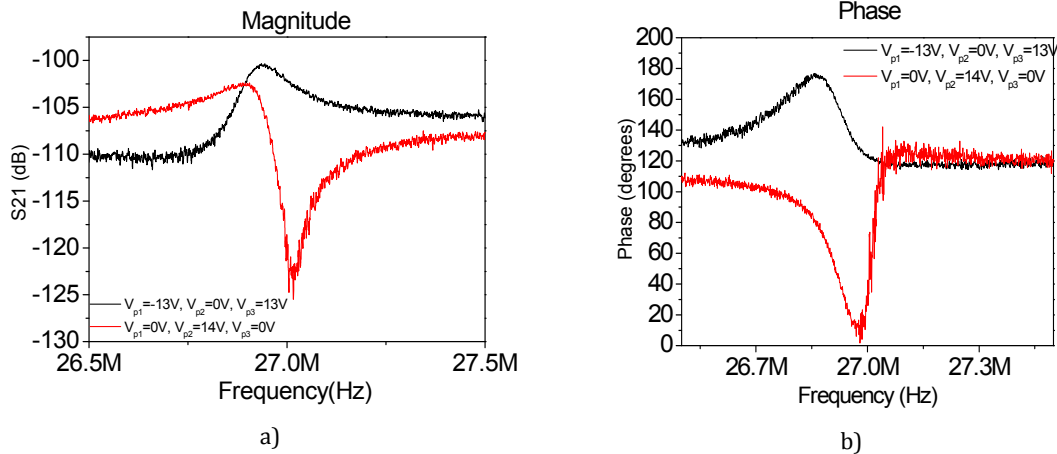
Figure 3.27 Magnitude a) and phase b) of the two port configuration.

3.6.2 ELECTRICAL PHASE INVERSION IN A C-C BEAM WITH ONE PORT

In the classical one port configuration set up (section 3.2.1), the phase inversion never takes place because there is only one gap. In order to have 2 independent ports, a variation of the one port set up is considered. The motional current is read on the movable part and the input AC signal is applied to the driver while an extra electrode has been included in order to create a second gap that allows the phase inversion in the one port configuration. The study of this specific method will be useful to understand the phase inversion in more

complex systems such as the electrical and mechanical coupled filters presented in Chapter 4.

3.6.2.1 THEORY AND PERFORMANCE.

The one port configuration diagram is shown in Figure 3.28. The input electrode is used to apply the AC voltage and an inductively coupled DC voltage. The measurement of the induced current is realized in the movable part where the load resistance and a bias-T are placed. The second electrode is used for DC voltage.

Figure 3.28 One port configuration diagram. C_1 and C_2 correspond to the input and output capacitances. The load resistance indicates the sensing is realized at the beam.

Figure 3.29 shows the electrical equivalent circuit of the modified one port configuration.

Figure 3.29 Simplified equivalent circuit of the C-C Beam resonator measured using the one port configuration with an extra electrode. C_{o1} and C_{o2} correspond to the static capacitance between the input electrode and the resonator and between the resonator and the second electrode.

The output current for the first lateral mode is:

$$I_{OUT} = I_{m2} + \phi_{21}\, I_{m1} + I_{m1} + \phi_{12}\, I_{m2} + I_{C_{o1}} + I_{C_{o2}} \tag{3.58}$$

Current gain can be calculated using expressions (3.47), (3.48) and (3.49). Similar to the two-port configuration, the motional current in the second gap, I_{m2}, can be considered much lower than the motional current, I_{m1}, since it depends on the output voltage, which is lower than the input voltage V_1. The scheme shows two capacitance contributions. C_{o1} is the static capacitance between the input electrode and the resonator and directly related with the input voltage. C_{o2} is the static capacitance between the second electrode and the resonator. Due to its small value, its impedance can be neglected in front of R_o *(50Ω)*. The direct capacitance between the input electrode and the resonator is considered as the most significant feedthrough contribution. Taking into account the previous consideration the output current can be rewritten as in expression (3.59):

$$I_{OUT} = I_{m1}\left(\phi_{21} + 1\right) + I_{C_{o1}} \tag{3.59}$$

In Table 3.5 the output currents for different biasing conditions are summarized.

Table 3.5 Summary of the current gain for symmetrical bias conditions of the C-C Beam resonator under one port characterization set up.

Biasing Condition	Electromechanical coupling factors	Current gain	I_{out} at the resonator
$(V_{p1}-V_{p2})=-(V_{p3}-V_{p2})$.	$\eta 1=\eta 2$	$\phi_{21}=\dfrac{\eta_2}{\eta_1}=1$	$2I_{m1}+I_{co1}$
$(V_{p1}-V_{p2})=(V_{p3}-V_{p2})$.	$\eta 1=-\eta 2$	$\phi_{21}=\dfrac{\eta_2}{\eta_1}=-1$	I_{co1}

It can be seen how the phase inversion is never achieved. In perfectly symmetric resonator where the gaps and voltages are completely symmetric at both sides of the resonator, the phase inversion is not possible since the motional current only can be null or twice of the motional current. Actually, the fabricated resonator not will be symmetric and a gap mismatching is always expected. If no voltages and gaps symmetry is applied to the resonator, the current gain is $\phi_{21}>1$ or $\phi_{21}<1$ and the phase inversion is achieved.

3.6.2.2 ELECTRICAL CHARACTERIZATION

In Figure 3.30 the measurement results of the one-port configuration (Figure 3.28) with extra electrode is compared with classical one port configuration (Figure 3.4). The red line shows the one-port measurement and the black line shows the one port with an extra electrode. Note that the black line resonant peak is 3dB higher than the one port measurement due to the addition of 2 motional current in the load resistance. The feedthrough far from the resonance depends only on C_{o1}, which presents the saem value for both set-ups
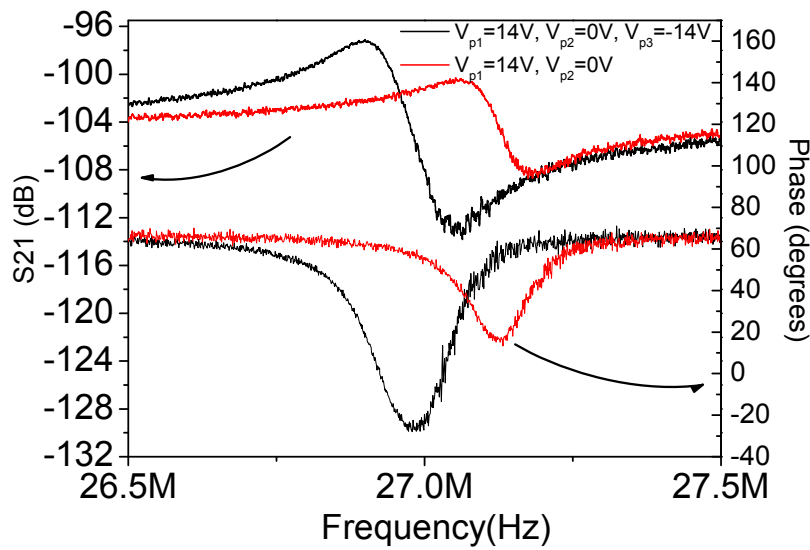
Figure 3.30. Phase and magnitude of the one port measurement set-up for the C-C beam resonator. The voltages applied at each port are V_{p1}=14;V_{p2}=0V V_{p3}=-14V (black line) and V_{p1}=14;V_{p2}=0V V_{p3}=0V (red line)

Black line in Figure 3.31 a) and b) shows the measurement of the resonator under $(V_{p1}-V_{p2})=(V_{p3}-V_{p2})$. Note that regarding the conditions summarized in Table 3.5 the motional current should have been cancelled. For the abovementioned voltage condition the current gain is ϕ_{21}=-1 and the motional current is theoretically cancelled. However, the experiment shows that the motional current is present. In addition, the antiresonance peak is observed at lower frequency than the series resonance. The results suggest that both transduction capacitances are different.

a)
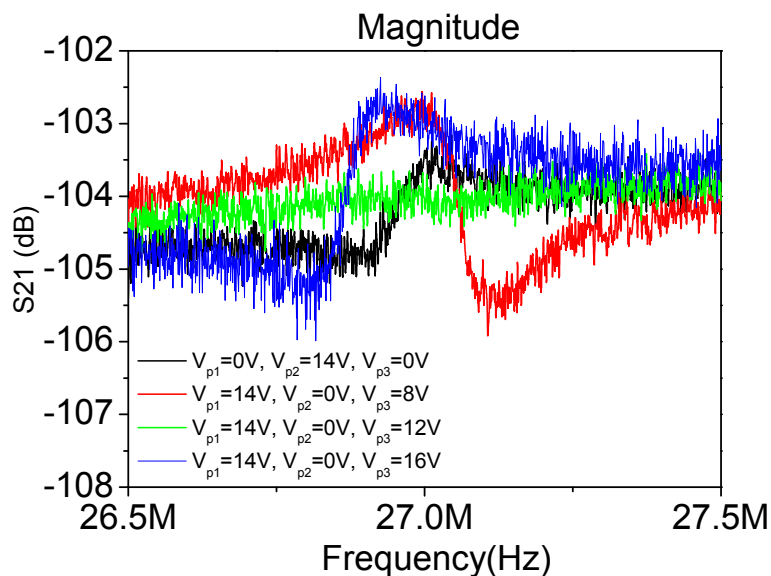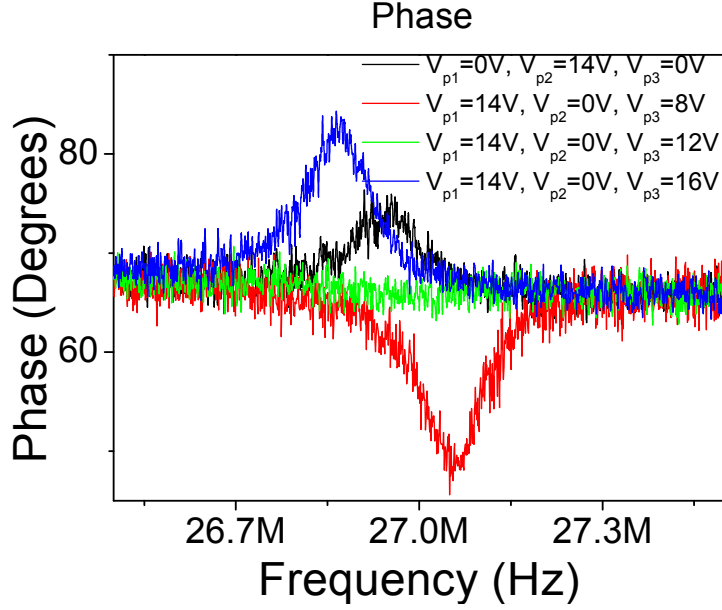
Phase

b)

Figure 3.31 Magnitude a) and phase b) of the frequency response of the C-C Beam resonator under one port characterization set-up and $V_{in1} \neq 0V$ and $V_{in2}=0V$

The results obtained require a deep analysis of the performance of the resonator. Combining expression (3.47) and (3.48) into (3.49) and representing the capacitances as in (3.4) the current gain can be represented as:

$$\phi_{21} = -\frac{\eta_2}{\eta_1} = -\frac{(V_3-V_2)\frac{\partial C_2}{\partial x}}{(V_1-V_2)\frac{\partial C_1}{\partial x}} = -\frac{(V_3-V_2)\frac{C_{o2}}{s_2}}{(V_1-V_2)\frac{C_{o1}}{s_1}} \tag{3.60}$$

Note that a small x displacement has been considered. In expression (3.60), s_1 and s_2 are the fabricated input and output gaps. Depending on the input or output capacitance values the current gain and the output current can be expressed (see Table 3.6). If the input capacitance is bigger than the output capacitance, the motional current is non-inverted. On the contrary, if output capacitance is bigger than the input the motional current is inverted.

Table 3.6. Summary of the current gain values for the biasing voltage condition $(V_{p1}-V_{p2})=(V_{p3}-V_{p2})$. The relation between the input and output capacitances will fix current gain.

Biasing Condition	Electromechanical coupling factors	Current gain	I_{out} at the resonator
$\dfrac{C_{o1}}{s_1} > \dfrac{C_{o2}}{s_2}$	$\eta_1 > \eta_2$	$\phi_{21} > -1$	$I_{OUT} = |\phi_{21}+1| I_{m1} + I_{C_{o1}}$
$\dfrac{C_{o1}}{s_1} < \dfrac{C_{o2}}{s_2}$	$\eta_1 < \eta_2$	$\phi_{21} < -1$	$I_{OUT} = -|\phi_{21}+1| I_{m1} + I_{C_{o1}}$

Since the measurement corresponding to the balanced voltage polarization $(V_{p1}-V_{p2})=(V_{p3}-V_{p2})$, shows the antiresonance before the series resonance it can be concluded

than the output capacitance, C_2 is bigger than the input capacitance. The capacitance difference can be compensated if unbalanced biasing voltage is applied. In fact, in the resonator under study, if the voltage applied in the input gap is increased respect the voltage applied in the ouput gap, the input capacitance can reach the same value than the output capacitance. If that happens, the motional current can be cancelled since the current gain is ϕ_{21}=-1 (see green line in Figure 3.31).

3.7 CONCLUSIONS

In this chapter, different characterization techniques have been explained. In the first part of the chapter, few techniques addressed to suppress the feedthrough current have been detailed.

The first technique proposes two different set up configurations in other to alleviate the coupling of the input signal directly to the output. The two set ups proposed are summarized as follow:

-**One port** this set up offers high levels of the motional signal at the output however a stronger feedthrough level has detected.

-**Two port set up** diminish the feedthrough signal since the AC signal is not directly coupled to the output by means of the static capacitance between the driver and the resonator. In this case, the feedthrough is transmitted through the substrate or by means of fringing fields. This technique is the most simple and used in this work.

The **layout optimization** has been presented as a possible technique to suppress the feedthrough in a C-C Beam. In this work a 4 electrodes beam resonator hav been implemented. Two electrodes have been placed at each side of the beam. One of the electrodes at each side of the beam has been used to apply the AC voltage. The other two electrodes have been used only to apply DC voltage. The analysis of the output current has shown that the feedthrough component related with the capacitance difference produced by the fabrication tolerances can be canceled by a smart biasing of the DC electrode. At the same time the motional current that depends on the AC excitation voltage and the DC voltage difference between the two signal electrodes and the beam remains constant.

The **non linearity** of the MEM devices is presented as a third option to cancel the feedthrough. This methodology is based on decoupling the feedthrough current and the motional current in the frequency domain. The first alternative is based on the mixing of two AC signals. The input signal is applied to the driver and a local signal is applied on the movable part. Both signal frequencies have to accomplish that its summation has to be similar to the resonant frequency of the MEMS. The motional current is detected at the resonant frequency while the feedthrough current is detected at the input signal frequency. On the other approach, the input signal frequency is a half of the resonant frequency of the MEMS.. The motional current is at the resonant frequency but the feedthrough travels at a half of the resonant frequency. Both non linear methods suffer losses due to the conversion in comparison with the direct method (one port, or two ports).

Capacitance compensation techniques based on the subtraction of two feedthrough currents have been presented in this chapter. Three alternatives have been presented.. The first one uses two twin resonators and a signal inverter in one of them in order to

obtain two identical 180º phase shifted feedthrough signals. One of the resonators is used as a dummy while the other is conveniently biased to obtain its motional current. At the output, both feedthrough currents are subtracted and only the motional current of the enabled resonator remains. The main problem of this technique is that both resonators have to be equals and sometimes it is not possible due to the fabrication tolerances. The second technique, developed by Seshia, proposes the use of a variable capacitor instead of a dummy resonator to adjust exactly its value to obtain the feedthrough current than the enabled resonator. The integration of the variable capacitor is still to be optimized. In this work, the introduction the differential amplifier as the alternatives to the previous method is presented. In this case two similar resonators are connected to the differential and non differential inputs of the circuit; the electronic subtract the feedthrough signal and amplify the motional current. Despite the drawback is the same that the method of the twin resonator presented the amplification of the motional current is a large advantage.

In the last part of the chapter the **phase inversion** phenomena is extensively studied. This phase inversion phenomena occurs when the feedthrough current is still present at the output of the device and 180º shifted from the motional current. The phase inversion has been studied at electromechanical equivalent circuit model level by analyzing the different current contribution for a C-C beam in its two-port configuration. Furthermore a variation of the one port configuration with an extra electrode has been included to explain the phase inversion in one port measurements.

3.8 REFERENCES

[1]   S. Pourkamali, G. K. Ho, and F. Ayazi, "Low-Impedance VHF and UHF Capacitive Silicon Bulk Acoustic Wave Resonators; Part I: Concept and Fabrication," *Electron Devices, IEEE Transactions on,* vol. 54, pp. 2017-2023, 2007.

[2]   G. K. Ho, K. Sundaresan, S. Pourkamali, and F. Ayazi, "Low-motional-impedance highly-tunable I^2 resonators for temperature-compensated reference oscillators," in *Micro Electro Mechanical Systems, 2005. MEMS 2005. 18th IEEE International Conference on*, 2005, pp. 116-120.

[3]   G. K. Ho, K. Sundaresan, S. Pourkamali, and F. Ayazi, "Temperature Compensated IBAR Reference Oscillators," in *Micro Electro Mechanical Systems, 2006. MEMS 2006 Istanbul. 19th IEEE International Conference on*, 2006, pp. 910-913.

[4]   J. Arcamone, E. Colinet, A. Niel, and E. Ollier, "Efficient capacitive transduction of high-frequency micromechanical resonators by intrinsic cancellation of parasitic feedthrough capacitances," *Applied Physics Letters,* vol. 97, pp. 043505-043505-3, 2010.

[5]   A. T. H. Lin, J. E. Y. Lee, J. Yan, and A. A. Seshia, "Enhanced transduction methods for electrostatically driven MEMS resonators," in *Solid-State Sensors, Actuators and Microsystems Conference, 2009. TRANSDUCERS 2009. International*, 2009, pp. 561-564.

[6]   S. A. Bhave, G. Di, R. Maboudian, and R. T. Howe, "Fully-differential poly-SiC Lame mode resonator and checkerboard filter," in *Micro Electro Mechanical Systems, 2005. MEMS 2005. 18th IEEE International Conference on*, 2005, pp. 223-226.

[7]   M. Palaniapan and L. Khine, "Micromechanical resonator with ultra-high quality factor," *Electronics Letters,* vol. 43, pp. 1090-1092, 2007.

[8]   S.-S. Li, Y.-W. Lin, Z. Ren, and C. T. C. Nguyen, "An MSI Micromechanical Differential Disk-Array Filter," in *Solid-State Sensors, Actuators and Microsystems Conference, 2007. TRANSDUCERS 2007. International*, 2007, pp. 307-311.

[9]   J. L. Lopez, J. Verd, J. Giner, A. Uranga, G. Murillo, E. Marigo, F. Torres, G. Abadal, and N. Barniol, "High Q CMOS-MEMS resonators and its applications as RF tunable band-pass filters," in *Solid-State Sensors, Actuators and Microsystems Conference, 2009. TRANSDUCERS 2009. International*, 2009, pp. 557-560.

[10]   L. Yu-Chia, T. Ming-Han, C. Wen-Chien, L. Sheng-Shian, and F. Weileun, "High-Q, large-stopband-rejection integrated CMOS-MEMS oxide resonators with embedded metal electrodes," in *Solid-State Sensors, Actuators and Microsystems Conference (TRANSDUCERS), 2011 16th International*, 2011, pp. 934-937.

[11]   L. Lin, C. T. C. Nguyen, R. T. Howe, and A. P. Pisano, "Microelectromechanical filters for signal processing," in Micro Electro Mechanical Systems, 1992, MEMS '92, Proceedings. An Investigation of Micro Structures, Sensors, Actuators, Machines and Robot. IEEE, 1992, pp. 226-231.

[12]   J. E. Y. Lee and A. A. Seshia, "Parasitic feedthrough cancellation techniques for enhanced electrical characterization of electrostatic microresonators," *Sensors and Actuators A: Physical,* vol. 156, pp. 36-42, 2009.

[13]   J. R. Clark, M. A. Abdelmoneum, and C. T. C. Nguyen, "UHF high-order radial-contour-mode disk resonators," in Frequency Control Symposium and PDA Exhibition Jointly with the 17th European Frequency and Time Forum, 2003. Proceedings of the 2003 IEEE International, 2003, pp. 802-809.

[14]   J. R. Clark, W. T. Hsu, M. A. Abdelmoneum, and C. T. C. Nguyen, "High-Q UHF micromechanical radial-contour mode disk resonators," *Microelectromechanical Systems, Journal of,* vol. 14, pp. 1298-1310, 2005.

[15]   A. Uranga, J. Teva, J. Verd, J. L. Lopez, F. Torres, J. Esteve, G. Abadal, F. Perez-Murano, and N. Barniol, "Fully CMOS integrated low voltage 100 MHz MEMS resonator," *Electronics Letters,* vol. 41, pp. 1327-1328, 2005.

[16]   G. Piazza, R. Abdolvand, and F. Ayazi, "Voltage-tunable piezoelectrically-transduced single-crystal silicon resonators on SOI substrate," in *Micro Electro Mechanical Systems, 2003. MEMS-03 Kyoto. IEEE The Sixteenth Annual International Conference on*, 2003, pp. 149-152.

[17]   D. Weinstein, H. Chandrahalim, C. Lih Feng, and S. A. Bhave, "Dielectrically Transduced Single-Ended to Differential MEMS Filter," in *Solid-State Circuits Conference, 2006. ISSCC 2006. Digest of Technical Papers. IEEE International*, 2006, pp. 1236-1243.

[18]   J.Yan, A.Seshia, K. L. Phan, and J. T. M. v. Beek, "Mechanical Phase Inversion for Coupled Lamé mode Resonator Array Filters,," in *IEEE Int. Conference on Micro Electro Mechanical Systems*, Tucson, Arizona, Jan 13-17, 2008, pp. 1024-1027.

[19]   Y. Xu and J. Lee, "Single-device and On-chip Feedthrough Cancellation for Hybrid MEMS Resonators," *Industrial Electronics, IEEE Transactions on,* vol. PP, pp. 1-1, 2011.

[20]   H. Zhu and J. E. Y. Lee, "System-level circuit simulation of nonlinearity in micromechanical resonators," *Sensors and Actuators A: Physical*.

[21]   J. L. Lopez, J. Teva, A. Uranga, F. Torres, J. Verd, G. Abadal, N. Barniol, J. Esteve, and F. Perez-Murano, "Mixing in a 220MHz CMOS-MEMS," in *Circuits and Systems, 2007. ISCAS 2007. IEEE International Symposium on*, 2007, pp. 2630-2633.

[22]   H. A. C. Tilmans, "Equivalent circuit representation of electromechanical transducers: I. Lumped-parameter systems " *Journal of Micromechanical and Microengineering,* vol. 7, 1995.

[23]   J. Yan, A.A. Seshia, K.L. Phan, P. G. Steeneken, and a. J. T. M. v. Beek, "Narrow Bandwidth Single-resonator MEMS Tuning Fork Filter   " in *IEEE International Frequency contro Symposium*, Geneva Switzerland, May 29-June 1, , pp. 1366-1369.

[24]   J. Yan, A.A. Seshia, K. L. Phan, and a. J. T. M. v. Beek, "Internal Electrical Phase Inversion for FF-Beam Resonator arrays and Tuning Fork Filters," in *IEEE, Int. Conference on Micro Electro Mechanical Systems*, 13-17 Jan, 2008, pp. 1028-1031.

[25]   J. Yan, A.A. Seshia, K. L. Phan, and J. T. M. v. Beek, "Internal Phase Inversion Narrow Bandwidth MEMS Filter," in *IEEE Int. Ultrasonics Symposium*, Beijing, China, 2-3 Nov, 2008   pp. 705-708.

[26]   J. Giner, A. Uranga, F. Torres, E. Marigo, J. L. Munoz Gamarra, and N. Barniol, "A CMOS-MEMS filter using a V-coupler and electrical phase inversion," in *Frequency Control Symposium (FCS), 2010 IEEE International*, 2010, pp. 344-348.

Chapter.4 CMOS-MEMS FILTERS, THEORY, DESIGN, FABRICATION AND TESTING.

This chapter is focused on MEMS filters. The different types of coupled filter (mechanical and electrostatic coupled filters) as well as parallel and dual filters are presented. The complete developing flow is explained and detailed. This chapter offers a detailed explanation of all the steps involved in the filter achievement: from the design stages up to the electrical characterization and results discussion.

4.1 INTRODUCTION

RF filters are one of the key components in wireless communications. They are essential echelons in the RF chains and are one of the cornerstones in the new transceivers architecture. This chapter is focused on MEMS-CMOS filter for RF applications.

In section 4.2, a basic definition of filters as frequency range selectors is given. All the important specifications are detailed. The importance of the MEM filter into the RF applications as well as the new architectures achievable due to the advances in MEMS filtering structures are reviewed. In addition, an extended presentation of the state of the art in mechanical coupled resonator filters, electrostatic coupled resonator filter and dual filters is included.

In section 4.3, we will move to the coupling theory as a basic concept but not the only one, to design a bandpass filter. In this section, the coupled oscillators systems are studied as a starting point to understand the coupling theory. The differentiation between the electrical coupling and mechanical coupling will be explained. Unlike the previous coupled filters, the parallel filtering technique is introduced. The advantages and disadvantages between bot design strategies will be discussed.

Section 4.4 focuses on the mechanically coupled resonators filter. The low velocity coupling technique used to obtain narrow bandwidths onto the micro scale as well as the U and V-filter are presented in this section.

Section 4.5 presents the electrostatic coupled resonators filters. In this section a detailed analysis of the different characterization topologies for this filter is presented as well as the corresponding electromechanical models.

The parallel filtering results are presented in section 4.6. Finally, in section 4.7 our particular approach to the dual filtering is presented.

4.2 FILTERS

This chapter is focused on the design, fabrication, testing and optimization of MEM resonator based filters. The RF filters are used to select a particular frequency or frequencies range within the radiofrequency spectrum. Although there are many types of filters as needs exist in telecommunications (stop band, hairpin, notch....) this work is centered on the band pass filters.

The bandpass filter is a type of passband filter. A passband filter allows a signal comprised inside the operation frequency range of the filter being processed. An ideal bandpass filter has a completely flat passband (red line in Figure 4.1). A flat band means that no gain or attenuation is applied to the RF signal. Out of its operation frequency range the signal frequency spectrum is completely attenuated. The transition between the passband and the attenuated frequency region is abrupt.

Figure 4.1 Diagram of an idea (red) and an actual filter (green))

Unfortunately, the real filter performances are far from those of an ideal filter. The real filter does not attenuate all frequencies outside the operating frequency range; in particular, there is a region out of the passband where frequencies are attenuated but not rejected. This is known as the filter roll-off. Generally, the filter design aims to make the roll-off as narrow as possible, thus allowing the filter to perform as close as possible to its intended design. Often, this is achieved at the expense of passband or stop-band ripple.

The filter bandwidth is the difference between the upper and lower cutoff frequencies, f_1 and f_2 (see Figure 4.1). The shape factor, SF, is the ratio of bandwidths measured at two different attenuation values. The typical bandwidth ration is calculated at 20dB from the maximum filter level. The shape factor is calculated by expression (4.1):

$$SF_{20dB} = \frac{BW_{-20dB}}{BW_{-3dB}}$$

(4.1)

An ideal filter has a SF_{20dB}=1. However, in actual implementations a shape factor as lower as possible is required.

The Q factor of a filter is the relation between the passband frequency range and the center frequency, f_c. It can be calculated by:

$$Q = \left(\frac{f_2 - f_1}{f_c} \right)^{-1} \tag{4.2}$$

Where f_1 and f_2 are the frequencies at 3dB. The aforementioned parameters, center frequency, bandwidth Q, stop band rejection are the design premises are taken into account in the MEMS-CMOS design filters presented in this chapter.

4.2.1 RF-MEMS FILTER APPLICATION IN COMMUNICATION SYSTEMS

In wireless communication systems, the filter plays an important role. It selects the frequency range that corresponds to a particular application. Depending on the operating frequency and the bandwidth, the filters are classified into channel filters or band selection filters. The channel filter selects a specific frequency range inside a band, for instance a particular channel filter could select one of the 512 channels present into the downlink of the GSM mobile communication standard. On the contrary, the band selection filter allows an application such CDMA to be discriminated between the different application present in the electromagnetic spectrum. The type of RF architecture will determine the use of each type of filter.

The RF architectures are divided in three topologies depending on the type of the antenna provided signal processing:

5) 1) The l*ow IF* architecture down converts the signal provided by the LNA and the antenna to low frequencies in order to be digitally processed.

6) 2) The *zero-IF* architecture down converts the signal to frequencies near to the DC

7) 3) The *super heterodyne* transceiver uses more than one down converters in order to prepare the signal for the demodulation stage

The two first transceivers presented belong to the direct conversion transceivers family. The direct conversion transceiver scheme is depicted in Figure 4.2. After the antenna, a band selection filter discriminates the application band of interest. In the mixing stage, the signal is down converted directly to low IF or baseband. This architecture begun to be used at early 80's[66]. This scheme requires fewer components than the super-heterodyne transceivers. It has the advantages of image frequency suppression. However, it requires very selective filters in order to select the corresponding channel at high frequencies. In a current wireless communication standard (for instance GSM), the application band is located a 900MHz and the channel bandwidth is 200KHz, therefore the required Q for the channel filter is 4500. However, the most serious problem is the DC offset in the baseband section of the receiver that follows the mixer. This offset appears in the middle of the down converted signal spectrum, and may be larger than the signal itself, and much larger than thermal and flicker noise. It can distort or mask the desired signal. Besides the band selection filter that has to operate at

high frequencies, the low IF or zero IF filters can be implemented using MEM resonators that work in the range of MHz with acceptable Q factors.
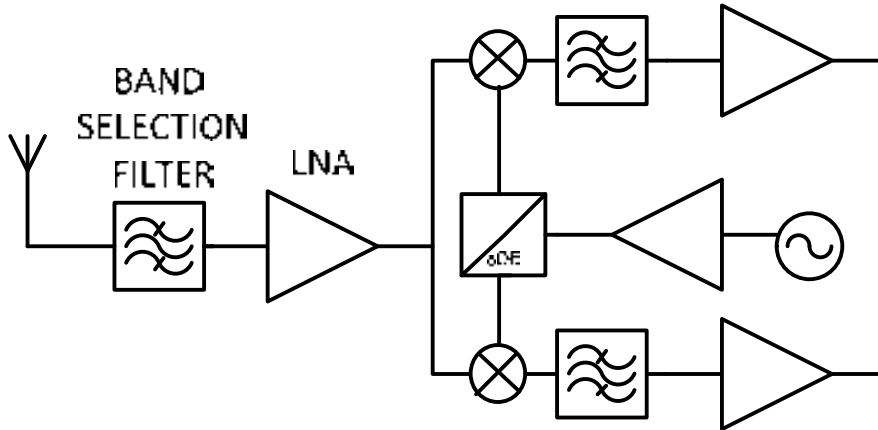
Figure 4.2 Direct conversion diagram

The third alternative based on the use of super-heterodyne architecture is one of the most used alternatives in the wireless communication world [66]. Almost the 98% of the current systems uses it. The super-heterodyne transceiver (see Figure 4.3) is formed by different down conversion stages. The use of several filtering and down converting stages relaxes the requirement for the filters performance.
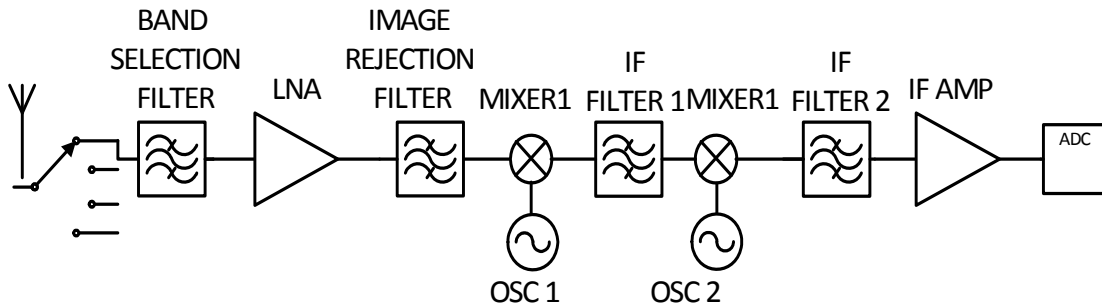
Figure 4.3 Super heterodyne receiver architecture.

Other aggressive architectures have been proposed recently to obtain the maximum beneficial from advances in the MEMS field. Multi IF filter benches, multi band selection filters could be implemented taking advantage of the MEM filters performance [67]. The use of these complex structures could save space in the handset and could increase the versatility and the performance of the devices. The presented strategies may require the use of dual band filters that can further reduce the dimensions of the whole RF front end by including the transmission and the reception RF chain in the same chip.

As it has been shown in previous paragraphs, filters are one of the fundamental parts in any RF receiver/transmitter chain. The use of MEMS is an integration, low power, batch fabrication and cost reduced solution. This chapter is focused exclusively in MEMS filters.
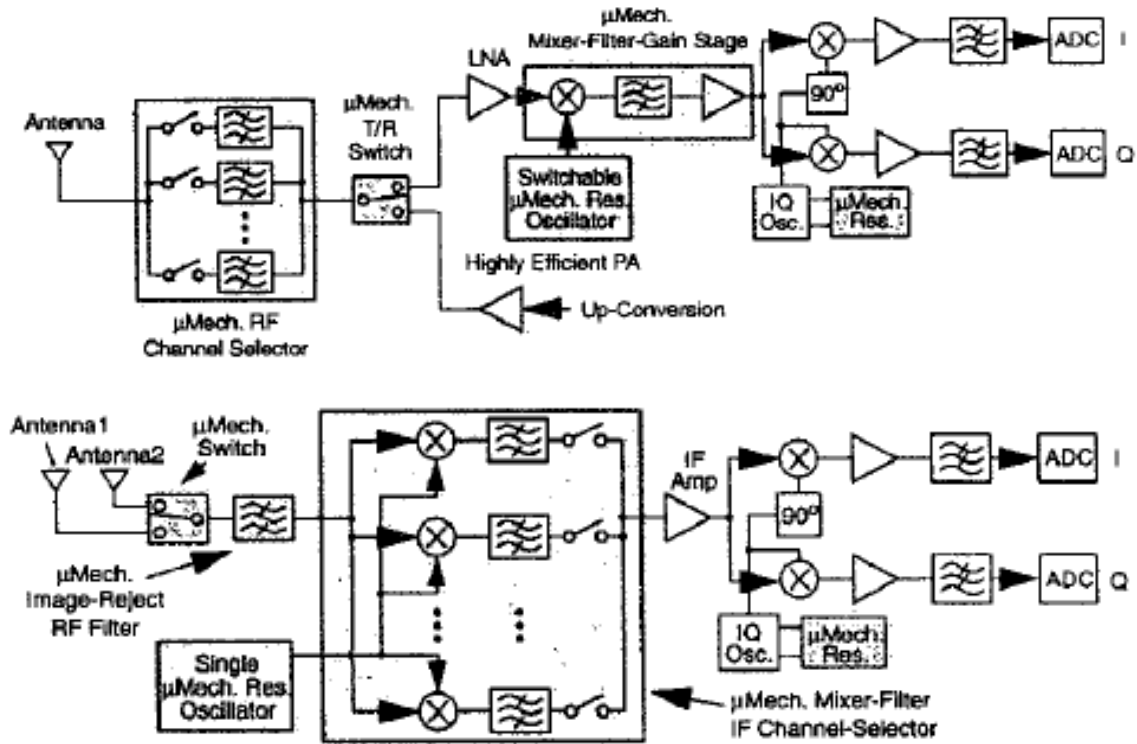
Figure 4.4 Different wireless transceivers architectures based on filter arrays [67]

4.2.2 MICROELECTROMECHANICAL FILTERS. STATE OF THE ART

One of the straight forward applications of MEMS is the filtering because of their high frequency selectivity and high quality factor [68]. A stand-alone MEMS resonator, due to his frequency behavior, can be considered as a filter. If the Q factor of the resonator is high enough it presents a very narrow bandwidth (BW). The combination of the resonators electrically or mechanically [21, 61, 69-70] coupled or by means of the combination of them into a parallel-resonators filtering systems [22] increases the performances: the coupling can controls the bandwidth of the filter.

One of the most important issues in MEMS filters is the impedance matching. MEMS filters designers have always been looking for the 50Ω impedance. The use of dielectrically transduced filters [70],arrayed resonators [71] or piezoelectric layers [72] has been proved to reduce the motional impedance. However, due to the microelectronics integration capability of the last MEMS approaches, fundamentally based on the CMOS integration capability, the 50Ω matching requirement has been almost forgotten [73]. Currently both circuitry input impedance and the MEMS motional impedance can be matched at tens or hundreds of kΩ.

In the following paragraphs, an extended review of the main developing in the field of mechanically and electrically coupled resonators filters as well as the parallel filtering structures and the last advances in dual filters are shown.

In the field of mechanical coupled resonator filters, Mottie et al.[69] have designed 400 kHz and 1.7MHz centre frequency second order filters with both a beam and a V-shaped mechanical coupling. They used Poly-MUMPS technology to fabricate their structures. In

the filter presented, the movement is in plane. In that approach the angle of the V-shaped coupling is one of the most important design parameters since the bandwidth of the filter depends on it.

Nguyen et al. [74] presented one of the first micromechanical coupled filters based on two vertical clamped-clamped beam resonators. The filter works at 7.8MHz center frequency and it obtains a 35dB out-of-band rejection. The structures were fabricated using a polysilicon-based process similar to the process used in IC technologies. The fabrication flux is based on different films deposition and lithographic patterning. In their process the most important achievement is that the sacrificial oxide, which define the wide of the gap, is 1300A.

Arellano [75] proposed a proof of concept to use nanowires to couple a pair of beam resonators. In his first approximation, a nanowire was fabricated on a SOI wafer and it was patterned by means of a focus Ion Beam (FIB). This alternative also provides the tunability of the bandwidth by means of resizing the nanowire coupler after the fabrication. The narrow bandwidth is achieved because of the big dimensions difference between the resonant and the coupler. However, this technique is not a practical alternative to provide a high volume fabrication solution since the mechanical tuning has to be made filter by filter. The final filter prototype offers a 17.84MHz filter with 114kHz BW. A poor out-of-band rejection of 6dB was measured.

Van Beek et al.[76-79] have worked on different types of coupling to obtain a bandpass filter perform. Their work reviews the mechanical coupling, the electrostatic coupling and the influence of the phase inversion on the passband shape.

In 2005 an attempt to the VHF filters was made by Demirci et al. [80]. The filter was based on squared microresonator arrays aiming to reduce the motional resistance and the relaxation the coupler sizing requirements. A torsional bar couples two arrays to obtain two resonance modes and thus the filter behavior. Finally, the filter electrically measured is centered at 68.1MHz and 190kHz bandwidth.

Weinstein [70] combines the mechanical coupling of a disk and a ring resonators along with the dielectrically and differential transduction to obtain a filter in the range of 400MHz with 8dB insertion losses and very high rejection of 50dB. One the reasons to use the dielectrically transduction is to decrease the motional impedance up to tens of ohms.

In the field of electrical coupled filters, next paragraphs show the most relevant works are shown. For example, Pourkamaly has been working [61, 81] on different types of electrical couplings to get filters. In [61] two types of implementation were presented. The first is a filter formed by two HARPSS fabricated resonators. They are coupled through a coupling capacitance that was connected between the two resonators. Both resonators are fabricated in separate substrates and are connected to the coupling capacitance by means of wire bonding. He obtained a filter centered at 600kHz with a stop band rejection of 54dB and a SF_{20dB} =3. The Q factor of the filter is 9930. This approach presents a large coupling capacitance that distorts the pass band of the filter. To overcome this problem, an alternative based on an integrated capacitance is presented. The resonators were fabricated in SOI substrate. It is worth to note that the junction between the output electrode of the first resonator and the input electrode of the second resonator forms the
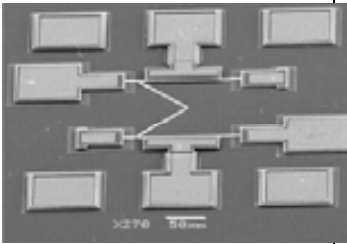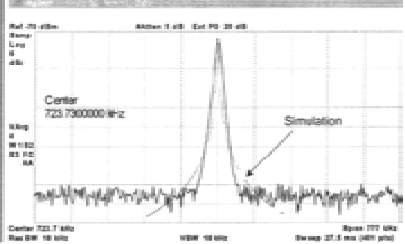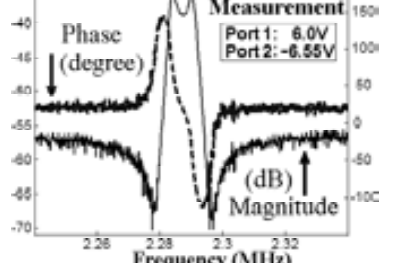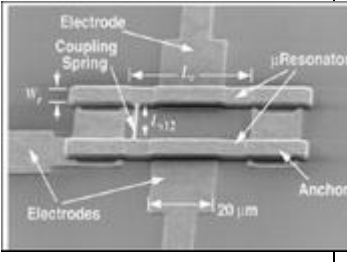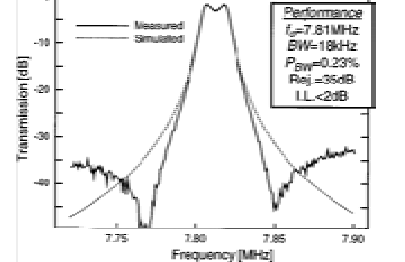
integrated capacitance. Both resonators are biased independently and that allows the bandwidth of the filter be controlled by means of biasing voltages..
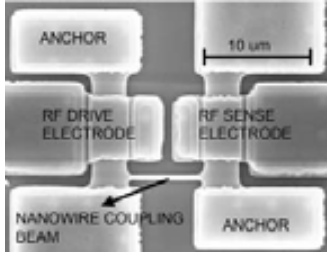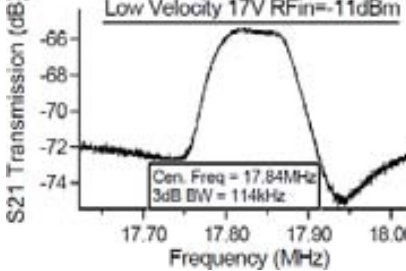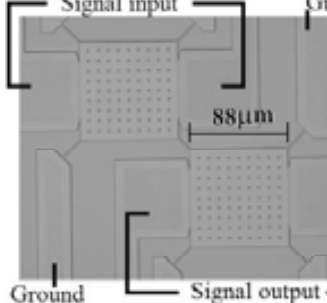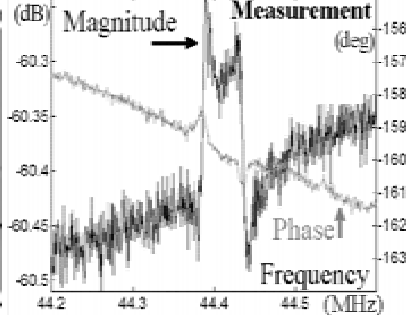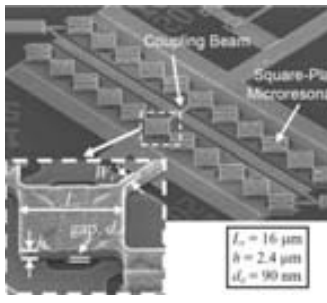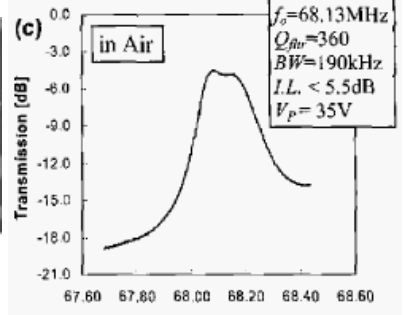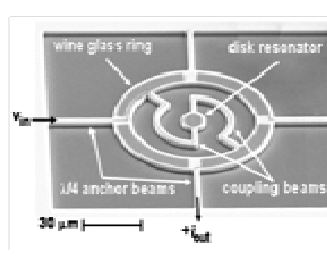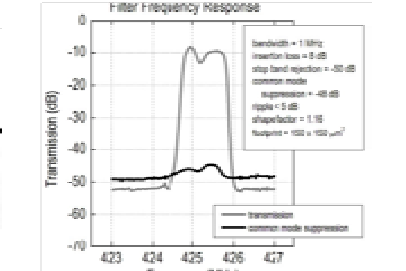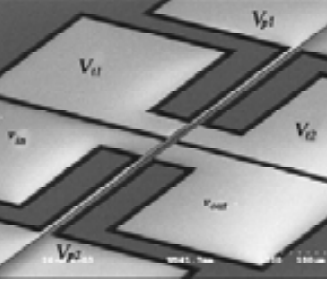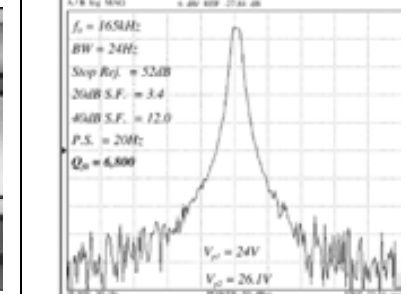
Finally, in [61], several resonators were connected in cascade through buffers or amplifiers in order to eliminated the load effect of each resonator. A wide study of the Q factor dependence on the number of coupled resonators was made. The main benefit of this type of filter, compared with previous filters explained, is that a 2xQ is obtained bycascading three resonators.
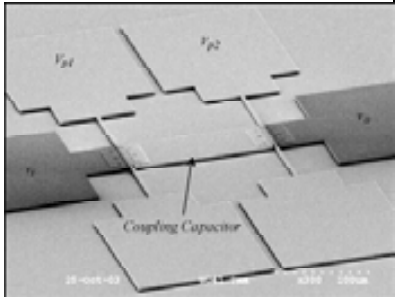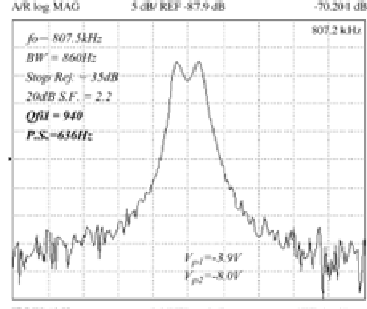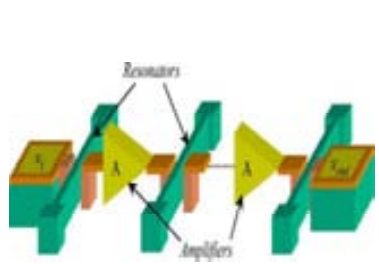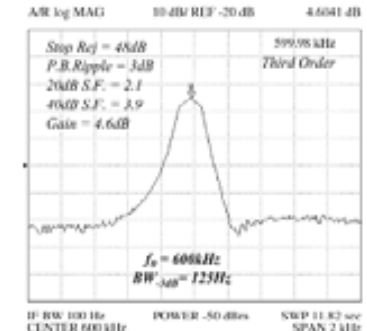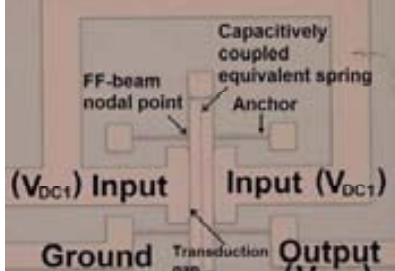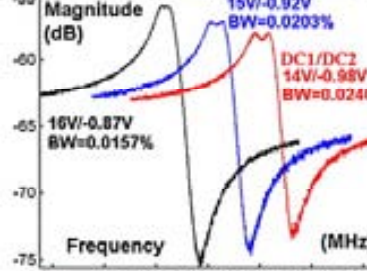
However, the previous approach still requires an electrical coupling element. To avoid it, Pourkamaly presented a filter with no coupling element: the electrostatic coupled resonators filter [61]. Electrostatic coupling is an electrical-based passive coupling technique that does not require any distinct coupling elements. In this approach, the electrostatic forces between their resonating bodies couples two closely spaced resonators and it results in a higher order resonant system. Both resonators are biased independently and the differential voltage between the resonant structures controls the electrostatic coupling and thus the bandwidth of the filter. For a voltage of 20V in the first resonator and 22.6V in the second resonator, Pourkamaly obtained a filter centered at 167kHz with a 44Hz bandwidth.

The highest frequency electrically coupled filter found in the literature was presented by J. Yan in [82] where two free-free beams were electrostatically coupled to obtain a 4.13MHz filter with less than 1kHz bandwidth.

Table 4.1 Summary of the most relevant works on the mechanical coupled resonator and electrical coupled resonator filters field. The table is sorted in mechanical and electrical coupling

	Mechanical coupling		
PolySilicon [69]			f=1.7MHz BW=400kHz Rip=n.r. SF_{20dB} =n.r. SR =n.r.
SOI [76]			f=2.27MHz BW=8Hz Rip<3dB SR =n.r. SF=1.65
Polosylicon [74]			f=7.8MHz BW=18kHz Rip=1.8dB SF_{20dB} =2.58 SR =35dB

SOI+Nanowire [75]			f=17.9MHz BW=114kHz Rip<1dB SR =6dB
Poly Silicon [79]			f=44MHz BW=44kHz Rip<0.1dB SR=n.r SF=n.r.
Polysilicon[80]			f=68.13MHz BW=190kHz IL<5.5dB SR=n.r. SF=n.r.
Silicon, high-k transduction [70]			f=425MHz BW=1MHz Rip<5dB SR =50dB
Electrical Coupling			
SOI [62]			f=165kHz BW=44Hz Ripp1.8dB SF_{20dB} =2.1 SR =52dB

SOI[61]			f=807kHz BW=860Hz Ripp1.8dB SF$_{20dB}$ =2.2 SR =35dB
SOI+IC [61]			f=600kHz BW=860Hz Rip=3dB IL=-4.6dB SF$_{20dB}$ =2.1 SR =35dB
SOI [77]			f=4.13MHz BW=990Hz Rip=1.5dB SF$_{20dB}$ =n.r. SR =n.r.

The coupling elements constraints and the new programmability filtering requirements of the new RF transceiver proposals caused that the parallel filtering emerged in the last years [22, 83-84]. In this filters the bandpass is formed by the electrical signals provided by two or more parallel-connected MEMS resonators.

In the field of parallel filtering Lopez et al. [22] used two C-C beams working at 22MHz to fabricate a RF filter. The output current of both resonators is subtracted and amplified by the IC circuitry. The filter is centered at 21.76MHz achieving a bandwidth suitable for GSM of 200kHz. This filter offers a ripple of 0.9dB and 2.97 SF$_{20dB}$ a 30dB out of band rejection in air conditions.

Li et. al. [85] used two sub-filters based on arrayed-disk resonators for a parallel-class filter. A complicated micro fabrication process is used to obtain a filter with a bandwidth composed by the two sub-filters (see Figure 4.5). This process allows obtaining 80nm gaps. This filter introduces a method for the channel selection based on the activation of one or other sub-filter by means of the activation voltage. This fact avoids the uses of switches, and it decreases the effective cost of implementation, and eliminates a potential reliability concerns. The bandpass formed by the two sub-filters that are enabled at the same time is centered at 163.1MHz and it has a 0.16% bandwidth. Due to the use of

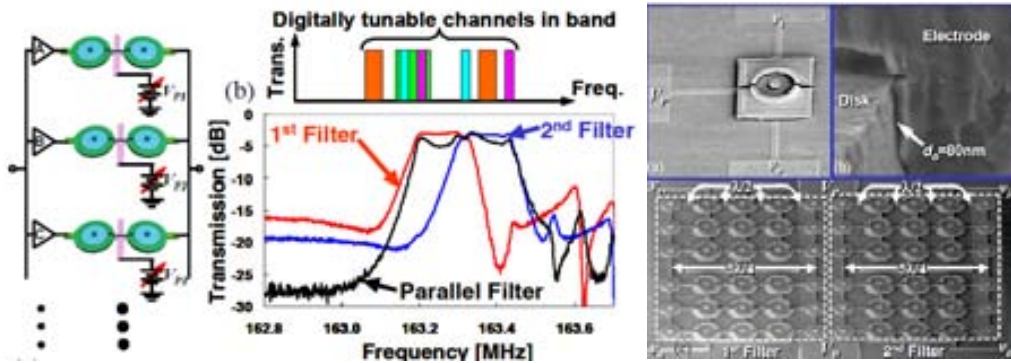several arrayed resonators, the motional impedance is reduced and the insertion losses achieved are 2.73dB.

Figure 4.5. System level performance of the filter. the graph shows the bands of the two sub-filter (red and blue lines) and the complete filter (black line). At right a SEM image of a single resonator with a detail of the 80nm gap. The lower image shows the complete dual filter [85].

In the field of dual filters Zou et al. [86] presented a filtering structure based on a single resonator with different controllable resonant modes. The structure is formed by a central square proof that has four identical beams in its sides (see Figure 4.6). The central proof plays two roles: a) anchoring of the beams and b) weak coupling between the beams. The C-C beam resonators move in their lateral first mechanical mode and they are enabled by means of the proper biasing voltage. In this way, it is possible to obtain either stop-bands or pass bands depending on the voltage applied. A pair of adjacent resonators forms each band of the dual band filter. The performance of each band is described as follows: for the lower band, the center frequency is 130 KHz and the bandwidth is 140Hz. The SF is 1.45. The higher frequency band is centered a 131.5Khz and the bandwidth is 155Hz. The SF is 1.39. The main problem of this filter is that the ripple of each band is 13.1dB. Furthermore, the stop band rejection of each band diminishes critically when the two filters are working at the same time. However, the structure offers a good programmable featuring since the band can pass or stop the corresponding frequency. In this way, multiple working options can be achieved.
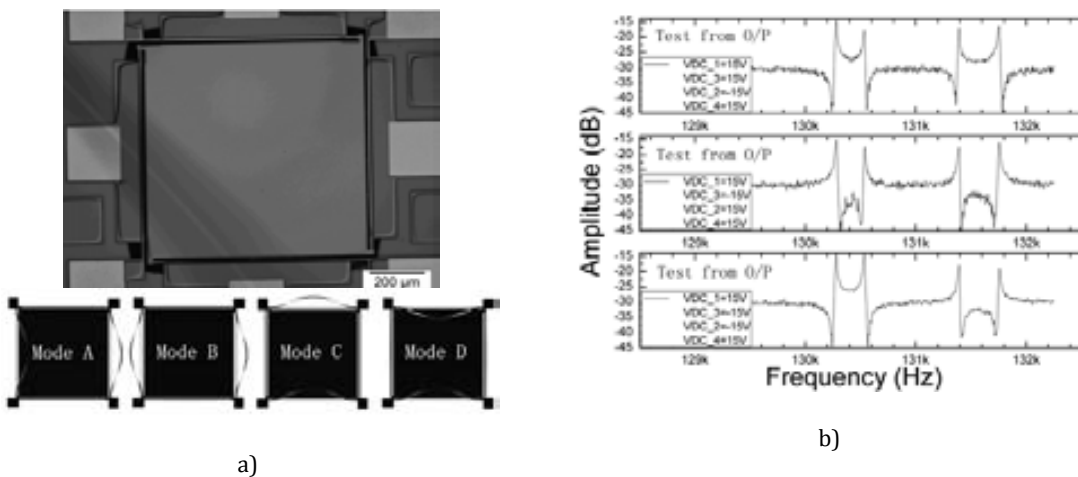

a)

b)

Figure 4.6 a) SEM image of the micromechanical structure proposed by Zou [86]. The lower figures show the mechanical modes. The graphs in b) shows the different pass bands or stop band achievable by using a proper biasing the beams.

4.3 THEORY OF FILTERS

This section is focused on explaining one of the essential principles in coupled resonators filters: the coupling. The coupling will be detailed considering the case consisting of two identical coupled resonators. After the physical exposition, its translation into the electrical circuit will be explained and the coupling role into the behavior of the circuit will be studied. However, actual resonators are not always similar. In addition, they are affected by the spring softening. For this reason, the explanation of the coupling theory between two different resonators under the effects of external disturbances is expressed in this chapter. Once the effect of the coupling over the whole system behavior is explained the difference between the two types of couplings, mechanical and electrical, will be done.

4.3.1 COUPLED RESONATORS

In the first part of this section, the coupled system formed by two identical mass-spring resonators that are coupled by a spring will be analyzed. In the second part, a coupled resonator system formed by two different resonators that are affected by the spring variation will be analyzed and the constituent differential expressions will be solved.

4.3.1.1 IDEAL CASE

In chapter 2, the modeling of the resonator as a dump-spring-mass system was explained. In this section, for simplicity, the dumper is considered null. This implies that the resonator has not energy losses. The resonator is considered a simple harmonic oscillator. The movement is described by expression (2.16):

$$m_1 \frac{\partial^2 x}{\partial t^2} + k_1 x = 0 \qquad (4.3)$$

where m is the mass and k is the stiffness of the resonator. The coupled resonator system can be modeled as in Figure 4.7. The resonator displacements, x_1 and x_2, to the right are considered positives whereas the displacements to the left are considered negatives. The coupling stiffness is modeled by means of k_c.

Figure 4.7 Coupled harmonic oscillator system where m defines the masses of the oscillator while k_1, and k_c are the stiffness of the resonator and the coupler.

Considering the harmonic solution for expression (2.16), the resonant frequency for the resonator is:

$$\omega_1 = \sqrt{\frac{k_1}{m_1}} \tag{4.4}$$

Since the resonators are coupled by a generic spring, the single resonator frequency is modified by the presence of the coupler. "Grounding" one of the resonators, for instance, resonator 2, the resonance frequency can be obtained. The term grounding is used to denote that one of the resonators is rigidly fixed. (see Figure 4.8)
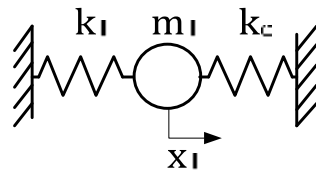
Figure 4.8 Diagram of a two springs and mass with the grounded resonator 2

The total force produced by each spring can be written as:

$$F = -k_1 x_1 - k_c x_1 = -x_1 \left(k_1 + k_c \right) \tag{4.5}$$

Expression (4.5) suggests that if the mass is in a non equilibrium position it will be under the force exerted by the two springs. One of them is pulling it and the other of is pushing it. In that case, the resonance frequency of the resonator is calculated by means of expression (4.6):

$$f_c = \frac{1}{2\pi} \sqrt{\frac{k_1 + k_c}{m_1}} = \frac{1}{2\pi} \sqrt{\frac{k_1}{m_1}} \sqrt{1 + \frac{k_c}{k_1}} = f_1 \sqrt{1 + \frac{k_c}{k_1}} \tag{4.6}$$

However, if any resonator is grounded, it is interesting to analyze the movement of each particle in Figure 4.7 taking into account the influence of the coupling element. The equation of movement for each resonator is shown in (4.7) and (4.8)

$$m_1 \frac{\partial^2 x_1}{\partial t^2} + k_1 x_1 - k_c (x_2 - x_1) = 0 \tag{4.7}$$

$$m_1 \frac{\partial^2 x_2}{\partial t^2} + k_1 x_2 + k_c (x_2 - x_1) = 0 \tag{4.8}$$

Expressions (4.7) and (4.8) show the response if both masses have been displaced from its equilibrium point. In order to decouple the equations and obtain the simple harmonic movement differential equation, it is necessary to add and subtract the equations (4.7) and (4.8) to obtain:

$$\frac{\partial^2 (x_1 + x_2)}{\partial t^2} + \frac{k_1}{m_1}(x_2 + x_1) = 0 \tag{4.9}$$

$$\frac{\partial^2 (x_1 - x_2)}{\partial t^2} + \frac{k_1 + 2k_c}{m}(x_1 - x_2) = 0 \tag{4.10}$$

Equation (4.9) includes the term (x_1+x_2) that is referred to the in phase movement in that both resonators are moving at the same direction. On the other hand, equation (4.10) includes the term (x_1-x_2) that is the movement of the resonators with a 180º phase.

The frequency for each mechanical mode is:

$$\omega_1 = \sqrt{\frac{k_1}{m_1}} \tag{4.11}$$

$$\omega_2 = \sqrt{\frac{k_1 + 2k_c}{m_1}} \tag{4.12}$$

The bandwidth can be defined as the mode resonance separation. Expression (4.13) shows the two mode frequencies subtraction. Since $k_c \ll k_r$ the Taylor's approximation can be used

$$BW = \omega_2 - \omega_1 = \sqrt{\frac{k_1}{m_1}} - \sqrt{\frac{k_1 + 2k_c}{m_1}} = \sqrt{\frac{k_1}{m_1}}\left(1 - \sqrt{1 + \frac{2k_c}{k_1}}\right) \approx \sqrt{\frac{k_1}{m_1}}\left(\frac{k_c}{k_1}\right) \tag{4.13}$$

The center frequency of the system is calculated by means of expression (4.14):

$$f_c = \frac{f_1 + f_2}{2} \tag{4.14}$$

where f_1 and f_2 are the resonant frequencies two resonance mode. If small coupling factor is considered, the center frequency is the same that the individual resonator. The coupling factor will determine the bandwidth of the filter. Expressions shown in this section have demonstrated that the bandwidth and the center frequency changes with the variation of the coupling factor, *i.e* changing k_c.

4.3.1.2 COUPLED DIFFERENT RESONATORS WITH SPRING VARIATION

The case described in section 4.3.1.1 corresponds to the simplest case where identical masses and spring constants for the resonators have been considered. In this section, a coupled resonator system with different non idealities is presented. Both resonator masses are different, m_1 and m_2, as well as their spring constants, k_1 and k_2. The resonant frequency of each resonator is:

$$\omega_1 = \sqrt{\frac{k_1}{m_1}} \tag{4.15}$$

$$\omega_2 = \sqrt{\frac{k_2}{m_2}} \tag{4.16}$$

Both resonators are linked by means of a spring with value k_c. (see Figure 4.9). In addition, it is possible to include, at the same time, the effects of the spring softening over the frequency behavior of the system. This variation is modeled by Δk and it has been added to the resonator 1 for simplicity, but it can be actually applied to any resonator.
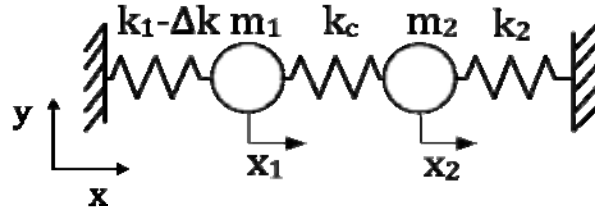

Figure 4.9 Coupled harmonic unequal oscillators system with the spring softening.

If the damping is negligible, the equation of motion is:

$$M\ddot{x} + Kx = 0 \tag{4.17}$$

where the mass and stiffness matrix are:

$$M = \begin{pmatrix} m_1 & 0 \\ 0 & m_2 \end{pmatrix}, \quad K \begin{pmatrix} k_c + k_1 + \Delta k & -k_c \\ -k_c & k_c + k_2 \end{pmatrix} \tag{4.18}$$

The natural frequencies are obtained if $\left|K - \omega^2 M\right| = 0$. The solution can be obtained by means of expression (4.19)

$$\omega^2 = \frac{k_2 m_1 + k_c m_1 - \Delta k m_2 + k_1 m_2 + k_c m_2}{2m_1 m_2}$$
$$\frac{\pm\sqrt{-4\left[k_2 k_c - \Delta k(k_2 + k_c) + k_1(k_2 + k_c)\right]m_1 m_2 + \left[k_2 m_1 + (-\Delta k + k_1)m_2 + k_c(m_1 + m_2)\right]^2}}{2m_1 m_2} \tag{4.19}$$

Equation (4.19) shows the angular resonant frequency of the two normal modes, ω_1 and ω_2 as a function of stiffness, masses and spring variation. Equation (4.20) shows the relation between the two squared angular frequencies.

$$\omega_2^2 - \omega_1^2 = \frac{\sqrt{-4\left[k_2 k_c - \Delta k(k_2 + k_c) + k_1(k_2 + k_c)\right]m_1 m_2 + \left[k_2 m_1 + (-\Delta k + k_1)m_2 + k_c(m_1 + m_2)\right]^2}}{m_1 m_2} \tag{4.20}$$

The minimum bandwidth is obtained when the electrical spring softening corresponds to equation (4.21). In that case, the difference between frequencies only depends on coupler stiffness k_c and resonator masses (see expression (4.22)).

$$\Delta k = \left| \frac{\left(k_2 m_1 - k_c\, m_1 + k_1 m_2 + k_c m_2 \right)}{m_2} \right| \tag{4.21}$$

$$\omega_2^2 - \omega_1^2 = \frac{2 k_c^{\;2}}{\sqrt{k_c^{\;2} m_1 m_2}} \tag{4.22}$$

In Figure 4.10 a graph that shows the squared angular resonant frequencies of the two normal modes is depicted (red and black line) as well as the squared angular frequency difference (red line) for a particular coupled resonator system. The graph emphasizes the bandwidth dependence with the stiffness variation.
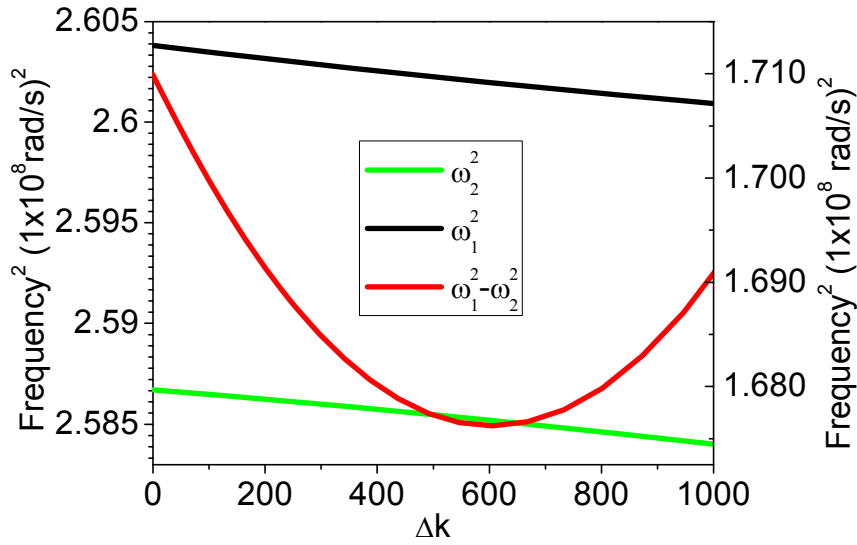

Figure 4.10 Variation of the angular frequency for each resonator of the system (blue and blak line. Red line shows ω_2^2-ω_1^2 for a coupled system with *k₁=9268N/m, k₂=9250N/m, m₁=358fg, m₂=357fg*, k_c=30N/*m*

Red line in Figure 4.10 shows the minimum of the squared voltage difference for two different coupled resonators. Depending on the masses and springs values, the minimum difference will vary. The system can be simplified if both resonators are considered equals and the stiffness variation is still present. In this case, the minimum bandwidth is achieved at *Δk=0.* The minimum bandwidth can be obtained by means of expression (4.23)

$$\omega_2^{\;2} - \omega_1^{\;2} = \frac{\sqrt{\left(\Delta k \right)^2 + 4 k_c^{\;2}}}{m} \tag{4.23}$$

Expression (4.23) suggests that it is possible to change the bandwidth of the resonator by varying the effective spring of the resonator.

4.3.1.3 ELECTROMECHANICAL MODEL

In this section, the effect of the coupling into the electrical response of the equivalent electrical circuit of the coupler resonator system is studied. The electromechanical model of a simple resonator was explained in chapter 2. The coupler can be modeled as shunt capacitor with a value:

$$C_c = \frac{1}{k_c}$$

(4.24)

In chapter 2, the resonator was modeled as an RLC electrical resonator. In this part of the text the same approach is used to model two identical resonators and the equivalent circuit in Figure 4.11 can be obtained. Note the shunt capacitor corresponds to the coupling spring.
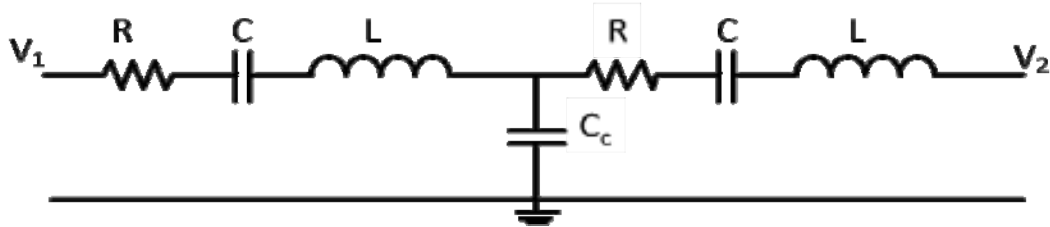

Figure 4.11 Electrical model of the filter. the C_u models the effect of the coupling over the response of the two resonators.

The bandwidth of the coupler resonator electrical circuit shown in Figure 4.11 can be calculated by means of expression (4.25)

$$BW = f_o \frac{C}{C_c}$$

(4.25)

where

$$f_o = \frac{1}{2\pi\sqrt{LC}}$$

(4.26)

$$C = \frac{1}{k_1}$$

(4.27)

The effect of the coupling on the electrical response can be observed in the simulations results that are shown in the Figure 4.12. In the figure, the equivalent circuit frequency response is shown as a function of the relation between the motional capacitance C and the coupling capacitance C_c. Therefore, according to expression (4.25), the normal modes separation depends on the relation between the resonator and coupler stiffness. The coupler and resonator have to be similar in terms of stiffness in order to have two separated peaks and therefore a large bandwidth. However to achieve narrow bandwidth the resonator stiffness has to be larger than the coupler.
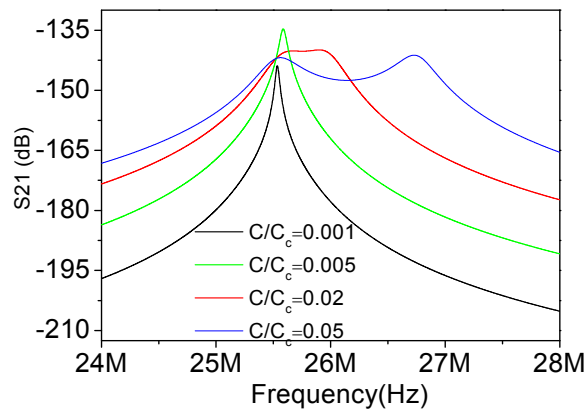
Figure 4.12. Simulation result of the circuit of the Figure 4.11. An increasing of the coupling factor increases the separation of the resonant frequencies.

4.3.2 TYPES OF COUPLINGS

In the previous section, the effect of the coupling on the resonant normal modes separation has been studied. The influence of the coupling into the equivalent electrical circuit has been analyzed. In order to couple actual resonators, different techniques can be used: mechanical coupling and electrostatic coupling. The mechanical coupling is based on the use of a physical component to link both resonators. On the contrary, if the electrostatic force is used to transmit the vibration energy from one resonator to the other, an electrostatic coupling is used. In this section, different types of couplings used in the thesis and its advantages and disadvantages will be discussed.

4.3.2.1 MECHANICAL COUPLING

The mechanical coupling is based on a mechanical link that couples two or more resonators. This coupling has to be designed in order to transmit the mechanical energy from one resonator the other. The C-C beam resonators used in this work are working in its first lateral mode (in-plane mode). Therefore, the mechanical coupler has to be optimized to work in its lateral mode. Different coupler shapes can be conceived to accomplish that task. Among all the possible coupler topologies, in this work two particular mechanical couplers are used:

1)U-Coupler: its shape correspond to the "U" letter.

2)V-Coupler. its shape correspond to the "V" letter.

The coupler dimensions and shape will fix the coupler stiffness, k_c. As it will be seen the coupler design is a critical step in the design flux because it will fix the bandwidth of the filter. However, a fine-tuning can be realized after the fabrication by means of changing the spring softening as it was shown in (4.20).

In the micro world, both the resonator and the coupler have similar dimensions. Thus, the stiffness constant will be similar and then the bandwidth (difference between two normal resonant modes) achieved will be wide (see expression (4.13)). For these reasons, different mechanical coupling techniques are required in order to achieve narrow bandwidth mechanical coupled resonators filters. The range of coupling techniques comprises among others, the low-velocity technique and the use of resonator arrays that

allow to increase the equivalent stiffness of one of the composite resonators in order to relax the coupler stiffness constraints for a particular bandwidth. In addition, since the resonator and the coupler are similar sized, the coupler can add a significant mass to the resonators and change their resonant frequency. The mass addition consequences will be studied in this chapter.

4.3.2.2 ELECTROSTATIC COUPLING.

Although mechanical coupled resonant filters offer the bandwidth and frequency tuning capability, they are strongly interrelated. It implies that bandwidth tuning produces a center frequency shift at the same time. In addition, the coupler adds a mass to the whole device and it shifts down the filter operation frequency. To solve these problems, the electrostatic coupling seems to be a powerful alternative. This type of coupling is based on the transmission of the mechanical energy through an electrostatical link formed between the two resonators. This coupling, unlike the mechanical coupling, depends on the resonator dimensions, the separation between them and the DC voltage applied to each one. The DC voltage precisely, allows changing the coupling level between the resonators and it offers the possibility to have, not only a center frequency tuning but also bandwidth tuning independently as main advantage compared with the mechanical coupling.

4.3.3 PARALLEL FILTERING

Both the mechanical and electrostatic coupled filters belong to the series resonator filter family. In this sort of filters, the resonators are place in series one after the other and properly coupled. The opposite concept is the parallel filtering that was introduced by Clark in [87]. The frequency responses of two electromechanical resonators with different operation frequencies, f_1 and f_2 are added to obtain a combined response. Diagram in Figure 4.13 shows a simplified schematic of parallel filtering device formed by two resonators.

Note that between the two resonant frequencies (filter bandwidth), both responses are in-phase and produce the passband. Out of the resonance, the responses are out-of-phase (see Figure 4.14). In this case both signals subtracts to each other improving the roll off and the out of band rejection. The bandwidth of the filter is the difference of both resonance frequencies $|f_1 - f_2|$

The parallel filtering can be take one step further by replacing the resonator by coupled resonator filters (or series filter) as in Figure 4.15. Resonator 1 has been replaced by sub-filter 1 and the sub-filter 2 has replaced the Resonator 2. The filters present the bandwidth BW_1 and BW_2. The working principles are the same than in previous approach but in this second approach, the global response is the combination of two filtering responses. The proper design of each filter can provide a filter with twice sub-filter bandwidth.
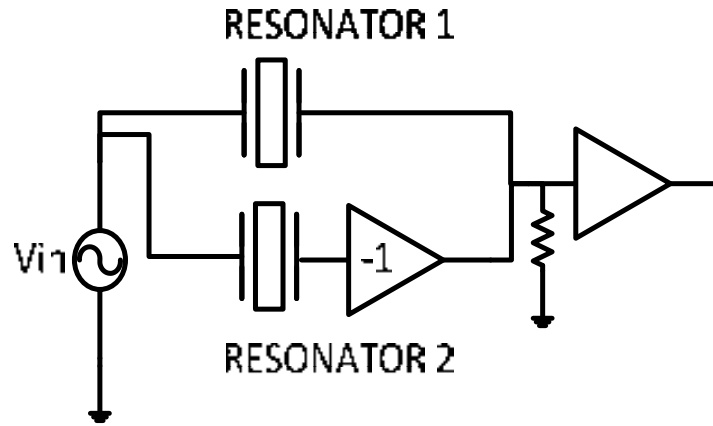
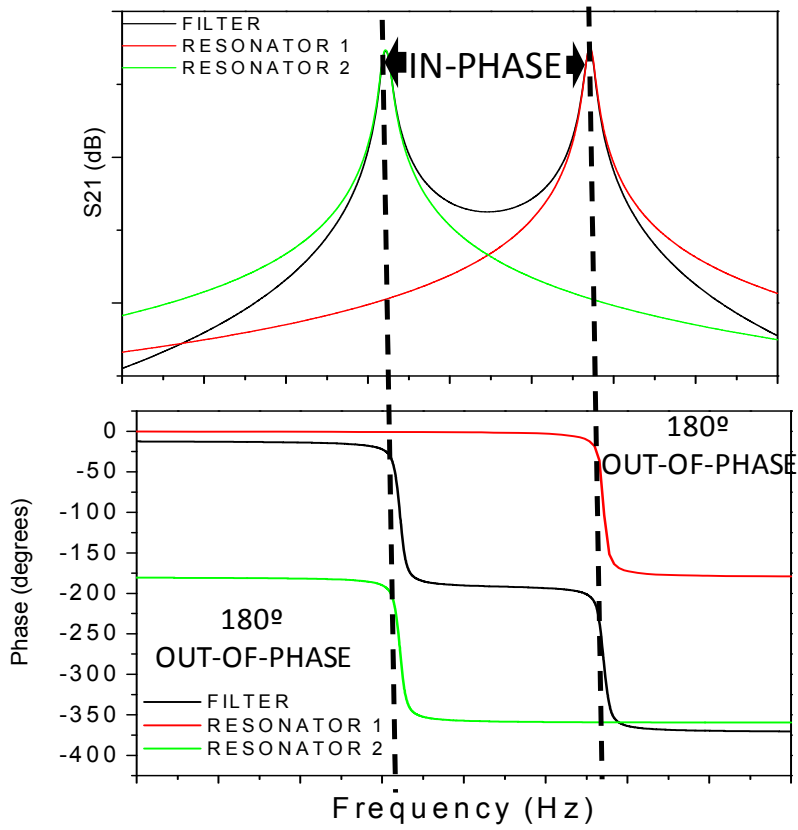Figure 4.13 Diagram of the parallel resonator filter.

Figure 4.14. Simulation of the magnitude and phase of the parallel filter.
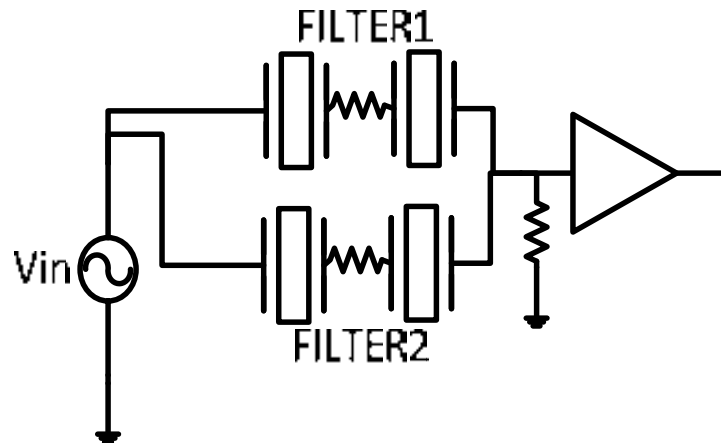

Figure 4.15 Diagram of the parallel filter with two sub-filters.

The parallel filter avoids the requirement of a mechanical coupling element between the resonators. It offers the self-switched bank filter capability by the simple DC voltage application. However, it requires a more complex system and external circuitry to perform the signal processing.

4.4 CMOS-MEMS RESONATORS MECHANICALLY COUPLED

In this section, our work addressed to the mechanical coupled filter is presented. The use of CMOS-MEMS C-C beams coupled with different mechanical structures allows obtaining different filters. The low-velocity coupling technique [74] introduced in section 4.4.1 will be explained. This technique is used as the base method to join similar sized coupler and resonators and to obtain narrow bandwidths at the same time. This section ends with the U-Filter and V-Filter design, characterization, and conclusion.

4.4.1 LOW VELOCITY COUPLING

In mechanical coupled resonator filters, the bandwidth is strongly dependent on the relation between mechanical coupler and the resonator stiffness. For general cases, (see expression (4.28)) the bandwidth can be rewritten as:

$$BW = \frac{k_c \cdot f_o}{k_r(y')}$$

(4.28)

Where k_c is the stiffness of the coupler and $k_r(y)$ is the stiffness in the coupling point of the resonator. The constituent resonator operation frequency is f_o

In the micro mechanical world is difficult to fabricate resonators and couplers with dimension so different that the stiffness ratio allows us to obtain narrow filters. Let us remember that Arellano tried to use nanowires to unbalance the stiffnesses relation between the resonators and the coupler and to achieve narrow bandwidths [75]. However, since in our approach both the resonator and the coupler are similar, we include the concept of low-velocity coupling technique in a C-C beam resonator.

The movement frequency in a C-C beam is the same independently on the position over the beam. Therefore, the velocity is different on each point of the beam since the displacement of the structure varies with the position. In the C-C Beam first lateral mechanical mode the maximum displacement occurs at the very center of the resonator while near the anchors both the displacement and the velocity are lower.

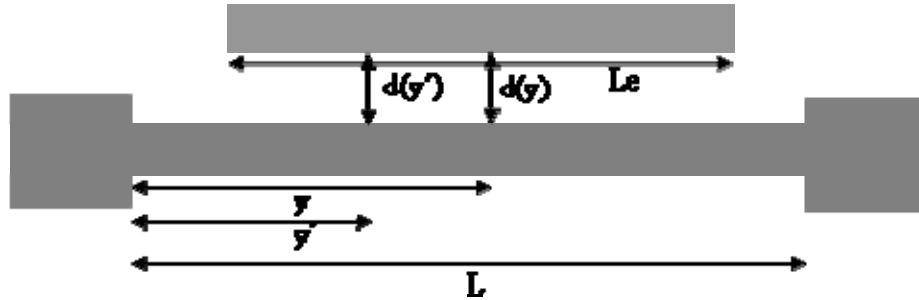In order to obtain the fundamental expression Figure 4.16 shows the diagram of a C-C beam resonator.

Figure 4.16 Scheme of the C-C Beam and the electrode for the analysis

The equivalent mass at a location y' on the resonator is given by expression (4.29)

$$m(y') = \frac{\rho W t \int_0^L X(y')^2 \, d(y')}{X(y)^2} \tag{4.29}$$

where ρ, W, t and L are density of the material, the width and the thickness of the beam and the length of the resonator respectively. $X(y')$ and $X(y)$ are the lateral displacement related to the y' position (coupling node) on the beam and the displacement on the centre of the beam respectively (the mode shape expression was detailed in Chapter 2). The resonator stiffness coefficient referred to the position y' is:

$$k_{r(y')} = \omega_0^2 \cdot m(y') \tag{4.30}$$

where ω_0 is the natural angular frequency the first lateral mechanical mode under study. Finally, the damping of the mode has to be defined and it is expressed by the following expression:

$$c_r(y') = \frac{\sqrt{k_r(y')m_r(y')}}{Q} = \frac{\omega_o m_r(y')}{Q} = \frac{k_r(y')}{\omega_0 Q} \tag{4.31}$$

where Q is the mechanical quality factor. Expression (4.30) suggests that the stiffness increases with the distance to the center of the beam (because the effective mass is lower near to the anchors) and takes the lowest value in the very center (where the mass is bigger). The segment of the resonator close to the anchors, where the stiffness is bigger is called low velocity coupling point

Figure 4.17 shows the electrical equivalent circuit of the resonator that includes the mechanical impedance transformation corresponding to the coupling point. The RCL branch corresponds to expressions (4.32), (4.33)and (4.34) that was deeply detailed in

chapter 2, as well as the electromechanical coupling transformer in expression (4.35). Note that the mass and stiffness (m_r and k_r) are taken in the middle of the beam. In addition, the mechanical transformer turn ratio is given by the relation between the resonator stiffness in the coupling point, $k_{r(y')}$ and the resonator stiffnes in the very center k_r (expression (4.36)).

$$c_r = \frac{\omega_0 m_r}{Q} \tag{4.32}$$

$$L_m = m_r \tag{4.33}$$

$$C_m = \frac{1}{k_r} \tag{4.34}$$

$$\eta_e = \frac{V_p C_0}{s} \tag{4.35}$$

$$\eta_c = \sqrt{\frac{k_r(y')}{k_r}} \tag{4.36}$$
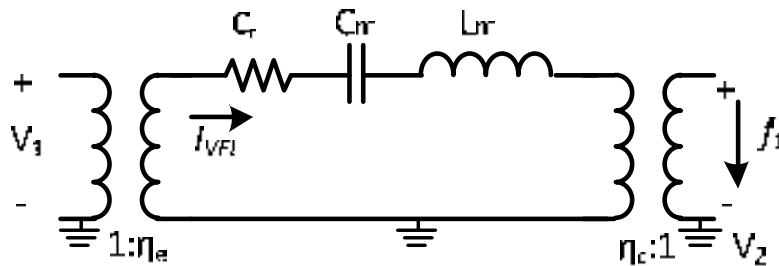
Figure 4.17. Schematic of the equivalent RLC circuit of the resonator. The first transformer shows the electromechanical coupling and the output transformer is the impedance transformer. Its turn ration is a relation between the coupler and resonator stiffness at the coupling point.

In Figure 4.18 the complete equivalent circuit of a mechanical coupled filter is depicted. The coupler has been modeled by a shunt capacitance C_c between the two impedance transformers. The feedthrough capacitance between the input and the output, C_{TH}, has been included.
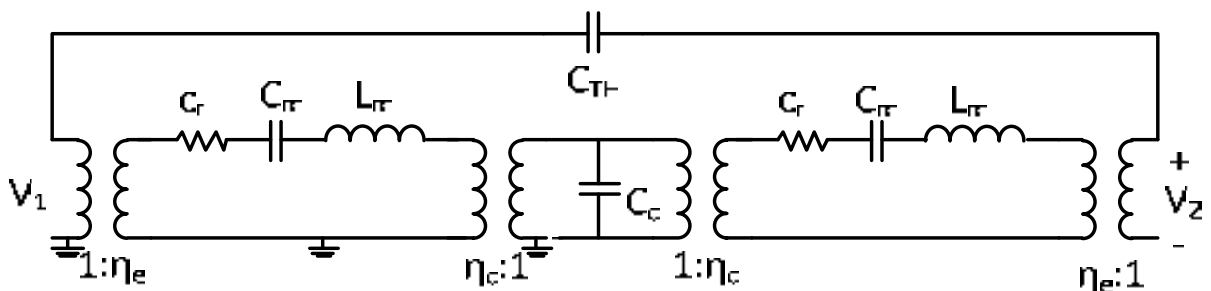

116

Figure 4.18 Schematic of the complete filter including the transformer that models the electrostatic transduction at the input and output and the impedance transformer that models the mechanical coupling of the resonator.

The mechanical impedance transformer plays an important role in the filter frequency response. In expression (4.38), the bandwidth is calculated as a function of the stiffnesses relation. The impedance transformer turn ratio, η_c, is bigger if the coupling point is near the anchors. In this case, the bandwidth tends to be narrower. On the contrary, if the coupling point is set near to the beam center the mechanical impedance transformer turn ration decreases and the bandwidth gets wider. The simulation results of the previous circuit prove this phenomenon (see Figure 4.19)
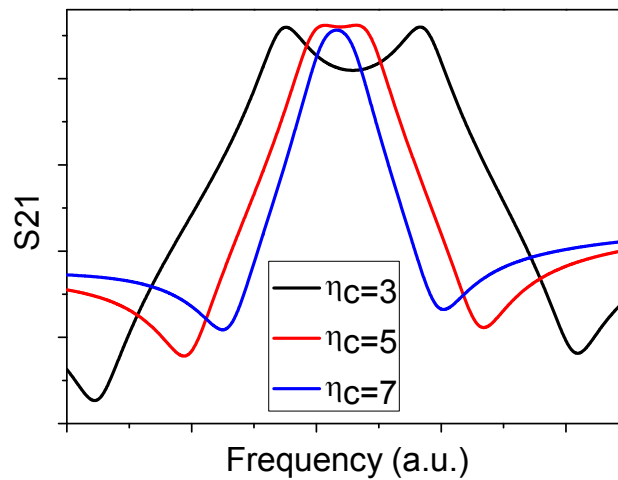

Figure 4.19 Simulation result of the circuit in Figure 4.18. The bandwidth decrease with the mechanical impedance transformer turn ratio η_c

Actually, the filter model presented in Figure 4.18 corresponds to the first approximation model. Note that the electrical model of the mechanical coupler has been considered as a mass less device and only the stiffness has been considered. However, in the micro world, resonators and coupler dimensions are in the same scale. Therefore, they are comparables in terms of masses. Thus, the mass added by the coupler will affects the frequency response of the filter. The electrical counterpart of the mass is an inductance. Considering the coupler mass, m_c, and assuming that the coupler is symmetrically placed between the resonators, the same additional mass will be charged on both resonators. The value of the inductances is:

$$L_c = \frac{m_c}{2} \tag{4.37}$$

Figure 4.20 shows the complete electrical equivalent circuit if the mechanically coupled filter including the effect of the coupler mass.
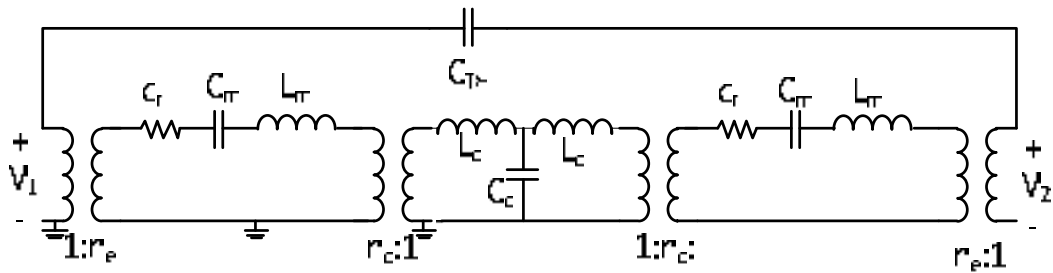
Figure 4.20 Diagram of a filter based on two resonators. It is similar to the presented in Figure 4.18 but in this case the mass introduced by the coupler is modeled by the inductors *Lc*

The mass addition due to the coupler will decrease the filter center frequency. In Figure 4.21 the simulation results of different coupler masses are included. The coupler masses are labeled as a scaling factor of the resonator mass. Note the bigger masses correspond to lower filter center frequencies. Simulation shows that an variation on the coupler mass does not affect to the bandwidth.
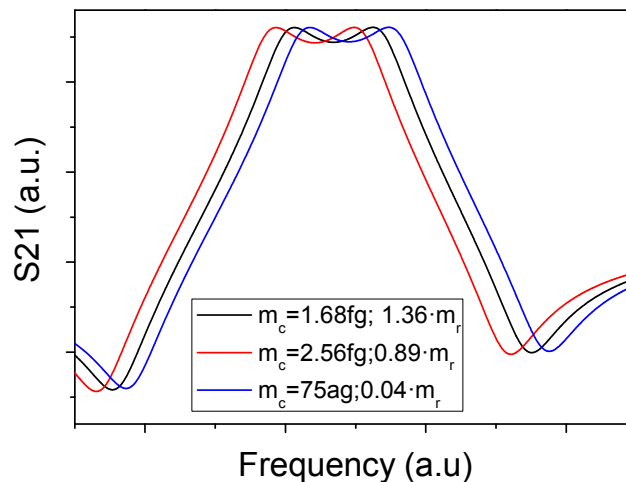

Figure 4.21 Variation of the center frequency of the filter with the variation of the mass introduced by the coupler. The legend of the graph indicates the mass of the coupler and the relation with the mass of the resonator. All the values are arbitrary units.

The procedure flow (see Figure 4.22) used to design the mechanical filters starts with the resonator design that fixes the center frequency of the filter. Following, the U-coupler is designed. Once the resonator and the coupler are designed, the selection of the coupling point is a crucial step in order to define the bandwidth of the filter. After the fabrication, the electrical test of the structure is performed. Furthermore, different prototypes have been fabricated to study the bandwidth dependence on the coupling position as well as the coupler dimensions.

118

Figure 4.22. Mechanical coupled filter design flux diagram.

4.4.2 U-FILTER

A U-shaped coupler has been used to design the called U-filter. The U-shaped coupler has been set to allow the transmission of the mechanical energy of the lateral mode from one resonator to the other. Figure 4.23 a) shows the SEM image of the fabricated filter. The inset figure shows a detail of the coupler where the main dimensions are labeled. The coupling position is L_3. Figure 4.23 b) shows the mechanical modes that have been simulated by means of Coventorware. The out-of-phase mode is observed at lower frequency than the in-phase mode.
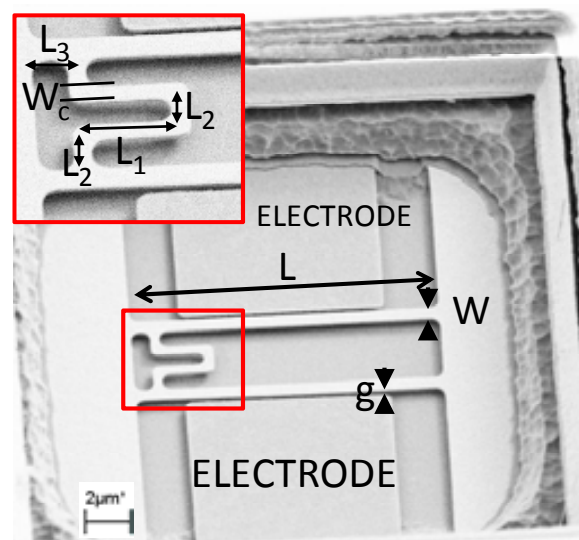
a)
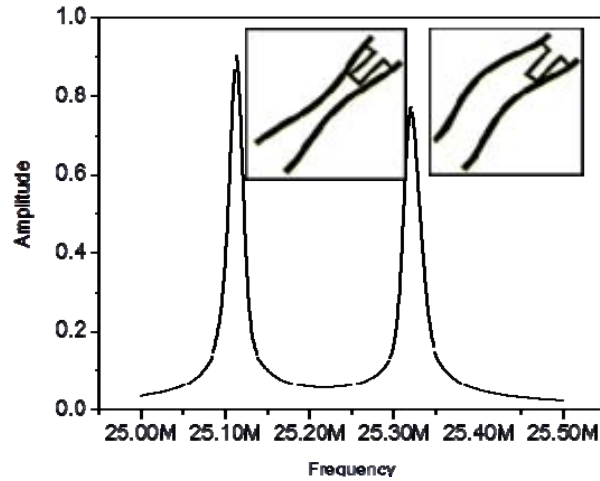
b)

Figure 4.23 SEM image of the fabricated filter. It shows the complete filter with the excitation and reading electrodes. The inset shows a detail of the coupler. b) Coventor harmonic simulation.

4.4.2.1   DESIGN OF THE RESONATOR

The first step in the design process begins with the design of the resonator that determines the center frequency (f_o). The Polysilicon capacitance module present in the commercial CMOS technology (AMS 0.35μm) has been used to implement the filter. In particular, the polysilicon 1 layer has been used to design both the coupler and the movable part of the brigdes while the polysilicon 2 is used to design the excitation and read-out drivers. The selected 13.2 μm long and 500 nm wide C-C beams, with a gap between the structure and the electrodes of 100nm present a Q of around 4400 in vacuum and 226 in air [22]. The resonant frequency is observed at 25MHz

4.4.2.2   DESIGN OF THE COUPLER

The mechanical coupler has to be designed to:

Allow the transmission of the mechanical energy from one resonator to the other.

Load the resonator with as little mass as possible.

The geometry selected for the coupler has been obtained from [88]. The U-shape suspensions allow, in principle, the displacement in the three space axes. As it is shown in the inset of Figure 4.23, two long arms, with length L_1, and three shorter arms, with length L_2, forms the coupler. The width of the coupler is W_c, and the distance of the coupling point to the anchors is L_3. The stiffness for this geometry is detailed in equation (4.38)

$$k_c = \frac{3EI}{2L_1^{\,2} \cdot \left(2L_1 + 3L_2\right)} \qquad (4.38)$$

where E is the Young's modulus and I corresponds to the second moment of inertia ($I=W_c^3 t/12$, where t is the beam thickness) for each segment of the coupler. Lengths L_1, L_2, and L_3, correspond to the coupler dimensions in Figure 4.23.

In order to load the resonator with as little mass as possible the minimum dimensions for the coupler have been selected. The coupler width is $Wc=350\ nm$ and it is fixed by the CMOS technology. The length of each segment of the coupler has been selected taking into

account the same premise, not to load in mass. A coupler length of L_1=2.5 μm and a minimum of L_2=1 μm have been set. Once the dimensions have been chosen, the stiffness constant can be obtained using a mechanical simulator (Coventor). In Figure 4.24 the simulated coupler is shown. The first figure shows the relaxed structure. Second and third figures show the expanded and compressed coupler.
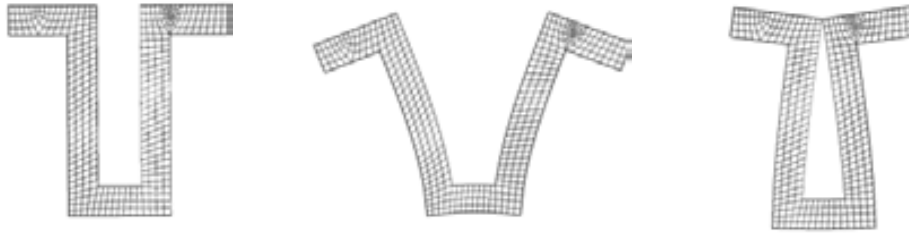

Figure 4.24. Coupler mechanical deformation under tension and external force to obtain the stiffness constant.

Considering that the minimum width obtainable from polysilicon in AMS technology is w_c=350nm and assuming that $L1=2.5\mu m$. the stiffness values obtained in MATLAB and Coventor are 9.2N/m and 9.692N/m respectively.

The filter bandwidth can be calculated using expression (4.39).

$$B = \frac{k_c \cdot f_o}{k_{r(y)}}$$

(4.39)

where $k_{r(y)}$ corresponds to the effective stiffness of the beam in a certain position (y) respect the anchors [3], B is the required bandwidth, and k_c is the stiffness of the coupler [3].

4.4.2.3 SELECTION OF THE COUPLING POSITION

Figure 4.25 shows the dependence of the bandwidth of the filter with the coupling position for the dimensions designed. The position, designated by L_3 is simulated for all the values between 150nm and 6.5μm, that is almost the half-length of the micromechanical resonator. As it can be observed in the graphic, the bandwidth is very sensitive to the position of the coupler (note that both axes are logarithmic). For bandwidth in the range of interests, $i.e.$ wireless channel filters bandwidth, the bandwidth changes from 200kHz (GSM filters) to 500MHz (filters for UMTS) for a variation of the coupling position of less than 4.5μm (from 1.5μm to 6μm).
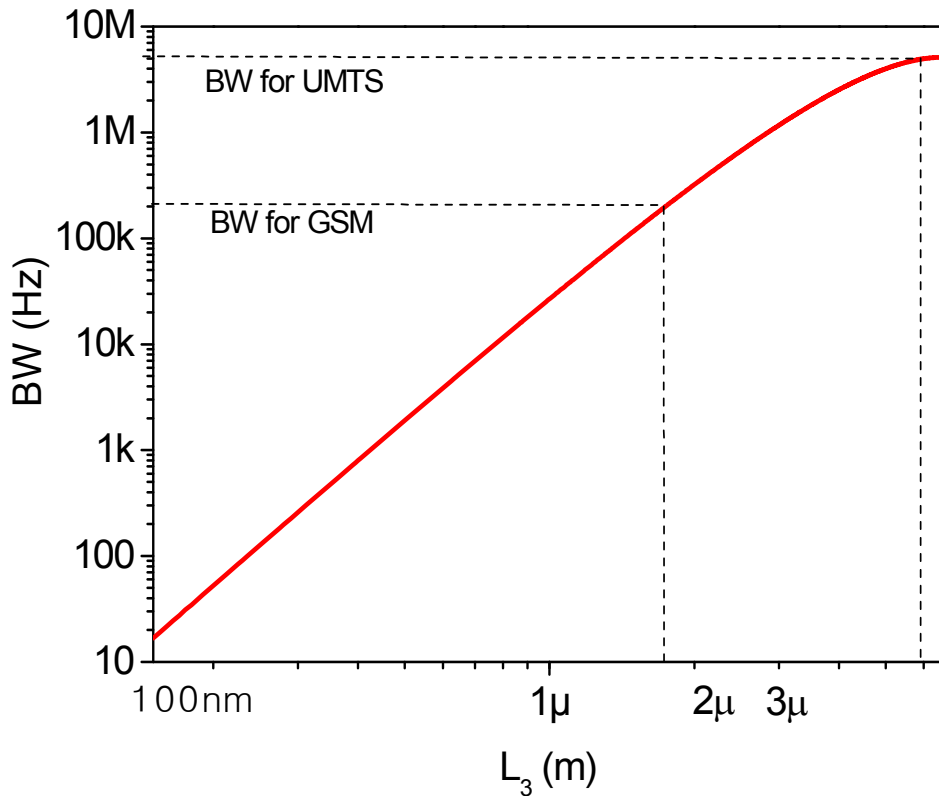
Figure 4.25 Variation of the Bandwidth for the fabricated filter with the coupling position of the U-coupler.

Different filter prototypes have been developed in this work. The main difference between them is the coupling position that has been set at L_3, 500nm 1µm, 1.2µm and 1.5µm in order to demonstrate the coupling position bandwidth dependence.

In Figure 4.26 the simulated frequency response of the mechanical coupled filter is shown. The simulation corresponds to different coupling points.
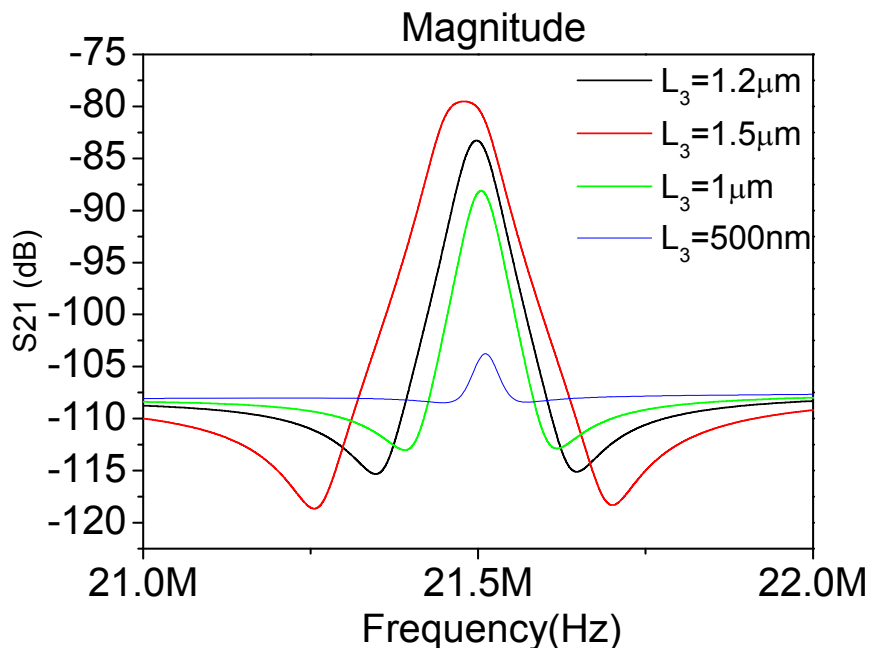
Figure 4.26 Variation of the simulated bandwidth with different coupling position. The green line shows the bandwidth for $L_3=5\mu m$ the red line for 2.4 μm and the black line *1.7μm*

4.4.2.4 CHARACTERIZATION OF THE FILTER

The set up for the electrical characterization is presented in Figure 4.27. A E5100A network analyzer is used to drive the filter and to read the motional current. The biasing voltage is applied directly to the structure.
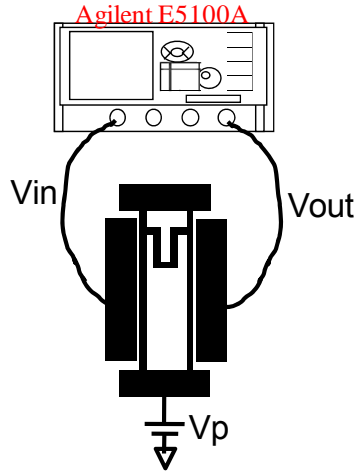

Figure 4.27. Set up for the electrical characterization. The biasing voltage is directly applied to the movable part. The AC signal is driven into de resonator through the input electrode and the output current generated over the reading electrode is read by the second port of the Network analyzer.

Figure 4.28 shows the transmission coefficient, both magnitude and phase, of the filter through a probe station in air conditions and without termination resistances. The movable structure is biased with different DC voltages, V_p, while a 2 dBm AC signal provided by a network analyzer (E8357A from Agilent) is applied to the excitation electrode. It can be seen how the spring softening due to the bias voltage allows a fine tuning of the center frequency of the filter. The response depicted presents two notches at both sides of the bandpass as it can be seen in the inset. Notches enhance the stop band attenuation close to the frequency pass band. This behavior corresponds to the mechanical phase inversion mechanism [79]. The out-of-phase movement is present at lower frequencies than the in-phase mode, as can be seen in Figure 4.28 b) contributing to improve the stop-band ratio.

a)

b)
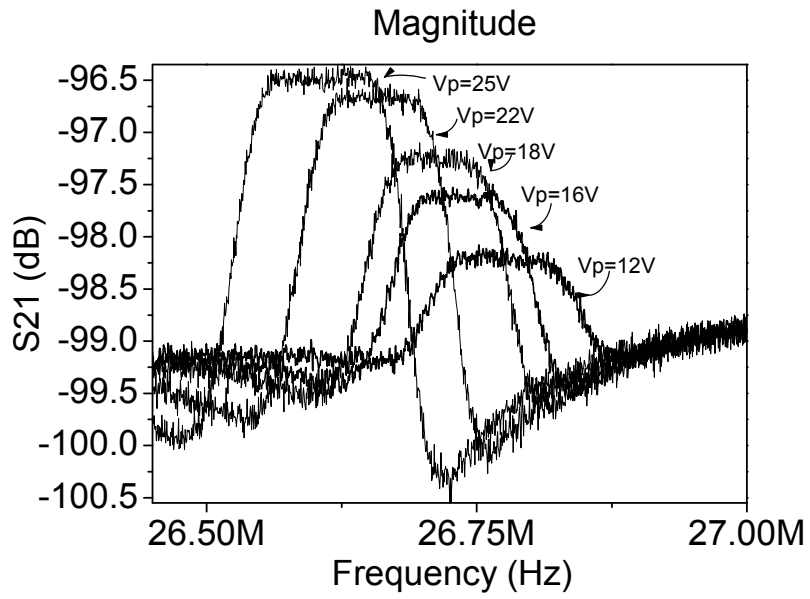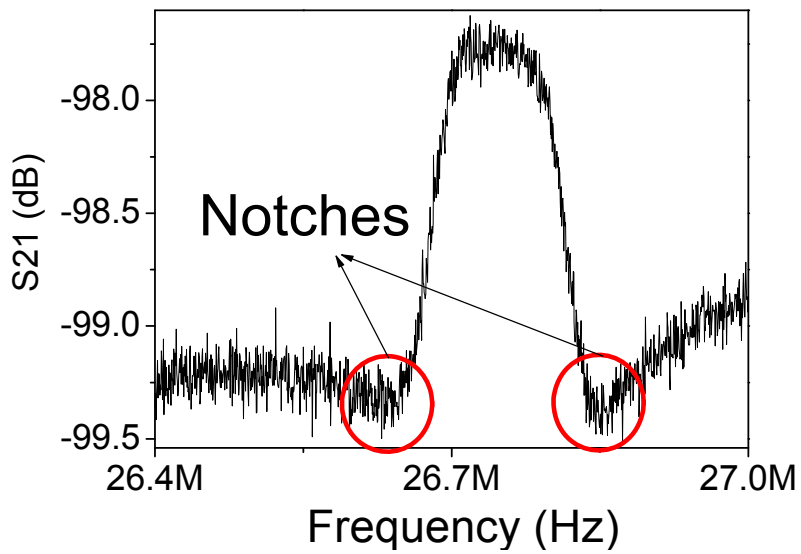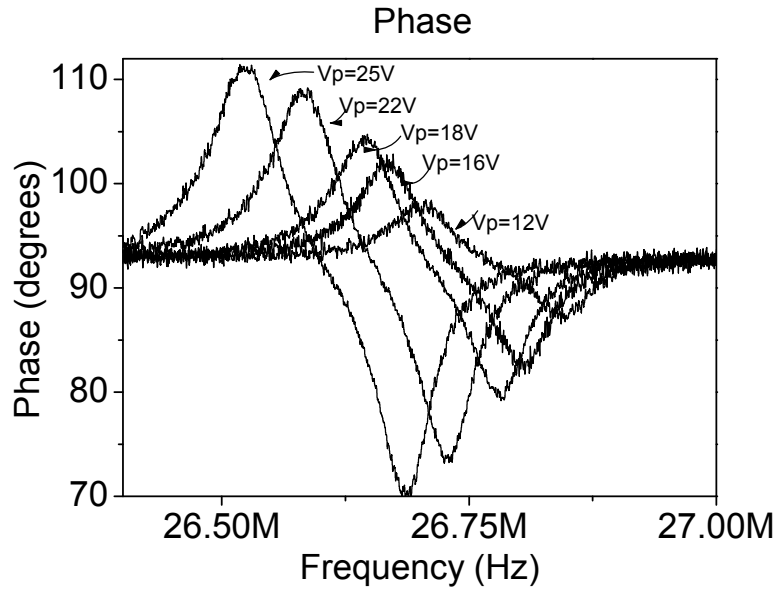
Phase

c)

Figure 4.28 Magnitude *a)* and phase *c)* of the S21 parameter of the U-filter. b) shows the presence of the notches due to the phase inversion of the filter.

The fabricated band pass filter presents a very low passband distortion (less than 0.1dB) without using any specific resistive termination, a central frequency of 26,7 MHz and a bandwidth of 120 kHz (with a bias voltage of 18V). Unfortunately, the magnitude measurement shows quite high insertion losses that correspond to the large motional resistance present in the CMOS-MEMS resonators compared with the input impedance of the test equipment (50Ω). In this way, we have computed the bandwidth at 0.5dB. An active matching impedance using CMOS circuitry enhance the insertion losses as it has been demonstrated in [89].

Table 4.2. Designed and fabricated dimension of the U-Filter.

Dimension	Layout	Fabricated
Length, L	13.2µm	13.2µm
Width, W	500nm	570nm
G	100nm	110nm
L_1	1 µm	1µm
L_2	2.5 µm	2.4µm
L_3	1 µm	1.2 µm
Coupler Width, Ws	350nm	440nm
$k_{r(y=L3)}$	5958N/m	5204N/m
k_c	9.7N/m	21.23 N/m
BW (expression (4.28))	40 kHz	115 kHz
V	25V	25V

The final dimensions differ from the previous designed and produce an unexpected result. In Table 4.2 the difference between the fabricated and designed dimensions is detailed. The increment of the beam width results into an increment of the resonance frequency. The increment of the coupling position, *L_3,* as well as the coupler width

125

produces an increment in the coupler stiffness, k_c , and therefore an increment on the bandwidth of the filter as it has been seen in Figure 4.25.

Figure 4.29 shows the expected quadratic dependence of the center frequency with the bias voltage (expression (4.20)) due to the spring softening effect. It provides a frequency tunability factor of 13 ppm/V². In Figure 4.29 a variation of the bandwidth (corresponding to a fractional bandwidth between 0.52% and 0.4%) with the applied bias voltage to the MEMS movable part is observed. This variation is due mainly to the spring softening. Although an increase of the bandwidth with the DC voltage would be expected, a minimum is obtained at 20V. This behavior is attributed to the difference between the effective stiffness of each resonator, produced by the tolerances in the fabrication process (10% for Polysilicon structures).
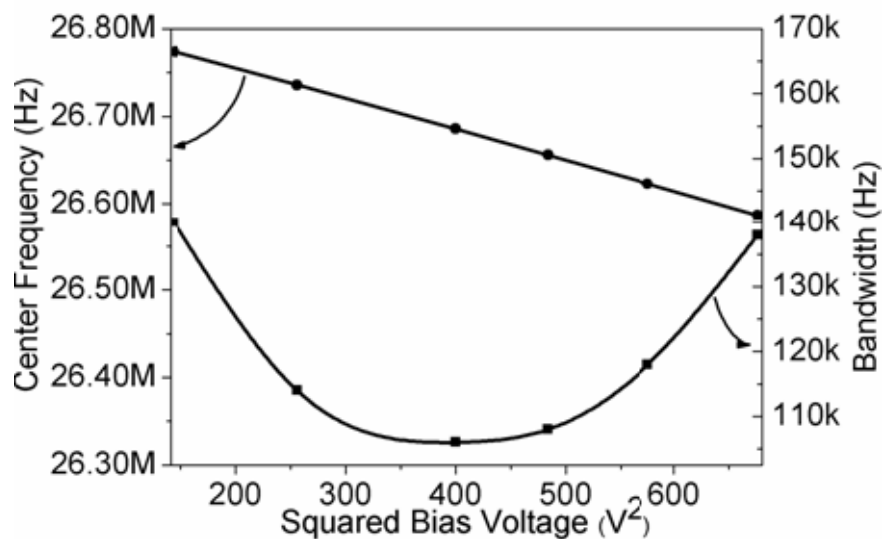

Figure 4.29. Center frequency variation and bandwidth at 0.5dB of the filter as a function of the applied bias.

4.4.2.5 STUDY OF THE FILTER RESPONSE FOR DIFFERENT COUPLING POSITION.

In order to study the influence the coupling position different alternatives have been implemented. Different coupling position have been studied and the frequency response has been measured for each prototype..

Coupling position:L_3=1.2μm

The coupling position is set at 1.2μm. Measurements in Figure 4.30 show the magnitude (a) and the phase b) for the filter with the coupler located at 1.2μm. In order to fix a criteria that allow us to compare the bandwidth of this filter with the presented in the Figure 4.28, bandwidth is taken at 0.5dB from the maximum value of insertion losses at Vp=18V. In this case, the filter is centred at 25.81MHz and presents a bandwidth of 273kHz.
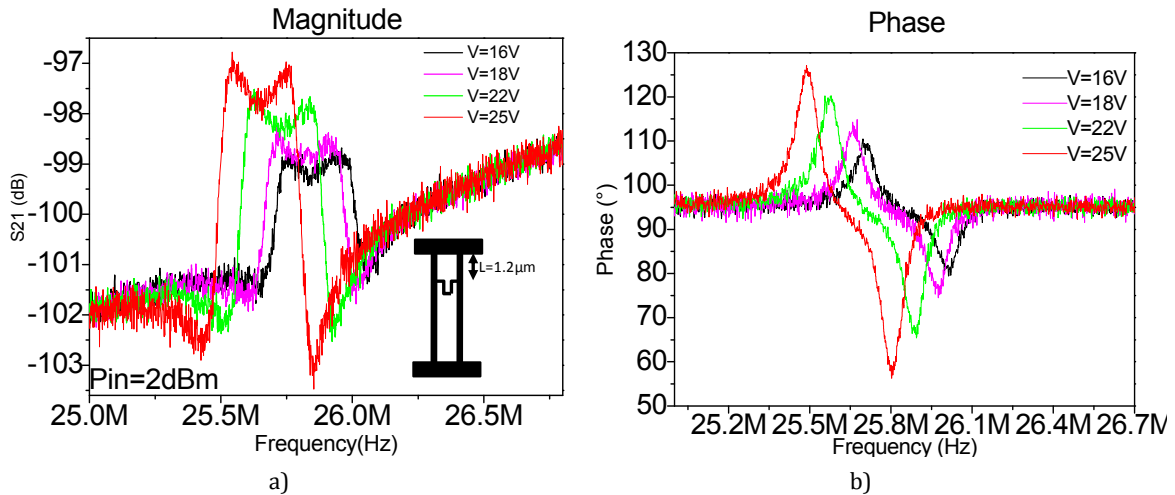
Figure 4.30 Measurement of magnitude (a) and phase (b) for different values of V for the filter with a L=1.2μm

Coupling position: L_3=1.5μm

Figure 4.31 shows the measurement for different voltage values. It shows a DC sweep of the voltage applied to the filter. Unexpectedly, the filter shows a stop band response where a bandpass response should appear. It suggests that a mechanical behavior variation occurs respect from the previous prototypes. Coventor simulations are required to study that behavior.
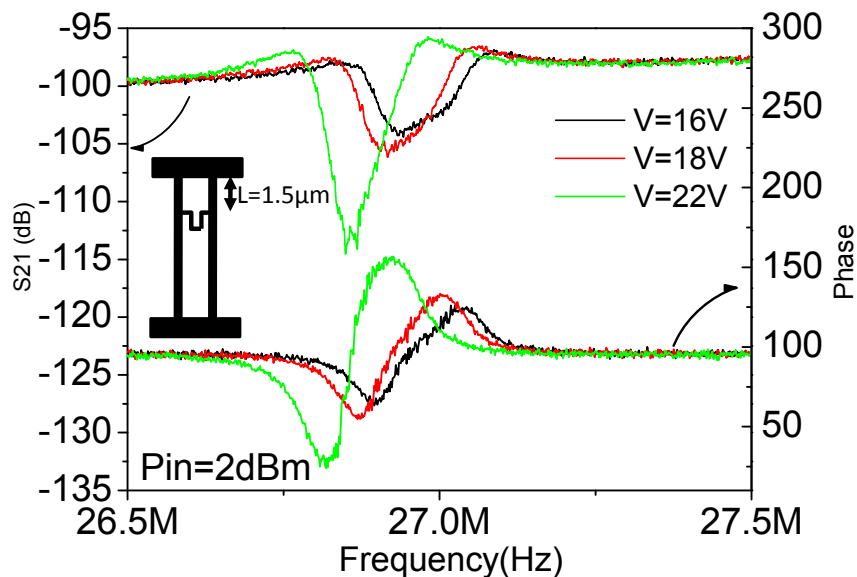

Figure 4.31 Measurement of magnitude and phase for different values of V for the filter with a L_3=1.5μm.

The 1.5μm coupled point filter has been simulated. The Coventor simulation results demonstrated that the in-phase mode occurs at lower frequency than the out-of-phase mode. This suggests that the position of the coupler can produce the mechanical phase inversion of the resonant modes.

To solve this problem, and achieve the filter bandwidth the electrical phase inversion is induced by changing the biasing conditions. The diagram in Figure 4.32 describes the set-up that has been used to characterize the filter. The input AC signal is applied to the

driver through a bias Tee, which is depicted as a capacitance and an inductance. The DC voltage applied to the driver, V_{p1}, as well as the voltage in the readout, V_{p3}, is inductively coupled. A DC voltage is applied directly on the movable part. In this way, three independent voltage sources are available and the biasing conditions can be modified in order to achieve the phase inversion. Figure 4.33 shows the magnitude and phase of the filter under non electrical phase inversion condition (black line). The electrical biasing is similar to the applied to the electrode to obtain the results shown in Figure 4.31. The red line shows the frequency response under electrical internal phase inversion.

Figure 4.32 Electrical characterization set-up for the mechanical coupled resonator filter. The DC voltage on the driver and the readout are inductively coupled.

a)
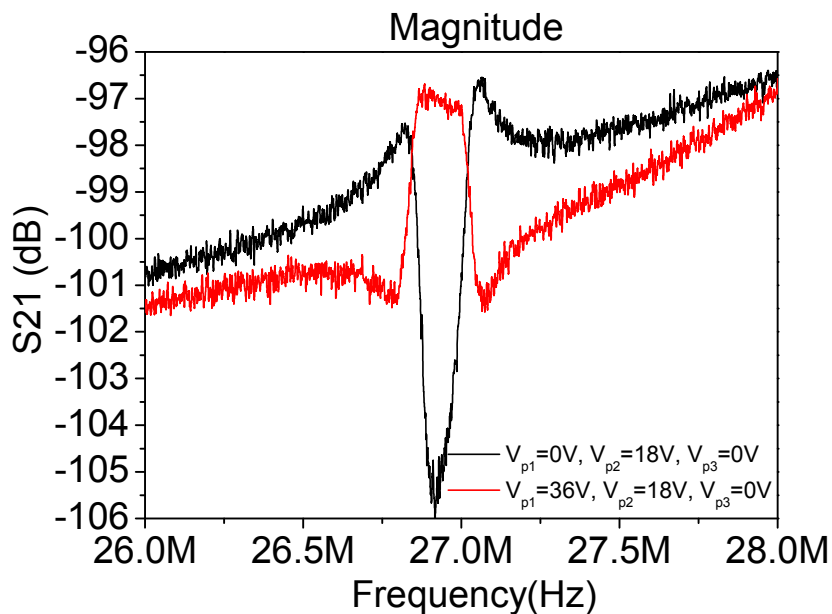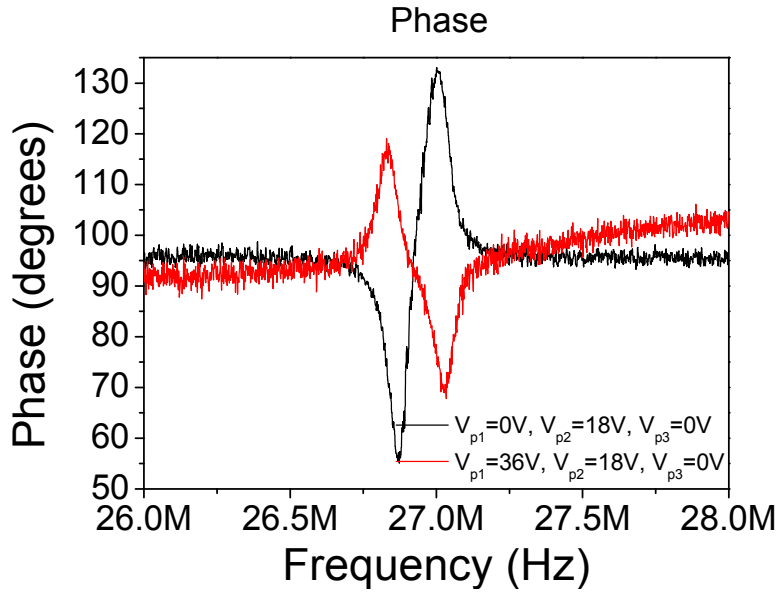
Phase

b)

Figure 4.33 Magnitude and phase of the mechanical coupled resonator filter with $(V_{p1}-V_{p2})=-(V_{p3}-V_{p2})$ (red line) and $(V_{p1}-V_{p2})=(V_{p3}-V_{p2})$ (black line)

Note that both the inverted and non-inverted conditions are set in order to keep the voltage symmetry in the input and output electrodes. In Figure 4.34, the frequency softening of the filter under electrical internal phase inversions is reported. The inset shows the phase behavior.
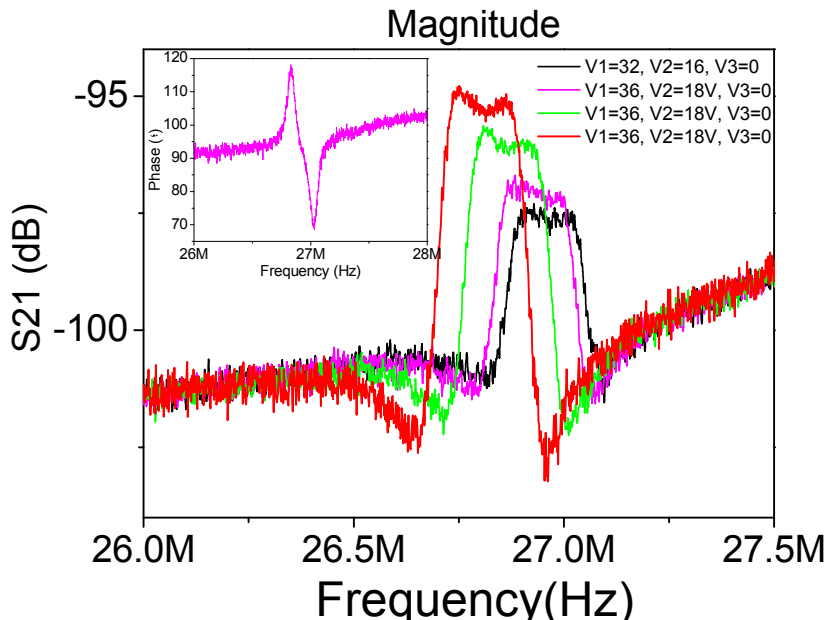
Magnitude

Figure 4.34 S21 Parameter of the filter under electrical phase inversion.

4.4.2.6 DISCUSSION.

After the analysis of the design expression and the measurements an study of the difference between the predicted behavior and thee results obtained in the electrical test

stage are needed to be presented. In Table 4.2, the variation of the fabricated dimensions respect the designed dimensions have been listed. The fabrication tolerances on the coupler are critic from the bandwidth point of view. The coupler stiffness, k_c for the actual fabricated coupler (dimensions in Table 4.2) is 22.3N/m that represents a 230% respect the designed coupler. This value represents a 2.3 factor of the predicted bandwidth. In addition, the increment on the beam width distorts the effectives stiffness on the coupling point $k_{r(y)}$. SEM image in Figure 4.35 shows a coupler detail. The coupling position is not an infinitesimal point as it has been considered in the design stage but it is actually a coupling area comprised between the 940nm from the anchors to 1.34μm. This can distorts the bandwidth achieved. In addition, the coupler stiffness has been calculated and simulated considering shaped corners. However, the fabricated coupler shows rounded corners that can affect to the mechanical behavior.
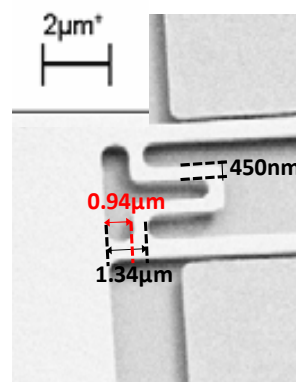

Figure 4.35 Zoom of the coupler after the releasing process-

Unce the fabricated dimensions are extracted the electromechanical model can be simulated. The comparison between the simulated response and the measurement of an arbitrary U-shape filter is commented.

In Figure 4.18, the mechanical coupled resonator filter equivalent electrical circuit was presented. All expressions used to calculate the lumped element values have been explained in chapter 1 and in this chapter. A particular U-filter has been electrically characterized The frequency response magnitude is shown in the black line in Figure 4.36. The Advance Design System (ADS) [90] schematic editor and simulator has been used to predict the frequency response of the electrical equivalent circuit. The values of the lumped element have been obtained by means of the constituent expression presented in Chapter 1 and within this chapter. The dimensions used to obtain that values are extracted directly from the SEM image using a Caliper Software [91].

In Table 4.3 the extracted dimensions are listed in the second column. Dimensions and the corresponding mechanical parameters have been used as input values of the electrical circuit. The electrical simulated response is shown in red line in Figure 4.36 b). Note that a big difference exists between the simulated and measured response. The simulated response shows a shifted frequency response compared with the measurement. This result suggests that the extracted resonator dimensions are incorrect. In addition, the simulated response presents less insertion losses than the measured one. In the following

paragraph a qualitative explanation about the difference between the measurement and the simulations are presented.

The frequency can be explained by means of a little error in the beam length measurement. In fact, an error of 100nm in measurement can increase the resonator mass and decreases the resonator stiffness. Both parameters modify the resonant frequency of the resonant and hence, the center frequency of the beam. In the third column in Table 4.3 shows the adjusted values of the length found by means of the tuning of the simulated electrical stimulation. An increment of 100nm in the resonator length adjust perfectly the center frequency of the resonator

The lower insertion loses shown by the simulated response can be attributed to two causes: First of all, since the measurement of the fabricated dimensions has been done from the top of the SEM, any possible out of plane misalignment produced by the under etching have not been taken into account. The misalignment decreases the coupling area between the electrode and the resonator and then the electroemechanical coupling factor decreases. On the other hand, the error in the gap measurement due the measurement software can produce an increment of the coupling factor. Using the simulation tuning the equivalent gap found to fit the simulation with the measurement is 180nm.
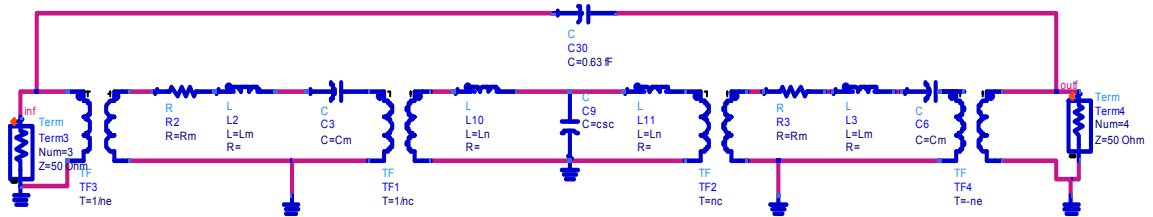
a)
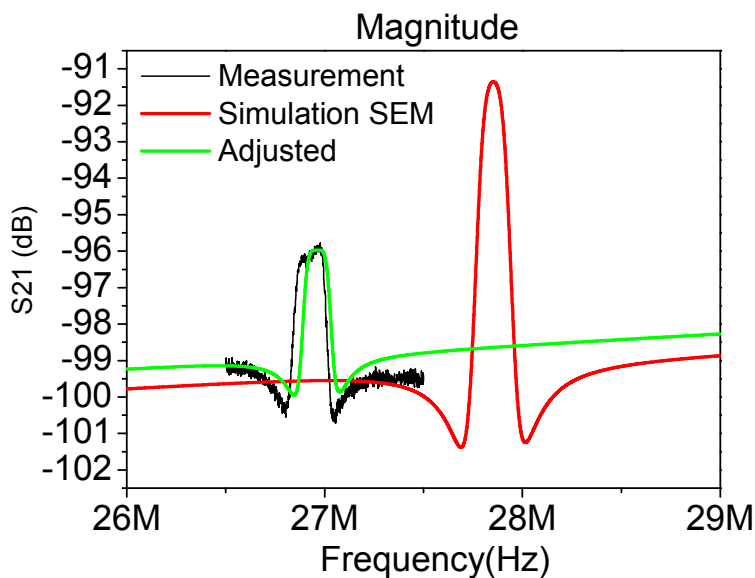
b)

Figure 4.36. Equivalent electrical circuit provided by the Advanced Design System electrical Simulator, a) Frequency response of the actual resonator (black line), simulated circuit with values extracted of the SEM image (red line) and adjusted simulation (green line).

Table 4.3. Listed of SEM extracted and adjusted dimensions.

Dimension	SEM Measure	Adjusted
Length, L	13.4μm	13.5μm
Width, W	600nm	600nm
Gap, g	120nm	180 nm
L_1	1 μm	1μm
L_2	2μm	2μm
L_3	1.3 μm	1.3 μm
m	2.0668 fg	2.17 fg
Coupler Width, Ws	400nm	440nm
k_e	63 N/m	62N/m
η_c	11.55	11.55
η_e	$2.23 \cdot 10^{-8}$	$1.04 \cdot 10^{-8}$
Coupler mass, m_c	1.2 fg	1.2 fg
k_c	36 N/m	36 N/m
Damping, c_r	$1.5586\ 10^{-9}$	$1.06 \cdot 10^{-9}$
Feedthrough capacitace, C_{TH}	680aF	680aF

4.4.3 V-FILTER

The previous U-coupler is very susceptible to fabrication tolerances. The two corners of the mechanical coupler tend to be rounded, which affects the filter performance. One of the possible enhancements is to reduce the coupler complexity. In this chapter, an alternative for the coupler is presented. The aim here is to design a simpler coupler that allows the transmission of the energy. Some studies with the V filter were carried out by Motiee in [69] and we will try to go further in its analysis and study its CMOS integration.

The V-Filter [92] diagram is presented in Figure 4.37. The main coupler characteristic is the symmetry of the coupler respect to the half of the union angle α. This angle and the length of each arm are the design parameters.
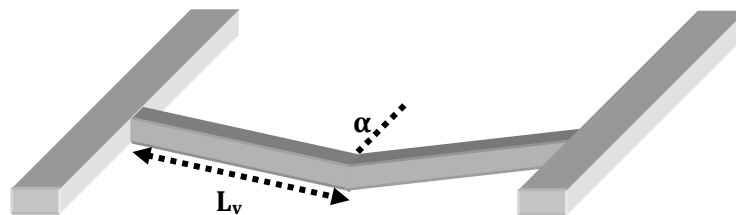

Figure 4.37 Diagram of the two resonator based filter with the V-coupler.

The design flux is similar to the one presented in Figure 4.22 and it is described in the following sections. The resonators have been designed to work around 25MHz (500nmx13.2μm)

4.4.3.1 DESING OF THE COUPLER

Like in the U-coupler design, the aim of the V-Coupler design is to avoid the mass loading as much as possible. One of the solutions is to fabricate the mimum dimensions for the polysilicon width. The coupler width is $W_c=350nm$. The V-shaped spring constant can be obtained by means of expression (4.40) [88]. From the expression, k_c is inversely proportional to the length of one of the arms, L_V, and the square of the angle between them.

$$k_c = \frac{6EI}{L_V^3 \cos^2 \alpha} \tag{4.40}$$

Where E is the Young's modulus and I is the second moment of inertia ($I=W_c^3t/12$). Figure 4.38 shows the coupler stiffness values for different angles and different lengths of the arms. The angle is directly related with the coupler stiffness so when the angle increases k_c increases. This means that the structure becomes more rigid in the direction of the movement. On the other side, an increasing in the length of each arm makes the spring softer. It implies a decreasing of the k_c.

The length of each arm is fixed at $L_v=3\mu m$ because it has been considered a total length (2 L_v)as a half of the resonator length (13.2μm)and the angle of the coupler is $2\cdot\alpha=70°$. In this case, the k_c obtained is 53N/m.
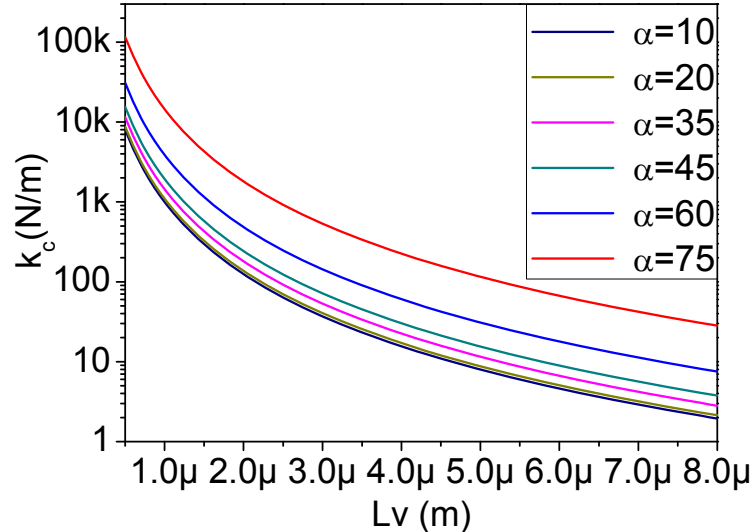
Figure 4.38 Variation of the stiffness constant of the coupler for different values of the angle and the length of L_v

4.4.3.2 SELECTION OF THE COUPLING POINT

Once the dimension for the coupler has been selected, the next step is to select the coupling position. In this case, since the coupler stiffness is $k_c=53N/m$ the coupling position is chosen by means of Figure 4.39 that represents the relation between the bandwidth and the coupling point. The coupling position to achieve a bandwidth of around 200kHz is 1μm.
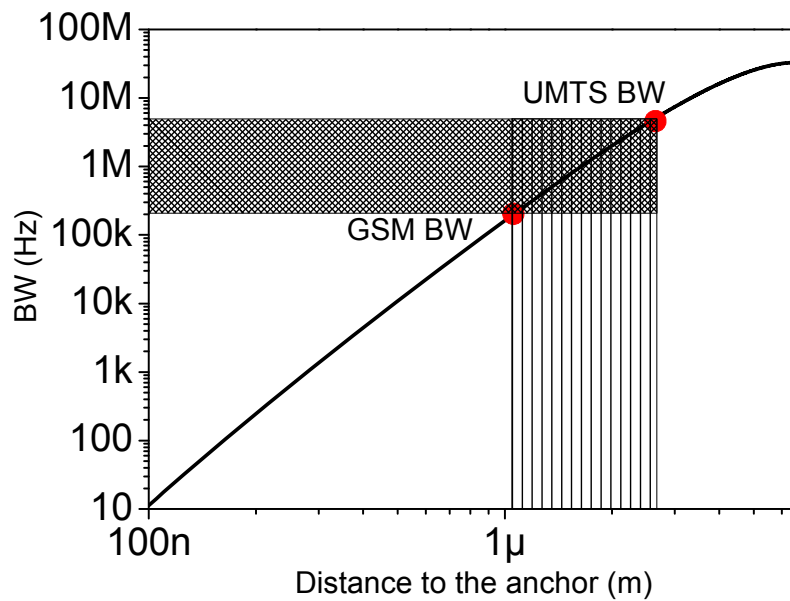
Figure 4.39 Selection of the coupling point over the CC-beam for the coupler with a $k_c=90N/m$

A FEM simulation (Coventor) of the proposed filter in Figure 4.40 shows that the in phase movement happens at lower frequency than the out-of-phase mode. This FEM simulation suggests that the electrical phase inversion should be applied to obtain the filter response.
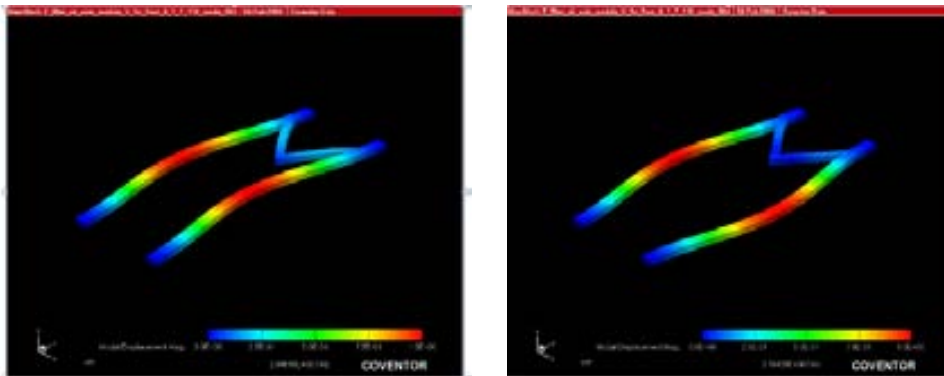
Figure 4.40. FEM simulation extracted from CoventorWare. The in phase mode take place at 21.9MHz while the out-of-phase mode is at 28.9MHz.

The fabricated resonator is shown in the SEM image in Figure 4.41. The Poly 1 is used to fabricate the movable part comprised by the two resonators and the V-shaped coupler. Driver and readout electrode are fabricated using the Poly 2. The gap between the two polysilicon layers is 100nm.
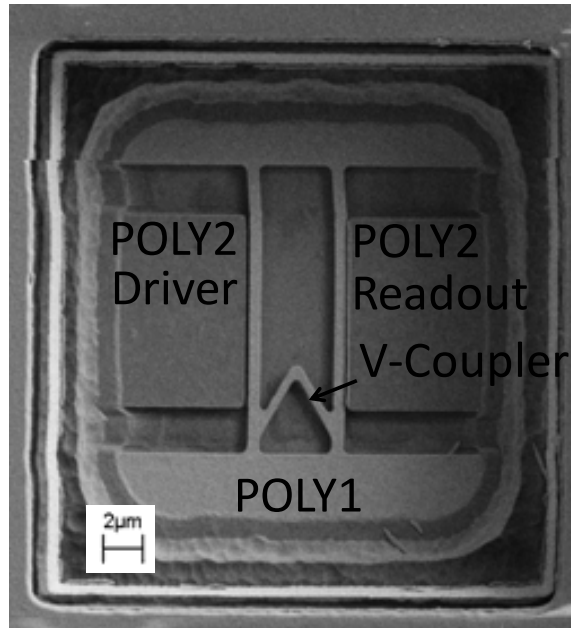
Figure 4.41. SEM image of the V-filter. The gap between the movable part and the driver and readout electrode is designed at 100nm. The angle of the V corner is 70º and is couplet at 1 um from the anchor.

In Table 4.4 A summary of the designed and fabricated dimensions is shown

Table 4.4 Designed and fabricated dimensions

| Dimension	Layout	Fabricated
Length, L	13.2μm	13.2μm
Width, W	500nm	600nm
g	100nm	110nm
L_v	3μm	3.5μm
angle	70º	62.5º
Coupler Width, Ws	350nm	415nm
Coupling point	1μm	2 μm
fc	25MHz	29MHz μm
BW	200kHz	2MHz

4.4.3.3 ELECTRICAL CHARACTERIZATION OF THE V-FILTER

The characterization set-up is detailed in Figure 4.42. The set-up corresponds to the two-port measurement. It has been carried out using a Cascade probe station, DC sources and the E5100A network analyzer. The time dependent voltage is applied over the input electrode. In order to read the motional current in the output electrode, a bias voltage is applied over the movable part, V_p.. The motional current is read at the readout.
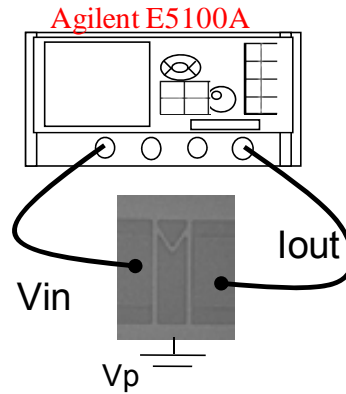
Figure 4.42 Set up for the direct measurement in air conditions of the V-Filter. The Bias voltage is applied directly over the structure, the AC signal is pumped into the resonator through the input electrode, and the motional current is read at the output electrode

In Figure 4.43 magnitude (a) and phase (b) are represented for different biasing voltages. The global response of the filter is not a bandpass filter response but a stop band filter. The phase measurement shows the in phase mode at lower frequency than the output of phase mode.

a)
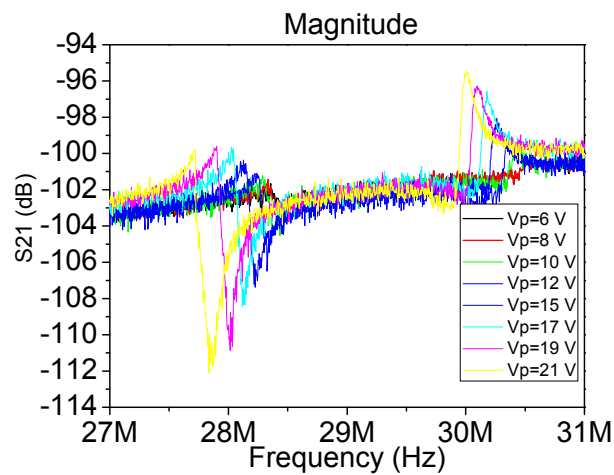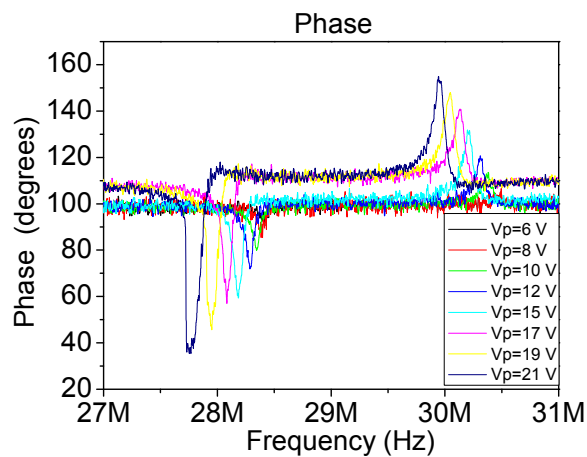
Figure 4.43 Electrical characterization of the V-. Magnitude (a) and phase (b) are shown for different bias voltages. The frequency of the in-phase mode is 28.2MHz while for the out-of-phase mode is 30.1MHz.

In this part the use external electrical phase inversion has been applied to obtain the filter like. The set-up for this measurement is presented in Figure 4.44. By means of the proper polarization of the ports, it is possible to obtain the phase inversion and obtaining the response shown in Figure 4.45. The measured filter is centered at 29MHz and presents an unexpected bandwidth of almost 2MHz.
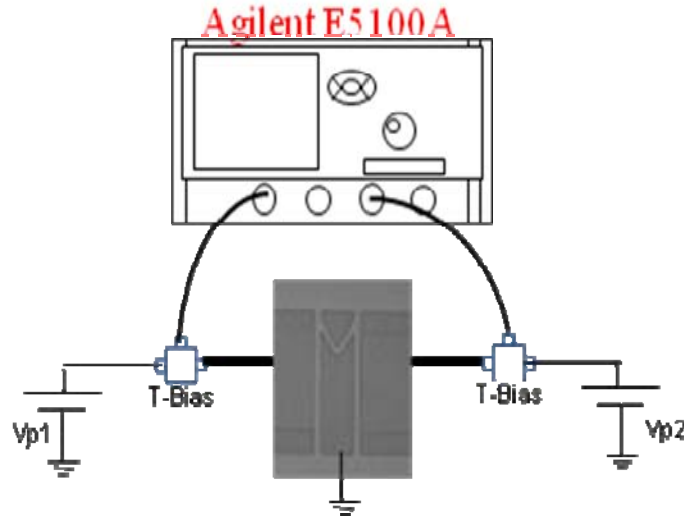
Figure 4.44. Set-up for the phase inversion measurements. Two T-bias are used to polarize the input electrode (V_{p1}) and the output electrode (V_{p2}).
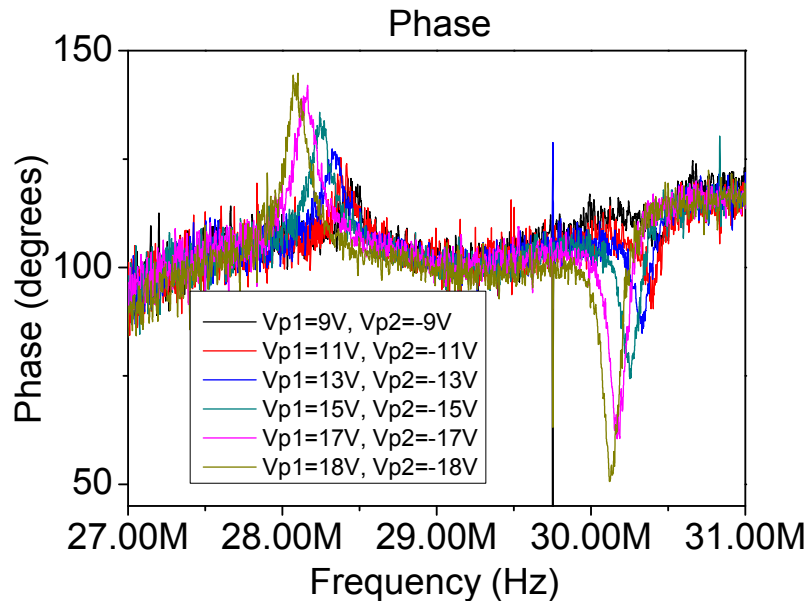
b)

Figure 4.45 Response of the filter using the set-up depicted in Figure 4.44. The electrical phase inversion has been applied.

4.4.3.4 DISCUSSION OF THE RESULTS

The bandwidth of the V-Filter measured presents an unexpected 2MHz bandwidth. In addition, the center frequency is shifted up to 29Mhz. That unexpected increment in the bandwidth is ascribable to the variation in the fabricated coupler dimensions and coupling point respect the designed ones. In the following paragraph we propose possible causes for the frequency and bandwidth variation.

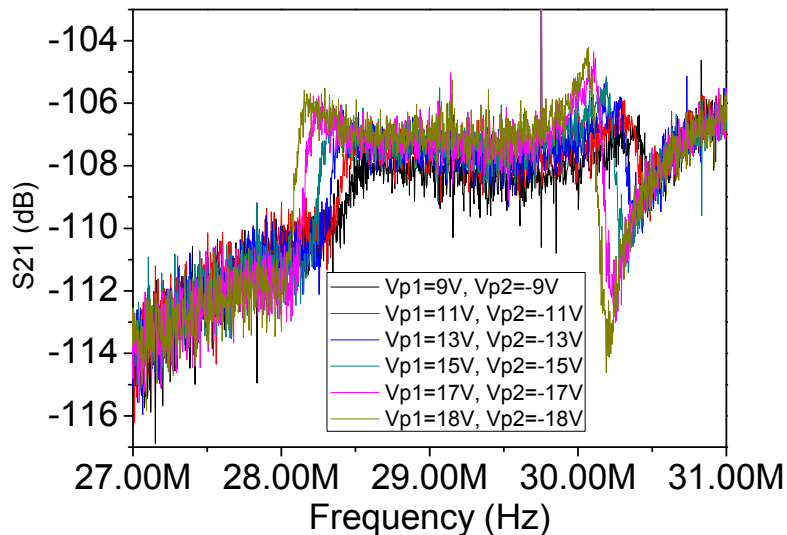According with the theoretical BW, the 2MHz bandwidth is achieved if the coupler is placed at almost 2µm from the anchors. In Figure 4.46, the SEM images of the filter are shown. Figure 4.46 a) shows a detail of the coupling interface between the coupler and the resonator. The intersection between the axial center of one of the coupler arms is located at the coupling point CP1, that is located at 1µm from the anchor. However, due to the fabrication process tolerances the coupling point becomes a large coupling area (not a coupling point). One of the ends of the coupling area is placed at 2µm away from the anchors. On the other hand, straight corners are very difficult to achieve in the CMOS technology, which tends to round all the angles. It may be observed in Figure 4.39 that a large variation on the coupling point may produce a bandwidth variation from 200kHz to 1MHz

The increment on the minimum coupler width, from 350nm to 415nm, is directly related with the stiffness constant, that changes from 53N/m to 90N/m that affects the bandwidth of the filter too. A wider beam has a higher moment of inertia and therefore a higher stiffness. As wide the coupler is higher the larger the bandwidth is.

In Figure 4.46 b a 62.5º angle is shown, that is lower that the designed angle (designed at 70º). The angle reduction implies a decrement on the minimum bandwidth achievable. That could compensate the increasing produced by the coupling point variation.

138

In order to explain the increment in the working frequency it is necessary to go to the dimensions of the resonators. In that case, the length of the beam is the same that the expected one. Nevertheless, there is an increment in the width of the resonator of more than a 20%. The resonators were designed to be 500nm and the fabricated width is 600nm as it can be seen in Figure 4.46 c)

a)

b)

c)
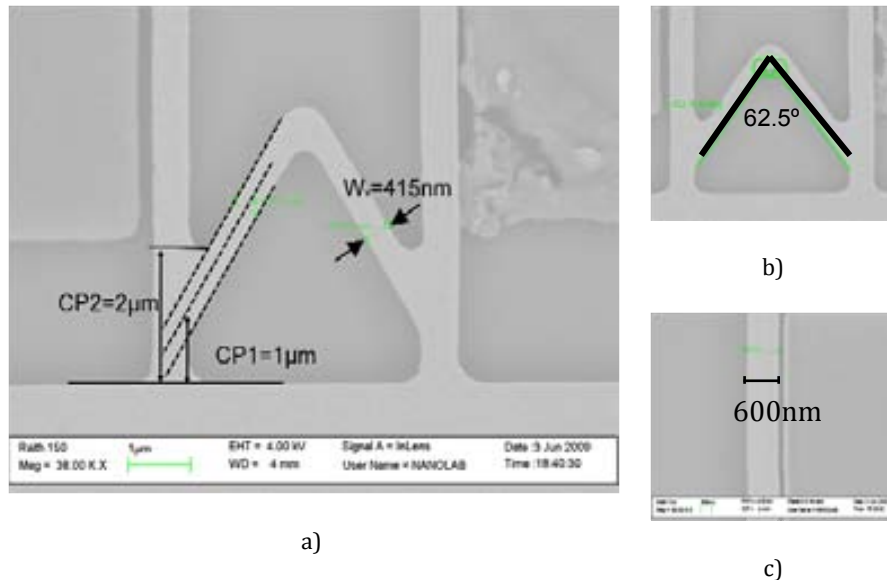
Figure 4.46 SEM Image of the filter with the measurements of the physical dimensions for the coupling for the axe of the coupler and the real coupling point of the fabricated one a). Real angle after the fabrication b), width of the resonator c)

In Table 4.4 a summary of the designed and fabricated dimensions is shown. As a conclusion, the V-coupler, due mainly to the joint angle between the resonator and the coupler, is much more susceptible to the fabrication tolerances.

4.5 ELECTROSTATICAL COUPLED MEMS-CMOS RESONATOR FILTER

The mechanical coupled resonator filters studied in section 4.4 have shown very good performances when working as channel filters. However, bandwidth of the filter is susceptible to the fabrication tolerances since the mechanical coupling issues determine the bandwidth of the filter. In this section, the electrostatical-coupled resonator filter is presented as an alternative to solve this problem. The electrostatical coupler resonator filters do not have any physical coupling elements that can be affects by the fabrication tolerances. In addition, the electrostatic link can be modified after the fabrication by means of the application of different voltages at both sides of the link. Since the coupler will determine the bandwidth it can be tuned by these voltages.

4.5.1 ELECTROSTATIC COUPLING FUNDAMENTALS

Figure 4.47a) shows the diagram of an electrostatic coupled filter with two beams. The electrode and the independent voltage sources are shown in the graph. The electrostatic coupled resonator filters are based on the same C-C beam resonators that have been used

to implement the mechanical filter. The two close resonators are electrostatically coupled by means of the different potential between them. Figure 4.47 b), shows detail of the gaps to identify them in the following paragraphs. If the first lateral mechanical mode is considered, Figure 4.48 shows a diagram of two resonators with length *L.* As it has been seen in previous section, the coupler plays a role in the out-of phase mode, while in the in-phase mode the coupler presence is quasi neglected. In order to consider the electrostatical coupling effect both resonators are considered to move in its out-of-phase mode. In this case, the electrostatic coupling is modeled by differential springs distributed along the beam (red rectangles in Figure 4.48).

a)

b)

Figure 4.47 a) Diagram of an electrostatic coupled filter. The independent voltage source bias the electrode and the beams. B) detail and nomenclature of the three different gaps

If the resonator is divided into small parts of length *dy* (see Figure 4.48), the electrostatic force between each one of these parts is modeled graphically as springs and mathematically by means of expression (4.41)

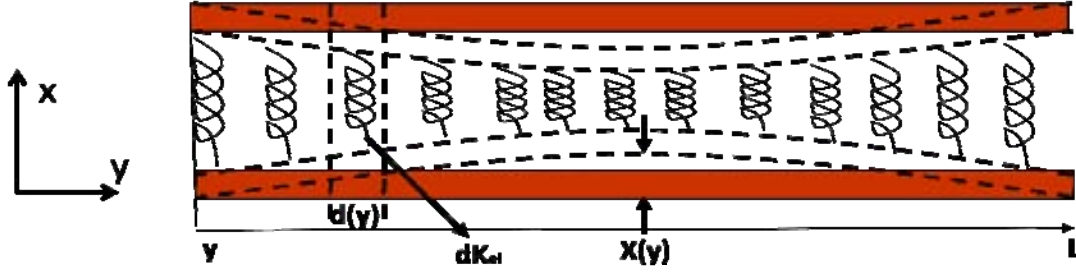$$df = \frac{\partial dWc}{\partial x} = \frac{1}{2}(\Delta V_p)^2 \frac{\partial dC}{\partial x} \qquad (4.41)$$

Figure 4.48. Scheme of the division of the two CC-Beams into small part of length *dy*. The spring models the electrostatic force between all the parts.

where *df* is the electrostatic force between two parts, *dWc* is the total energy stored in the "small capacitor", *x* is the total displacement of the parallel plates towards each other, and ΔV_p is the voltage difference between the resonators (Vp_1-Vp_2, being V_1 the voltage applied to resonator and Vp_2 the voltage applied to the other resonator). Finally, *dC* is the capacitance between two segments. Each pair of parallel elements is considered as a capacitance. The gap changes with the resonant movement and this movement is considered smaller than the static gap between both parallel plates. The capacitance variation can be rewritten as:

$$\frac{\partial dC}{\partial x} \approx \frac{\partial dC_o}{s_c}\left(1+\frac{x}{s_c}\right)$$

(4.42)

where s_c is the static gap between the resonators and dC_o is the rest of the value of *dC*. Finally, the electrostatic force corresponds to (4.43):

$$df = \frac{1}{2}(\Delta V_p)^2 \frac{dC_o}{s_c}\left(1+\frac{x}{s_c}\right)$$

(4.43)

Regarding expression (4.43), the electrostatic force is always atractive between the resonators. On the other hand, the force applied by the mechanical stiffness of the resonators presents a 180º phase with the displacement. For that reason, the electrostatic stiffness is modeled as a negative stiffness between resonators and it is expressed as:

$$dK_e = -\frac{df}{\partial x} = -\frac{(\Delta V_p)^2 \varepsilon t dy}{s_c^3}$$

(4.44)

Where *t* is the thickness of the resonator and ε is the electrical permittivity of the surrounding material (air in our case).

The degree in which each element of the electrostatic stiffness can contribute to the frequency response depends inversely on the effective mechanical stiffness at certain location on the beam. The larger the effective mechanical stiffness is, the weaker the effect of the electrostatic stiffness on the resonator frequency is. Therefore:

$$dK_{e,eff} = X(y)^2 dK_e$$

(4.45)

Where the *X(y)* is the normalized mode shape function for the first flexural mode (more detail about the mode can be found in Chapter 2). In order to define the overall

effective electrostatic stiffness respect to the central position of the beam, the effective electrical stiffness at all points along the beam should be integrated.

$$K_{e,eff} = \int_0^L X(y)^2 dK_e = -\frac{\varepsilon t \left(\Delta V_p\right)^2}{s_c^3} \int_0^L X(y)^2 dy \qquad (4.46)$$

Expression (4.46) leads to expression (4.47) if it is calculated numerically for the first mechanical lateral mode.

$$K_{e,eff} = -0.39 \frac{\varepsilon t \left(\Delta V_p\right)^2}{s_c^3} L \qquad (4.47)$$

Expression (4.47) shows that the critic parameter is the gap between the resonators, s_c. Its cubic dependence will contribute to modify dramatically the coupling and therefore, the bandwidth. In addition, it has to be noted that the electrical stiffness is negative compared with the mechanical coupler stiffness. From expression (4.11) and (4.12), the out-of-phase mode will take place at lower frequencies than the in-phase mode. In Figure 4.49 the system level simulation response of an electrostatical coupled resonator filter is depicted. The out-of-phase mode is observed at lower frequency that the in-phase mode. f_0 is the resonant frequency of the stand alone resonator.

Figure 4.49. System Level Simulation result of the electrostatically coupled resonator filter.

4.5.2 DESIGN OF THE FILTER

The design flux is similar to the scheme followed for the mechanical filter. Again, in this case, the coupling is very strong limited by the technological process. The AMS 0.35μm do not allow fabricating any coupling gap between the resonators so that constrain is used as initial step for the electrostatic filter prototype design. Since the design rules imposed by the foundry are broken to obtain the structures different fabrication trial have been done to obtain the best prototype. They are explained in 4.5.3. The minimum gap is s_c=350nm between two Poly 1 C-C beam resonators. In addition, the same C-C beam

resonators that have been used in the mechanical coupled filter are used in the electrostatical coupled filter (*LxWxt=13.2µmx500nmx280nm*). Hence, the electrical stiffness between the resonators is a predefined parameter given by expression (4.48)

$$K_{e,eff} = \left(\Delta V_p \right)^2 2.97 \cdot 10^{-4}$$ (4.48)

The bandwidth of the filter can be calculated by means of expression (4.49).

$$BW = \frac{K_{e,eff}}{k_r} f_o$$ (4.49)

Where k_r is the mechanical stiffness at the resonator center.

Expressions (4.48) and (4.49) indicate the bandwidth achieved by the electrostatic coupled resonator filter can be, in theory, lower than the mechanic filter one. The bandwidth of both filters, mechanical coupled and electrostatic coupled, are strongly determined by the technology. However, the relation between the coupler and resonator stiffnesses in the electrostatic coupled filter allows narrower bandwidth to be achieved.

4.5.3 FABRICATION

Different electrostatic coupled filters have been fabricated in order to obtain the best gaps, widths, and layers configuration. In this section, the different prototypes used are briefly described and the final option adopted is presented.

Polysilicon 1 vs Polysilicon 2: towards the 40nm gap

As it was explained in the introduction chapter the CMOS-MEMS fabrication using commercial CMOS technologies has many advantages but a few disadvantages too. Since the design rules are often broken gaps, widths and the other dimensions can be perturbed depending on the fabrication tolerances.

In the electrostatic coupled resonator filter, the gaps between the resonators are one of the critical fabrication parameters. In order to achieve the narrowest possible gaps the spacer technique is used. This technique consists on the use the interpolysilicon oxide that is 40nm thick as a sacrificial layer between two polysilicon 1 and polysilicon 2 layers. The filter has been fabricated using a sequence of poly1 and poly 2 layers as shown in Figure 4.50. The first electrode was fabricated with Poly 1, the resonator 1 was made of Poly 2, its counterpart was fabricated using Poly1 and finally the last electrode was made of Poly2. The SEM images after the releasing process show a high dimension variability due to the fabrication tolerances. Although the resonators were designed to be 500nm wide the fabricated dimension for the Resonator 1 (Poly2 that is a conformal layer) is 360nm. The resonator 2 width is 560nm. The resonance frequencies of the resonator were theoretically too different and the prototype was discarded.
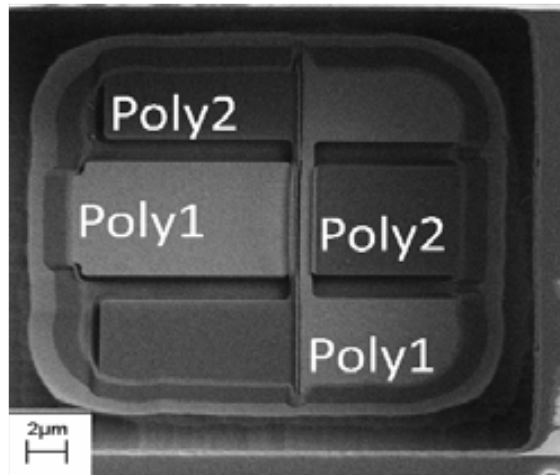
a)
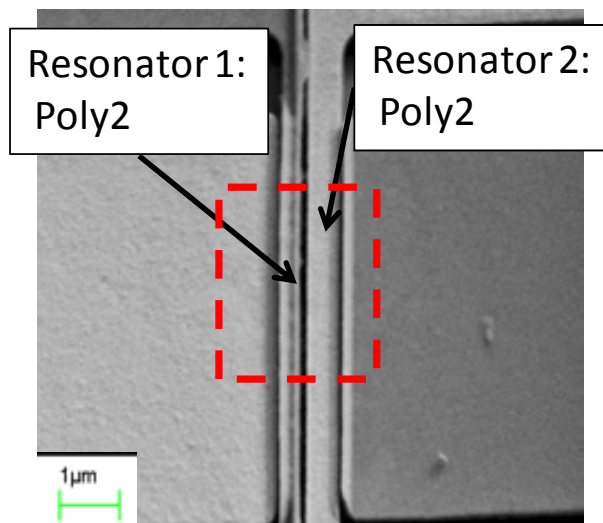
b)
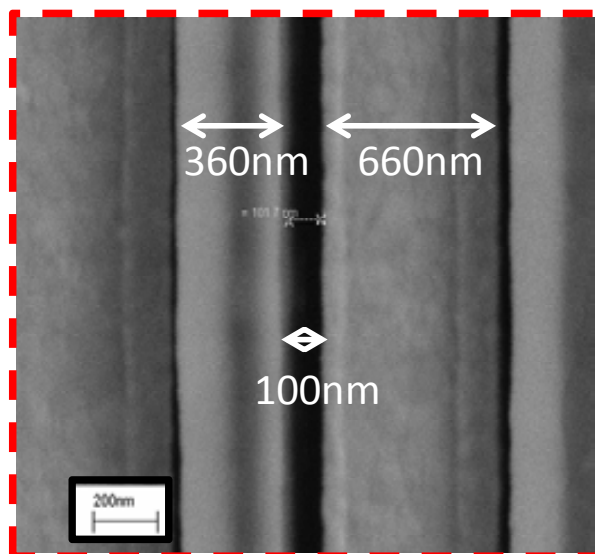
c)

Figure 4.50. SEM image of the 40nm gap electrostical coupled filter. a) tope view of the filter b) detail of the two resonators. c) Zoom of the inter-resonator gap.

Poly1 vs Poly1: 100nm gap

In order to relax the technological restriction and to avoid the use of the Poly 1 and poly 2 adjacent resonators, a second prototype was fabricated. In this case, both resonators were designed using the Poly 1 layer and the electrodes were fabricated using the Poly 2 layer. A 100nm gap between the resonators and the electrodes was designed. The same distance was designed between the two resonators.

Figure 4.51 shows a SEM micrograph of the fabricated filter. As it can be observed the inter-resonator gap has been suppressed due to the fabrication tolerances. Instead of two separated resonators, a "super" beam resonator has been fabricated between the two electrodes. The lack of the coupling gap caused the prototype to be discarded.
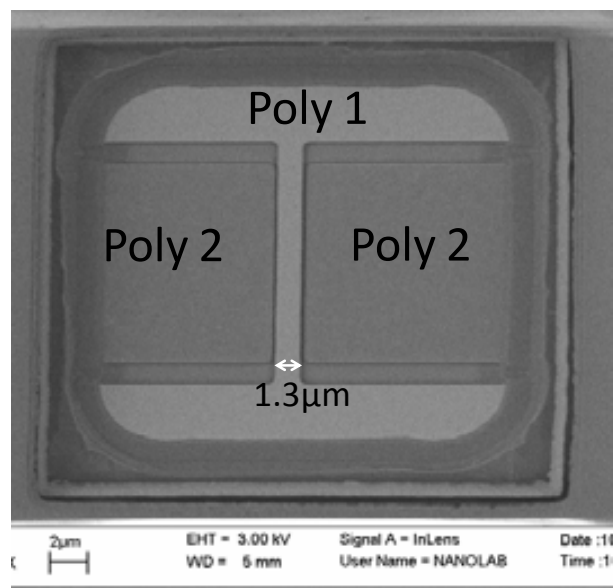
Figure 4.51. SEM image of the Poly1 vs Poly 1 electrostatically coupled resonator filter.

Poly1 vs Poly1: 350nm gap

From previous prototypes, the need for a secure margin between the two Poly 1 resonators was detected. In this case, a 350nm gap between them was designed. In addition, to keep the geometrical symmetry, both the resonators and the electrodes were fabricated using the same Poly 1 layer. For this reason, all the gaps of the prototype were designed to be 350nm. Figure 4.52 shows a SEM image of the fabricated electrically coupled resonator filter.
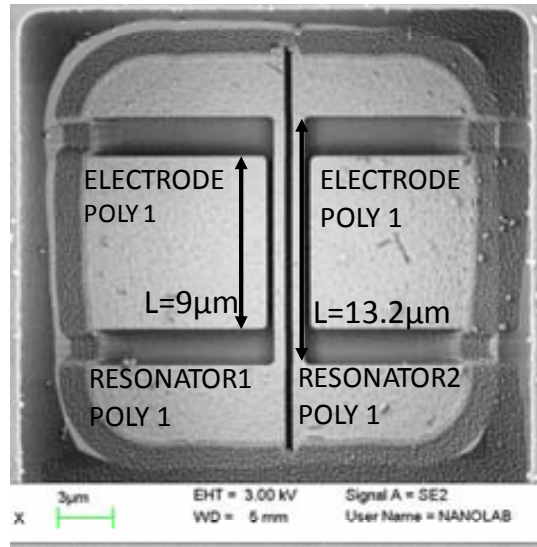
Figure 4.52 Scanning Electron Microscopy of the electrically coupled filter. The length of each beam is L=13.2μm, the wide of the electrode is $L_e=9\mu m$. Both the electrode and the beams are fabricated using the Poly 1 layer in order to keep the same coupling areas for all the gaps (350nm).

The second column in Table 4.5 shows the designed dimensions as well as the center frequency of the resonator under a 20V biasing voltage (V_{po}-V_{p1}= V_{p2}-V_{p3}=20V) and the bandwidth achievable as a function of the differential voltage between the resonators. It strongly emphasizes the bandwidth quadratic voltage dependence. The third column shows the physically measured dimensions after the fabrication. Note that an increment on the coupling gap has been measured between the resonators. The coupling level is affected directly by the fabrication tolerances.

Table 4.5. Summary of the designed and fabricated electrostatically coupled resonator filter.

Dimension	Layout	Fabricated
Length, L	13.2μm	14.3μm
Width, W	500nm	630nm
s	350nm	360nm
s_c	350nm	400nm
k_r	34.6N/m	50N/m
fo(20V)	22.5MHz	24MHz
k_{eff}	$(\Delta V_p)^2 \cdot 2.97 \cdot 10^{-4}$	$(\Delta V_p)^2 \cdot 9.7 \cdot 10^{-5}$
BW	193 $(\Delta V_p)^2 \cdot$	46.9$(\Delta V_p)^2$

4.5.4 ELECTRICAL CHARACTERIZATION

The electrical test of the electrically coupled resonator filter evolves different interesting issues. Four different contact pads allow the interconnection of the device with the DC sources and the network analyzer. As demonstrated in Chapter 3, the characterization set-up determines the performance of the MEM device. In this section, different measurement set-up possibilities are analyzed. The phase behavior of each one is explained using the electrical model.

Two topologies are proposed. On the one hand, the two-port configuration that consists on the excitation at the input electrode and read motional current at the output

electrode. On the other hand, one of the resonators is used to read the movement produced by an AC excitation signal applied to the further electrode.

4.5.4.1 INTERNAL ELECTRICAL PHASE INVERSION FOR THE TWO PORT SET-UP

The diagram of the two-port configuration is shown in Figure 4.53. The AC excitation voltage is applied to the input electrode. The output current is read at the out electrode. The movement of the first beam is transferred to the second beam due to the electrostatic coupling with the second beam.

Figure 4.53 Diagram of the electrostatically coupled resonator filter. In the figure the DC voltage applied to each port is shown as well as the AC source applied to the driver. The motional current is read at the readout.

In Figure 4.54 the equivalent electrical circuit is shown. The electrostatic coupling factor damping inductance and motional capacitance can be calculated using expressions (4.32)(4.33)(4.34)and (4.35). The dimension can be obtained from Table 4.5. C_{TH} corresponds to the feedthrough capacitance between the input electrode and the readout. The coupling capacitance is obtained by means of expression (4.50)

$$C_c = \frac{1}{K_{e,eff}} = -\frac{1}{0.39\frac{\varepsilon t \left(\Delta V_p\right)^2}{s_c^3}} \tag{4.50}$$

Note that the capacitance is negative.

The sign of the electromechanical coupling factor depends on $(V_{po}\text{-}V_{p1})$ for η_e and on-$(V_{p3}\text{-}V_{p2})$ on η_e'. The sign will determine the phase inversions.

Figure 4.54. Equivalent electrical circuit if the electrostatically coupled resonators filter.

4.5.4.2 READOUT AT THE SECOND RESONATOR.

In this set-up, (see Figure 4.55) the excitation AC voltage is applied on the driver. The four ports are biased and the second electrode is used only for applying a DC voltage. The motional current is read on the second resonator. The output current is the contribution of two terms: a) the current induced by the variation of the capacitance between the two resonator (for the out of phase mode) and between the second sensing resonator and the electrode and b) the current induced by the variation of the capacitance between the electrode and the resonator (in the in-phase mode). For this characterization set-up, the equivalent circuit of the two mechanical modes is obtained and the currents contributions are analyzed.

Figure 4.55. Diagram of the set-up that uses the second resonator to read the motional current

Analysis of the In-Phase Mode

The equivalent circuit for the in-phase mode is redrawn in Figure 4.56 a). Since the inter-resonator gap remains constant, if the resonator movement is considered perfectly symmetric, the current gain between them is $\phi_{21}=0$. The feedthrough current is modeled by a capacitance from the input electrode, to the second resonator, where the load resistance is placed. Both the motional current and the feedthrough current are added in the load resistance for the in phase mode as is shown in expression (4.51)

$$I_{oi} = I_{FT} + \phi_{31}I_{M1} \tag{4.51}$$

Since the inter resonator capacitance does not change in the in phase mode, only the input and output capacitance vary. The variation relation is illustrated in (4.52)

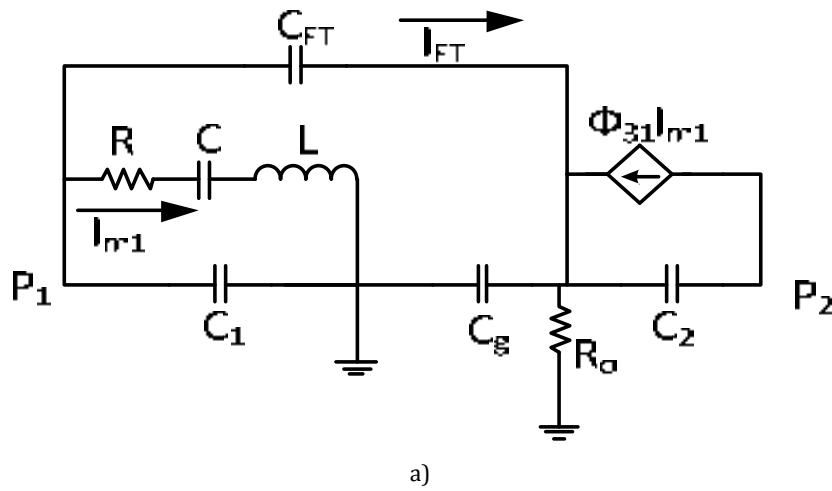$$\frac{\partial C_1}{\partial x} = -\frac{\partial C_2}{\partial x} \tag{4.52}$$

The electromechanical coupling factors for the two gaps are:

$$\eta_1 = \left(V_{po} - V_{p1}\right)\frac{\partial C_1}{\partial x} \tag{4.53}$$

$$\eta_3 = \left(V_{p3} - V_{p2}\right)\frac{\partial C_2}{\partial x} \tag{4.54}$$

The corresponding current gain is the output gap is.

$$\phi_{31} = \frac{\eta_3}{\eta_1} \tag{4.55}$$

a)
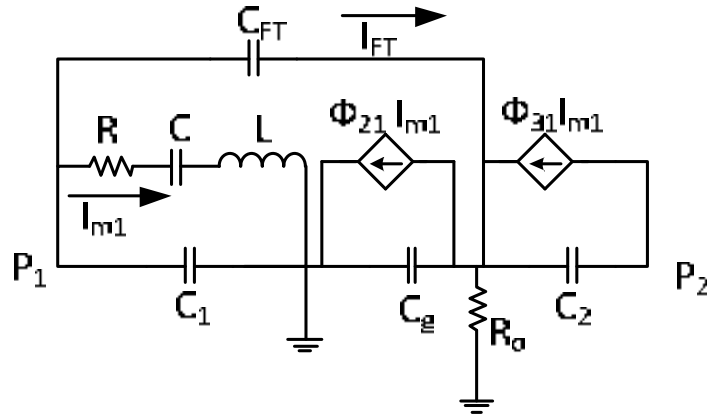
b)

Figure 4.56. Equivalent electrical circuit for the in-phase (a) and out-of-phase mode (b). the excitation is applied n the driver and the other electrode is used only to applied bias voltage. Both diagrams include the feed through current, C_{TH}

For the in-phase mode the relation between voltages, coupling factors and current gains are summarized in Table 4.6. Since the feedthrough current travels from the driver, P_1, to the second resonator the phase inversion takes place if the current gain is $\phi_{31}=-1$.

Table 4.6. Summary of the coupling factor and current gain for the in-phase mode of the electrostatic coupled resonator filter sensing at the second electrode.

Voltages	Electromechanical coupling factors	Current gain
$(V_{po}-V_{p1})=-(V_{p3}-V_{p2})$	$\eta_1=\eta_3$	$\phi_{31}=1$
$(V_{po}-V_{p1})=(V_{p3}-V_{p2})$	$\eta_1=-\eta_3$	$\phi_{31}=-1$

Analysis of the In-Phase Mode

For the out-of-phase mode (see Figure 4.56 b)) the three gaps have to be taken onto account. In this case, the capacitance between the two resonator changes in time since the movement of the two resonator is 180º shifted. They are getting closer and farther at the same time. The load capacitance will collect the current provided by gap 2 variation capacitance, the current due to the variation of the second electrode to second resonator capacitance and the feedthrough capacitance as illustrated in expression (4.56)

$$I_{out} = I_{FT} - \phi_{21}I_{M1} + \phi_{31}I_{M1} \qquad (4.56)$$

The variation for the each gap capacitance is illustrated in expressions (4.57) and (4.58):

$$\frac{\partial C_1}{\partial x} = -\frac{\partial C_g}{\partial x} \qquad (4.57)$$

$$\frac{\partial C_1}{\partial x} = \frac{\partial C_2}{\partial x} \qquad (4.58)$$

The electromechanical coupling factor for each gap are described by means of expressions (4.59), (4.60) and (4.61):

$$\eta_1 = \left(V_{po} - V_{p1}\right)\frac{\partial C_1}{\partial x} \tag{4.59}$$

$$\eta_2 = \left(V_{p2} - V_{p1}\right)\frac{\partial C_g}{\partial x} \tag{4.60}$$

$$\eta_3 = \left(V_{p3} - V_{p2}\right)\frac{\partial C_2}{\partial x} \tag{4.61}$$

The current gains for each gap are:

$$\phi_{21} = \frac{\eta_2}{\eta_1} \tag{4.62}$$

$$\phi_{31} = \frac{\eta_3}{\eta_1} \tag{4.63}$$

The out-of-phase mode current gains relation is summarized in Table 4.6. The first column corresponds to the voltage condition applied to the excitation electrode and the two resonators. This voltage is the voltage applied in gaps 1 and 2. The electromechanical coupling factors for the two gaps, η_1 and η_2 are shown in the third column. The relation of the voltages applied in gaps 1 and 3 are shown in the second columns. The second term in the third column shows the relation between its corresponding electromechanical coupling factors. The last column corresponds to the current gain for each gap.

Table 4.7. Summary of the coupling factor and current gain for the out-of-phase mode of the electrostatic coupled resonator filter sensing at the second electrode.

Voltages, Gap 1 and 2	Voltages Gap 1 and 3	Electromechanical coupling factors	Current gain
$(V_{po}\text{-}V_{p1})=(V_{p2}\text{-}V_{p1})$	$(V_{po}\text{-}V_{p1})=(V_{p3}\text{-}V_{p2})$	$\eta_1=\text{-}\eta_2, \eta_1=\eta_3$	$\phi_{21}=-1\ \phi_{31}=1$
	$(V_{po}\text{-}V_{p1})=\text{-}(V_{p3}\text{-}V_{p2})$	$\eta_1=\text{-}\eta_2, \eta_1=\text{-}\eta_3$	$\phi_{21}=-1\ \phi_{31}=-1$
$(V_{po}\text{-}V_{p1})=\text{-}(V_{p2}\text{-}V_{p1})$	$(V_{po}\text{-}V_{p1})=(V_{p3}\text{-}V_{p2})$	$\eta_1=\text{-}\eta_2, \eta_1=\eta_3$	$\phi_{21}=1\ \phi_{31}=1$
	$(V_{po}\text{-}V_{p1})=\text{-}(V_{p3}\text{-}V_{p2})$	$\eta_1=\text{-}\eta_2, \eta_1=\text{-}\eta_3$	$\phi_{21}=1\ \phi_{31}=-1$

The main difference between the two characterization set-ups of the electrostatic coupled resonator filter is the control of the phase in the first and second resonant mode independently. Figure 4.57 and Figure 4.58 show the magnitude and phase of the simulated frequency response of the electrostatical coupled resonator system under all the voltage combination that have been shown in Table 4.7. The filter response is obtained in the red line in Figure 4.57. The voltage applied in this case are: $(V_{po}\text{-}V_{p1})=\text{-}(V_{p2}\text{-}V_{p1})$ and $(V_{po}\text{-}V_{p1})=\text{-}(V_{p3}\text{-}V_{p2})$
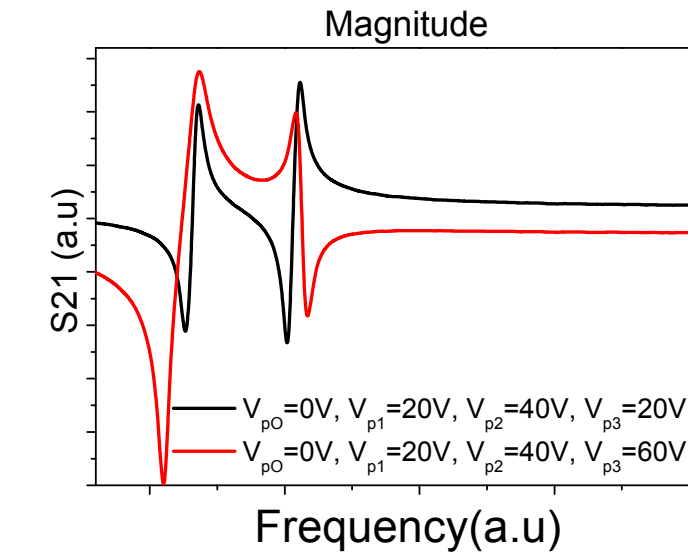
a)
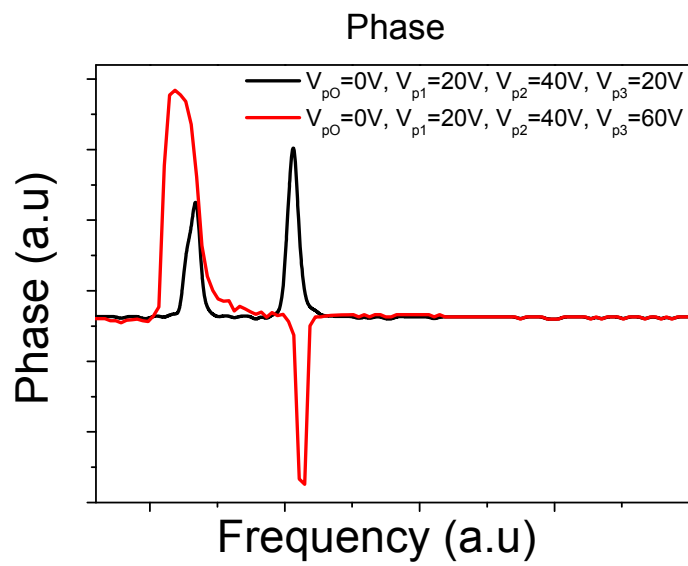
b)

Figure 4.57. Magnitude and phase of the frequency response of the electrostatically coupled resonator system sense at the resonator 2. The out-of phase mode is constant and the in-phase mode is phase inverted.

a)

b)
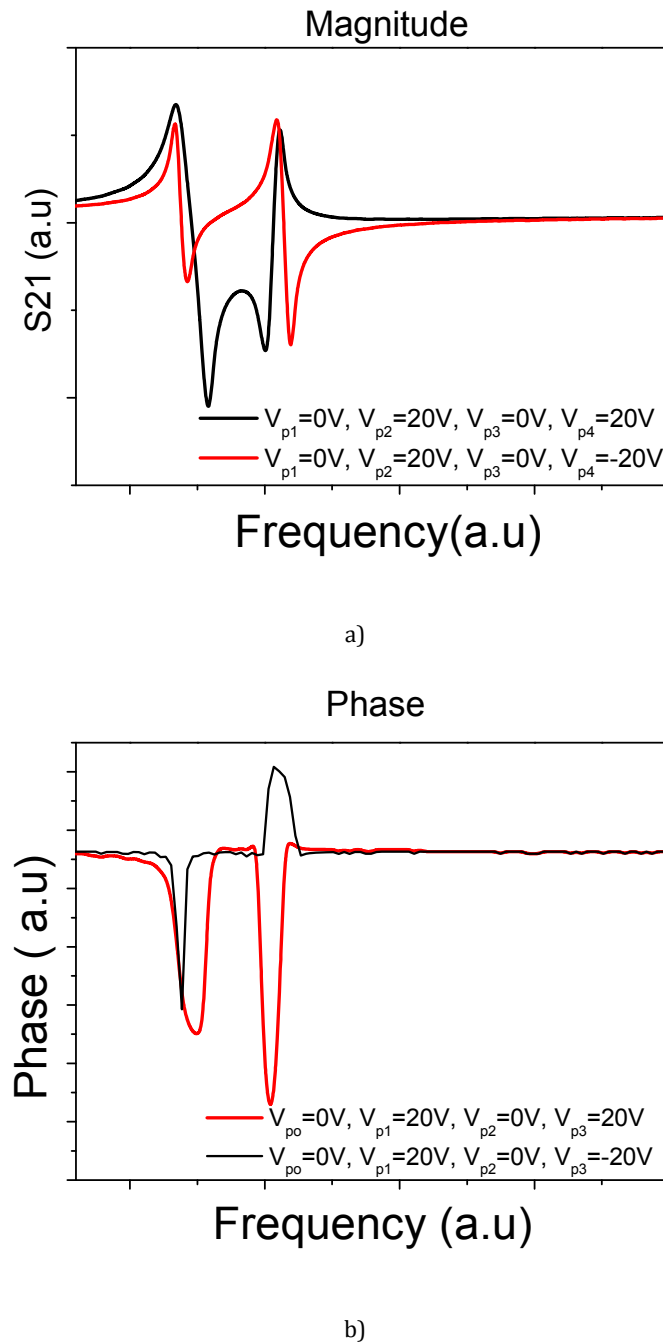
Figure 4.58. Magnitude and phase of the frequency response of the electrostatically coupled resonator system sense at resonator 2. The in-phase mode is constant and the out-of-phase mode is phase inverted.

4.5.4.3 CHARACTERIZATION

In the characterization stage of this coupled filter two main problems have arisen:

On one hand the measurement on the readout electrode has not been achieved probably because the motional current received is lower than the feedthrough and only the feedthrough coupling is detected.

On the other hand, if the readout is performed through the second resonator not all the combination of voltages desired could be implemented due to two important reasons. a) The voltage required to achieve the coupling between the two resonators is quiet large

due to the large gaps and small coupling areas. b) The large voltage difference required to obtain both the coupling and the internal electrical phase inversion usually breaks the sacrificial oxide located under the anchors or electrode burning the polysilicon and destroying the device.

In Figure 4.59 the measured frequency response of the electrostatically coupled resonator system is shown. The measurement has been performed over the second electrode The biasing condition, set at $(V_{po}-V_{p1})=-(V_{p2}-V_{p1})$ and $(V_{po}-V_{p1})=-(V_{p3}-V_{p2})$, ensures the filter response. Note that the first mode, known as the out of phase mode is phase inverted and the in-phase mode is non inverted.

The bandwidth varies from 90KHz to 197KHz using voltage difference between the resonator from 23V to 40V. Note that the center frequency is fixed at 22.54MHz for all the voltage range.
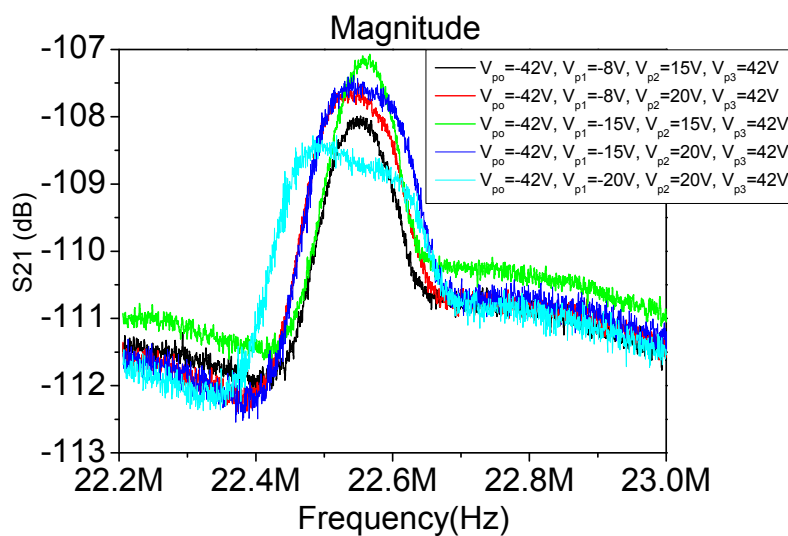
a)
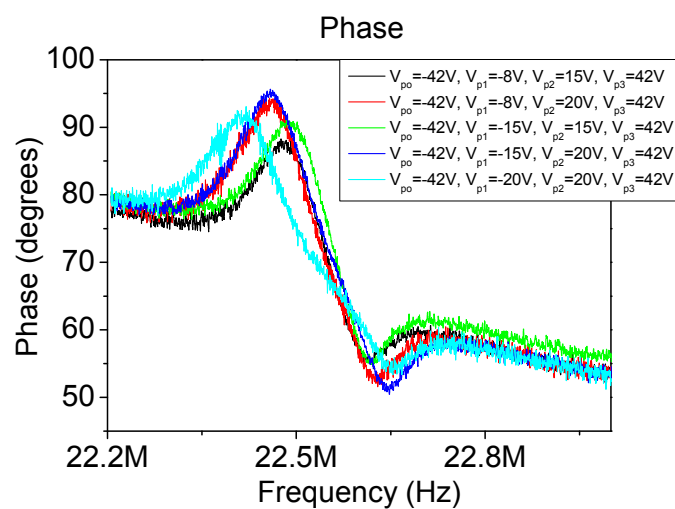
b)

Figure 4.59 Measured magnitude and phase of the electrostatically coupled resonator system measured on the resonator 2. The biasing condition produces a filter like response.

4.5.5 CONCLUSIONS AND RESULTS DISCUSSION

In this section the design, simulation, fabrication, and characterization an electrostatic coupled resonator filter have been presented. This sort of filters require narrow gaps in order to obtain strong coupling and the large bandwidth tenability. However, as it has been shown in the fabrication part of this section the technological constraint difficult this goal. Different approaches have been tried and the best option is the use of polysilicon 1 to fabricate both resonators and the electrodes separated by 350nm gap. Finally a band pass filter centered at 22.5MHz with an independently tunable bandwidth has been achieved.

4.6 PARALLEL FILTERING

As commented in the introduction the parallel filter offers a different approach to obtain band pass filter. The principle of operation consists on the addition of the electrical signal provided by two or more parallel connected resonators.

In this section a review of the work presented by J. Lopez in [22]. In that case two C-C beam resonators were coupled electrically by means of a CMOS differential amplifier. The advantages of that kind of integration are:

1) The increment of the output signal and thus, the decrement of the losses due to the impedance mismatching.

2) The differential configuration allows eliminating the effect of the parasitic capacitance if both resonators are physically similar

The signals supplied for the two C-C Beam resonators are subtracted and amplified by the differential stage. If the two resonators are working at different frequencies of resonance, both resonant peaks will be amplified at the output. Furthermore, the two parasitic currents will be subtracted, therefore the filter roll off will be increased. But not only the Q of the filter is increased but the stop band rejection will also be increased.

The objective of this design is to obtain and enhancement respect the filter achieved in [22]. To do that a reduction of the gap is introduced (from 150 to 100nm). In addition in the aforementioned filter the beam were fabricated using the minimum dimensions of the technology, therefore, in the new prototype the width has been increased up to 500nm to ensure a lower variation on the fabricated dimensions.

4.6.1 DESIGN

Figure 4.60 shows the optical image and a SEM detail of the resonator of the filter. The resonator dimensions used in his works are summarized in Table 4.8. The third column of the table shows the dimensions used in our new design. The resonator are the same that has been used in the series filters (electrostatic coupled and mechanical coupled)
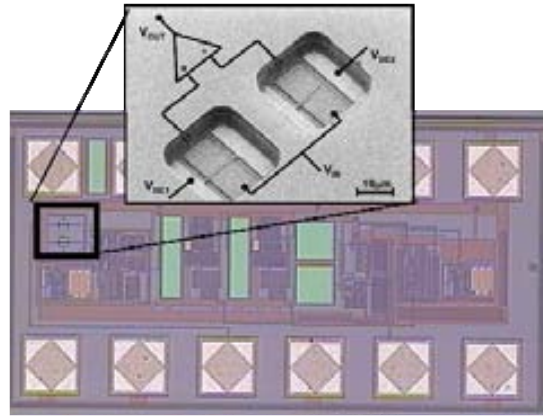
Figure 4.60 Optical image and the SEM image of the fully integrated filter based on two electrically coupled CC beam resonator [93]

Table 4.8 Summary of the dimensions and performances of the filter in [22, 93] and in the present reviewed work

Parameter	[22, 93]	This Work
Length	13μm	14μm
Width	350nm	500nm
Gap	150nm	100nm
Q res	220	270
f0	22MHz	23MHz
BW filter	200kHz	180khz
SF20dB	2.97	2.89
SF40dB	-	12.83
SBrej	30dB	42dB

4.6.2 CHARACTERIZATION

The filter has been fabricated using the same principle as in [22]. The circuitry and the mechanical devices are sharing the same die. Both resonators share the same input pad (V_{in} and V_3). However, they have two independents DC bias pads available that allows the enable or disable any resonator independently (V_1 and V_2). Each C-C beam is connected to the positive and inverter amplifier inputs respectively.

Figure 4.62 shows the magnitude of the two resonators separately. In order to obtain the magnitude of Resonator 1 (Black line) a bias voltage is applied over the structure and then the motional current produced by the movement induced by an AC voltage applied in the input electrode is read while the bias voltage over Resonator 2 is 0V. Summarizing, Resonator 1 is ON and Resonator 2 is OFF. Otherwise, the differential amplifier subtracts the capacitance current provided by the two resonators that is always present at the outputs. To obtain the magnitude of Resonator 2 the inverse process is applied: Resonator 2 is enabled by means of the DC voltage application and Resonator 1 is OFF. The Q for Resonators 1 and 2 are 273 and 260 for 18 and 17V respectively. The working frequencies for the resonators are 23.101MHz and 22.949MHz
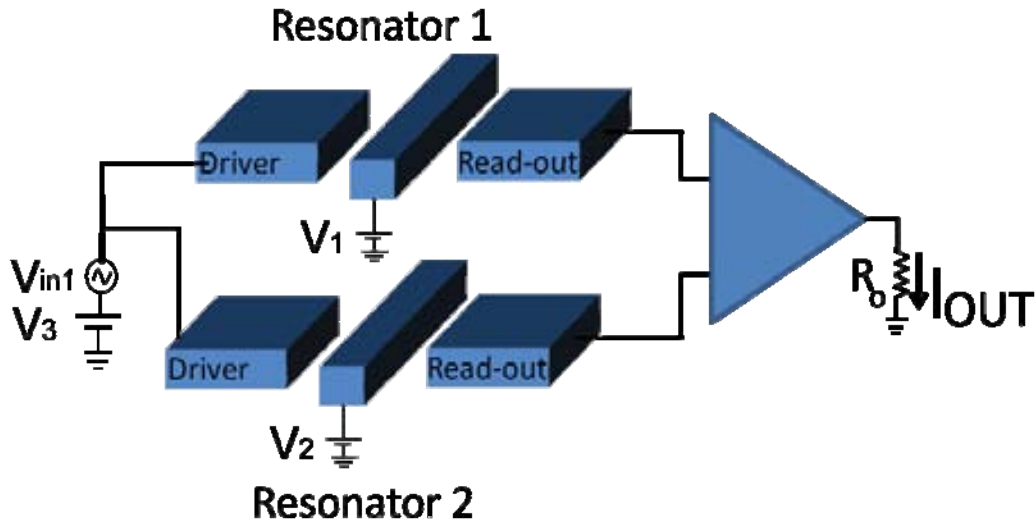
Figure 4.61 Diagram of the characterization set-up.
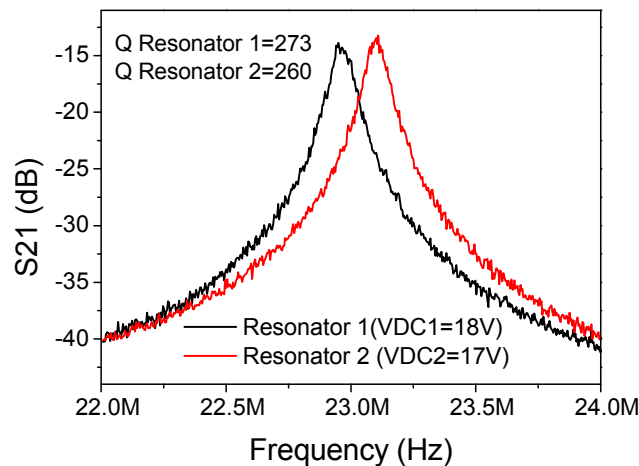
Figure 4.62 Magnitude of the resonance for the two resonator separately. The Q is obtained for different values of biasing voltage.

In Figure 4.63 the electrical characterization of the two resonators working together as a filter is shown. The resonators have been biased at 16V and 17V respectively. An impressive frequency response has been obtained at the amplifier output. The insertion losses have been reduced to 10dB compared with the stand alone series filter measured in the previous section. A 180kHz bandwidth has been measured at 23.2MHz center frequency. Due the feedthrough current subtraction the filter presents a very high out of band rejection of around 42dB and the selectivity, which is illustrated by the shape factor at 20dB is 2.89.

The phase inversion mechanisms used in the series filter and in the stand-alone resonantor to control the relation between the feedthrough and motional current may be used in the parallel filter to control the position of the antiresonance valley. Figure 4.64 shows the electrical measurement of the filter. A DC voltage of 23V has been applied at the input electrode of both resonator and the same DC voltages have been applied at the movable bodies. The phase inversion is observed in the two resonant and the

157

antirresonance peak of the filter appears at lower frequencies than the bandpass. Note the antiresonance peak is observed at right of the bandpass filter in Figure 4.63
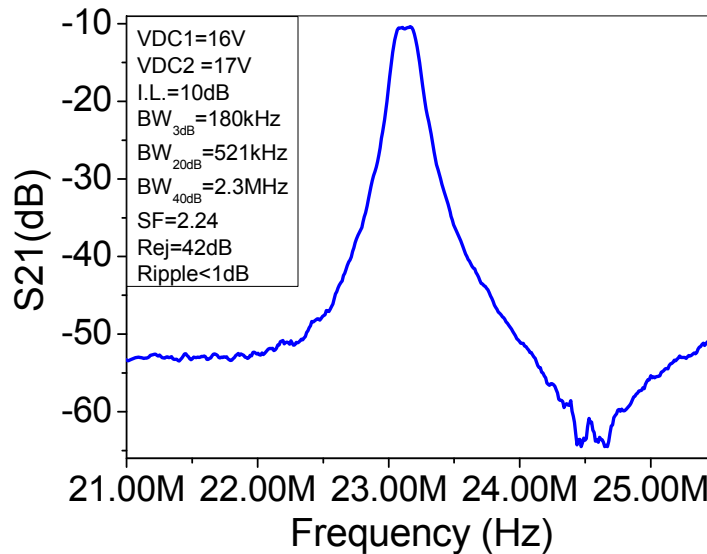
Figure 4.63 Response of the filer for voltages of 16V and 17V for Resonator 1 and Resonator 2.
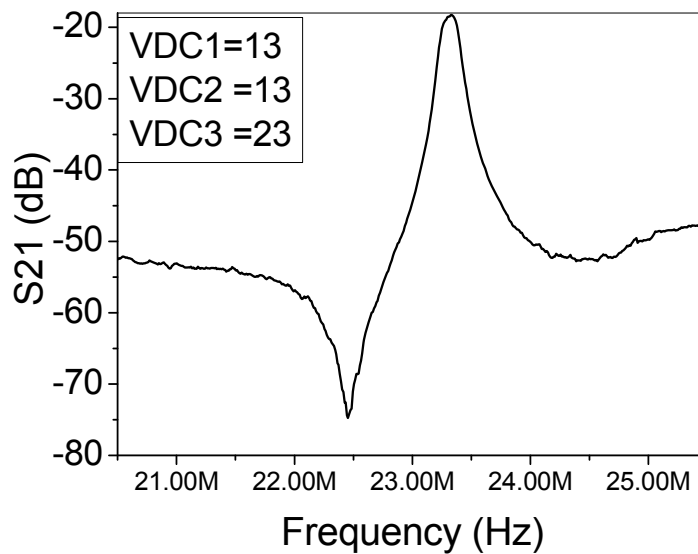
Figure 4.64 Response of the filter for different biasing voltages. The objective has been to change the position of the notches due to the subtraction of the motional current provided by each resonator. The biasing voltage of the two resonators is 13V while a biasing voltage of *Vdc3=23V* is applied on the input electrode by means of bias T

4.6.3 CONCLUSIONS

The parallel filter presented in this work improves the performance of its antecessor [22] in terms of shape factor and out of band rejection as observed in Table 4.8. However, the bandwidth can not be fixed in the mechanical design stage since it depends on the

voltage applied and the tolerances of fabrication. Compared with the previous work the phase inversion has allow to control the position of the notch.

4.7 TWO MECHANICAL FILTERS ELECTRICALLY COUPLED.

In this section, we present a combination of parallel and series filter. The proposed filter topology is composed of two CMOS-MEMS band pass filters (as the ones in [94]) mechanically coupled and a differential amplifier. Both filters are connected in parallel through the differential amplifier (see Figure 4.65 b)

4.7.1 DESIGN

The on chip amplifier configuration allows sensing and amplifying the output current obtained from each CMOS-MEMS filter by means of two transimpedance amplifiers (TIA), one for each filter. The two TIA outputs are then connected to the input of the differential amplification stage, which is basically a common source differential stage. It presents a differential gain of 87 dB and a CMRR of 40 dB. Therefore, the differential amplifier is intended to combine the two filters response, generating a dual band and to enhance the out-of band rejection, as it will be shown.
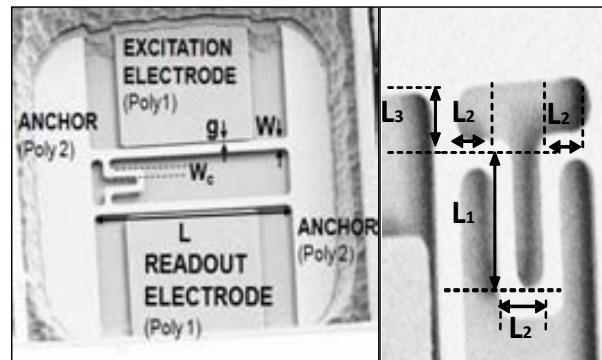
a)
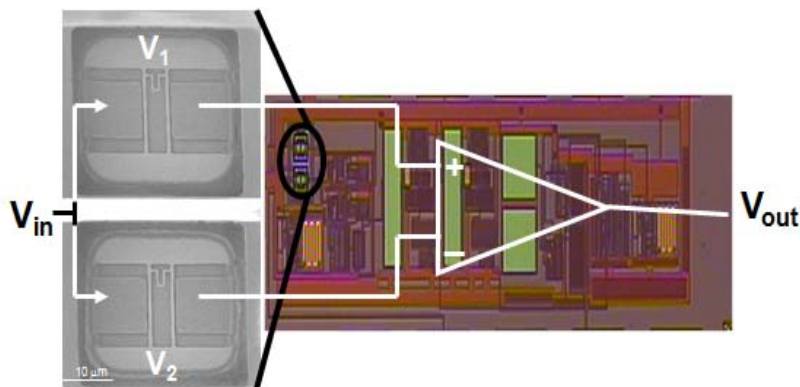
b)

Figure 4.65a). SEM image of an individual CMOS MEMS filter (left) along with a detail of the U shape coupler. Dimensions of the fabricated device: *g=130nm, W=600nm, L=13.2μm, W$_c$=400nm, L$_1$=2.4μm, L$_2$=1μm, L$_3$=1.2μm.* b) Optical image of the fully

Figure 4.65 shows a SEM image of an individual CMOS-MEMS filter along with a detail of the coupler with relevant dimensions. The MEMS structure is fabricated using the layers of the capacitance module of the AMS 0.35 μm CMOS technology. Poly 1 is used to implement the movable structure while poly 2 is used for both excitation and readout electrodes [54]. To allow a direct post-processing of the MEMS, a pad cut has been defined over the resonator area along with two vias (via3 and via2) that removes the inter metal oxide over the resonator. A mask less wet etching is performed to release the structure. The area under the defined window is exposed during a short period of time to a solution based on HF. Figure 4.65 b) shows the optical image of the fully integrated filter, composed of the mechanically coupled MEMS devices along with the CMOS circuit.

Each clamped-clamped beam has been designed with a resonant frequency of 27.5 MHz (f_o). This frequency corresponds to the in-phase mechanical mode. The out-of-phase resonant mode occurs at a higher frequency. The filter bandwidth (the frequency span between the two mechanical modes) is determined by the position of the coupler, L_3 in figure 1a [94].

4.7.2 MODELING

Figure 4.66shows the small equivalent electrical circuit of the dual filter, composed of two mechanical filters (FILTER 1 and FILTER2) with a differential amplifier. The electromechanical model was detailed in section 4.4. The values of the RCL parameters of the resonators correspond to the dumping, stiffness and mass that are obtained from the dimensions measured on the SEM image. A 220 quality factor has been used to compute the damping according to experimental results with same resonator value [22].
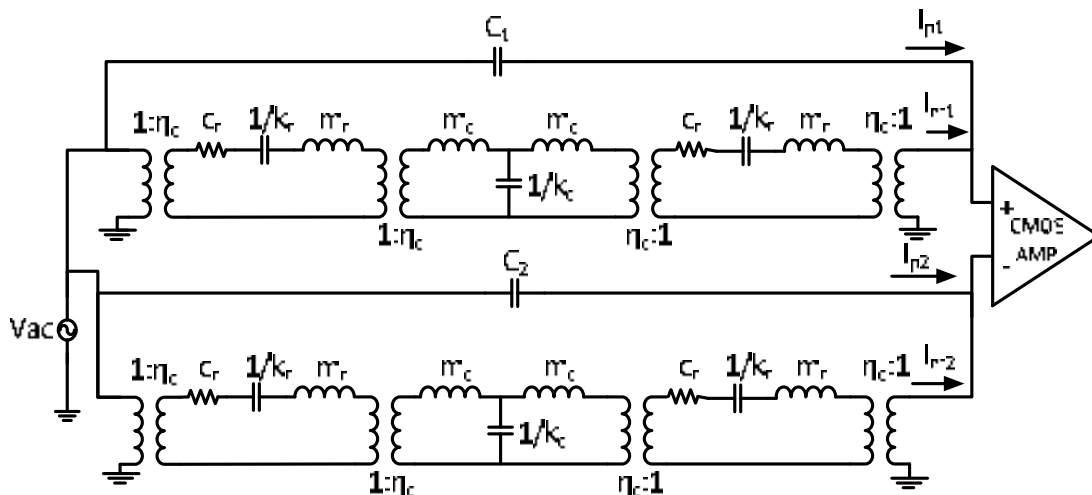
Figure 4.66. Electrical equivalent circuit of the two mechanical filters with a block diagram of the differential amplifier. Each C-C Beam resonator is modeled as a RLC branch while the U- coupler is modeled as a T-network (with two inductors, mc, and one capacitor, 1/k$_c$). The inductance, mc, has a value equivalent to half mass of the coupler.

The T network models the mechanical coupler, which is considered as a transmission line with less than λ/8 effective length [95]. The values of the inductances and, capacitance correspond to the mass of each arm with length L_1 (see Fig. 1a) and the stiffness of the coupler (m_c, $1/k_c$).The two η_c ratio transformers model the mechanical impedance transformation dependent of the coupling position. The expression for η_c is:

$$\eta_c = \sqrt{\frac{k_{ry=L_3}}{k_c}}$$

(4.64)

where $k_{ry=L3}$ corresponds to the stiffness constant of the clamped-clamped beam at the coupling point, L_3, and the k_c is the stiffness constant of the coupler [74]. Figure 4.67 shows the variation of the coupling transformer ratio with the coupling position (in red line) and the variation of the filter bandwidth [94]. The maximum relative bandwidth is achieved when the coupling position is located at the very center of the resonator. In this case, dimensions of the beam fix a maximum of 80% relative bandwidth.

Table 4.9 shows the nominal values for the main mechanical parameters of each c-c beam (damping, effective mass, spring constant, electromechanical coupling factor...). These values correspond to the main electrical parameters of the filter electrical model (resistance, inductance, capacitance...) Values of the parameters have been obtained using the dimensions shown in the SEM images and the expressions in [74]. A *160 GPa* Young modulus and a *2330 kg/m³* mass density have been considered for the Polysilicon layer.
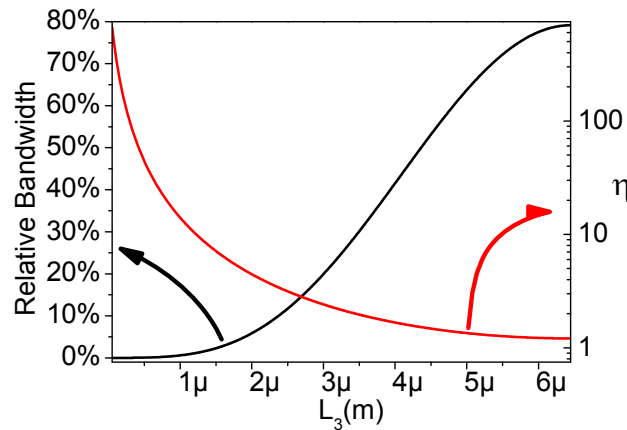
Figure 4.67. Bandwidth (black line) and ηc (red line) versus the coupling point, L$_3$.

In order to design and study the performance of the implemented filter, simulations have been done using an electrical simulator, where the microelectromechanical structure has been modeled as the electrical circuit shown in Figure 4.66 with the values shown in Table 4.9. We want to point out how the electrical model used is always a linearization of the MEMS behavior. The topology proposed allows obtaining both a single and a dual-band pass filter depending on the MEMS bias voltage used (V_1 and V_2 applied directly to the resonators, see Figure 4.65 b). The use of a zero polarization voltage on one of the two

MEMS resonators (V_1 or V_2) cancels the mechanical current, Im_i, of the corresponding filter and only the parasitic current, Ip_i, remains.

Table 4.9Micromechanical filter circuit element Values. (V_{DC}=24V, Q=220)

Parameter	Symbol	Value
Resonator Electromechanical coupling factor	η_e	$1.149 \cdot 10^{-9}$ C/m
Resonator Stiffness	k_r	61.34 N/m
Resonator Mass	m_r	$2.0711 \cdot 10^{-15}$ g
Resonator Damping	c_r	$1.286 \cdot 10^{-9}$ Ns/m
Coupler Electromechanical Coupling factor	η_c	11
Coupler Stiffness	k_c	47.6 N/m
Coupler Mass	m_c	$1.0513 \cdot 10^{-15}$ g
Lumped Elements Values (Used in the electrical simulator)		
Turn Ratio of the input and output transformers	η_e	$1.149 \cdot 10^{-9}$
Capacitance	$C = 1/k_r$	0.0163 F
Inductance	$L = m_r$	$2.0711 \cdot 10^{-15}$ H
Resistance	$R = c_r$	$1.286 \cdot 10^{-9}$ Ω
Turn Ratio of coupling transformer	η_c	11
Shunt Capacitor	$C = 1/k_c$	0.021F
Coupler inductance	$L = m_c$	$1.0513 \cdot 10^{-15}$ H

The response of the device in this case corresponds to a single band pass filter. If $V_1 \neq 0$ and $V_2 \neq 0$ a dual band pass filter is obtained. In both cases the differential amplifier allows enhancing the filter response compared with [94] in terms of insertion losses and out of band rejection since the parasitic currents are subtracted.

In Figure 4.68 the results of the simulations of the electrical equivalent circuit (Figure 4.66) are depicted. Figure 4.68 a) corresponds to the simulation of the single band pass filter, where the mechanical current (Im_2) has been cancelled and only the parasitic currents Ip_1, Ip_2 and Im_1 remain. Note the IL due to the impedance mismatching between the excitation source and the MEMS.

Figure 4.68 b) demonstrates the versatility and capabilities of the proposed CMOS-MEMS as a dual band pass filter. In this case, the four peaks corresponding to each resonant mode of the two mechanical coupled filters are shown. The spring softening effect is used to tune the filters to a desired center frequency, just modifying the stiffness (k_r'). Each filter bandwidth Δf_i is physically controlled with the coupler position. A variation in the coupler position implies a variation of the ratio transformers, η_c, which allows obtaining two filters with different bandwidths Δf_1 and Δf_2. As an example, the red line in Figure 4.68 b) shows the response of the device when the coupling position (L_3) has been increased in FILTER 2. As it is expected, the bandwidth Δf_2 increases since the out-of-phase mode frequency shifts up. The depth of inter band notch depends on the value of the

coupling position. The values used to achieve the dual band response are detailed in Table 4.9.
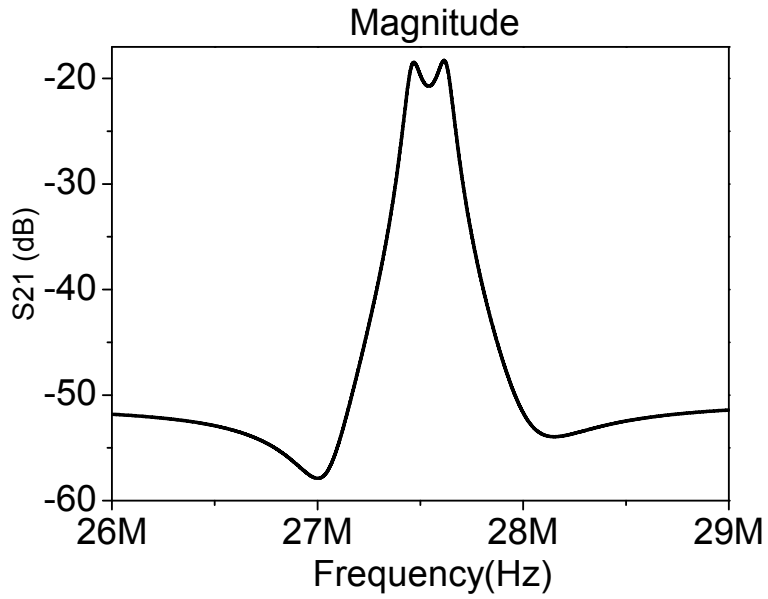
a)
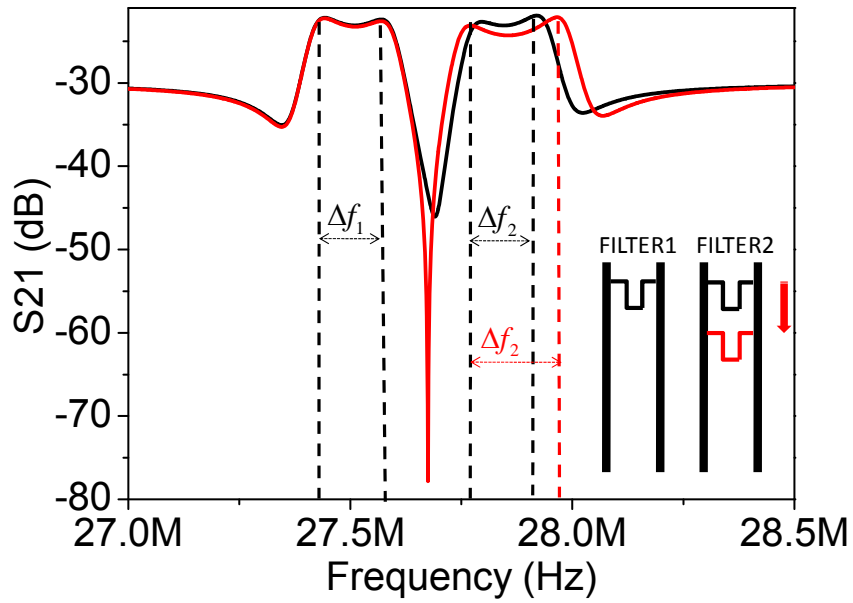
b)

Figure 4.68 a) Simulation results of a single band filter obtained when a zero polarization voltage is applied on one of the two MEMS resonators (V_1 or V_2). b) Simulation results of a dual band pass filter for two different coupling positions. The black line is obtained when the two filters present the same coupling position while in the red line an increase of the coupling position (L_3) of the second filter has been taken into account.

4.7.3 RESULTS AND DISCUSSION.

An electrical characterization of the implemented filters has been made using a network analyzer, Agilent E5100A, connected at the output of the CMOS differential amplifier, and a probe table under air conditions. The filter is excited using electrostatic force and its movement is read through the capacitive current. To characterize the implemented filter two different experiments have been performed.

In the first measurement a single band pass filter has been characterized. A time dependent voltage has been driven into both MEMS filter through the input electrode while the filters are biased with 0V and 24 V respectively (Figure 4.69). In this case, the circuit amplifies the motional current provided by the MEMS, which is biased at 24V, and the parasitic currents are subtracted. Compared to our previous works [94] an improvement of the out of band rejection and a shape factor as low as 2 are obtained. This improvement is attributed to the effect of the differential amplifier along with the symmetry in the implemented layout that allows achieving very similar parasitic capacitances ($C_1 \approx C_2$). Figure 4.69 a) also shows the simulation result (red line) in order to compare it with the test results. A slight difference in frequency between the measurement and the model response is attributed to the error in the optical physical dimensions measurement and the difference in the assumed polysilicon Young modulus and density. The parasitic capacitance values, $C1$ and $C2$ have been adjusted by a simple tuning (*C1=45.6aF, C2=40.7aF*).

a)

164
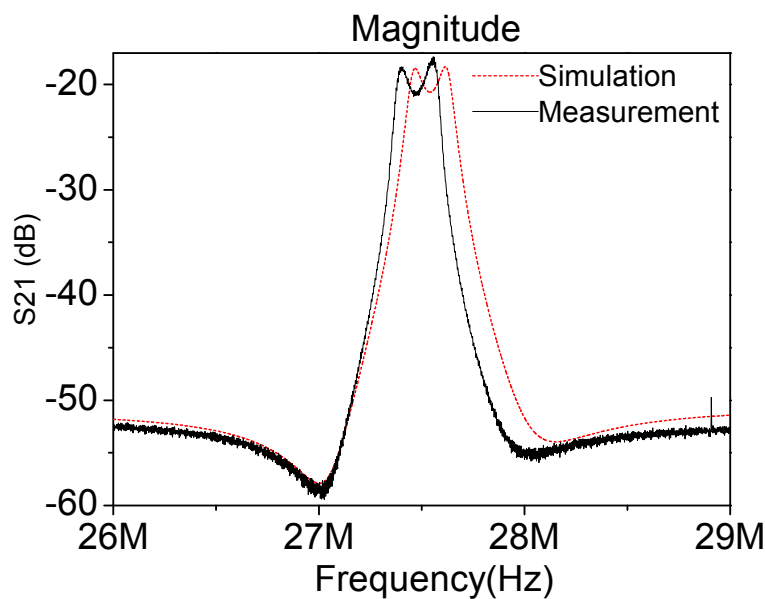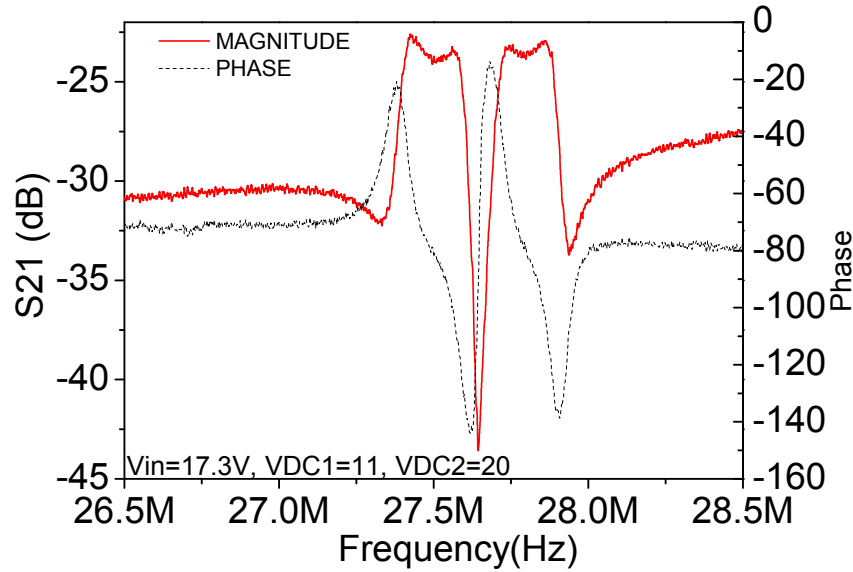
b)

Figure 4.69. a) Single filter electrical measurement with V1=24V and V2=0V(black line) versus simulation results (red line) b) electrical characterization of the dual band RF filter. A 22dB notch is present between the two pass bands (V1=20V, V2=11V).

In the second experiment the two filters are biased with voltages of $V_1=20V$ and $V_2=11V$. The time variant signal, V_{in}, is summed to a DC voltage (not present in the schematic on Figure 4.66) of 18.7V to achieve the electrical phase inversion necessary to obtain the notches at both sides of the interesting bands. Figure 4.69 b) shows the frequency response (magnitude) of the two band pass channel selector filter, the left one centred at 27.5MHz with a bandwidth of 190 kHz while the right one is centred at 27.8MHz with a bandwidth of 182kHz, achieving an inner stop band of -22 dB. In both filters the out of band rejection is around 10dB and they present a low ripple in the pass band (less than 1dB).

4.7.4 CONCLUSIONS

In previous section we have proven how the combination of both mechanical and electrical coupling enhances the response of fully integrated CMOS-MEMS filters in terms of out of band rejection (35dB) and shape factor ($SF_{20dB}=2$), making the resulting filter competitive compared with the works found in the literature. Moreover, the use of two filters increases the functionalities of the device, since a dual band pass filter can be easily obtained just applying the optimal polarization voltages. Therefore, we demonstrate the possibility to widen the functionalities of the CMOS-MEMS devices by using mechanics and electronics in the same die, which represents another step towards a fully integrated front-end for communication systems.

4.8 CONCLUSIONS OF THE CHAPTER

In this chapter, a about the MEMS-CMOS filters have been presented. Mechanically coupled resonator filters, electrostic coupled resonator filters, parallel filtering and dual

filters have been explored. All the design steps have been studied and the electrical characterization has been discussed. All the results presented in this chapter are compared with another works in the literature. The comparison has been divided into the four types of filter presented in this chapter: mechanical, electrostatical, parallel, and dual filtering. The filter used to do the comparison has been selected to work at the same frequency (HF).

Table 4.9 summarizes the performance of the mechanical filter presented in this work: U-Filter, V-filter and the U- Filter plus IC in its single band operation regime. When connected to a differential amplifier, the U-Filter overcomes the limitations of the stand-alone counterpart in terms of out of band rejection, shape factor and insertion losses. The filter shows the highest stop band rejection (SR= 35dB) with a very competitive shape factor (SF=2). A wider bandwidth is obtained by the V-filter. Note that all the stand alone CMOS MEMS filters present a very high insertion losses due specially to the high motional resistance of the devices. This high motional resistance produces a high impedance mismatching between the filter impedance the input resistance of the test equipment. The integration with the circuitry solves this problem.

In the field of electrostatic coupled resonator filters our work constitutes one of the highest frequency alternatives (see

Table 4.11). Furthermore, it presents the lower ripple. As a drawback, a high insertion losses and a poor out of band rejection is obtained. From the mechanical coupler resonator filter conclusion the integration with the IC could improve these two parameters.

Our parallel filter presents one of the higher out of band rejection in this type of filters. An impressive 42dB was obtained in the characterization stage on air condition.

In Table 4.13 the main characteristics of the CMOS MEMS dual band pass filter designed in this work with the state of the art [86] are shown. From this table, it is demonstrated the highest performance obtained with the CMOS-MEMS approach in terms of very low ripple and comparable stop band rejection.

Table 4.10. Performance of Single Band Pass mechanical coupled resonator filter.

Work	f_o (MHz)	BW (kHz), %BW	Ripple (dB)	Stop Band Rej. (dB)	IL (dB)	SF_{20dB}	V_{DC}	Tech.
V-Filter[32](this work)	29	2000,6%	<1dB	7.5	-	-	18V	CMOS
U-Filter+CMOS IC (air) (This Work)	27.45	220, 0.8%	3	35	17	2	25V	CMOS
U-Filter [34](this work)	26.7	120, 0.44%	0.9	2.5	96	-	21V	CMOS
Nanowire coupler[5]	17.84	114, 0.64%	0.1	6	66	-	17V	SOI
C-C Beams[3]	7.81	18, 0.23%	1.5	35	1.8	2.31	35V	SOI
DETF[12]	2.29	8.23, 0.36%	2.7	21	38	1.63	6V	SOI

Table 4.11. Summary of the electrostic coupled resonator filter

Work	f_o (MHz)	BW (kHz), %BW	Ripple (dB)	Stop Band Rej. (dB)	IL (dB)	SF$_{20dB}$	Tech.
Electrostatic Coupling (this work)	22.54	90, 0.4%	<1dB	4	108	-	CMOS
Electrostic Coupling [20]	4.13	0.99, 0.023%	1.5	-	56	-	SOI
[5]	0.165	0.044, 0.026%	1.8	52		2.1	SOI

Table 4.12. Summary of parallel filtering

Work	fo (MHz)	BW (kHz), %BW	Ripple (dB)	Stop Band Rej. (dB)	IL (dB)	SF20 dB	VDC	Tech.
Electrical Coupling (this work)	23	180, 0.8%	<1dB	42	10	2.24	21V	CMOS
Electrical Coupling [16]	21.76	200, 0.9%	0.9	30	7	2.97	21V	CMOS

Table 4.13. Performance for Dual Filters

Work	f_1 / f_2	BW_1/BW_2	Ripple (dB)	SB Rej. (dB)	V_{DC}	Technology
Dual-Filter in this work	27.5MHz /27.8MHz	190kHz/182kHz	1	9	20/11	MEMS-CMOS
Single MEMS dual filter [20]	131.5kHz /130.7kHz	155Hz/140Hz	13.2	15	15/15	SOI

4.9 REFERENCES

[1]   A. A. Abidi, "Direct-conversion radio transceivers for digital communications," in *Solid-State Circuits Conference, 1995. Digest of Technical Papers. 42nd ISSCC, 1995 IEEE International*, 1995, pp. 186-187, 363-4.

[2]   C. T. C. Nguyen, "RF MEMS for wireless applications," in *Device Research Conference, 2002. 60th DRC. Conference Digest*, 2002, pp. 9-12.

[3]   C. T.-C. Nguyen, "MEMS Technology for Timing and Frequency Control," *IEEE Transaction on Ultrasonic, Ferroelectrics and Frequency Control,* vol. 54, N,2, pp. 251-270, February 2007.

[4]   L. Sheng-Shian, M. U. Demirci, L. Yu-Wei, R. Zeying, and C. T. C. Nguyen, "Bridged micromechanical filters," in *Frequency Control Symposium and Exposition, 2004. Proceedings of the 2004 IEEE International*, 2004, pp. 280-286.

[5]   S.Pourkamaly and F.Ayazy, "Electrically Coupled MEMS Bandpass Filter, Part I. With Coupling Element

" *Sensors and Actuators,* vol. 122, pp. 311-316, 2005.

[6]   M. Motiee, R. R. Mansour, and A. Khajepour, "Novel MEMS, Filter for On-Chip Transceiver Architecture, Modeling and Experiment," *journal of Micromechanical and Microengineering,* vol. 16, pp. 407-418, 2006.

[7]   D. Weinstein, H. Chandrahalim, C. Lih Feng, and S. A. Bhave, "Dielectrically Transduced Single-Ended to Differential MEMS Filter," in *Solid-State Circuits Conference, 2006. ISSCC 2006. Digest of Technical Papers. IEEE International*, 2006, pp. 1236-1243.

[8]   J. L. Lopez, J. Verd, A. Uranga, J. Giner, G. Murillo, F. Torres, G. Abadal, and N. Barniol, "A CMOS-MEMS RF-Tunable Bandpass Filter Based on Two High-Q 22-MHz Polysilicon Clamped-Clamped Beam Resonators," *Electron Device Letters, IEEE,* vol. 30, pp. 718-720, 2009.

[9]   S.-S. Li, Y.-W. Lin, Z. Ren, and C. T. C. Nguyen, "An MSI Micromechanical Differential Disk-Array Filter," in *Solid-State Sensors, Actuators and Microsystems Conference, 2007. TRANSDUCERS 2007. International*, 2007, pp. 307-311.

[10]   H. Fatemi, B. P. Harrington, H. Zeng, J. Carlisle, and R. Abdolvand, "50Ohm-terminated 900MHz monolithic lateral-extensional piezoelectric filters on ultrananocryslalline diamond," in *Micro Electro Mechanical Systems (MEMS), 2011 IEEE 24th International Conference on*, 2011, pp. 744-747.

[11]   X. Yuan, L. Sheng-Shian, L. Yu-Wei, R. Zeying, and C. T. C. Nguyen, "1.52-GHz micromechanical extensional wine-glass mode ring resonators," *Ultrasonics, Ferroelectrics and Frequency Control, IEEE Transactions on,* vol. 55, pp. 890-907, 2008.

[12]   F.D.Bannon, J.R.Clark, and C.T.-C.Nguyen, "High-Q HF Microelectromechanical Filters," *IEEE Journal of Solid-State Circuits,* vol. 35, pp. 512-526, Abril 2000

[13]   N. Arellano, E. P. Quevy, J. Provine, R. Maboudian, and R. T. Howe, "Silicon nanowire coupled micro-resonators," in *Micro Electro Mechanical Systems, 2008. MEMS 2008. IEEE 21st International Conference on*, 2008, pp. 721-724.

[14]   J. Yan, A.A. Seshia, K.L. Phan, P. G. Steeneken, and a. J. T. M. v. Beek, "Narrow Bandwidth Single-resonator MEMS Tuning Fork Filter   " in *IEEE International Frequency contro Symposium*, Geneva Switzerland, May 29-June 1, , pp. 1366-1369.

[15]   J. Yan, A.A. Seshia, K. L. Phan, and a. J. T. M. v. Beek, "Internal Electrical Phase Inversion for FF-Beam Resonator arrays and Tuning Fork Filters," in *IEEE, Int. Conference on Micro Electro Mechanical Systems*, 13-17 Jan, 2008, pp. 1028-1031.

[16]   J. Yan, A.A. Seshia, K. L. Phan, and J. T. M. v. Beek, "Internal Phase Inversion Narrow Bandwidth MEMS Filter," in *IEEE Int. Ultrasonics Symposium*, Beijing, China, 2-3 Nov, 2008   pp. 705-708.

[17]   J.Yan, A.Seshia, K. L. Phan, and J. T. M. v. Beek, "Mechanical Phase Inversion for Coupled Lamé mode Resonator Array Filters,," in *IEEE Int. Conference on Micro Electro Mechanical Systems*, Tucson, Arizona, Jan 13-17, 2008, pp. 1024-1027.

[18]   M. U. Demirci and C. T. C. Nguyen, "A low impedance VHF micromechanical filter using coupled-array composite resonators," in *Solid-State Sensors, Actuators and Microsystems, 2005. Digest of Technical Papers. TRANSDUCERS '05. The 13th International Conference on*, 2005, pp. 2131-2134 Vol. 2.

[19]   S.Pourkamall and F.Ayazy, "Electrically Coupled MEMS Bandpass Filter, Part II. Without Coupling Element," *Aensors And Actuators,* vol. 122, 2005.

[20]   J. Yan, A. A. Seshia, K. L. Phan, and J. T. M. van Beek, "Internal electrical and mechanical phase inversion for coupled resonator-array MEMS filters," *Sensors and Actuators A: Physical,* vol. 158, pp. 18-29, 2010.

[21]   S.Pourkamaly and F.Ayazy, "Electrically Coupled MEMS Bandpass Filter, Part II. Without Coupling Element," *Sensors And Actuators,* vol. 122, 2005.

[22]   S.-S. Li, L. Yu-Wei, Z. Ren, and C. T. C. Nguyen, "A Micromechanical Parallel-Class Disk-Array Filter," in *Frequency Control Symposium, 2007 Joint with the 21st European Frequency and Time Forum. IEEE International*, 2007, pp. 1356-1361.

[23]   S.-S. Li, Y.-W. Lin, Z. Ren, and C. T. C. Nguyen, "Self-switching vibrating micromechanical filter bank," in *Frequency Control Symposium and Exposition, 2005. Proceedings of the 2005 IEEE International*, 2005, p. 7 pp.

[24]   S.-S. Li, Y.-W. Lin, Z. Ren, and C. T.-C. Nguyen, "A Micromechanical Parallel-Class Disk-Array Filter," in *Frequency Control Symposium, 2007 Joint with the 21st European Frequency and Time Forum. IEEE International*, 2007, pp. 1356-1361.

[25]   X. Zou, J. Yan, and A. A. Seshia, "Voltage programmable dual-band bandpass/bandstop filter response in a single micro-electro-mechanical device," in *Solid-State Sensors, Actuators and Microsystems Conference (TRANSDUCERS), 2011 16th International*, 2011, pp. 836-839.

[26]   J. R. Clark, F. D. Bannon, III, W. Ark-Chew, and C. T. C. Nguyen, "Parallel-resonator HF micromechanical bandpass filters," in *Solid State Sensors and Actuators, 1997. TRANSDUCERS '97 Chicago., 1997 International Conference on*, 1997, pp. 1161-1164 vol.2.

[27]   N. Lobotniu and E. Garcia, *Mechanics of Microelectromechanical Systems*: Kluwer Academic Publishers, 2005.

[28]   J. Giner, A. Uranga, J. L. Muñoz-Gamarra, E. Marigo, and N. Barniol, "A fully integrated programmable dual-band RF filter based on electrically and mechanically coupled CMOS-MEMS resonators " *Journal of Micromechanical and Microengineering* vol. 22, 2012.

[29]   *www.home.agilent.com*.

[30]   http://www.iconico.com/caliper.

[31]   J. Giner, A. Uranga, F. Torres, E. Marigo, J. L. Munoz Gamarra, and N. Barniol, "A CMOS-MEMS filter using a V-coupler and electrical phase inversion," in *Frequency Control Symposium (FCS), 2010 IEEE International*, 2010, pp. 344-348.

[32]   J. L. Lopez, J. Verd, A. Uranga, J. Giner, G. Murillo, F. Torres, G. Abadal, and N. Barniol, "A CMOS-MEMS RF-Tunable Bandpass Filter Based on Two High- Q 22-MHz Polysilicon Clamped-Clamped Beam Resonators," *Electron Device Letters, IEEE,* vol. 30, pp. 718-720, 2009.

[33]   J. Giner, A. Uranga, F. Torres, E. Marigo, and N. Barniol, "Fully CMOS integrated bandpass filter based on mechanical coupling of two RF MEMS resonators," *Electronics Letters,* vol. 46, pp. 640-641, 2010.

[34]   J.L.Lopez, J.Verd, J.Teva, G.Murillo, J.Giner, F.Torres, A.Uranga, G. Abadal, and N.Barniol, "Integration of RF-MEMS Resonators on Submicrometric Commercial CMOS Technologies," *Journal of Micromechanical and Microengineering,* vol. 19, p. 10, 2009.

[35]   W. Kun and C. T. C. Nguyen, "High-order medium frequency micromechanical electronic filters," *Microelectromechanical Systems, Journal of,* vol. 8, pp. 534-556, 1999.

Chapter.5 VHF AND UHF INTEGRATED RESONATORS

The main communication standards are allocated in the VHF and UHF range. Time control MEM resonators are required to enable low consumption low fabrication cost frequency sources. In this chapter all the steps from the design to the electrical characterization of two optimized Longitudinal Bulk Acoustic Wave resonators (LBAR) to work in the aforementioned frequency range are presented.

5.1 INTRODUCTION

In the way to replace the off chip component on the wireless communication transceivers [1], MEMS resonators have to be capable to work and offer acceptable Q factors at higher frequencies. Wireless technologies such as Global System for Mobile Communication (GSM), High Speed Downlink Packet Access (HDSPA) or Universal Mobile Telecommunication System (UMTS) are allocated in the range of Very and Ultra High Frequency, VHF and UHF respectively, which covers the range from 30MHz till 2GHz. In addition, these standards require of resonators with Q of tens of thousands [2]. There are four premises that researchers look in their investigations: high frequency, High Q, transduction method and integration. Each work presented in this chapter is focused on one, two or three of those points but there is not exists the perfect resonator.

In order to achieve high frequency resonators the size shrinking is the first technique used in microelectromechanical engineering[3]. Currently great efforts to obtain Nanowires (NW)[4] and Carbon Nanotubes (CNT's)[5-7] resonators are made. However, the size reduction produces a Q factor decreasing ,a reduction of power handling [8] and high susceptibility to environmental fluctuations such us temperature or molecules deposition [9]. The two last issues related with the environmental factors, can be solved by using a proper packaging of the resonators.

In order to alleviate the power handling problems as well as to obtain higher Q factors, the research on new resonator constituent materials with higher mechanical velocity has been done in recent years. Diamond [10] has been demonstrated as good material for MEMS devices. It presents a high acoustic velocity (high Young's modulus and low density) and a low phonon dispersion rate. Another way to increase the Q factor in resonators is the exploration of more complex resonant modes that avoid the energy losses through the anchors such us the whispering gallery mode (WGM)[10]. The WGM disk keeps the

mechanical resonance on the perimeter of the circular structure avoiding the mechanical energy losses through the stem.

On the other hand, piezoelectric materials are widely used in high frequency resonators and filters. The combination of Zinc oxide (ZnO) [11], a piezoelectric material, with single silicon substrate (SCS) has been investigated to obtain high frequency and high Q resonators. Other piezoelectric material such as Aluminium Nitride (AlN) presents a high acoustic velocity and it is the core of the most of Surface Acoustic Wave resonators (SAW)[12] and Bulk Acoustic Wave resonators (BAW)[13-14]. Recently, the research has been addressed towards new composite materials that increase the microelectromechanical device performances [15].

The transduction method used to excite and to measure the microelectromechanical device is critic from the performance point of view. Different works found into the literature demonstrates that high frequency resonators capacitive transduced offers a higher Q compared with other excitation and read methods [16-17]. However, the capacitive transduction along with the use of dielectrically electrostatic transduction presents motional resistances in the order of 1MΩ[18-19]. In contrast to the capacitive transduction, the piezoelectric thin film transduction allows to obtain lower motional resistances. [15]. However, the piezoelectric transduction offers limited Q at high frequencies. To overcome this problem a mixture between both transduction methods has been conceived [16].

High *Qxf* (quality factor x operating frequency) product is the goal for high-frequency resonators. Both *Q* and *f* are mandatory requirements for new transceiver architectures. On one hand, very good mechanical devices can be obtained, and on the other hand the proper frequency device can easily be designed and fabricated. Nevertheless, the total system performance enhancement will be achieved if the integration of mechanical and electronics could be achieved [2, 20]. There are many works related with the integration of micromechanics into commercial CMOS technologies. The use of micromachined technologies and materials with CMOS compatible temperature ceiling such as sputtered nickel [21] have been investigated. Another alternative is based on the epitaxial silicon growth [22] above the MEM structure that allows to create a substrate where a CMOS process can be implemented. The problem is that many commercial CMOS foundries could hesitate to accept other foundries wafer. Finally, a more innovative approach is used inter leave integration [23]. The use of intrinsic layer of a commercial CMOS technology takes advantage of the robustness of the technology to obtain fully integrated VHF and UHF resonators [24-26].

The VHF and UHF MEMS fabrication on a commercial CMOS technology offers enormous advantages compared with other technological integration approaches in terms of cost, and fabrication robustness. The polysilicon capacitance module present in the AMS 0.35 allows to obtain very narrow air gaps, up to 40nm, using the spacer technique [27]. that overcomes the thinness of the constituent layers. Albeit a limit it frequency appears to be found in the monolithic integrated CMOS resonator [24] this approach is still very attractive for the industries and other groups are still developing new approaches based in this idea [28-30]

This chapter is focused on the fabrication of fully integrated VHF [25]and UHF CMOS-MEMS resonators [26]. The in section 5.2 the state of the art on high frequency resonators is presented. After that, we present both approaches we have obtained: the enhanced LBAR in section 5.3 and the hyperboloid resonator in section 5.4. Both sections present the design fabrication and electrical test. In section 5.5 a discussion about the obtained results and its comparison with the state of the arte is included.

5.2 STATE OF THE ART

In this section a more detailed overview of the most impacting works in the field of Very, Ultra and Super high frequency MEM resonator is exposed. In some of the most relevant works on the field are summarized sorted by its resonant frequency. In this section few features of each one of them are extended.

One of the first works in longitudinal bulk acoustic resonators was performed by Mattila in [31]. His 12MHz bulk resonator was fabricated in a SOI wafer. Its dimensions are 290μm length and 10 μm width. The Q achieved by means of a capacitive readout through an amplifier was 100.000.

Pourkamali achieved very good quality factor in the VHF range in [32-33], using a extensional bulk mode of a wide beam supported by thin anchors. His particular fabrication process (HARPS) allow them to obtain a very high aspect ratio to achieve very think structures along with narrow gaps and increase, in this way, the coupling area between the resonator and the electrodes. The resonator is excited electrostatically and the movement is read by means of a capacitive detection.

The used of novel very tinny structures, as commented in section **¡Error! No se encuentra el origen de la referencia.** has been deeply studied in Roukes group. They studied the Q and losses effects of the scalability of different kinds of nanostructures [34]. In this research Feng [4] used nanowires beam to obtain a 100MHz resonators with Q=1825. The resonators were fabricated using Silicon Carbide. The magneto motive transduced was used to measure the frequency response of the resonator. With this work they applied the scaling of structures to achieve higher frequencies.
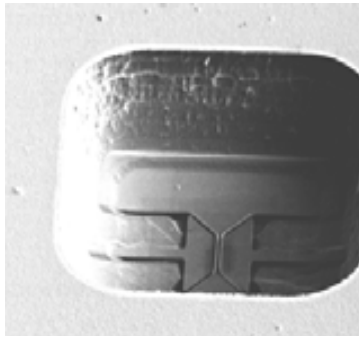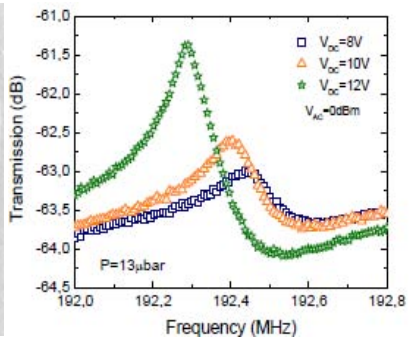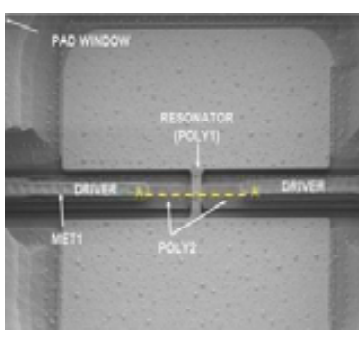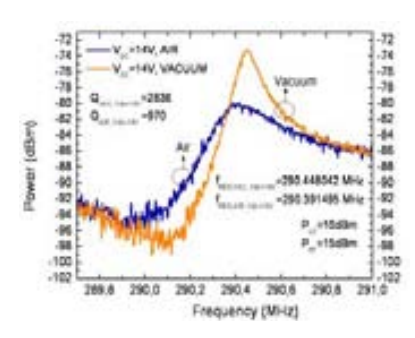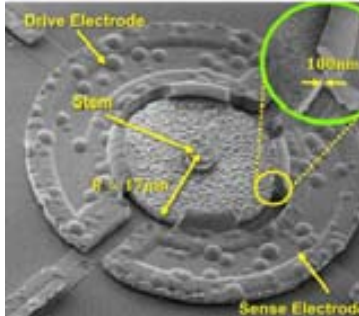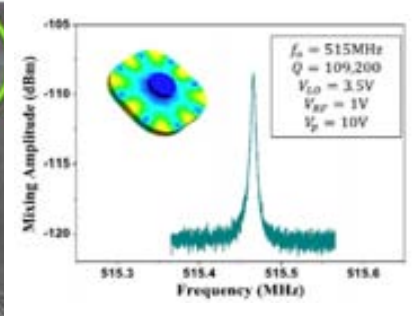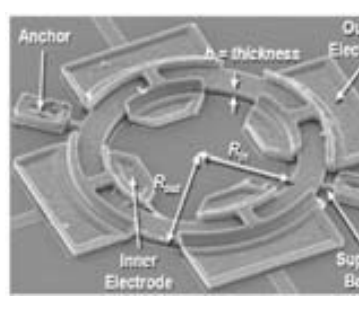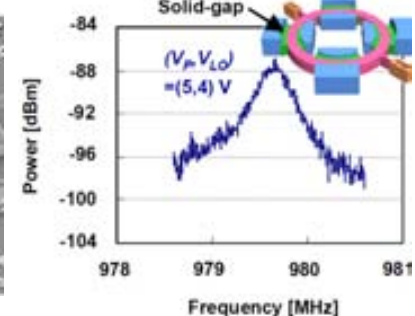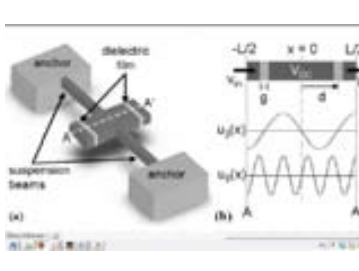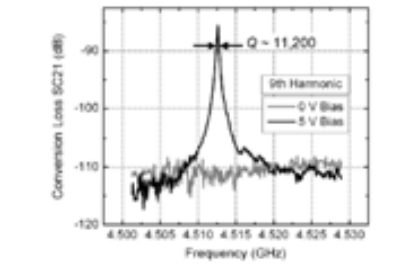
Nguyen group developed a disk resonator to operate at 160MHz [8] via a polysilicon-based, self-aligned, fully-planar wafer-level surface-micromachining process. . Their work was addressed to solve the integration problems by using polysilicon and solve the anchor losses in stemmed disks. The self alignement technique avoids the Q decrement due to the misalignment of the stem. The radius of the disk, 17μm, fixes the resonance frequency at 160MHz. Q of more than 22.000 and very good performance in third harmonic intermodulation were achieved. The disk resonator have similar scalability problem than flexural resonators. The resonant frequency depends directly on the radius. Ring resonator presented in the following paragraph solves this problem.
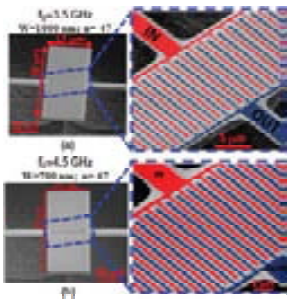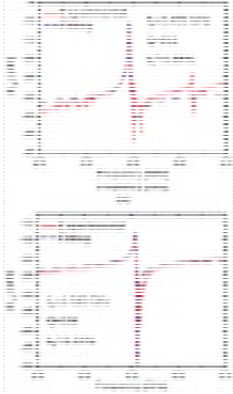
One of the most aggressive approach to overcome the always present integration problems of VHF and UHF resonator was presented by Teva in [24] where a flexural 4μm length CC beam was fabricated and tested using the mixing techniques. The Q's on air and in vacuum are 970 and 2386 respectively for flexural mode. The fabricated resonator have gap of around 40nm using the oxide spacer technique. Different attempts using this approach were realized in this direction as in [35].

The use of CMOS compatible material motivated the Rochelieu *et.al.* work [10]. They used a microcrystal diamond to construct a Disk resonator based on the previous work in the same group [36-37]. At the same time they explored the Whispering Gallery mode, that enables a dramatically reduction of the anchor losses to achieve a Q>109.000 for a 515MHz disk resonator.

Table 5.1 Summary of different MEM resonators. (sorted by ascendant frequency)

Device		Properties	Measurement
HF LBAR Silicon Resoantor Capacitively transduced			F=12MHz Q=100.000 Qxf=12x10^{12} Lxt=260µmx10µm G=950nm [31]
VHF Bulk Acoustic Resoantor Silicon, Capaciteve Transduced			f=81MHz Q$_{air}$=33.400 Qxf=2.7x10^{12} LxW=540µmx50µm g=65nm [32-33]
VHF SiC Nanowire Magnetomitive Transduction			f=100MHz Q$_{air}$=1825 Qxf(air)=1.8x10^{11} LxWxt=3µmx55nm x55nm [4]
VHF Disk Resoantor, Poly-Si, Capacitivelly transduced			f=157.9MHz Q$_{air}$=20500 Qxf=3.2x10^{12} Rxt=17µmx3µm g=70nm [8]

VHF MEMS -CMOS C-C Beam Electrostatic transduced			f=192MHz Q_{air}=300 Q_{vac}=1000 $Qxf(air)$=2x10^{11} L=4μm g=40nm [35]
VHF MEMS -CMOS C-C Beam Electrostatic transduced			f=290MHz Q_{air}=970 Q_{vac}=2386 $Qxf(air)$=8.2x10^{11} L=4μm g=40nm [38]
UHF WGM Disk Resonaot. Micro-Crystal diamond,			f=515MHz Q_{air}=109.000 Qxf=5.6x10^{13} Rxt=17μmx3μm g=100nm Rx=714kΩ [10]
UHF Ring Resoantor Poly-Si Capacitively Tranduced			f=990MHz Q_{air}=3200 Qxf=3.17·10^{12} R_ixR_t=32μmx50 μm t=2μm g=28nm [39]
SHF BAW Resoantor. Dielectrically Tranduced			f=4.5GHz Q_{air}=11200 Qxf=5.3·10^{13} Lx W =8.5μmx40 μm t=2.5μm g=15nm [18-19]

CMR Piezoelectric Resonator Piezoelectrically tranduced			f=4.5GHz Q_{air}=353 Qxf=1.58·10^{12} LxW=8.5µmx700nm n=67 [14]

However, disk resonators present scaling problems to reach frequencies above 1GHz. This problem is solved using ring resonators whose frequency is dependent on the internal and external radium ratio [39]. In this work a ring resonator working at 990MHz is presented. The mechanical wine glass mode is enabled by means of the electrostatic excitation. Electrodes are placed around the inner and outer perimeter. The fabrication is based on a customized process whose start point is a doped silicon wafer that allows the parasitic current be avoided. In this work a solid gap of 28nm is fabricated in order to decrease the motional resistance almost 5x compared to the measurements of the same resonator with air gap. The internal radius is 32µm and the external is 50µm, and the voltages employed in the mixing measurement are set in the range of 5 to 10 V.

More innovative proposals were presented by the couple Bhave and Weinstein [18-19]. Their series of works based on the use of dielectrically traduced resonators allowed them to reach the impressive 4.5GHz limit. The Q factor on air is 11.200 and the fabrication processes they use define gaps as narrow as 15nm filled with silicon nitride. The Qx f factor of 5·10^{13} is a milestone in the high frequency resonators filed.

Far from the afore mentioned frequency, in the range so called Super High Frequency (SHF) the use of different kind of material is required: Piezoelectric materials. In this range of material devices the Surface Acoustic Wave resonator (SAW) and the Film Bulk Acoustic Resonator (FBAR) dominates the market [13, 40]. However the SAW resonator is difficult to integrate with the electronics. For FBAR, since the operation frequency depends on the piezoelectric layer thickness, it is difficult to obtain different devices that operate at different frequency in the same wafer. However, Piazza et al [14] proposed using piezoelectric material resonator working in its contour resonance mode to solve the multifrequencies availability in the same wafer. They use a sandwich of AIN between two electrodes which are patterned in 62 electrodes whose width is 700nm. The frequency achieves is 4.52Ghz with a 356 quality factor.

Hundreds of proposals can be found in the literature. Ones addressed to achieve the highest frequency, other addressed to obtain higher and higher Q factor. The research of new materials new architectures, new resonant modes and new transduction method or combination of them is still alive. What is the best option will depend on the designer requirements

5.3 VHF Resonator. Enhanced LBAR.

The VHF resonator section starts with the Longitudinal Bulk Acoustic Resonator (LBAR) modeling. The design expression used to obtain the resonance frequency of the device is given. Since different structural modifications have been included in the resonator, Coventor simulations are required in order to predict the operation frequency of the resonator. After the simulation, the fabrication and the electrical test results are presented.

5.3.1 Longitudinal Bulk Acoustic Resonator (LBAR).Modeling and Design

In this section the first longitudinal mode is studied. This mode will be electrically modeled and the design expressions for the resonant frequency will be extracted.

a)

b)

Figure 5.1.a) 3D diagram for a simple longitudinal Bulk Acoustic Resonator (LBAR). The lower figure shows the explanation and compression of the BAR in the *y* direction. b) shows the electrodes and the resonator as well as the excitation sources and the DC biasing on the resonator.

In Figure 5.1 a 3D diagram of the classical LBAR is shown. In its first resonant mode the two arms expands and compress at the same time. The maximum movement is ob

served in its free ends while in the center of the beam the total displacement is null. Since not effective vibration occurs at the center of the structure this point is used to fix the structure through the anchors.

The modeling starts with the Hooke's equation for the stress and strain of the beam resonator that is calculated in expression (5.1):

$$T = E \cdot S \tag{5.1}$$

Where T is the stress, E is the Young's modulus and S corresponds to the strain due to the beam displacement and calculated using expression (5.2):

$$S = \frac{\partial U}{\partial y} \tag{5.2}$$

where U is the movement of any part of the beam. The force of a small beam segment Δy is:

$$F = A(T(y - \Delta y) - T(y)) = A \frac{T(y - \Delta y) - T(y)}{\Delta y} \Delta y \approx A \frac{\partial T}{\partial y} \Delta y \tag{5.3}$$

Where A is the beam cross-section defined by the width and thickness ($w \cdot h$). The segment Newton's equation is described in expression (5.4):

$$F = m \frac{\partial^2 U}{\partial t^2} = \rho A \frac{\partial^2 U}{\partial t^2} \Delta y \tag{5.4}$$

The wave equation for the longitudinal displacement U can be written as (5.5) combining (5.1), (5.2) and (5.3):

$$EA \frac{\partial^2 U}{\partial y^2} = \rho A \frac{\partial^2 U}{\partial t^2} \tag{5.5}$$

where ρ is the material density. The solution of this equation can be approximated [41]by :

$$U = \left(a e^{jpy} - b e^{-jpy} \right) e^{-j\omega_o t} \tag{5.6}$$

Where p is a variable and a and b are the coefficients of the displacement solution. Replacing (5.6) into (5.5) and solving it the angular frequency can be obtained as:

$$\omega_o = \sqrt{\frac{E}{\rho}} p \tag{5.7}$$

The boundary conditions are fixed by considering that there are no stress and no stress gradient at the free ends of the resonator ($y=L/2$):

$$E \frac{\partial U}{\partial y} \bigg|_{y=L/2} = 0 \tag{5.8}$$

And

$$\left. \frac{\partial T}{d_y} \right|_{y=L/2} = 0 \tag{5.9}$$

The solution is:

$$U = \sin(py)e^{j\omega_o t} \tag{5.10}$$

Where $p=n\pi/L$ for the n resonant model. Since the first resonant longitudinal mode is considered, n will take the value of 1 ($n=1$).

The forced movement of the resonator is described by expression (5.11):

$$\rho A \frac{\partial^2 U}{\partial t^2} + \gamma A \frac{\partial U}{\partial t} - EA \frac{\partial^2 U}{\partial y^2} = F(y,t) \tag{5.11}$$

Where γ is the damping and $F(y,t)$ is the electrostatic force that can be written as:

$$F(y,t) = \frac{f(t)}{2} \left[\delta(y - L/2) - \delta(y + L/2) \right] \tag{5.12}$$

Assuming that the solution of expression (5.5) is:

$$U(y,t) = y(t)\sin(py) \tag{5.13}$$

and substituting (5.13) into (5.11) the expression obtained is:

$$\rho A \frac{\partial^2 y}{\partial t^2} \sin(py) + \gamma A \frac{\partial y}{\partial t} \sin(py) - EAyp^2 \sin(py) = F(y,t) \tag{5.14}$$

If expression (5.14) is multiplied by the mode shape $sin(py)$ and integrated over the arm length it leads to:

$$\rho A \frac{\partial^2 y}{\partial t^2} \frac{L}{2} + \gamma A \frac{\partial y}{\partial t} \frac{L}{2} - EAp^2 \frac{L}{2} y = f(t) \tag{5.15}$$

From the analogy with the movement equation of an harmonic oscillator under damping the mass, spring and dumper values can be obtained as:

$$M = \rho A \frac{L}{2} \tag{5.16}$$

$$K = EAp^2 \frac{L}{2} = EA \frac{\pi^2}{2L} \tag{5.17}$$

$$D = \gamma A \frac{L}{2} \tag{5.18}$$

The first longitudinal mode occurs when the length of one of the arms is equal to quarter of the longitudinal acoustic wavelength [31] as it is shown in expression (5.19)

$$f_{BAR} = \frac{v_{BAR}}{\lambda} = \frac{1}{2L}\sqrt{\frac{E}{\rho}} \qquad (5.19)$$

Where the E, ρ and L are the Young's modulus the material density and the length of total released arm respectively. The velocity of the acoustic wave traveling through the structure can be calculated using expression (5.20)

$$v_{BAR} = \sqrt{\frac{E}{\rho}} \qquad (5.20)$$

In Figure 5.2 the mechanical equivalent circuit of the resonator is shown.
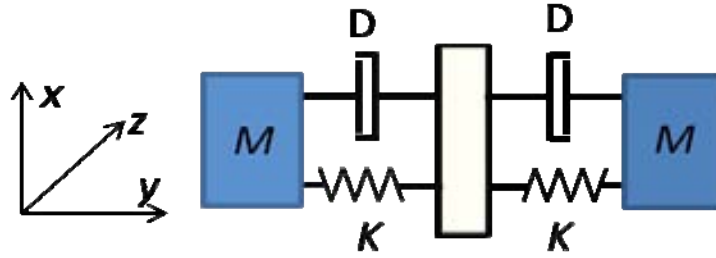
Figure 5.2. Mechanical model of the LBAR

The force exerted into the resonator at the resonant frequency due to the AC and DC voltage applied as indicated in Figure 5.2 b) corresponds to:

$$F(t) = V_{DC}V_{AC}\frac{\partial C}{\partial y}\sin(\omega t) \qquad (5.21)$$

Where C is:

$$C = \frac{\varepsilon_o \cdot W \cdot h}{s - y(t)} \qquad (5.22)$$

Where $y(t)$ is the harmonic gap variation From expression (5.21) the electromechanical coupling coefficient can be identified by expression

$$\eta = V_{DC}\frac{\partial C}{\partial y} \qquad (5.23)$$

The current generated by the movement and the voltage difference in one of the resonator arms can be calculated using:

$$i = \frac{\partial V_{ac}}{\partial t}C + V_{DC}\frac{\partial C}{\partial t} = \frac{\partial V_{ac}}{\partial t}C + \eta\frac{\partial y}{\partial t} \qquad (5.24)$$

The first term corresponds to the feedthrough current due to the static capacitance between the resonator and the electrode. The second term corresponds to the motional current, i_m that depends on the movement. The free ends move with a velocitity that can be written as (5.25):

$$v = \frac{\partial y}{\partial t} = \frac{i_m}{\eta} \qquad (5.25)$$

Furthermore, force can be approximated by $f=\eta V_{ac.}$ The movement equation can be rewritten using the current analogy as:

$$\frac{M}{\eta^2}\frac{\partial i_m}{\partial t} + \frac{D i_m}{\eta^2} + \frac{K}{\eta^2}\int i_m dt = V_{ac} \qquad (5.26)$$

Expression (2.62) corresponds to the RLC circuit that models the LBAR resonator arm. The complete equivalent circuit is depicted in Figure 5.3. In the circuit, C_o is the direct static capacitance between each electrode and the resonator. The load resistance, R_o is hanged from the movable part to the ground to read the current.

Figure 5.3 Complete equivalent small signal electrical circuit.

5.3.2 ENHANCED LBAR

This section focuses on the improvement of the LBAR introduced in section 5.3.1. The coupling area presented by the LBAR, formed by a beam, is quite small and this fact increases the motional impedance of the resonator. The enhancement consists on the addition of two masses at the ends of the free arms. The modification presents two advantages: a) to avoid the effect of residual stress after the releasing process [42] and b) to increase the coupling area between the resonator and the electrodes. The diagram of the modified resonator can be observed in Figure 5.4.

Since the structure is very different from the simple LBAR (see Figure 5.1), the frequency expression (5.19) is not valid to calculate the resonant frequency of the new resonator because it does not include the mass addition. For this reason, Coventor FEM simulator is used to obtain the exact resonant frequency. In Figure 5.4, the simulation results obtained through modal analysis of the resonator is shown. The modal node (a node is the point on the structure when the total amount of displacement is null) is located in the very centre of the structure.

Figure 5.4: FEM modal simulator of the longitudinal motions. The compression and the expansion of resonator occurs at *f=280MHz*.

Layer	Thickness	Minimum line width	Minimum line separation
Poly1	280nm	350nm	450nm
Poly2	200nm	650nm	500nm
IOX	40nm	-	-

Since the mass added has a large area compared with the rest of the resonator, two releasing holes of 500nm diameter have been opened on each mass in order to make easier the removal of the silicon oxide present under the structure. The summary of the dimensions used to design the improved LBAR are shown in Table 5.2. Observe the difference between the resonant frequency using expression (5.19) and the simulated response that supposes a 52% frequency reduction .

Table 5.2 . Summary of the main dimensions and material parameters used to design the LBAR

Parameter	Value
Total length of the Resoantor *(L)*	7 μm
Width of the center (W)	850nm
Coupling width(W_c)	3.5 μm
Young's modulus (E)	160 GPa
Polysilicon density *(ρ)*	2330 kg/m^3
PolySi thickness	280 nm
Resonant Frequency (Coventor)	280MHz

Resonant frequency (using expression (5.19))	591MHz

5.3.3 FABRICATION

The AMS 0.35μm technology is used for the resonator fabrication. The polysilicon 1 that presents a thickness of around 280nm is used as a constituent material of the movable part and the electrodes are made using the Poly 2 layer. The layout has been drawn to keep a zero distance between the Poly 1 and the Poly 2. The conformal interpoly oxide disposition will plays the role of spacer to ensure a 40nm gap. Figure 5.5 shows a SEM image of the fabricated resonator.

Figure 5.5 SEM micrograph of the polysilicon LBAR. The fabricated dimensions are labeled on the picture and the remaining oxide after the etching can be observed under the two electrodes.

5.3.4 ELECTRICAL CHARACTERIZATION

The VHF resonator electrical characterization has been carried out by means of the same electrical connection set up shown in Figure 5.6. The AC signal provided by the Agilent E5071B network analyzer is applied directly to the resonator body through a bias-Tee. The biasing voltage, V_p, is added to the input AC signal. The movement induced by the excitation is capacitively read in the electrodes that are short-circuited between them and connected to the second port of the network analyzer. The measurement of the VHF resonator has been carried out at room pressure and temperature.

Figure 5.6 Set up of the measurements. The signal and the biasing voltage is pumped into the resonator trough a bias-T. The movement induced by the electrostatic excitation is read on the electrodes.

The frequency response, both magnitude and phase, is shown in Figure 5.7 a) and b) respectively. The voltages applied on the structure are 9V, 15V and 21V for an AC power of 3dBm. The resonance peak is -68.5dB at 258.5MHz using V_p= 21V while the maximum phase shift is 9º.

a)   b)
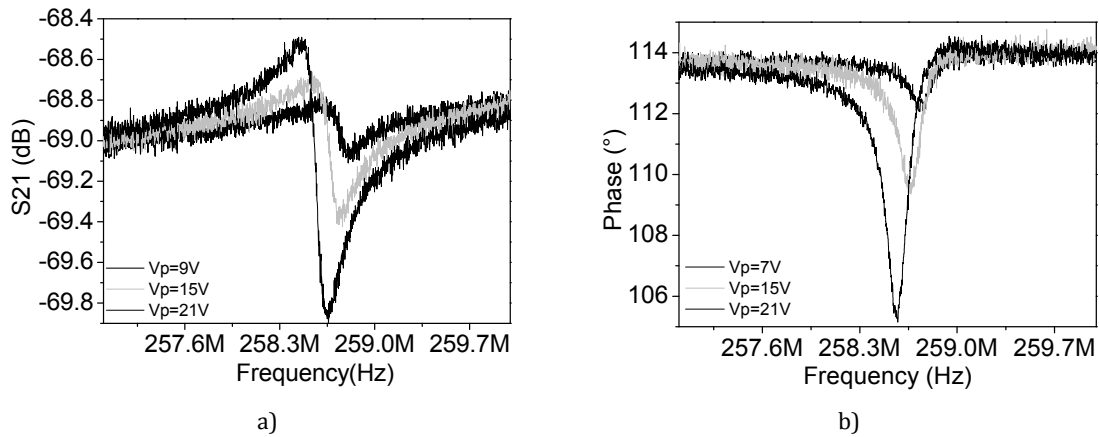
Figure 5.7 Result of the measurement of the VHF resonator. The magnitude a) and phase b) are measured for different values of voltages, 9, 15 and 21 V.

The measurement shows a large feedthrough signal. In one hand, this feedthrough is promoted by the direct static capacitance between the electrode and the resonator (*C's* in Figure 5.3). To be more comprehensive, this effect is similar to the effect obtained in the one port set-up analyzed in chapter 3. On the other hand, the high operation frequency decreases the impedance of the feedthrough current. The low resonant peak suggests that the motional impedance and the static capacitance impedance are in the same order.

5.3.5 DISCUSSION AND CONCLUSIONS

In this section the design simulation fabrication and characterization of an enhanced LBAR has been carried out. The classical LBAR has been modified in order to increase its coupling area in order to reduce the motional impedance. However the results present an unexpected high motional impedance.

One of the main problems is the energy lost. At VHF operation frequency, one of the most important effects is the anchors losses [43]. Despite in our design the anchors have been placed on a nodal point (where theoretically the vibrations are null) the fabrication tolerances could have displaced it. In this case, the solution is to design the anchor as an acoustic impedance inverter. The impedance inverter is an anchor whose length is a quarter of the acoustic wavelength [44]. These anchors will isolate mechanically the movement from the substrate.

5.4   Hyperboloid LBAR

In this section, the design of an innovative shaped LBAR is presented. Unlike the improved resonator presented in section 5.3, the transduction area dimensions are included in the design expressions. Furthermore, the co-fabrication of the MEM device along with an electronic amplifier is presented in order to investigate the enhancement produced by the circuitry. The name of the resonator is attributed to its shape (see Figure 5.8) that is equal to a geometric hyperboloid counterpart.

5.4.1   Design

The resonant frequency of the LBAR based on the Mattila resonator is achieved taking into account only the longitude of the arms *L* (see equation (5.19)). This equation does not include any variation in the width of the resonator. A change in the width of the resonator will increase the effective mass of the resonator and will change the stiffness constant. The result will be a change in the resonant frequency. The following paragraphs will explain a method to obtain the LBAR resonant frequency expression that includes all the physical dimensions of our new design.

Figure 5.8 shows the diagram of the resonator, whose topology is similar to the suspensions founded in [45]. Similar to the principle of operation of the LBAR explained in previous section, the maximum displacement occurs at the free end of the structure while the center of the resonator presents zero movement. This center point is selected as anchorage point. The maximum displacement and the nodal point are the orange and blue zone respectively in the Coventor simulation result (Figure 5.9).

The design technique is based on the merger of two imaginary ellipses, with major and minor axes of length *a* and *b* respectively, over a rectangle with an area of $W_c x L$ (see Figure 5.8). The LBAR is defined by the area that separates the two ellipses. As it will be seen, the novel structure allows the coupling area width (W_c) to be predefined. In addition, the resonant frequency can be obtained by fixing all the other dimensions.

Figure 5.8 Diagram of the hyperbolic resonator. The lower figure shows the diagram of the superposed ellipsis used to obtaining the mass and the stiffness of the resonator.
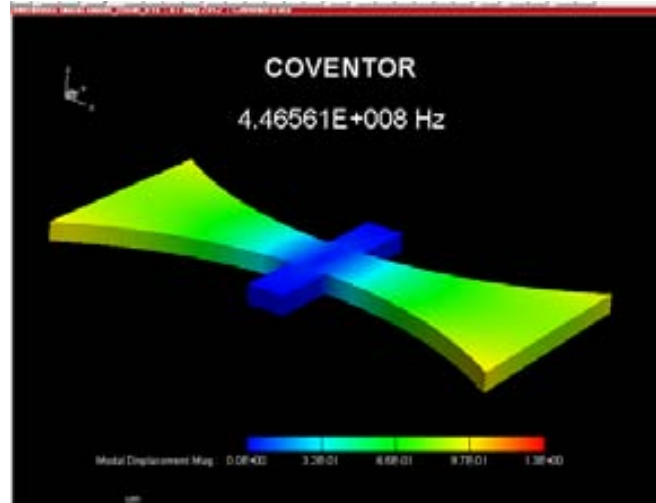
Figure 5.9. Modal analysis from Coventor. The longitudinal mode is observed at 446MHz.

Equation (5.27) allows the frequency to be obtained as a function of the structure stiffness (k_{HYP}) and the mass (m_{HYP}), for the first extensional mode. The mass is obtained by subtracting the mass of the imaginary ellipse ($M=a·b·\pi·t·\rho$) to the mass of the rectangle ($L·W·t·\rho$) in Figure 5.8. It is calculated in equation (5.28), where t and ρ are the thickness and density of the resonator respectively. The stiffness is obtained using expression presented in [45] and rewritten in (5.29)where E is the Young's modulus.

$$f_{HYP} = \frac{1}{2\pi}\sqrt{\frac{k_{HYP}}{m_{HYP}}} \tag{5.27}$$

$$m_{HYP} = (A - A_e)t\rho = \left[2a(2b+\omega) - \pi ab\right]t\rho \tag{5.28}$$

$$k_{HYP} = \frac{2Ebt}{\dfrac{4a(2b+w)}{\sqrt{w(4b+w)}}\arctan\sqrt{1+\dfrac{4b}{w}} - a\pi} \tag{5.29}$$

The design process starts with the coupling width (W_c) definition and therefore, the coupling area for each arm of the resonator. Design rules of the technology impose the minimum width of the device near the anchors (w). The ellipse minor axis is $b=(W_c-w)/2$ Finally, the major axis (a) that is the length of each arm, is determined by the resonant frequency, following expression (5.27).

To design the first prototype, the following criteria have been taken: the desired coupling area has to be similar the VHF resonator in order to compare the motional resistance and feedthrough current. In this way a 6µm free end width has been fixed (3 µm for each arm). The operating frequency is selected to be allocated in the free band of 434MHz. The narrowest part width has been chosen to be higher than the minimum width allowed by the CMOS technology but no so wide to difficult the releasing. An arbitrary value of 850 nm has been taken. To achieve the previous values the long and short ellipse axis, a and b ,are 1.075µm and 3.5µm.

187

In Figure 5.10, the relation between the frequency and the resonator length for a total coupling length ($2W_c$) of 6µm is shown. The required length for a 434MHz frequency resonator is 7µm.

Table 5.3. Summary of the geometric and physical magnitudes of the hyperbolic resonator.

Parametre	Value
Area of the ellipse	12.9 pm^2
Area of the rectangle (LxW_c)	21 pm^2
PolySi density (ρ)	2230 kg/cm^3
Length of the resonator (L)	7 µm
Coupling length $(2xW_c)$	6 µm
Ellipse ,minor axis (b)	3.5 µm
Ellipse major axis (a)	1.075 µm
Gap	80nm
Voltage	25V
Resonator stiffness (k_{HYP})	21935 N/m
Young modulus (E)	160 GPa
Minimum width of the resonator (w)	850 nm
PolySi thickness (t)	280 nm

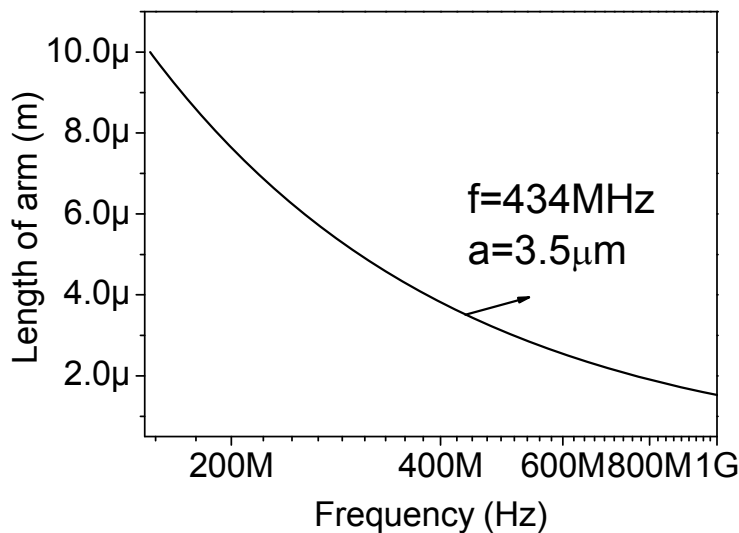

Figure 5.10 Resonance frequency vs length of the resonator for a fixed coupling area W_c=3µm.

5.4.2 FABRICATION

The new resonator has been fabricated using the polysilicon capacitance module present in the commercial CMOS technology of the Austria Microsystems (AMS) of 350 nm. The resonator has been dimensioned to operate in the free band of 434MHz. The SEM image in Figure 5.11 shows the hyperbolic resonator and the electrodes as well as the different postfabricated measured dimensions. The final dimensions obtained after the fabrication differ a little from the designed ones. The total length of the resonator is 7µm and the width of each transduction is set at 3.15µm. A gap of 80nm has been obtained.

Figure 5.11 SEM image of the hyperbolic resonator. The mains dimensions are printed over the micrograph as well as the elliptic design reference.

As in the previous resonator the releasing of the structure can be observed because the remaining oxide which covers partially the electrodes is far from the movable part.

5.4.3 CHARACTERIZATION

The resonator frequency response has been measured for two prototypes: a) stand alone resonator and b) fully integrated MEMS plus integrated amplifier in order to observe the improvements produced by the amplification. Both measurements have been carried out at room conditions (pressure and temperature).

For the stand-alone resonator, the measurement of the magnitude is shown in Figure 5.12 a). Note that different biasing voltages have been applied in order to observe the frequency variation with the voltage. The resonance peak is observed at 381.1MHz and 65.6dB. The noisy response can be enhanced by connecting an amplification stage at the output (electrodes) of the resonator. The amplification stage which is depicted inFigure 5.13 is detailed in [46]. The measurements are shown in Figure 5.12 b). The resonant frequency is 387.4MHz whereas the peak has a value of -39.17 dB.

To obtain a cleaner resonant peak the mathematical linearization has been done. In Figure 5.13 the linear frequency response is depicted. Note that only 0.03dB peak is observed at the resonant frequency.

A qualitative analysis of the results suggests the following: the fully integrated response shows a high-level signal compared with the stand alone-resonator. This is due to the amplification of the circuitry. However, the circuit amplifies both the feedthrough current and the motional current. The difference between the resonant peak and the feedthrough coupling level is the same for both approaches.

a)   b)
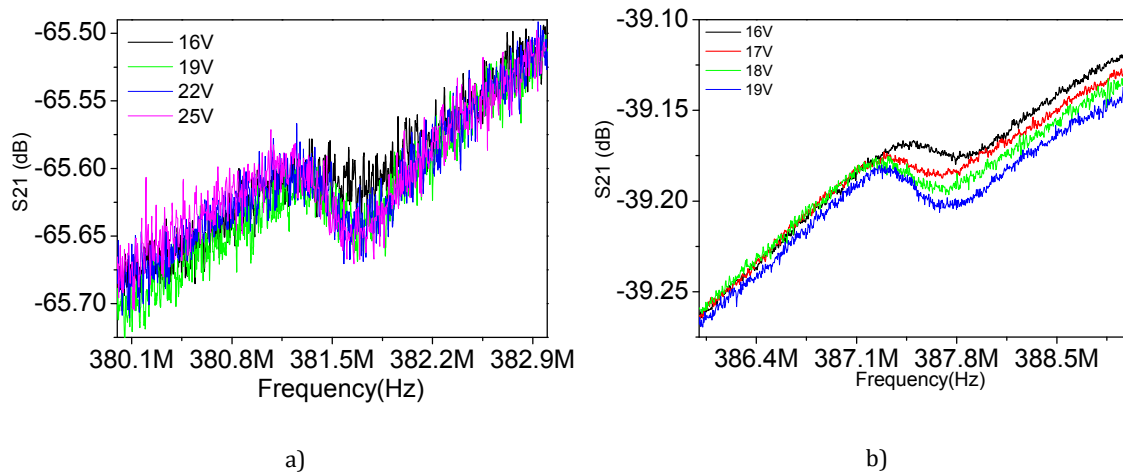
Figure 5.12 Measurements of the S_{21} for the stand alone Diablo resonator a) and the integrated with along the circuitry b)
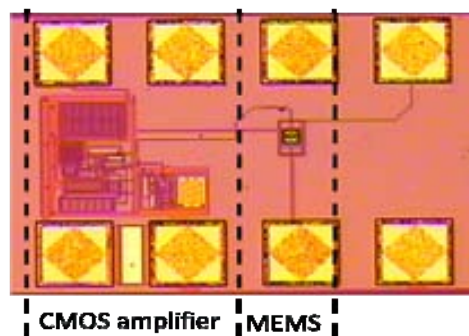
Figure 5.13 Optical image of the Hyperbolic resonator along with the amplification stage. The output of the resonator (electrodes) is connected to the input of the circuitry.

5.5 CONCLUSIONS

After giving a global vision of the efforts addressed to obtain frequency sources in the wireless communication range, our particular approach has been introduced. In this chapter, two resonators have been developed. The enhanced LBAR that is based on the most classical LBAR resonator has been designed and fabricated to operate in VHF range as it has been demonstrated in the characterization stage. The main problem of the fully integrated resonator is the anchoring losses and the high motional impedance.

The enhanced LBAR present the mass addition drawback. The mass added to the free ends of the arms decreases the resonant frequency. The mass addition is not included in the design equations and it forces a redesign to the structure to meet the frequency specifications. The hyperbolic resonator solves this problem by including all the

dimensions of the resonator into the design equations. Two prototypes of this device have been fabricated: the stand-alone resonator and the fully integrated prototype. The frequency response provide by the integrated approach (MEMS+IC) is clearer than the stand-alone resonator. Nevertheless, both results show the resonant peak around 385MHz with a poor resonant peak.
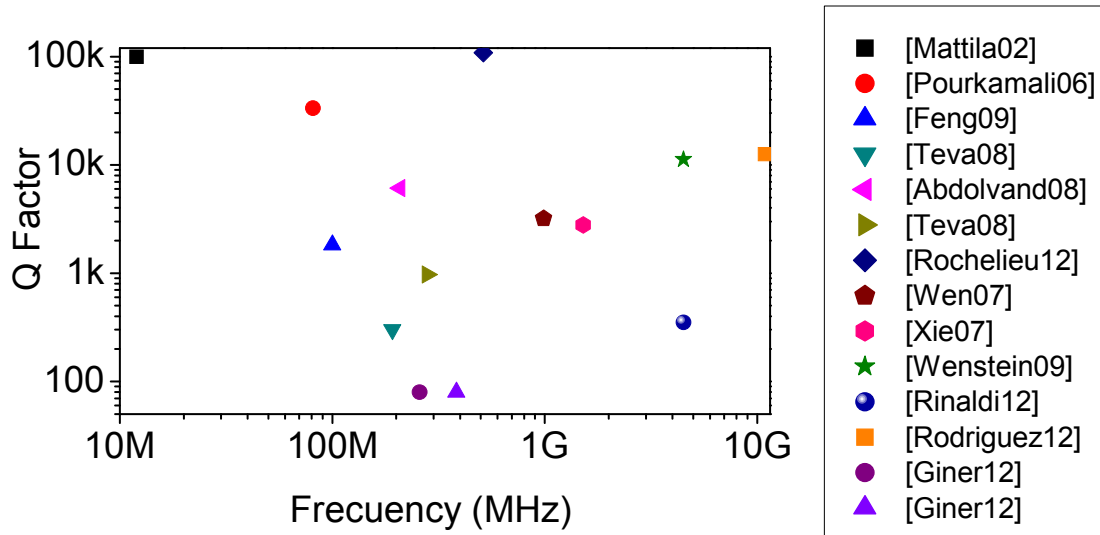
Figure 5.14 Overview of Q vs resonant frequency of the VHF, UHF and SHF resonators.

In Figure 5.14 an overview of some of the works referred to the VHF and UHF resonator presented in this chapter. Abscises denote the operating frequency and the vertical axe represent Q factor achieved. Note the resonators presented in this work are in the lower Q factor zone. The main reasons are the material properties and the non-optimized anchors. Further investigation of this resonator along with fully CMOS integration capability will enhance the Q factor until the communications suitable levels. On the other hand, the coupling area limits will improve the VHF and UHF resonators performance.

5.6 REFERENCES

[1] C. T. C. Nguyen, "MEMS technology for timing and frequency control," *Ultrasonics, Ferroelectrics and Frequency Control, IEEE Transactions on,* vol. 54, pp. 251-270, 2007.

[2] C. T. C. Nguyen, "RF MEMS for wireless applications," in *Device Research Conference, 2002. 60th DRC. Conference Digest*, 2002, pp. 9-12.

[3] A. Husain, J. Hone, H. W. C. Postma, X. M. H. Huang, T. Drake, M. Barbic, A. Scherer, and M. L. Roukes, "Nanowire-based very-high-frequency electromechanical resonator," *Applied Physics Letters,* vol. 83, pp. 1240-1242, 2003.

[4] X. L. Feng, M. H. Matheny, R. B. Karabalin, C. A. Zorman, M. Mehregany, and M. L. Roukes, "Silicon carbide (SiC) top-down nanowire electromechanical resonators," in *Solid-State Sensors, Actuators and Microsystems Conference, 2009. TRANSDUCERS 2009. International*, 2009, pp. 2246-2249.

[5] L. Wei-Chang, J. Yingqi, R. A. Schneider, H. G. Barrow, L. Liwei, and C. T. C. Nguyen, "Polysilicon-filled carbon nanotube grass structural material for micromechanical resonators," in *Micro Electro Mechanical Systems (MEMS), 2011 IEEE 24th International Conference on*, 2011, pp. 477-480.

[6] S. H. Lee, B. Min, S. S. Lee, S. I. Park, and K.-C. Lee, "High frequency carbon nanomechanical resonators embedded with carbon nanotube stiffening layers," *Applied Physics Letters,* vol. 97, pp. 183108-183108-3, 2010.

[7] W. Pengbo, Y. Xiaojun, J. Yingqi, L. Wei, and L. Liwei, "Electrostatic oscillation of CNT bundles," in *Micro Electro Mechanical Systems (MEMS), 2011 IEEE 24th International Conference on*, 2011, pp. 420-423.

[8] Y.-W. Lin, S.-S. Li, Z. Ren, and C. T. C. Nguyen, "Third-order intermodulation distortion in capacitively-driven VHF micromechanical resonators," in *Ultrasonics Symposium, 2005 IEEE*, 2005, pp. 1592-1595.

[9] J. R. Vig and K. Yoonkee, "Noise in microelectromechanical system resonators," *Ultrasonics, Ferroelectrics and Frequency Control, IEEE Transactions on,* vol. 46, pp. 1558-1565, 1999.

[10] T. O. Rocheleau, T. L. Naing, Z. Ren, and C. T. C. Nguyen, "Acoustic whispering gallery mode resonator with Q >109,000 at 515MHz," in *Micro Electro Mechanical Systems (MEMS), 2012 IEEE 25th International Conference on*, 2012, pp. 672-675.

[11] R. Abdolvand, H. Lavasani, G. Ho, and F. Ayazi, "Thin-film piezoelectric-on-silicon resonators for high-frequency reference oscillator applications," *Ultrasonics, Ferroelectrics and Frequency Control, IEEE Transactions on,* vol. 55, pp. 2596-2606, 2008.

[12] J. G. Rodriguez-Madrid, G. F. Iriarte, J. Pedros, O. A. Williams, D. Brink, and F. Calle, "Super-High-Frequency SAW Resonators on AlN/Diamond," *Electron Device Letters, IEEE,* vol. 33, pp. 495-497, 2012.

[13] R. Ruby, "A decade of FBAR success and what is needed for another successful decade," in *Piezoelectricity, Acoustic Waves and Device Applications (SPAWDA), 2011 Symposium on*, 2011, pp. 365-369.

[14]   M. Rinaldi, C. Zuniga, Z. Chengjie, and G. Piazza, "Super-high-frequency two-port AlN contour-mode resonators for RF applications," *Ultrasonics, Ferroelectrics and Frequency Control, IEEE Transactions on,* vol. 57, pp. 38-45, 2010.

[15]   C.-M. Lin, Y.-Y. Chen, V. V. Felmetsger, D. G. Senesky, and A. P. Pisano, "AlN/3C–SiC Composite Plate Enabling High-Frequency and High-Q Micromechanical Resonators," *Advanced Materials,* vol. 24, pp. 2722-2727, 2012.

[16]   L.-W. Hung and C. T. C. Nguyen, "Capacitive-piezoelectric AlN resonators with Q>12,000," in *Micro Electro Mechanical Systems (MEMS), 2011 IEEE 24th International Conference on*, 2011, pp. 173-176.

[17]   L. Yu-Wei, L. Sheng-Shian, R. Zeying, and C. T. C. Nguyen, "Low phase noise array-composite micromechanical wine-glass disk oscillator," in *Electron Devices Meeting, 2005. IEDM Technical Digest. IEEE International*, 2005, pp. 4 pp.-281.

[18]   D. Weinstein and S. A. Bhave, "Internal Dielectric Transduction in Bulk-Mode Resonators," *Microelectromechanical Systems, Journal of,* vol. 18, pp. 1401-1408, 2009.

[19]   D. Weinstein and S. A. Bhave, "Internal Dielectric Transduction of a 4.5 GHz Silicon Bar Resonator," in *Electron Devices Meeting, 2007. IEDM 2007. IEEE International*, 2007, pp. 415-418.

[20]   C. T. C. Nguyen, "Integrated Micromechanical Radio Front-Ends," in *VLSI Technology, Systems and Applications, 2008. VLSI-TSA 2008. International Symposium on*, 2008, pp. 3-4.

[21]   W.-L. Huang, Z. Ren, Y.-W. Lin, H.-Y. Chen, J. Lahann, and C. T. C. Nguyen, "Fully monolithic CMOS nickel micromechanical resonator oscillator," in *Micro Electro Mechanical Systems, 2008. MEMS 2008. IEEE 21st International Conference on*, 2008, pp. 10-13.

[22]   K.-L. Chen, S. Wang, J. C. Salvia, R. Melamud, R. T. Howe, and T. W. Kenny, "Wafer-Level Epitaxial Silicon Packaging for Out-of-Plane RF MEMS Resonators With Integrated Actuation Electrodes," *Components, Packaging and Manufacturing Technology, IEEE Transactions on,* vol. 1, pp. 310-317, 2011.

[23]   A. E. Franke, J. M. Heck, K. Tsu-Jae, and R. T. Howe, "Polycrystalline silicon-germanium films for integrated microsystems," *Microelectromechanical Systems, Journal of,* vol. 12, pp. 160-171, 2003.

[24]   J. Teva, G. Abadal, A. Uranga, J. Verd, F. Torres, J. L. Lopez, J. Esteve, F. Perez-Murano, and N. Barniol, "From VHF to UHF CMOS-MEMS monolithically integrated resonators," presented at the Micro Electro Mechanical Systems, 2008. MEMS 2008. IEEE 21st International Conference on, 2008.

[25]   J. Giner, A. Uranga, E. Marigo, J. L. Munoz-Gamarra, and N. Barniol, "UHF CMOS-MEMS bulk acoustic wave resonator," in *Frequency Control and the European Frequency and Time Forum (FCS), 2011 Joint Conference of the IEEE International*, 2011, pp. 1-4.

[26]   J. Giner, A. Uranga, J. L. Muñoz-Gamarra, E. Marigo, and N. Barniol, "VHF monolithically integrated CMOS-MEMS longitudinal bulk acoustic resonator," *Electronics Letters,* vol. 48, pp. 514-516, 2012.

[27]   J.L.Lopez, J.Verd, J.Teva, G.Murillo, J.Giner, F.Torres, A.Uranga, G. Abadal, and N.Barniol, "Integration of RF-MEMS Resonators on Submicrometric Commercial CMOS Technologies," *Journal of Micromechanical and Microengineering,* vol. 19, p. 10, 2009.

[28]   C. Wen-Chien, L. Ming-Huang, F. Weileun, and L. Sheng-Shian, "High-q integrated CMOS-MEMS resonators with deep-submicron gaps," in *Frequency Control Symposium (FCS), 2010 IEEE International*, 2010, pp. 340-343.

[29]   C. Wen-Chien, L. Ming-Huang, F. Weileun, and L. Sheng-Shian, "Realizing deep-submicron gap spacing for CMOS-MEMS resonators with frequency tuning capability via modulated boundary conditions," in *Micro Electro Mechanical Systems (MEMS), 2010 IEEE 23rd International Conference on*, 2010, pp. 735-738.

[30]   W.-C. Chen, C.-S. Chen, K.-A. Wen, L.-S. Fan, W. Fang, and S.-S. Li, "A generalized foundry CMOS platform for capacitively-transduced resonators monolithically integrated with amplifiers," in *Micro Electro Mechanical Systems (MEMS), 2010 IEEE 23rd International Conference on*, 2010, pp. 204-207.

[31]   T. Mattila, J. Kiihamäki, T. Lamminmäki, O. Jaakkola, P. Rantakari, A. Oja, H. Seppä, H. Kattelus, and I. Tittonen, "A 12 MHz micromechanical bulk acoustic mode oscillator," *Sensors and Actuators A: Physical,* vol. 101, pp. 1-9, 2002.

[32]   S. Pourkamali, G. K. Ho, and F. Ayazi, "Low-Impedance VHF and UHF Capacitive Silicon Bulk Acoustic-Wave Resonators; Part II: Measurement and Characterization," *Electron Devices, IEEE Transactions on,* vol. 54, pp. 2024-2030, 2007.

[33]   S. Pourkamali, G. K. Ho, and F. Ayazi, "Low-Impedance VHF and UHF Capacitive Silicon Bulk Acoustic Wave Resonators; Part I: Concept and Fabrication," *Electron Devices, IEEE Transactions on,* vol. 54, pp. 2017-2023, 2007.

[34]   X. L. Feng, R. R. He, P. D. Yang, and M. L. Roukes, "Quality Factors and Energy Losses of Single-Crystal Silicon Nanowire Electromechanical Resonators," in *Solid-State Sensors, Actuators and Microsystems Conference, 2007. TRANSDUCERS 2007. International*, 2007, pp. 1325-1326.

[35]   J. Teva, G. Abadal, A. Uranga, J. Verd, F. Torres, J. L. Lopez, J. Esteve, F. Perez-Murano, and N. Barniol, "VHF CMOS-MEMS resonator monolithically integrated in a standard 0.35um CMOS technology," in *Micro Electro Mechanical Systems, 2007. MEMS. IEEE 20th International Conference on*, 2007, pp. 779-782.

[36]   W. Jing, Z. Ren, and C. T. C. Nguyen, "1.156-GHz self-aligned vibrating micromechanical disk resonator," *Ultrasonics, Ferroelectrics and Frequency Control, IEEE Transactions on,* vol. 51, pp. 1607-1628, 2004.

[37]   W. Jing, R. Zeying, and C. T. C. Nguyen, "1.14-GHz self-aligned vibrating micromechanical disk resonator," in *Radio Frequency Integrated Circuits (RFIC) Symposium, 2003 IEEE*, 2003, pp. 335-338.

[38]   J. Teva, G. Abadal, A. Uranga, J. Verd, F. Torres, J. L. Lopez, J. Esteve, F. Perez-Murano, and N. Barniol, "From VHF to UHF CMOS-MEMS monolithically integrated resonators," in *Micro Electro Mechanical Systems, 2008. MEMS 2008. IEEE 21st International Conference on*, 2008, pp. 82-85.

[39]   H. Li-Wen, C. T. C. Nguyen, Y. Xie, Y.-W. Lin, S.-S. Li, and Z. Ren, "UHF Micromechanical Compound-(2,4) Mode Ring Resonators With Solid-Gap Transducers," in *Frequency Control Symposium, 2007 Joint with the 21st European Frequency and Time Forum. IEEE International*, 2007, pp. 1370-1375.

[40]   R. C. Ruby, P. Bradley, Y. Oshmyansky, A. Chien, and J. D. Larson, III, "Thin film bulk wave acoustic resonators (FBAR) for wireless applications," in *Ultrasonics Symposium, 2001 IEEE*, 2001, pp. 813-821 vol.1.

[41]   W. Weaver Jr, S. P. Timoshenko, and D. H. Young, Eds., *Vibration Problems in Engineering*. New York: Wiley, 1992, p.^pp. Pages.

[42]   Y. Youngjoo, P. Myoungkyu, and C. Kukjin, "A sticking model of suspended polysilicon microstructure including residual stress gradient and postrelease temperature," *Microelectromechanical Systems, Journal of,* vol. 7, pp. 339-344, 1998.

[43]   K. Y. Yasumura, T. D. Stowe, E. M. Chow, T. Pfafman, T. W. Kenny, B. C. Stipe, and D. Rugar, "Quality factors in micron- and submicron-thick cantilevers," *Microelectromechanical Systems, Journal of,* vol. 9, pp. 117-125, 2000.

[44]   L. Sheng-Shian, L. Yu-Wei, X. Yuan, R. Zeying, and C. T. C. Nguyen, "Micromechanical "hollow-disk" ring resonators," in *Micro Electro Mechanical Systems, 2004. 17th IEEE International Conference on. (MEMS)*, 2004, pp. 821-824.

[45]   N. Lobotniu and E. Garcia, *Mechanics of Microelectromechanical Systems*: Kluwer Academic Publishers, 2005.

[46]   A. Uranga, J. Teva, J. Verd, J. L. Lopez, F. Torres, G. Abadal, N. Barniol, J. Esteve, and F. Perez-Murano, "CMOS integrated MEMS resonator for RF applications," in *Circuits and Systems, 2006. ISCAS 2006. Proceedings. 2006 IEEE International Symposium on*, 2006, p. 4 pp.

CONCLUSIONS

This PhD thesis has focused on developing CMOS resonator and filters for RF application. This thesis explore most far fields such as mechanical and electrical coupling and novel topologies to reach the VHF and UHF frequencies.

The results obtained can be summarized point by point in the following list:

The electromechanical model of resonator has been studied and the model and measurement can be fitted for almost all the designs presented in this work.

The electromechanical model has been modified in order to include the phase inversion mechanism for simple resonator, and coupled resonator filter. The model can be used for filter if the motional current is read at the output electrode or if the current is read in one of the movable resonator in the electrostatic filters.

The mechanical and electrostatical coupling has been implemented successfully using the CMOS-MEMS approach to obtain different HF filters. In particular two types of coupler have been developed: the U-Filter and the V-Filter. The U-filter has shown better performance in terms of narrow bandwidth and ripple (200kHz BW over 25MHz center frequency and a ripple less that 0.1dB) in its stand-alone version. The V-coupler is more sensitive to the fabrication tolerances.

The mechanical coupling has motivated the explorations of the applicability of the low-velocity coupling in CMOS-MEMS resonator to obtain narrow bandwidth filter.

The integration of the filters with the circuitry has been shown to increase the performance and to widen the applications. Through this SoC approach, a bandpass filter with a very competitive SF of 2.49 has been obtained. Furthermore, two filters parallel coupled have demonstrated the feasibility of a dual band filter. The dual band filter has shown very good performances compared with the current state of the art (see conclusion is Chapter 4).

The parallel filter presented in this work reach a very high out of band rejection of 52dB positioning it between the best filters.

Different VHF and UHF resonator has been designed fabricated and measured. Novel topologies and expressions have been presented as a first time to include all the dimensions in a LBAR design expressions. Resonator has show poor quality factor due to anchor losses experienced by the structures.

Comparison between results obtained in this thesis and the current state of the art is detailed in filter chapter (Chapter 4) and in the VHF and UHF resonator chapter (chapter 5)

FINAL REMARKS

In this work the frequency control in coupled MEM resonator filter and bulk acoustic resonator has been demonstrated. However, we consider that some issues should be taken into account in further developments of RF MEMS by means of AMS CMOS technology.

Despite the advantages in terms of integration, the use of CMOS technology offers, the thin structural layers used to fabricate the filters and the resonator is a limitation. In electrostatically excited and capacitively read resonators the large motional resistances of our devices introduces the mismatching issues between the mechanical part and circuitry or measurement equipment. In this work, the use of circuitry has solved partially this problem. However, in the future, the IC and MEMS designers have to be work together in order to obtain a 0-insertion losses SoC RF building block. MEMS designer has to achieve lower motional resistance (not necessarily in the 50Ω range) by reducing gaps (using other sub-micrometric technologies and the IC designer has to redesign the amplifier in order to match the input impedance to the motional impedance.

On the other side, due to the scaling problems related with the electrostatically actuated and read resonators (feedthrough, decreasing coupling area) other transduction mechanisms such as piezo resistive and resonant gate transistors have to be explored.

Finally, the development of the 0-level package is an important issue. Only the vacuum encapsulation can elevate the performance of our CMOS MEMS devices up to nowadays of chip components.

PUBLICATION LIST

JOURNALS

J. Giner, A. Uranga, J. L. Muñoz-Gamarra, E. Marigo, and N. Barniol, "VHF monolithically integrated CMOS-MEMS longitudinal bulk acoustic resonator," *Electronics Letters,* vol. 48, pp. 514-516, 2012.

J. Giner, A. Uranga, J. L. Muñoz-Gamarra, E. Marigo, and N. Barniol, "A fully integrated programmable dual-band RF filter based on electrically and mechanically coupled CMOS-MEMS resonators " *Journal of Micromechanical and Microengineering* vol. 22, 2012.

J. Giner, A. Uranga, E. Marigò, J. L. Muñoz-Gamarra, E. Colinet, N. Barniol, and J. Arcamone, "Cancellation of the parasitic feedthrough current in an integrated CMOS–MEMS clamped-clamped beam resonator," *Microelectronic Engineering,* 2012.

E. Marigó, J. L. Muñoz-Gamarra, G. Vidal, **J. Giner,** F. Torres, A. Uranga, and N. Barniol, "Cross coupled beams CMOS–MEMS resonator for VHF range with enhanced electrostatic detection," Microelectronic Engineering, vol. 88, pp. 2325-2329, 2011.

J. Giner, A. Uranga, F. Torres, E. Marigo, and N. Barniol, "Fully CMOS integrated bandpass filter based on mechanical coupling of two RF MEMS resonators," Electronics Letters, vol. 46, pp. 640-641, 2010.

J. L. López**, J. Giner**, G. Murillo, F. Torres, E. Marigó, A. Uranga, G. Abadal, and N. Barniol, "Third-mode 48MHz free–free beam resonator used as a RF balun," Microelectronic Engineering, vol. 87, pp. 1256-1258, 2010.

E. Marigó, J. L. Lopez, G. Murillo, F. Torres, **J. Giner**, A. Uranga, G. Abadal, J. Esteve, and N. Barniol, "Zero-level packaging of MEMS in standard CMOS technology," Journal of Micromechanics and Microengineering, vol. 20, p. 064009, 2010.

J. L. Lopez, J. Verd, A. Uranga, **J. Giner,** G. Murillo, F. Torres, G. Abadal, and N. Barniol, "A CMOS-MEMS RF-Tunable Bandpass Filter Based on Two High-Q 22-MHz Polysilicon Clamped-Clamped Beam Resonators," Electron Device Letters, IEEE, vol. 30, pp. 718-720, 2009.

J.L.Lopez, J.Verd, J.Teva, G.Murillo, **J.Giner**, F.Torres, A.Uranga, G. Abadal, and N.Barniol, "Integration of RF-MEMS Resonators on Submicrometric Commercial CMOS Technologies," Journal of Micromechanical and Microengineering, vol. 19, p. 10, 2009.

A.Uranga, J.Verd, J.L.Lopez, J.Teva, F.Torres, **J.Giner**, G.Murillo, G.Abadal, and N.Barniol, "Electrically Enhanced Readout System for a High Frequency CMOS-MEMS Resonator," ETRI Journal, vol. 31, no.4, pp. 478-480, August 2009.

G. Murillo, G. Abadal, F. Torres, J. L. Lopez, **J. Giner,** A. Uranga, and N. Barniol, "Harvester-on-chip: Design of a proof of concept prototype," Microelectronic Engineering, vol. 86, pp. 1183-1186, 2009.

CONFERENCES

J. Giner, A. Uranga, J. L. Muñoz-Gamarra, E. Marigó, E. Colinet, J. Arcamone, and N. Barniol, "Cancellation of the Parasitic Current in an Integrated CMOS-MEMS Clamped-Clamped Beam Resonator," *37th International Conference on Micro and Nano Engineering11-13 September* 2011

E. Marigó a, J.L. Muñoz-Gamarra, **J. Giner**, A. Uranga and N. Barniol, "CMOS-MEMS Dogbone resonator with capacitive and piezoresistive sensing capabilitie Participation, *37th International Conference on Micro and Nano Engineering11-13 September* 2011

J. Giner, A. Uranga, E. Marigo, J. L. Munoz-Gamarra, and N. Barniol, "UHF CMOS-MEMS bulk acoustic wave resonator," in *Frequency Control and the European Frequency and Time Forum (FCS), 2011 Joint Conference of the IEEE International*, 2011, pp. 1-4. 2011

J. Giner, A. Uranga, F. Torres, E. Marigo, J. L. Munoz Gamarra, and N. Barniol, "A CMOS-MEMS filter using a V-coupler and electrical phase inversion," in *Frequency Control Symposium (FCS), 2010 IEEE International,* pp. 344-348, , 2010,

J. L. Muñoz-Gamarra, E. Marigo, **J. Giner**, A. Uranga, F. Torres, and N. Barniol, "Characterization of CMOS-MEMS resonator by pulsed mode electrostatic actuation," in *Frequency Control Symposium (FCS), 2010 IEEE International*, 2010, pp. 415-418.

E. Marigo, J. L. Muñoz-Gamarra, J. Giner, J. L. Lopez, F. Torres, A. Uranga, N. Barniol, and J. Verd, "Linear operation of a 11MHz CMOS-MEMS resonator," in *Frequency Control Symposium (FCS), 2010 IEEE International*, 2010, pp. 158-161.

J. Giner, A. Uranga, E. Marigó, F. Torres, N. Barniol, "A Fully Integrated Filter based on two Mechanical Coupled Lateral Microelectromechanical Resonators", *Design Circuits and Integrated Systems,* November 2010

Uranga, J. Verd, **J. Giner**, E. Marigó, J. Muñoz, N. Barniol; " RF CMOS MEMS oscillator with enhanced phase noise capabilities", *Design Circuits and Integrated Systems,* November 2010

E. Marigó, J.L. Muñoz-Gamarra, G. Vidal, **J. Giner**, F. Torres, A. Uranga, N. Barniol, " Cross Coupled Beams CMOS-MEMS Resonator for VHF Range with Enhanced Electrostatic Detection" *36th International Conference on Micro & Nano Engineering (MNE)* 2010

J.L. López, E. Marigó, **J. Giner,** J.L. Muñoz-Gamarra, F. Torres, A. Uranga, N. Barniol " CMOS-MEMS free-free beam resonators", *40th European Solid-State Device Research Conference (ESSDERC)* 2010

G. Murillo, J. Agustí, G.Abadal, F.Torres, **J. Giner**, E, Marigó, A.Uranga, N.Barniol, "Integration of an improved Harvester-on-Chip core dice on commercial SOI-based MEMS technology" *The 9th International Workshop on Micro and Nanotechnology for Power Generation and Energy Conversion Applications: PowerMEMS* 2009

J. Giner, A. Uranga, J. Verd, G, Murillo, E. Marigó, F. Torres, N. Barniol, G. Abadal "A Fully Integrated VHF electrically coupled Microelectromechanical Filter", *XXIV Conference on Design of Circuits and Integrated Systems*, 2009

J. Giner, A.Uranga, F. Torres, E. Marigó, G. Murillo, G.Abadal and N.Barniol, "A fully integrated CMOS-MEMS UHF Ring Resonator", *35th International Conference on Micro & Nano Engineering* (MNE), 2009

LL. Lopez, **J. Giner**, G. Murillo, F. Torres, A. Uranga, G. Abadal, N. Barniol, " Third-Mode 48 MHz Free-Free Beam Resonator used as a RF balum", 35th International Conference on Micro & Nano Engineering (MNE) 2009

J. L. Lopez, J. Verd, E. Marigo, A. Uranga, G. Murillo, **J. Giner**, F. Torres, G. Abadal and N. Barniol, "Title: Monolithically Integrated Double-Ended Tuning Fork- Based Oscillator with Low Bias Voltage in Air", *Eurosensors XXIII,* 2009

J. L. Lopez, J. Verd, A. Uranga, G. Murillo, **J. Giner**, E. Marigó, F. Torres, G. Abadal and N. Barniol, "VHF Band-Pass Filter Based on a Single CMOS-MEMS Double-Ended Tuning Fork Resonator", *Eurosensors XXIII,* 2009

J. Giner, A. Uranga, J. Verd, G. Murillo E. Marigó, G. Abadal1, F. Torres, and N. Barniol, "Towards VHF Fully Integrated Microelectromechanical Filters", *Memswave International Symposium on RF MEMS and RF microsystems,* 2009

J. L. Lopez, J. Verd, **J. Giner**, A. Uranga, G. Murillo, E. Marigo, F. Torres, G. Abadal, and N. Barniol, "High Q CMOS-MEMS resonators and its applications as RF tunable band-pass filters," in *Solid-State Sensors, Actuators and Microsystems Conference, 2009. TRANSDUCERS 2009. International*, 2009, pp. 557-560.

G. Murillo, G. Abadal, F. Torres, J. Ll. Lopez, **J. Giner**, A. Uranga and N. Barniol, "On the monolithic integration of CMOS-MEMS energy scavengers Participation *Conference on Design of Circuits and Integrated Systems* , 2008

J. Giner, C. Pey, H. Campanella, J. Esteve, A. Uranga, J. Ll. Lopez, G. Murillo, N. Barniol, G. Abadal, "2.25GHz FBAR 2mW Differential Oscillator", *Conference on Design of Circuits and Integrated Systems* , 2008

Authors: J. Ll. Lopez, G. Murillo, **J. Giner**, A. Uranga, G. Abadal, N. Barniol, "Fabrication of MEMS Resonators in the HF and VHF Range on a 0.18um CMOS Commercial Technology", *Conference on Design of Circuits and Integrated Systems* , 2008

G. Murillo, G.Abadal, F.Torres, J.Ll. Lòpez, **J. Giner**, H. Campanella, A.Uranga, J. Esteve, N.Barniol, " Novel designs of piezoelectric scavengers using FBAR technology, *The 8th International Workshop on Micro and Nanotechnology for Power Generation and Energy Conversion Applications: PowerMEMS* 2008

G. Murillo, G. Abadal, F. Torres, J.Ll. Lòpez, **J. Giner**, A. Uranga, N. Barniol, " Harvester-on-Chip: Design of a proof of concept prototype" *34th International Conference on Micro and nano engineering MNE* 2008
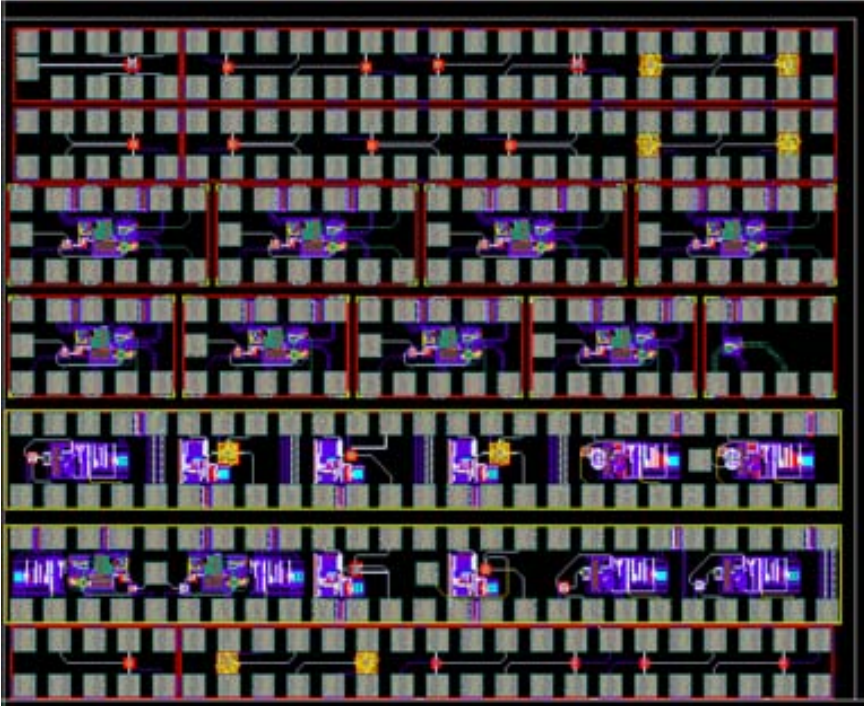
G. Murillo, G.Abadal, F.Torres, J.Ll. Lòpez**, J. Giner**, A.Uranga, N.Barniol, " Free-free beam resonator with optimized nodal anchors integrated in a commercial CMOS technology", *EuroSensors XXII, 2008*

J. L. Lopez, F. Torres, G. Murillo, **J. Giner**, J. Teva, J. Verd, A. Uranga, G. Abadal, and N. Barniol, "Double-ended tuning fork resonator in 0.35um CMOS technology for RF applications," in *Research in Microelectronics and Electronics, 2008. PRIME 2008. Ph.D.*, 2008, pp. 89-92.
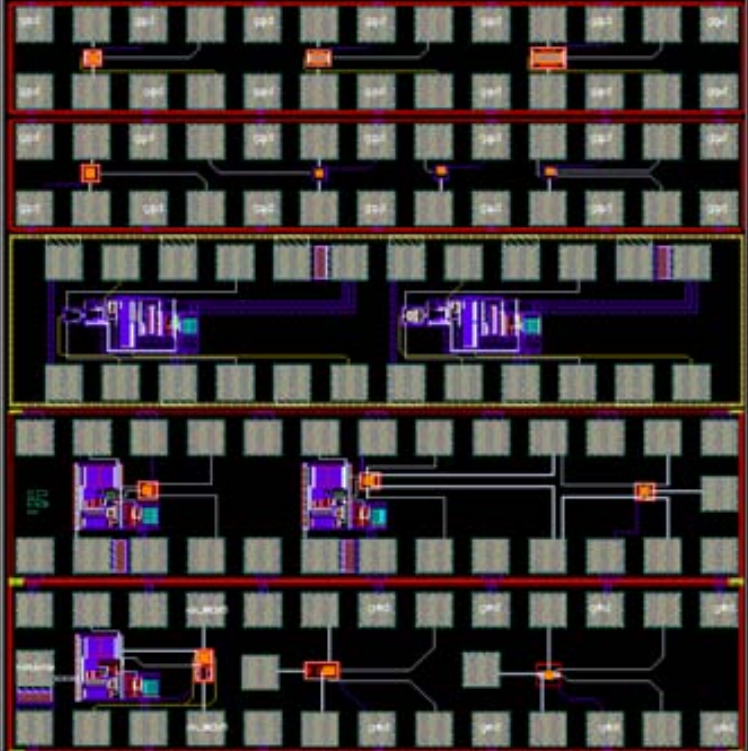
ANNEX 1 RUNS DESCRIPTION

This annex describes all the different runs that contain all the MEMS implemented along this thesis.
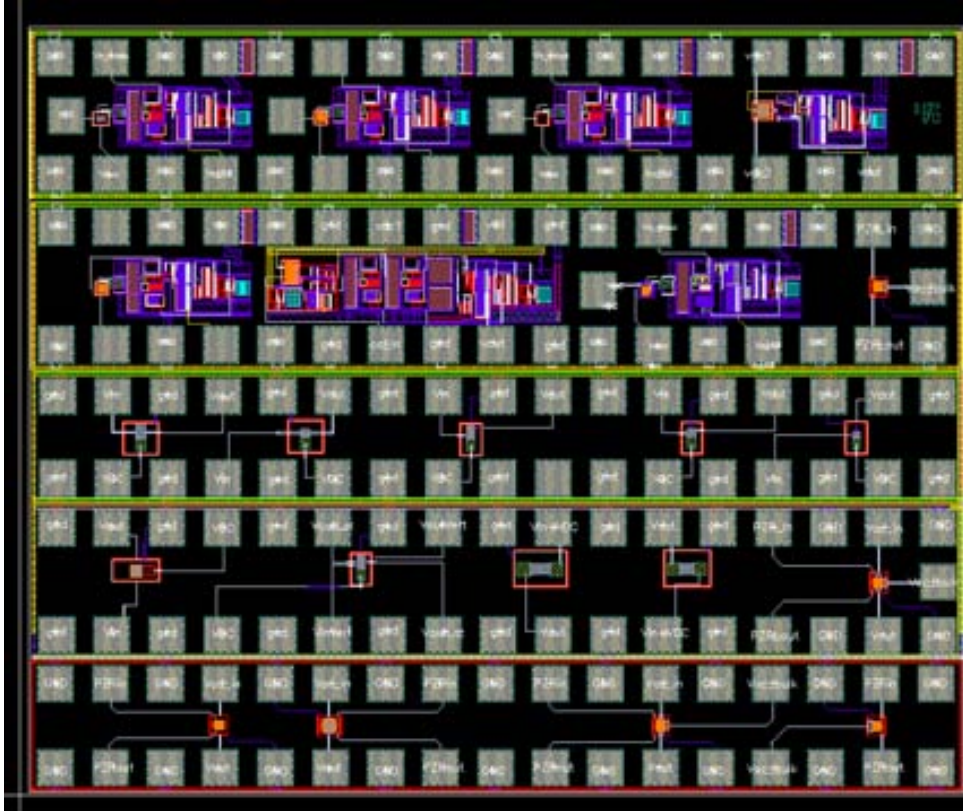
Run Code	12281	Technology	AMSC35B4C3
Date	March 2009	Area	2840µm x 3678µm
Run Description	This chip includes different coupled structures such as U-Filter with different coupling point, V-Filter, Coupled Beams, Electrostatic coupled filters and high frequency ring resonators. In addition, from the 3 to 6 row, MEMS have been integrated with the circuitry to fabricate oscillator and to enhance the aforementioned MEMS performance.		

Objectives	Study of different mechanical and electrical couplings Exploring different type of high frequency resonators
Relevant Devices	U-Filter coupled at different locations (Chapter 4) V- Filter (Chapter 4) Electrostatical coupled resonator filter (Poly1-Poly2) (Chapter 4)
Publications	J. Giner et.al, "A CMOS-MEMS filter using a V-coupler and electrical phase inversion," International Frequency Control Symposium (IFCS) 2010 J. Giner et. al "Fully CMOS integrated bandpass filter based on mechanical coupling of two RF MEMS resonators," *Electronics Letters,* 2010. J.Giner at. Al. A Fully Integrated Filter based on two Mechanical Coupled Lateral Microelectromechanical Resonators" DCIS 2010
Designers	Carles Pey, Arantxa Uranga, Eloi Marigò, Joan Giner

Run Code	12350	Technology	AMSC35B4C3
Date	December 2009	Area	3022µm x 3360µm
Run Description	The chip includes different mechanical structures such us mechanically coupled resonators and simple beam resonators connected differential amplifiers to observe the performance		

Objectives	Use a differential amplifier to subtract the parasitic capacitance. Study of the longitudinal acoustic resonance into CMOS poly layer
Relevant Devices	Dual band U-Filter-based (Chapter 4) Enhanced LBAR (Chapter 5) Hyperboloid LBAR (Chapter 5)
Publications	J. Giner et. al "A fully integrated programmable dual-band RF filter based on electrically and mechanically coupled CMOS-MEMS resonators " JMM 2012 J. Giner et.al "VHF monolithically integrated CMOS-MEMS longitudinal bulk acoustic resonator," Electronics Letters 2012. J. Giner et.al. "UHF CMOS-MEMS bulk acoustic wave resonator," IFCS 2011
Designers	Arantxa Uranga, Eloi Marigò, Joan Giner, Gabriel Vidal, Francesc Torres

Run Code	12434	Technology	AMSC35B4C3
Date	December 2010	Area	2058μm x 1890μm
Run Description	The chip contains four-electrodes C-C Beams		

Objectives	cancellation of the feedthrough current of a C-C Beam resonator intrinsically by using four electrodes.
Relevant Devices	Four electrodes C-C Beam (Chapter 3)
	J. Giner et. al "Cancellation of the parasitic feedthrough current in an integrated CMOS–MEMS clamped-clamped beam resonator," *MEE, pon el título de la revista*2012. J. Giner et.al "Cancellation of the Parasitic Current in an Integrated CMOS-MEMS Clamped-Clamped Beam Resonator," *MNE* 2011.
Designers	Joan Giner, Gabriel Vidal, Eloi Marigò, Arantxa Uranga

Run Code	12462	Technology	AMSC35B4C3
Date	April 2011	Area	2000µm x 1500µm
Run Description	The chip includes a variation of the electrostatic coupled resonator filter, LBAR resonators anchored by metal bias		

Objectives	Find the optimum dimensions for the electrostatic coupled resonator filter.
Relevant Devices	Poly1-Poly1 electrostatic filter (100nm) (Chapter 4)
	Poly1-Poly1 electrostatic filter (350nm) (Chapter 4)
Designers	Joan Giner, Gabriel Vidal, Eloi Marigò

Run Code	3335	Technology	AMSC35B4C3
Date	March 2012	Area	2000µm x 2466µm
Run Description	This chip includes differential amplifier with enhanced LBAR resonators.

Objectives	Cancellation of the feedthrough current in the LBAR resonators by means of the use of a differential amplifier
Relevant Devices	Differential amplifier with two enhanced LBAR (chapter 5)
Designers	Joan Giner, Eloi Marigò, Arantxa Uranga